Mode-locked quantum-dot lasers and amplifiers: Ultra-short pulse generation, amplification and stabilization

Modengekoppelte Quantenpunktlaser und Verstärker: Erzeugung, Verstärkung und Stabilisierung ultra-kurzer optischer Pulse

Zur Erlangung des Grades eines Doktors der Naturwissenschaften (Dr. rer. nat.)
genehmigte Dissertation von Dipl.-Phys. Lukas Drzewietzki aus Nikolai
2015 — Darmstadt — D 17

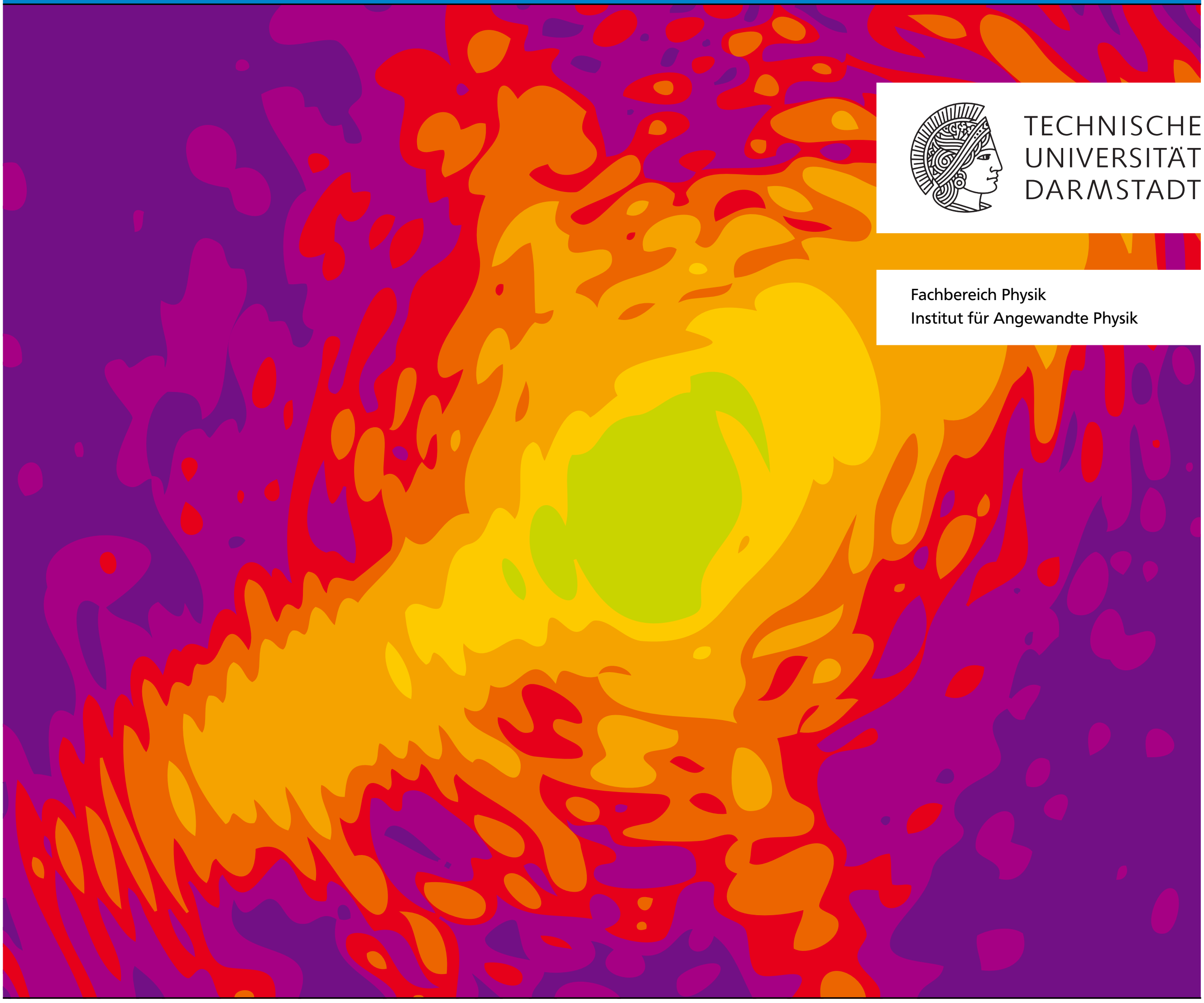

TECHNISCHE
UNIVERSITÄT
DARMSTADT

Fachbereich Physik
Institut für Angewandte Physik

Mode-locked quantum-dot lasers and amplifiers: Ultra-short pulse generation, amplification and stabilization
Modengekoppelte Quantenpunktlaser und Verstärker: Erzeugung, Verstärkung und Stabilisierung ultra-kurzer optischer Pulse

Genehmigte Dissertation von Dipl.-Phys. Lukas Drzewietzki aus Nikolai

1. Gutachten: Prof. Dr. Wolfgang Elsäßer
2. Gutachten: Prof. Dr. Thomas Walther

Tag der Einreichung: 17.12.2014
Tag der Prüfung: 16.02.2015

Darmstadt — D 17

Bitte zitieren Sie dieses Dokument als:
URN: urn:nbn:de:tuda-tuprints-46759
URL: http://tuprints.ulb.tu-darmstadt.de/4675

Erklärung zur Dissertation

Hiermit versichere ich, die vorliegende Dissertation ohne Hilfe Dritter nur mit den angegebenen Quellen und Hilfsmitteln angefertigt zu haben. Alle Stellen, die aus Quellen entnommen wurden, sind als solche kenntlich gemacht. Diese Arbeit hat in gleicher oder ähnlicher Form noch keiner Prüfungsbehörde vorgelegen.

Darmstadt, den 31.03.2015

(Lukas Drzewietzki)

Acknowledgment

I am thankful for all those people who have supported me in various ways over the past years and thus allowed the development and completion of this work.

- First of all I would like to thank my supervisor Prof. Dr. Wolfgang Elsäßer for the opportunity to conduct research in his group, for guidance and support and especially for the possibility to participate in the full spectrum of scientific life. In particular the manifold possibilities of attendance in scientific conferences and project meetings were a valuable experience.

- I thank Prof. Dr. Thomas Walther for the interest in my work and for kindly taking over the second assessment.

- I thank Dr. Stefan Breuer for the manifold of valuable scientific discussions, for his diversity of ideas and in particular for his ability to pinpoint the essentials and his ability to evaluate topics in a wide context.

- I thank the group of semiconductor optics for the possibility to get insight into a variety of topics and for the stimulating discussions.

- I thank our secretary for the support in a variety of organizational as well as non-organizational matters.

- I thank all the partners participating in the *FAST-DOT* project which I could be part of. It was a great pleasure to work with all these great people. In particular, I thank the *Semiconductor Integrated Optoelectronics and Photonics Group, Department of Electronics and Telecommunications, Politecnico di Torino, Italy* for the great collaboration and *III-V Lab, France* for the scientific stay in Palaiseau.

- I thank *Innolume* and *3-5 Lab* for providing and processing of the devices making this work possible.

- I thank the people of the precision mechanics workshop for the great and timely work and for bearing my projects. I also thank the people of both electronics workshops for providing valuable knowledge of the various peculiarities of electronics.

- I also want to thank all the individuals I became acquainted with during the past years in this vivid group. It was a pleasure to get to know you all.

Finally, I want to thank my parents for allowing me to make all this possible and also to my brother.

Contents

1 Introduction

> The noblest pleasure is the joy of understanding.
>
> Leonardo da Vinci

Ultra-short pulse lasers have been used to provide new insights in physics [1,2], biology [3], medicine [4], chemistry [5] and various other disciplines as a highly valuable tool [6]. Besides this supportive role as imaging or spectroscopic systems in the process of gaining knowledge they are also employed in the large field of telecommunications and signal processing [7,8]. A variety of properties are offered by these laser sources being important for a large field of applications. Ultra-short pulses are employed in time-domain spectroscopy [9] or nonlinear imaging [3], high repetition rates (RRs) are used for frequency comb sources [10], low RRs are used for life-time spectroscopy [11], high peak power is used for nonlinear imaging or nano-surgery [12], low optical line-widths are used for for multi-wavelength spectroscopy [13], low amplitude jitter (AJ) and low timing jitter (TJ) are used for data transmission and optical sampling [8,14], compactness and low fabrication cost are relevant for cost-sensitive applications and robustness and ease of operation is important for applications requiring long life-span sources.

One type of the most powerful ultra-short pulse generators are represented by **solid-state lasers (SSLs)** [15,16]. They offer pulse-widths in the single-digit femto-second range, very high peak power in the single-digit mega-Watt range [17] and very low TJ in the two-digit attosecond range [18]. However, these laser systems exhibit limitations including the overall cost, the increased dimensions, the complexity and the pre-alignment requirements. All these points mainly result from the multiple required optical elements of such laser systems. Furthermore, electrical synchronization requires additional opto-electrical components.

In contrast, pulsed **semiconductor lasers (SCLs)** offer the potential for the highest compactness, integrability, robustness and ease of operation together with optional direct electrical modulation capability and high wall-plug efficiency. Fabrication costs are generally lower. Two dominant pulse generation techniques are Q-switching and the various types of **mode locking (ML)** [19]. ML allows the convenient generation of a stable train of ultra-short pulses and was proposed 1964 in [20]. The **passive mode locking (PML)** relies on nonlinear losses and can be realized by Kerr-lens ML for SSLs or by an intra-cavity saturable absorber for SCLs. A mode-locked SCL consists of two optically connected sections forming the cavity: An electrically driven gain section and a electrically negatively biased saturable absorber section. PML offers the shortest-pulses due to the fast carrier dynamics and the highest RR due to the short monolithic cavities. Mode-locked SCLs based systems also offer the possibility of generation of peak power in the single-digit kilowatt range by additional external dispersion management and amplification stages [21].

The recent generation of SCLs is represented by **quantum-dot (QD)** based SCLs [22] which exhibit peculiar benefits for ML operation as well as a broadly tailorable emission wavelength in a range of 1050 nm to 1320 nm and also at 1550 nm [23] which is beneficial for bio-medical applications [24, 25]. Starting with the realization of the first semiconductor laser diode in 1962 [26], the proposal of a hetero-junction laser [27] massively increased efficiency. The demonstration of a double-hetero-structure laser [28] further increased efficiency leading to the shrinkage of the dimensionality of the active medium towards quantum-well lasers [29]. Hereby, quantum size effects take place if the dimension of the charge carrier confinement is reduced to the de Broglie wavelength of these charge carriers which is in the order of 10-20 nm. The theoretical electron and hole density of states (DOS) is then no longer a continuum but partially discrete as given by the quantum mechanical solution of a particle in a potential well. Extending this carrier confinement to three dimensions leads to QDs which were first theoretically investigated in [30] and first demonstrated in [31]. QD lasers are found to exhibit very broad gain bandwidths [32, 33] originating from the dot size dispersion which occurs during the Stranski-Kastranov growth process by molecular beam epitaxy (MBE). This broad gain bandwidth offers the additional possibility of wavelength tunability.

Passive ML is not an per se stable process but requires a delicate balance of a variety of parameters [34]. Indeed, since the early days of PML, undesired **amplitude instabilities** often represented by Q-switching (QS) or Q-switched mode-locking (QS ML) have been a major concern [35]. Also today, stability investigations of QD based SCLs [36, 37] are an important topic in experiment and theory. If stability is not achieved by design subsequent measures have to be taken. For example, stabilization by the use of an active opto-electrical feedback loop is a well-known concept and has been successfully applied to suppress amplitude instabilities of a SSL by gain control [38]. Hereby, PML SCLs offer the convenient advantage of being controlled directly and electrically by two different methods. They can be controlled by the the pumping current and by the bias voltage applied to the saturable absorber. Furthermore, the latter method allows higher control bandwidths due to the instantaneousness of the voltage based electric field. In contrast the current is limited by carrier relaxation times.

In this work, a novel, simple and passive opto-electrical control-loop is presented, investigated and explained which is able to suppress or eliminate amplitude instabilities thus accessing the increased potential of mode-locked lasers (MLLs) which therefore is investigated in the following.

One of the targets of recent QD based pulse emitters is to access applications that are currently covered by SSLs by **generation of ultra-short pulses and high peak power**. One important application is bio-medical nonlinear microscopy where cheap, compact and robust pulse sources are beneficial for widespread use of such techniques. The use of femto-second SSLs as excitation sources has allowed to improve the resolution of microscopy by multi-photon excitation or by exploiting non-linear excitation effects including second harmonic generation [39, 40]. Hereby, QD based MLL in particular offer the ideal wavelength range allowing for deep penetration depths [24, 25].

In this work, the generation of ultra-short pulses by novel gain-guided tapered MLL [41] will be investigated with an emphasis on stability, pulse-width and peak power. These gain-guided structures offer the benefit of a simplified fabrication process. Furthermore, amplification performance of novel gain-guided tapered semiconductor optical amplifiers (SOAs) will be investigated to increase the peak-power towards values which offer immediate application potential.

The **timing stability or TJ** is an important property of an optical pulse train for any kind of time-critical applications including optical sampling, clock recovery and optical comb generation [42, 43]. Although mode-locked SSL intrinsically offer the lowest TJ due to the high peak power and low pulse width [44] the mentioned advantages of mode-locked SCLs still apply. To reduce the TJ of mode-locked SCLs a variety of experimental possibilities exists [5]. Hereby, **optical or opto-electrical feedback** plays an recurring and important role. Initially, in 1968 regenerative indirect opto-electrical feedback (OE FB) was used to mode-lock a continuous-wave He-Ne laser [46]. This approach was successfully applied in 1990 to mode-lock an external cavity SCL by direct OE FB [47]. The first demonstration of a stabilizing effect of all-optical feedback (AO FB) on the general stability of a MLL was reported in 1990 for a synchronously pumped dye laser and was denoted *coherent photon seeding* [48]. A stabilizing effect of intra-cavity AO FB on stability of a mode-locked SCL was reported in 1993 [49]. Importantly, an OE FB configuration was presented in 2000 demonstrating the stabilizing effect of a *long-delay* feedback loop on TJ thus representing a new type of feedback category [50]. A thorough investigation of short-delay AO FB on TJ was given in 2002 demonstrating TJ reduction within a periodic locking-range defined by the inverse RR [51]. The first long-delay AO FB investigation and demonstration of strong TJ reduction was presented in 2009 in accordance with the mentioned long-delay opto-electrical feedback [52]. One year later the effect of long-delay AO FB on TJ has first been investigated for a QD based SCL and a **time domain explanation for TJ reduction was suggested** [53]. From here on other groups also recurringly investigated the effects of long-delay AO FB on TJ up to 2013 [54–56]. Numerical investigations were also carried out for short and intermediate delay-lengths demonstrating the stabilizing effect of AO FB on TJ in 2014 [57, 58]. However, an quantitative reproduction of experimental results and identification of the origin of the TJ reduction mechanism could not be provided so far.

In this work a systematic investigation of specifically selected feedback and locking schemes is conducted allowing to suggest, identify, verify and quantify the origin as well as the mechanism of the stabilizing effect of all these schemes with particular emphasis on experimental investigation and comprehensive modeling of the effects of AO FB on TJ. The final findings are extremely helpful for the development of new approaches toward TJ reduction.

This thesis is **structured** as follows. First, in chapter 2 the **theory and fundamentals** of QDs, ML and TJ which are useful for understanding the content of the following chapters are presented with an emphasis on TJ. In this spirit, this chapter also highlights some essential experimental aspects which are mandatory for understanding of the observed experimental results in the following chapters. In chapter 3 a simple, passive opto-electrical control-loop is presented, investigated and explained which is able to **suppress amplitude instabilities** thus accessing the increased potential of the investigated MLL which is exploited in the next chapter. In chapter 4 novel fully gain-guided **monolithic tapered MLLs** are investigated with a focus on pulse-width, peak power and stability. Subsequently, **tapered SOAs** are investigated in terms of the amplification properties of ultra-short pulses. The combination offers the generation of ultra-short pulses with very high peak power. In chapter 5 the topic of **control and reduction of TJ** is covered and a thorough investigation is performed supported by systematic experimental and modeling results allowing to access a comprehensive understanding of the underlying mechanism for the first time. Finally, in chapter 6 a **conclusion** is drawn and an outlook towards future work is given.

This work was developed within the framework of the project *FAST-DOT*.

2 Fundamentals

> Having understood the topic, literature makes finally sense.
>
> Student saying

The content of this chapter focuses on the depiction of theory and fundamentals which are useful for a comprehensive understanding of the findings presented in the following chapters. The introduction covers short pulse generation by semiconductor quantum-dot (QD) edge-emitting lasers using mode locking (ML) while emphasizing the topic of timing jitter (TJ). The description of experimental methods requires basic knowledge of the functionality of the common measurement instruments and focuses on investigation of ML. This chapter highlights some specific aspects and details which are mandatory for understanding the observed results of the following chapters.

2.1 Pulse generation: Mode-locking

In general, pulse generation by mode locking (ML) relies on the locking of the longitudinal optical modes of a multi-mode laser or in other words on the establishment of a fixed phase relation of all modes. This locking results in the generation of a train of equidistant optical pulses. The cavity round trip time of an oscillating pulse in the cavity corresponds to a repetition rate (RR) which is the frequency difference of the longitudinal optical modes. The shape of the optical spectrum of the laser output is in principle identical for continuous-wave (CW) or ML operation.

Assuming identical phases of the modes and according to the Fourier theory the pulse-width is inversely proportional to the number of locked modes or the corresponding width of the spectral envelope of these modes. Thus, the minimum pulse-width is limited by the available maximum gain bandwidth of the laser. This lower limit can be specified by the time-bandwidth-product (TBP). It is the product of pulse-width and spectral-width. The assumption of this minimum condition, using a Gaussian shape for the optical spectrum and for the shape of the pulse intensity and using the full-width at half-maximum (FWHM) measure for both widths yields a dimensionless value of ≈ 0.44 for the minimum TBP. The TBP is also a measure for pulse-broadening if the calculated value exceeds this fundamental lower limit. The TBP value depends on the shape of the spectrum and the shape of the optical pulse but also on the selected measure for the width. Besides the FWHM another measure of width is the second central moment corresponding to the variance. A pulse broadening occurs if the phases of the modes have at least a quadratic dependence on mode number which can be quantified by the non-zero group delay dispersion (GDD) (in units of s/Hz)[1]. The common and corresponding group velocity dispersion (GVD)

---

[1] Herby, the uncommon unit of s/Hz is chosen in contrast to the common s^2 to keep the physical meaning, namely a pulse delay as a function of frequency offset.

(in units of s/(Hz m)) is the GDD per units of length. This means that the group delay (GD) (in units of s) or group velocity (GV) (in units of $(\mathrm{s/m})^{-1}$) is not constant which means that different spectral intervals of an optical pulse are located at a different relative time with respect to the center-of-mass of the whole pulse. Such a pulse is called *chirped*.

The optical average power which is constant in CW operation is condensed to an optical pulse for ML operation. For a *rectangular* pulse-shape the peak power amounts to the average power divided by the duty-cycle the latter being the ratio of pulse-width to round-trip time of the pulse. This calculation just bases on the idea of redistribution of optical power. For other pulse shapes a correction factor has to be applied which will be shown in sub-section 2.3.1.

Locking of the optical modes can be achieved by various means [19]. Most of these various types of ML can be classified in three categories namely active ML, passive mode locking (PML) and a combination of both, hybrid mode-locking (HML). Active ML mostly relies on an electrical modulation of parts of the gain medium or on the modulation of a linear absorber or modulator at the RR and offers the advantage of low timing jitter (TJ) and the possibility of synchronized operation with external setups. The low TJ results from the external electrical modulation. This electrical modulation which represents amplitude modulation is responsible for the locking of the optical modes. However, the RR is limited due to electrical frequency limitations of the laser contacting or the gain medium itself. PML relies on a nonlinear or saturable absorption effect for example provided by an absorber element which basically rewards high intensities and therefore favors pulsed operation instead of CW operation leading to ML or Q-switched mode-locking (QS ML). The modulation and thus locking of the optical modes is accomplished by the oscillating pulse itself which RR corresponds to the optical mode spacing and thus the required modulation frequency. For a Fabry-Pérot cavity the absorber can be located at the back facet, at the output facet or in the middle of the cavity. The latter configuration can assist two counter propagating pulses within the cavity and is known as colliding pulse mode-locking (CPML). A Fabry-Pérot cavity is common for semiconductor laser (SCL) and a ring cavity is common for fiber-lasers. PML offers in principle the shortest optical pulses [59, Eq. (18)] and the highest RR. HML is basically PML with an additional modulation of the absorber or gain thus combining the benefits of PML with a low TJ. Hereby, the spatial localization of the nonlinear absorber for passive ML or modulator for active ML is essential for the locking of the modes which is obvious in the time-domain as is shown in the following section. However, single-cavity or single-section SCL have been reported which also exhibit ML [60,61]. Hereby the ML mechanism was attributed to originate from multi spatial-mode coupling or four-wave-mixing (FWM), respectively.

Passive ML of monolithic SCLs is the key issue in this work therefore it is outlined in more comprehensive detail. Common monolithic mode-locked lasers (MLLs) consist of one gain section being pumped by a constant gain current to provide gain and one absorber section being biased by a negative voltage to provide saturable absorption. Hereby, both sections are isolated electrically but the active medium is still optically connected. This optical connection ensures that no optical sub-cavities emerge.

PML operation requires nonlinear losses, which provide lower losses for higher intensities. A saturable absorber exhibits this required behavior but also introduces a time-dependence which manifest in a recovery time for pulsed optical excitation being also beneficial for PML operation [62]. Starting of PML operation can be comprehensively understood as follows. Starting from random intensity fluctuations saturable absorption provides lower losses for sufficiently high intensity bursts lasting shorter than the absorber recovery. If such a burst occurs it experiences lower losses as compared to its temporal surroundings thus being further amplified. In such a way a build-up of a ML pulse can be achieved which oscillates in the cavity as shown in Fig. 2.1a. The results in this figure are obtained by simulations [63]. In the figure, the absorber section is located from 0 mm to 0.35 mm, the gain section is located from 0.35 mm to 2.0 mm and the output facet is at 2.0 mm. During reflection at a time of 0 ps and a position of 2.0 mm the pulse experiences a loss of power of ≈-65 % due to the uncoated facets and the refractive index of the active medium of 3.7 for GaAs. Amplification occurs until the pulse reaches the absorber at 20 ps and 0.0 mm where a reflection, a pulse shortening and absorption occurs indicated by the lower power at 25 ps and 0.5 mm. Further amplification occurs until at 45 ps and 2.0 mm the pulse is coupled out again. This result shows that pulse power varies by a huge factor of ≈10 during oscillation which results from absorption of the absorber and output losses and has to be compensated by the gain for each round-trip. Shortening of the pulse results from absorption of the leading edge of the optical pulse thus also providing transparency for the peak of the pulse. If absorption regeneration occurs fast enough it will absorb also the trailing edge thus further shortening the pulse. Pulse broadening occurs in the gain section by a slightly higher amplification of the leading edge as compared the the peak of the pulse due to nonlinear gain or gain saturation. ML of SCL is therefore a highly dynamical process mainly due to the high losses as compared to a solid-state laser (SSL). The latter exhibits dominant output coupling losses of below 1 % [64].

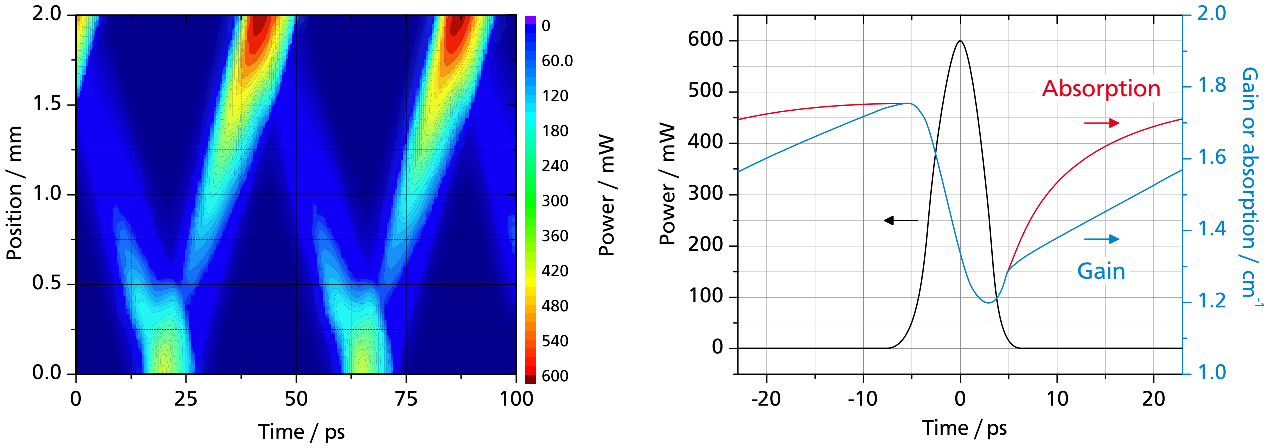

(a) **(b)**

Figure 2.1: (a) Simulated spatio-temporal depiction of an optical pulse inside a QD based MLL oscillating in a one-dimensional cavity. The absorber section is located from 0 mm to 0.35 mm, the gain section is located from 0.35 mm to 2 mm and the output facet is at 2 mm. The depiction is adapted from [63]. (b) Representative dynamics of absolute value of gain, loss and optical power for steady state ML condition with respect to the optical-pulse time-coordinates. Similar depiction can be found in [65].

The above time-domain ML description can also be used to define a quantitative ML condition. The saturation energy of the absorber must be lower than the saturation energy of the gain [66]. Correspondingly, the differential absorption must be higher than the differential gain both with respect to the carrier density. This means that the absorber has to saturate faster than the gain for a given pulse energy which results in a cut-off of the leading edge but an amplification of the whole pulse thus providing net-shortening of the pulse. The differential absorption can be commonly enhanced by applying a negative voltage to the absorber which increases absorption and accelerates absorption regeneration by increased carrier escape by tunneling. The generation of stable ML pulses in passively MLL lasers results from the temporal balance between the shaping effect induced by the absorption bleaching in the saturable absorber, the waveguide losses and the amplification and broadening mechanisms induced by gain saturation in the gain section, experienced by the ML pulse over a single round trip in the laser cavity.

Simulation of the mean optical pulse shape as well as the absolute value of gain and absorption of the respective sections for steady state ML condition[2] yields the commonly found representation shown in Fig. 2.1b. Hereby, it is emphasized that gain and absorption act subsequently but are shown together with respect to the pulse time-coordinates [67]. In addition, in these simulations gain and absorption section are regarded as elongated objects but spatial inhomogeneities, for example the carrier density, are not regarded. Now, the region of equal gain and loss, the transparency window for the steady state ML condition, allows for the existence of an optical pulse. Generic analytic solutions yield a squared hyperbolic secant shape (sech^2) for the intensity profile [59] whereas QD based MLL can yield a strong pulse-asymmetry [68]. Outside this transparency region losses are higher than gain thus preventing emission. However, if due to driving conditions a transparency or net-gain occurs outside the optical pulse, so-called trailing edge instability (TEI) and leading edge instability (LEI) may occur which can manifest as an amplitude instability [69]. Such undesired net gain may originate from ultra-fast components of the gain recovery, for example spectral hole burning [70], at low gain currents resulting in an TEI. Too high gain recovery may result in net gain in front of the pulse which occurs at high gain currents and results in an LEI. Furthermore, at high pulse energies a pulse breakdown induced by self phase modulation (SPM) and dispersion can occur [71]. Also undesired amplitude instabilities including Q-switching (QS) instabilities or QS ML originating from relaxation oscillation (RO) may occur for specific driving conditions or cavity geometries [72,73]. Such instabilities are addressed in chapter 3 where an approach is presented which reduces or even eliminates these instabilities. Furthermore, a PML always exhibits an inherent TJ where each optical pulse of a pulse train exhibits a small timing deviation with respect to an ideal equidistant pulse train. This timing instability will be addressed in detail in section 2.4. How both types of instabilities appear in measurements will be addressed in section 2.3.

The nonlinear saturable absorption also results in a hysteresis or bi-stability of the step-like power-current characteristic as observed in [9, 31]. In principle, pulsed operation is stable below the CW threshold current [75, Eq. (4.6)] as can be also comprehensively derived from Fig. 2.1b. There, in *stable* ML operation, summing up the gain and loss over the whole pulse repetition period (PRP) yields only losses which would be valid for low-power CW operation at this biasing condition. Thus, increasing the current just above the threshold and reducing it again below this threshold allows for ML. The observed

---

[2] Here, mirror losses are included thus no net gain exists around the pulse position.

sudden increase of the step-like power-current characteristic indicates that pulsations occur starting from threshold. Details on how ML appears in time and frequency domain can be found in section 2.1.

Having outlined the general principle of mode-locking in time-domain and highlighted the stability, in the next section the peculiar active medium which is composed of QDs is introduced and the benefits of these QDs with respect to ML operation are presented.

2.2 Quantum dot semiconductor lasers

Semiconductor quantum-dots (QDs) incorporated in the active medium represent the recent generation of semiconductor based lasers which are also used in the present work. The peculiarity is the density of states (DOS) of a QD resulting from its zero-dimensionality for the carriers and the inhomogeneous broadening of the energies of the QDs resulting from size variations resulting from the fabrication process. QDs are often embedded in a quantum-well (QW). The DOS of a medium can be calculated in momentum or k-space, by using the energy dispersion relation for quasi-free particles and the energy for quantum-confined particles in a box. This yields a square-root DOS for three-dimensional media (bulk), a sum of step functions for two-dimensional media (QW), a sum of $E^{-0.5}$ functions for one-dimensional media (quantum wire or quantum-dash) and a sum of degenerated Dirac-delta functions for zero-dimensional media (QD). The DOS is continuous (with respect to the summed energy in all dimensions) for all dimensionalities except for the QD which can be regarded as artificial atom. The inhomogeneous broadening results from an distribution of QD sizes. These properties are beneficial in terms of mode locking (ML) and pulse-generation as will be stated below.

- Assuming the same carrier amount for all these dimensionalities yields an increasing population and consequently inversion with decreasing dimensionality at the lowest energy. This results in a reduction of threshold current density as a function of dimensionality thus resulting in an advantage of QD lasers [22].

- Because the DOS is reduced for QD material as compared to QW material or bulk material less carriers are required to saturate the gain. In consequence the differential absorption da/dn is much higher at low carrier densities and the differential gain dg/dn is much lower at high current densities as stated and shown in [76, Fig. 1]. These two properties are beneficial for ML operation and generation of ultra-short pulses as stated in section 2.1.

- Active media based on QDs offer reduced spontaneous emission as compared to bulk media by the higher efficiency of population inversion and smaller waveguide losses [77].

- For QD media absorber saturation and regeneration occurs on sub-ps time-scales and gain exhibits ultra-fast recovery. Thermionic escape of the photo-generated carriers results in recovery times in the sub-100 ps range. Applying a negative voltage results in increased escape of the photo-generated carriers by tunneling yielding recovery times in the sub-ps range [62, 78, 79]. However, the quantum-confined stark-effect shifts the absorption towards higher wavelengths as a function of absorber voltage and can result in a detuning of the absorption spectrum with respect to the gain spectrum for high absorber voltages thus preventing ML for too high voltages [76].

- The inhomogeneous distribution of the QDs leads to an highly broadened spectral gain bandwidth in QD based lasers [33] allowing the generation of ultra-short pulses which require high bandwidths as stated in section 2.1.

- The wavelength range of 1.1 μm to 1.3 μm and at 1.55 μm which is achievable directly by QD media only is beneficial for bio-imaging applications due to the total optical windows of bio-tissues considering absorption and scattering [24, 25, 80].

An overview of the status, advances and trends of short-pulse generation using mode-locked lasers (MLLs) based on QD active media can be found in [76, 81–84]. So far, the shortest pulse-widths obtained using monolithic QD based two-section MLL amount to a value of 360 fs [85] and 393 fs [86] and the highest reported pulse peak power amounts to a value of 17.7 W [9].

2.3 Measurement methods

The output of a mode-locked laser (MLL) can be observed and analyzed in the time- and frequency-domain. The time-domain primarily allows to analyze the pulse shape and width. The frequency domain can be partitioned in three different regimes. A frequency of 0 Hz represents the average optical output power. The frequency range of >0 Hz to multiple-GHz covering the repetition rate (RR) and its harmonics allows to study the most important dynamics of a MLL including the RR signal itself and amplitude and timing instabilities. Finally the frequency range of 230 THz to 270 THz covers the optical spectrum of the MLL emitting at a wavelength around 1260 nm.

2.3.1 Time domain

The pulse-width of a MLL which lies in the sub-ps range is not accessible by using fast photo diodes and sampling oscilloscopes due to bandwidth limitations of typical photo diodes (≈40 GHz) and sampling oscilloscopes (≈40 GHz) allowing to access pulses longer than ≈25 ps only. In addition, extraction of a trigger signal at multi-GHz frequencies is difficult and may introduce additional timing jitter (TJ) which is introduced by a varying trigger-time. Although streak cameras offer a better sampling resolution of ≈1 ps it is still insufficient. Therefore, the most common approach relies on the optical auto-correlation (AC) or, more sophisticated but rare, the frequency resolved optical gating (FROG). Here, the focus lies on the second-order non-collinear optical AC. The corresponding basic theory can be found in [19, 87–89]. The time resolution of a typical second harmonic generation (SHG) based auto-correlator is limited by the crystal bandwidth dictated by the phase matching condition allowing for a minimum resolution in the ≈50 fs range. Alternatively, a two photon absorption (TPA) effect in an appropriate material can be used. Hereby, TPA is not limited by phase-matching and offers a time resolution in the femtosecond range [90] which is beneficial for ultra-broadband AC measurements of amplified spontaneous emission (ASE) [91].

Three types of optical AC exist as outlined in Fig. 2.2 from which the pulse-width can be extracted. First, they can be classified in 1st order and 2nd order which mean linear and non-linear optical interaction [19]. Nonlinear interaction can be achieved by means of SHG or TPA resulting in additional nonlinear mixing terms in the AC signal as compared to the simple interference. Second, depending on the available interferometric precision one obtains the interferometric 2nd order AC which additionally allows to extract the pulse-chirp. Applying a low-pass filter to this signal [91] or not having interferometric precision yields the common intensity AC which yields the pulse-width but does not distinguish whether a chirp exists or not. Also the square-root of the AC signal is proportional to the instantaneous intensity of the pulse. Indeed, simple interferometric 1st order AC allows to estimate the pulse-width which however may be falsified by chirp. Applying a low-pass filter to this latter signal or not having interferometric precision yields no signal. Despite this falsification one could say, that an optical auto-correlator *used for pulse-width estimation* requires a nonlinear process only to compensate for the poor scanning resolution.

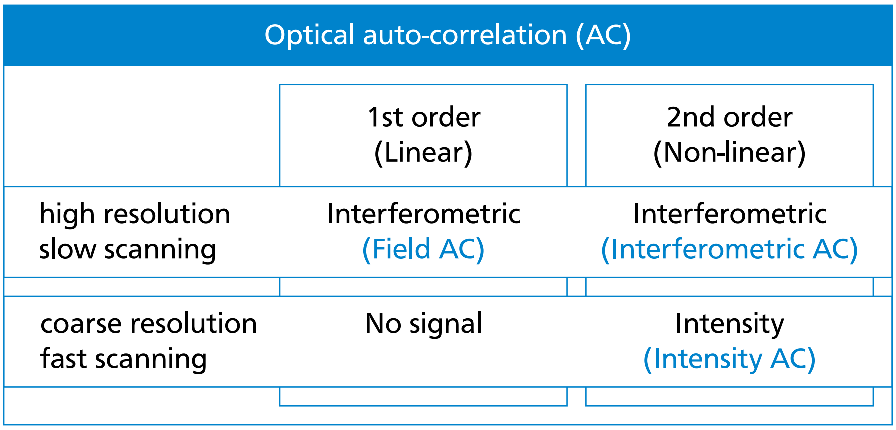

Optical auto-correlation (AC)

	1st order (Linear)	2nd order (Non-linear)
high resolution slow scanning	Interferometric (Field AC)	Interferometric (Interferometric AC)
coarse resolution fast scanning	No signal	Intensity (Intensity AC)

Figure 2.2: Classification of types of optical AC. Blue text denotes the common notation in literature.

For the 2nd order AC also a collinear and non-collinear beam setup can be selected. Both have different phase-matching conditions. For a collinear setup and an optical pulse train the well known ratio of 3 to 1 of peak to background-level is expected. For a noise burst a 2 to 1 ratio is expected. However, a collinear setup requires a perfect beam overlap of both beams over the whole delay range which is a huge challenge [88] and is even difficult to achieve with fiber-coupled commercial auto-correlators. In this work a non-collinear setup is chosen in order to not to have the background-level and thus having an increased dynamical detection range. The existence of a mode locking (ML) pulse train can be easier verified by the existence of cross-correlations at multiples of the pulse repetition period (PRP) instead of identification of the 3 to 1 ratio. In addition, as the used auto-correlator is free-space based to maximize sensitivity, beam shape and beam quality play a important role for the quality of the beam overlap within the crystal thus potentially preventing the observation of the expected ratio. For the estimation of the pulse-width it is not necessary that both beams have the same intensity or that the overlap of both beams is ideal. Furthermore, the width of an AC signal is fortunately not sensitive to TJ or amplitude jitter (AJ). However, a cross correlation is sensitive to TJ and can be used to estimate the TJ [92].

Pulse shape	Deconvolution factor	Peak power factor (f_{pk})	S_{norm}
Rectangle	1	1	1
Gaussian	$1/\sqrt{2} \approx 0.7071$	$2\sqrt{\ln(2)/\pi} \approx 0.9394$	0.6638
Squared hyperbolic secant (sech^2)	≈ 0.6482	$\ln\left(1+\sqrt{2}\right) \approx 0.8814$	0.5876
Lorentzian	$1/2$	$2/\pi \approx 0.6366$	0.3396
Single sided exponential	0.5	$\ln(2) \approx 0.693$	0.3354

Table 2.1: Deconvolution factors [87] and calculated peak power factors (f_{pk}) for selected optical pulse intensity profiles assumed for intensity AC. Also the calculated normalized mean signal intensity of a 2nd order nonlinear process (S_{norm}) is given.

The drawback of an optical auto-correlator as compared to a FROG is the high level of ambiguity with respect to the pulse-shape which directly results from the mathematical properties of the AC resulting in a loss of detail and a compulsory symmetry with respect to zero delay. Therefore a pulse shape for the intensity must be assumed to be able to estimate the pulse width. A squared hyperbolic secant shape (sech^2) is expected for the pulse intensity profile from early theory [59], a Gaussian shape is the most common assumed shape in literature and the Lorentzian shape or the single sided exponential shape of the AC can result from a strong pulse asymmetry. Hereby, the pulse exhibits a steep leading-edge and a slowly decaying trailing edge as shown in [93]. Mathematically applying an AC to an assumed pulse shape function in general leads to a mathematically different function [87]. However, the Gaussian function and the Lorentzian function are Eigenfunctions of the AC. Nevertheless, as an AC broadens the input signal, the full-width at half-maximum (FWHM) of the AC signal has to be multiplied by a deconvolution factor which depends on the pulse shape to obtain the FWHM of the optical pulse which is given in table 2.1 and can also be found in [87].

Commonly, to calculate the pulse peak power *solely* the RR, the average optical power and the pulse-width are used as stated in section 2.1 and as shown in Eq. (2.1).

$$P_{\mathrm{pk}} = \frac{P_{\mathrm{avg}}}{\nu_0 \Delta\tau} \tag{2.1}$$

Hereby, P_{pk} is the peak power, P_{avg} is the average power, ν_0 is the RR and $\Delta\tau$ is the FWHM pulse-width. However, to obtain a correct calculated peak power the pulse shape has also to be accounted for. This can be understood by assuming a pulse train composed of pulses with a peak power of 2 W, a pulse width of 1 ps and a PRP of 100 ps (10 GHz) together with a continuous-wave (CW) background with a constant power of 1 W. The common formula yields a calculated peak power of $1.01\ \mathrm{W}/(1\ \mathrm{ps} \cdot 10\ \mathrm{GHz}) = 101\ \mathrm{W}$ which does not match the actual power of 2 W. Thus, to estimate the correct pulse peak power a modified equation must be used which accounts for this discrepancy originating from the energy stored in the temporal wings of the optical pulse as given by Eq. (2.2) .

$$P_{\mathrm{pk}} = \frac{P_{\mathrm{avg}}}{\nu_0 \Delta\tau} f_{\mathrm{pk}} \ \text{with}\ f_{\mathrm{pk}} = \frac{wh}{A} \tag{2.2}$$

Hereby, f_{pk} is the correction factor which can be estimated from the width w, the height h and the area A of the assumed intensity function and is also given in table 2.1. Indeed, this factor is reported for sech^2 shaped pulses in [94]. This factor shows, that with respect to Eq. (2.1) the peak power has to be reduced significantly for non-rectangular pulse shapes which is taken into account in this work. This factor is essential for the validity of stated measurement results for applications.

Using Eq. (2.2) to calculate the peak power yields an interesting principle. Assuming pulse shapes other than Gaussian for fitting of the auto-correlation signal yields shorter pulse-widths due to the lower deconvolution factor. But the increased correction factor f_{pk} compensates this benefit for the peak power. Assuming a fixed FWHM of the *auto-correlation signal* the ratio of correction factor and deconvolution factor is almost constant with respect to different pulse shapes thus yielding a peak power which is almost independent on the assumed pulse shape.

The square-root of the maximum value of the auto-correlation signal is ideally proportional to the calculated pulse peak power as expressed by Eq. (2.2). Therefore, one could think of it as a device to estimate the peak power directly. However, in experiments it is also observed that, due to changes of the beam shape and thus the focal volume in the nonlinear-crystal, resulting in a changed second harmonic generation efficiency, or due to a change of the emission wavelength, resulting in a changed phase-matching condition, this peak value may deviate from the calculated pulse peak power. Furthermore, non-constant peak power of pulses within a pulse train lead also to a deviation because the observed maximum value of the square-root of the auto-correlation signal does not show the mean value of the peak power of the pulse train but the root mean square (RMS) value of peak power which represents a *nonlinear* averaging. Thus, an auto-correlator can be used to identify pulsed emission but can not be used for quantification of peak-power.

The discussed pulse shape considerations have also an impact on efficiency of the 2nd order nonlinear *imaging* which is mentioned in the introduction and represents a motivation for this work. This efficiency is motivated by the mean usable signal intensity S and consequently defined by the figure of merit (FOM) in literature shown in Eq. (2.3) [95].

$$\begin{aligned} S &\propto P_{\mathrm{pk}}^2 \nu_0 \Delta\tau = P_{\mathrm{pk}} P_{\mathrm{avg}} \\ \mathrm{FOM} &:= P_{\mathrm{pk}}^2 \nu_0 \Delta\tau = P_{\mathrm{pk}} P_{\mathrm{avg}} \end{aligned} \tag{2.3}$$

Hereby, the nonlinear signal intensity S is proportional to the squared peak power P_{pk}, the excitation duration $\Delta\tau$ which is the pulse width and the excitation frequency ν_0 which is the RR. Again, assuming *rectangular* pulses this definition can be *simplified* to the product of peak power times average power, as widely used in literature. The FOM is correspondingly defined. Furthermore, it is evident, that a sole reduction of the RR while keeping the peak power and the pulse width constant by using a passive cavity just decreases the signal intensity S and FOM as expected. However, to obtain comparability of the FOM with respect to different pulse-shapes the correction factor f_{pk} has to be accounted for by using the peak power calculated by Eq 2.2 and not Eq. (2.1) which leads to the correspondingly modified definition shown in Eq. (2.4).

$$\mathrm{FOM} = P_{\mathrm{pk}}^2 \nu_0 \Delta\tau = P_{\mathrm{pk}} P_{\mathrm{avg}} f_{\mathrm{pk}} \text{ with } P_{\mathrm{pk}} = \frac{P_{\mathrm{avg}}}{\nu_0 \Delta\tau} f_{\mathrm{pk}} \tag{2.4}$$

Nevertheless, also this corrected approach still has room for improvement of accuracy. This is the case because the nonlinear effect occurs for the instantaneous pulse shape $P(t)$ and not for the peak power P_{pk} with a duration of $\Delta\tau$. Thus, the mean signal intensity S of a 2^{nd} order nonlinear process can be accurately defined as given by Eq. (2.5).

$$S \propto \nu_0 \int_{-1/(2\nu_0)}^{+1/(2\nu_0)} P(t)^2 dt \tag{2.5}$$

Using the shapes from table 2.1 and assuming identical average power or pulse energy and identical FWHM pulse-width yields the normalized factors S_{norm} given in table 2.1 which show similar trends as the squared peak power factors f_{pk}. Thus, the calculated FOM according to Eq. (2.4) well considers the influence of the pulse shape and is used to calculate the FOM in this work. These considerations demonstrate the importance of the pulse shape for the peak power calculation as well as 2^{nd} order nonlinear imaging applications.

2.3.2 Optical frequency domain

In the optical frequency range an optical spectrum analyzer (OSA) is used to determine the spectrum of the MLL emission. Hereby, the FWHM of the spectral envelope is used to calculate the time-bandwidth-product (TBP). Under ML operation and assuming a Gaussian pulse-shape the optical spectrum will also exhibit a Gaussian shaped envelope. This is because a Gaussian function and its power as well as a hyperbolic secant function, which are assumed for the *electrical field* envelope of an optical pulse, both are eigenfunctions of the Fourier transform. The square of their absolute values represents the intensity. If the optical spectrum is irregular, a different measure for the width is more suitable which accounts for wings and gaps of the spectrum: A second central moment can be used or a squared power approach as used in [96]. The latter approach is used in chapter 3. As already stated in section 2.1 the minimum pulse-width is defined by the spectral envelope. With respect to optical cross-correlation measurements, which are performed in chapter 3 to characterize an optical pulse train, it is noted that the required long coherence length results from the width of one single optical line and not the spectral envelope which defines the minimum pulse-width. The optical line-width was found to be ≈15 MHz for a quantum-dot (QD) based MLL [97] resulting in a coherence length of 200 times the PRP of this laser. This means, that neighboring pulses are coherent to each other although the intensity vanishes between the pulses. This high coherence length thus allows for the observation of cross-correlations signals.

2.3.3 Radio frequency domain

The power spectrum (PS) in the radio-frequency (RF) domain is used to identify a manifold of information about the dynamics of the optical pulse train of a MLL. It allows to identify and quantify amplitude instabilities including Q-switching (QS) and Q-switched mode-locking (QS ML) which is treated in chapter 3. It also allows to identify and quantify timing instabilities or TJ which may originate from various sources as will be stated in section 2.4 and investigated in chapter 5. Also a coupling of timing and amplitude instabilities can be identified which will be also presented in chapter 3.

The shape of an ideal pulse train of a MLL in time-domain can be represented by a Gaussian pulse-shape convoluted with a Dirac-comb with a period corresponding to the PRP. To obtain the spectrum a Fourier-transform has to be applied. Hereby, the Fourier-transform of a convolution of two functions corresponds to a multiplication of the Fourier-transforms of these functions. Thus, in frequency domain a Dirac-comb, spaced by the RR, with an Gaussian envelope, which width is inversely proportional to the pulse-width, is expected. In a real MLL the Dirac-delta functions are broadened due to unavoidable TJ. This frequency comb is composed of the fundamental RR and its higher harmonics.

Using an photo-diode and an electrical spectrum analyzer (ESA) does not yield the *spectrum* of the optical output of the MLL but the so-called PS of the optical output[3] which indicates the *squared* magnitudes. A photo-diode measures optical power and generates a photo-current which results in a signal voltage. The ESA in turn displays the electrical power of this voltage across the internal 50 Ω resistor which depends quadratically on the voltage and thus quadratically on the optical power. This is useful because this directly measured PS is the commonly used spectral representation. Another very important aspect is the different behavior of signals with respect to measured power which are narrower or wider than the resolution bandwidth (RBW). It is known that a narrow signal, for example an typical 10 kHz RR line-width does not scale in power for RBWs higher than 10 kHz whereas broadband-noise always scales in power with RBW. This different behavior has to be accounted for to obtain valid results which are deduced from spectral magnitudes. For example, calculating the signal-to-noise ratio (SNR) of a narrow signal requires using the peak power of the signal, but to integrate the noise. This narrow signal must not be integrated for a correct estimation of power.

2.3.4 Quantification of instabilities

To gain quantitative insight into the effects of the mentioned instabilities including timing jitter (TJ), broadband amplitude jitter (AJ) and Q-switched mode-locking (QS ML) the power spectrum (PS) obtained by the electrical spectrum analyzer (ESA) can be evaluated. Hereby, TJ is a kind of frequency modulation, AJ is a kind of broad-band amplitude-modulation and QS ML is a kind of narrow-band amplitude-modulation. To demonstrate the effects of these instabilities on the PS Fig. 2.3 shows numeri-

---

[3] The term PS originates from electronics, where the square of a measured voltage signal represents its electrical power. Consequently the relative unit *dB* is valid for power only.

cally calculated PS for the three mentioned kinds of instabilities for different magnitudes or bandwidths of these instabilities. The numerical results are obtained by using a simple model which bases on discretized differential equations to simulate the TJ and AJ evolution. This evolution is subsequently applied to an ideal pulse train which is Fourier-transformed and squared to obtain the PS. This model is presented and described in detail in chapter 5. The exemplary mode-locked laser (MLL) was chosen to exhibit a typical repetition rate (RR) of 10 GHz corresponding to an pulse repetition period (PRP) of 100 ps, a typical pulse-width of 1 ps with a typical pulse-to-pulse timing jitter ($\mathrm{TJ}_{\mathrm{ptp}}$) of 100 fs which corresponds to an RR line width of 63 kHz. This measure of TJ ($\mathrm{TJ}_{\mathrm{ptp}}$) is ideally suited for passive mode locking (PML) and will be introduced in chapter 5 in detail. The AJ is quantified as relative root mean square deviation (RRMSD) which corresponds to a relative root mean square (RMS) value of the pulse amplitudes with respect to the mean pulse amplitude[4]. The RRMSD corresponds to the relative standard deviation (SD) for a high number of pulses[5]. The PS covers a frequency range from 0 Hz to 2.5 times the RR to allow for observation of the RR and its harmonic. The dashed line indicates an exemplary ESA noise-floor preventing observation of spectral features with weaker magnitudes. The number of simulated pulses amounts to $64 \cdot 10^3$ which leads together with the PRP of 10 GHz to a resolution bandwidth (RBW) of 156 kHz.

Fig. 2.3a shows the **PS for various pulse-to-pulse timing jitter ($\mathrm{TJ}_{\mathrm{ptp}}$) values**. Without TJ the PS is composed of Direc-delta functions. With TJ the PS is composed of Lorentzian functions at multiples of the RR as will be derived in section 2.4. With increasing TJ the width of the RR lines increases and the peak power decreases thus also showing a redistribution of signal power. The width of the RR is therefore a convenient measure for TJ [98] as will be also precisely derived in section 2.4. Hereby the 2nd harmonic is always broader than the 1st harmonic which corresponds to an increase of noise with harmonic number which was also stated in [99] for actively MLL. Because TJ is a kind of frequency-modulation, no signal components are observed around a frequency of 0 Hz. The highest shown $\mathrm{TJ}_{\mathrm{ptp}}$ of 10 ps corresponds to 10 % of the PRP and allows for a clear visualization of the characteristic shape of the PS but represents an unrealistically high value for real MLLs which will be presented in chapter 4.

Fig. 2.3b shows the **PS for various relative root mean square deviations (RRMSDs) of the magnitude of AJ** with a RRMSD bandwidth from 156 kHz to 1 GHz. This bandwidth-limited AJ (Gaussian shape in linear space) manifests as a noise pedestal for each harmonic of the RR with a suppression which does not depend on RR number. This was also stated in [99]. Because AJ is a kind of amplitude-modulation, the pedestal is also observed around a frequency of 0 Hz. With increasing RRMSD value the pedestal increases in magnitude with respect to the RR line. With an AJ bandwidth of 1 GHz and a large RRMSD value of 50 % the pedestal shows a surprisingly strong suppression of ≈-40 dB for a RBW of 156 kHz as indicated in the figure. At a typical RBW of 1 MHz the suppression would amount to $-40\text{ dB} + 10\log(1\text{ MHz}/156\text{ kHz}) = -32\text{ dB}$. Thus, with a RBW of 1 MHz the RR signal must be at least by +32 dB higher as compared to the ESA noise-floor to be able to identify this instability.

---

[4] $\mathrm{RRMSD} = \frac{1}{\langle A_i \rangle}\sqrt{\frac{1}{n}\sum_{i=0}^{n}\left(A_i - \langle A_i \rangle\right)^2}$ with $\langle A_i \rangle = \frac{1}{m}\sum_{i=1}^{m} A_i$

[5] The denominator is $n-1$ for a SD.

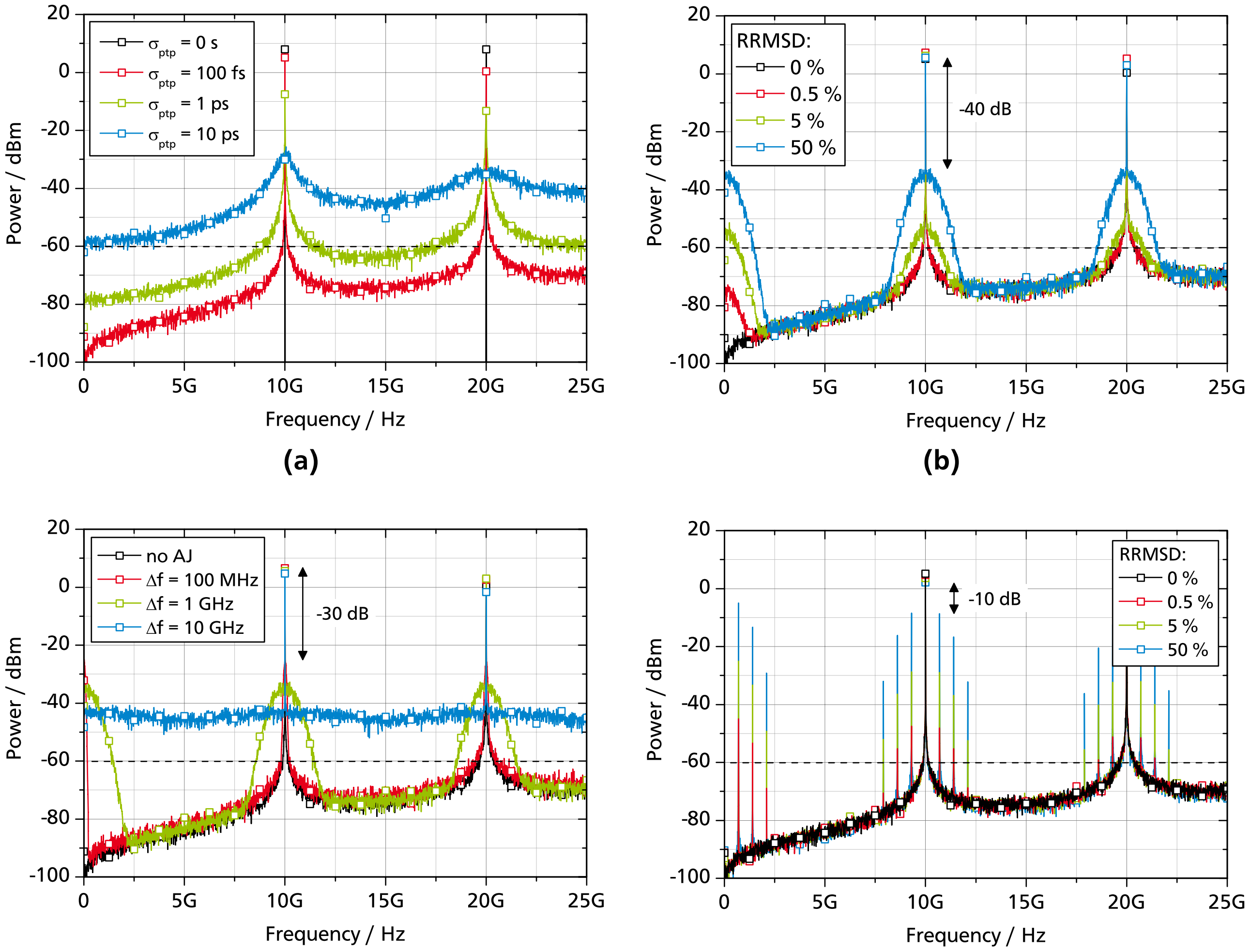

(a) **(b)** **(c)** **(d)**

Figure 2.3: Calculated PS of the optical power as obtained directly by an ESA. The RBW is 156 kHz for all plots. Shown are PS (a) for various TJ_{ptp} values for sole TJ, (b) for various RRMSDs of magnitude of AJ and a TJ_{ptp} of 100 fs, (c) for various bandwidths of AJ and a RRMSD magnitude of AJ of 50 % and a TJ_{ptp} of 100 fs (d) for various RRMSDs of magnitude of QS ML modulation and a TJ_{ptp} of 100 fs.

To demonstrate the **effect of the bandwidth of the AJ on the PS** Fig. 2.3c shows the PS for various bandwidths and a *fixed* RRMSD magnitude of 50 %. Reducing the bandwidth reduces the suppression down to a value of ≈-30 dB for a bandwidth of 100 MHz. Therefore not only the suppression but also the width of the pedestal have an strong impact on the RRMSD value of the AJ. Indeed, in experiments huge AJ bandwidths of up to 25 % of the RR can be observed which reflect strong amplitude instabilities which will be a topic of chapter 4.

To obtain these RRMSD values in experiment the signal-to-noise ratio (SNR) of the RR is required. The SNR is the power ratio of the integrated power spectral density (PSD) of the RR line and all the integrated noise PSD from >0 Hz to half of the RR if the maximal allowed bandwidth is desired. Higher frequencies as half of the RR are not relevant, because the pulse train amplitude cannot fluctuate faster than half of the RR. According to signal theory, half of the RR is also referred to as the Nyquist-frequency in literature [18]. The PSD is the PS divided by the used RBW. The RRMSD is given by the relation shown in Eq. (2.6).

$$\mathrm{RRMSD} = 10^{-\frac{\mathrm{SNR}}{20}} \tag{2.6}$$

This approach is verified by evaluation of the calculated results shown in Fig. 2.3b and represents a modification of the method proposed by von der Linde [99] which will be given by Eq. (5.1) in chapter 5. In [99, 100] the 1st and 2nd harmonic of the RR are used to estimate the AJ and TJ. In contrast, here, the RR (1st harmonic) and the power of the amplitude noise around 0 Hz are used instead. This offers the advantage of having a lower detection frequency requirement. In general, the noise-floor of the ESA should be as low as possible to minimize the lower detection-limit with respect to the AJ magnitude and thus the the RRMSD.

The mentioned SNR represents the *integrated* relative intensity noise (RIN) (in units of dB) of an optical pulse train within selectable frequency limits. Unfortunately, the experimentally obtainable detection limit is high which is due to the limited power-handling capability of common high-speed photo-diodes being insufficient to operate down to the the shot-noise limit. A new approach is proposed in [101] to improve shot noise limited TJ measurements of a mode-locked pulse train by exploiting shot noise correlations.

With respect to the broadband AJ in Fig. 2.3b also an multi-frequency narrow-band amplitude modulation is considered in Fig. 2.3d and represents **Q-switched mode-locking (QS ML)** which in turn represents an envelope modulation of the optical pulse-train whereby the modulation itself is not a sine-function but a pulse-train itself with a chosen frequency of 700 MHz. The characteristics and dependencies are the same as for broad-band AJ with the only difference of a low suppression of ≈-10 dB for a relative RRMSD value of the envelope modulation of 50 %. This low suppression is the result of the *narrow-band* amplitude modulation of QS ML showing that a suppression of more than −35 dB results in an insignificant amplitude modulation by Q-switching (QS) amounting to 5 % as observable in the figure.

2.3.5 Software: Measurement, evaluation and simulation

In the context of this work a library and measurement and evaluation programs have been developed with a strong focus on easy future extendability and flexibility. Hereby, the powerful framework *LabVIEW* is used. One program allows comfortable measurement of the timing phase noise power spectral density (TPN PSD) by a regular ESA. Another general measurement program allows to read out and evaluate various instruments as a function of different control parameters. One program, specifically designed for mode locking (ML), reads out different instruments, evaluates parameters and calculates derived parameters as a function of different control parameters. Finally, an additional evaluation program allowing easy browsing through recorded data-sets and allowing post-calculations from spectra is developed to cope with the high amount of data-sets and in particular to have the possibility to change evaluation of the given data. For the simulation part of this work *MATLAB* is used because it offers a variety of useful mathematical functions, can acquire RAM efficiently and has the possibility of parallelization of processes.

2.4 Timing jitter

The unavoidable timing fluctuation of an optical pulse train of a mode-locked laser (MLL) whereby each pulse exhibits a timing deviation with respect to an ideal reference clock is denoted as timing jitter (TJ). It is relevant for various applications and of constant interest in scientific research. On the one hand the aim of this section is to provide a concentrated and comprehensive overview on the most important and relevant topics of TJ in the field of mode-locked semiconductor lasers (SCLs) and to highlight uncommon aspects. On the other hand ideal noise-spectra will be derived to provide a quantitative connection of the microscopic noise parameters used in simulation and the characteristics of the noise spectra obtained in experiments.

In the following sub-sections the nomenclature of TJ will be defined and the various measures for TJ and their interrelations will be introduced. Subsequently the derivation of the noise spectra is provided and the most relevant noise sources will be introduced and quantified. Hereby, amplitude noise of the optical pulse train will be neglected because it is quantitatively insignificant as compared to timing noise for stably running MLL.

2.4.1 Definitions and nomenclature of timing jitter

Timing fluctuations of an optical pulse train can be well illustrated in time domain as depicted in Fig. 2.4. Hereby, each pulse of the optical pulse train t_k exhibits a timing deviation Δt_k with respect to an ideal reference clock T_0 due to a noise source. The reference clock corresponds to the repetition rate (RR) of the mode-locked laser (MLL) and is given by the mean of the pulse-to-pulse period T_k according to $T_0 = \langle T_k \rangle$. The timing deviation of a pulse k is subsequently given by $\Delta t_k = t_k - kT_0$.

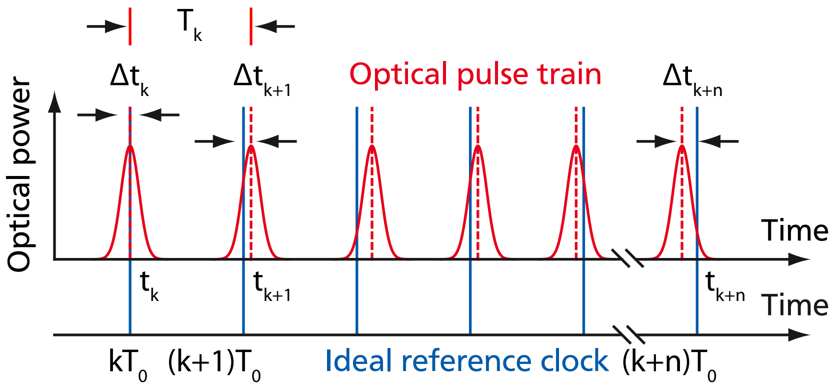

Figure 2.4: Schematic of timing jitter (TJ) of an optical pulse train (T_0: repetition rate (RR), Δt_k: instantaneous timing deviation, T_k: instantaneous pulse-to-pulse period)

At this point a classification into two categories can be made depending on the timing noise reference but independent of the noise source itself:

- The timing of a pulse t_k is influenced by a *stationary* timing noise source $\Gamma(k)$ (with an root mean square (RMS) value of Γ) which is *strictly* related to the reference clock kT_0. This assumption can be conveniently written as a pulse-timing of $t_k = \Gamma + kT_0$. This consequently leads to a timing deviation of $\Delta t_k = \sqrt{2}\Gamma$. In such a way the timing deviation sequence Δt_k is also *stationary*. Additionally assuming that $\Gamma \ll T_0$ the timing deviation Δt_k will most likely never exceed the mean repetition period T_0.

- The timing of a pulse t_k is influenced by a *stationary* timing noise source $\Gamma(k)$ (with a RMS value of Γ) again but which is now *strictly* related to the previous pulse timing t_{k-1}. This assumption can be conveniently written as a pulse-timing of $t_k = \Gamma + t_{k-1} + T_0$. This consequently leads to a timing deviation of $\Delta t_k = (\Gamma + t_{k-1} + T_0) - kT_0 = \Gamma + \Delta t_{k-1}$. This case is completely different as compared to the previous one because the timing-difference sequence Δt_k is unbounded now. The timing deviation Δt_k may easily exceed the mean repetition period T_0 for sufficiently high pulse numbers k. The timing deviation sequence Δt_k is *not stationary* and essentially follows a random walk (RW) characteristic.

Both cases correspond to existing MLL configurations. The stationary case applies to an actively MLL where an external modulation is used to lock the optical modes. Also a hybridly MLL exhibits stationary noise behavior whereby a free running passively MLL is modulated with an external signal to improve locking of the modes. The non-stationary case applies to a free running passively MLL without any external influence.

Based on the given quantities in Fig. 2.4 different measures of TJ can be deduced which can be found throughout literature [44, 98]. These quantities include the timing phase noise power spectral density (TPN PSD), the integrated timing jitter ($\mathrm{TJ}_{\mathrm{int}}^{(f_1,f_2)}$) (also known as the RMS TJ) and the line-width of the RR signal. It is essential to highlight the differences of each measure and their applicability. Hereby it is emphasized that the term timing jitter (TJ) is just a general term for *timing noise* which can be quantified by different measures. In addition limitations of each measure will be given with a focus on the two provided cases of stationarity of noise characteristics.

- The **timing phase noise power spectral density (TPN PSD)** $L_\psi(f)$ is a representation of the TJ of an optical pulse train in frequency domain. It is basically a power spectral density (PSD)[6] of the timing phase deviation of an optical pulse train in units of $\mathrm{rad}^2/\mathrm{Hz}$. It shows the magnitude of noise on different timescales. Fast timing fluctuations correspond to high offset frequencies. The highest allowed frequency offset corresponds to the half of the RR which is also referred to as the Nyquist-frequency in this context [18]. The TPN PSD contains most information of TJ and many features can be observed including the spectral shape, power-laws for parts of the spectrum and noise resonances or periodicities amongst other features. Initially, the units are $\mathrm{rad}^2/\mathrm{Hz}$.

---

[6] It is reminded, that the term PSD roughly denotes a squared Fourier-transform per unit bandwidth.

However, in literature the magnitude in units of dBc/Hz is more common which is defined by $10\log(L_\psi(f)\cdot 1\text{ Hz})$.

An equivalent alternative representation of TJ is given by the **timing noise power spectral density (TN PSD)** $L_t(f)$. It is basically a PSD of the timing deviation of an optical pulse train in units of s^2/Hz. Both spectral representations are related by $L_t(f) = (2\pi\nu_0)^{-2}L_\psi(f)$. This TN PSD representation is more common within the solid-state laser (SSL) or fiber laser community. The TN PSD is a absolute measure of TJ whereas the TPN PSD is a relative measure of TJ with respect to the pulse repetition period (PRP).

In experiments, the TPN PSD can be conveniently obtained from the power spectrum (PS) of an optical pulse train measured with a fast photo detector and an electrical spectrum analyzer (ESA) as introduced by von der Linde in [99]. Hereby, it is emphasized that the approach of von der Linde represents one way to obtain the TPN PSD of a MLL. This method is well suited for semiconductor MLLs. However, due to inherent instrument noise this method is not suitable for ultra-low-noise mode-locked SSL as in [64]. Hereby a different ultra-sensitive measurement technique was developed which bases on balanced optical cross correlation and a locking loop [102]. Two ideal and experimentally not limited TPN PSDs are shown in Fig. 2.5 representing exemplary stationary and non-stationary timing noise of the phase. The stationary case corresponds to a hybridly MLL and the non-stationary case corresponds to a free-running passively MLL. Both cases decrease with a f^{-2} power-law for high frequencies. The timing phase noise of the stationary case is flat for low frequencies whereas the timing noise of the non-stationary case diverges to infinity approaching a frequency of zero.

For sake of completeness it is convenient to introduce the **frequency noise power spectral density (FN PSD)** $L_f(f)$ in the context of mode locking (ML) which represents the fluctuations of the RR. It is related to the TPN PSD by $L_f(f) = f^2 L_\psi(f)$. Using this relation with the f^{-2} power-law of the TPN PSD of a free-running MLL results in a white frequency noise characteristic with a constant PSD. In such a way the RR is always bounded in contrast to the unbounded timing phase. It is therefore expected that the mean RR does not change on real-time-scale.

- The **integrated timing jitter ($\mathrm{TJ}_{\mathrm{int}}^{(f_1,f_2)}$)** also referred to as **root mean square (RMS) timing jitter (TJ)** represents a single-value measure of the TJ (in s) with respect to an ideal clock within a selectable frequency range. It can be well understood in the time domain. The estimation of the timing deviation sequence Δt_k in time domain requires a record length and a sampling rate, which correspond to two frequencies defining the observation range, which allow to calculate the RMS value of the timing variation $\mathrm{TJ}_{\mathrm{int}}^{(f_1,f_2)}$. In such a way and together with the TPN PSD the term *integrated* hints the definition of $\mathrm{TJ}_{\mathrm{int}}^{(f_1,f_2)}$ which is given by Eq. (2.7).

$$\sigma_{int} = \frac{1}{2\pi\nu_0}\sqrt{2\int_{f_1}^{f_2} L_\psi(f)} \tag{2.7}$$

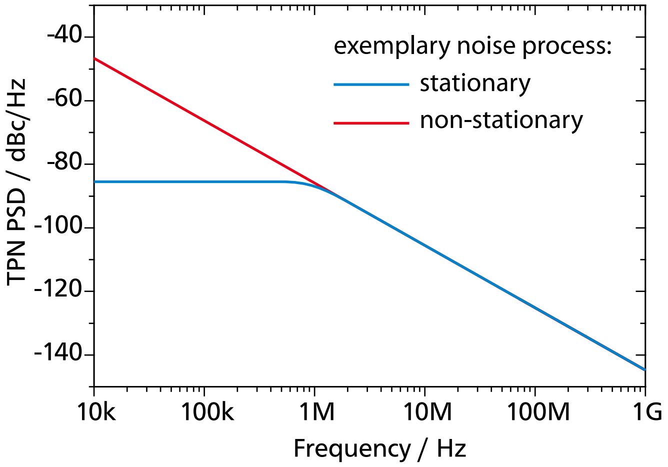

Figure 2.5: Exemplary ideal and experimentally not limited TPN PSD for a stationary and non-stationary timing phase noise process corresponding to an hybridly MLL and an free-running MLL, respectively.

The power density is integrated in the desired frequency range, the factor 2 accounts for the fact that $L_\psi(f)$ is mostly estimated and used as single-sided, the square root restores the correct unit of magnitude and the denominator converts the phase in a corresponding time. This measure of TJ allows for an application specific quantification of TJ depending on the requirements. It allows to specify long term stability or high frequency noise. However, comparability of different systems is rarely possible because different frequency ranges are used for calculation in literature. The highest possible fluctuation frequency of the amplitude of the optical pulses is half of the RR which consequently defines the highest valid integration frequency. The applicability of this measure may also be limited depending on the investigated system. Calculating the $\mathrm{TJ}_{\mathrm{int}}^{(f_1,f_2)}$ for the stationary case in Fig. 2.5 in the *full* frequency range from zero to half of the RR yields a finite value. However, calculating the $\mathrm{TJ}_{\mathrm{int}}^{(f_1,f_2)}$ for the non-stationary case again from zero to half of the RR yields an infinite value which nicely reflects the long term drift-off of the timing deviation of a free running MLL. Finally, in experiment, due to the limitation of the mentioned method of estimation of TPN PSD by von der Linde for a free-running MLL the lower integration frequency must be higher than the full-width at half-maximum (FWHM) of the RR line in order not to massively underestimate the TJ.

- The **pulse-to-pulse timing jitter ($\mathrm{TJ}_{\mathrm{ptp}}$)** is specifically useful to describe the non-stationary TJ characteristics of a stably and free-running MLL. It is defined by $\sigma_{ptp} = \left\langle t_{k+1} - t_k \right\rangle_k$. Hereby, $\langle\rangle_k$ denotes the mean value with respect to k. Using the pulse timing deviation for an exemplary non-stationary noise characteristic of $\Delta t_k = \Gamma(k) + \Delta t_{k-1}$ a finite value of $\mathrm{TJ}_{\mathrm{ptp}}$ of Γ is obtained as compared to $\mathrm{TJ}_{\mathrm{int}}^{(f_1,f_2)}$ which is infinite if the whole frequency range is integrated. Hereby, $\mathrm{TJ}_{\mathrm{ptp}}$ directly represents the timing noise source Γ which makes it the preferred TJ measure for a free-running MLL. The $\mathrm{TJ}_{\mathrm{ptp}}$ can be estimated from the FWHM $\Delta\nu_0$ of the TPN PSD or the PS by means of Eq. (2.8) taken from [98].

$$\sigma_{ptp} = \frac{1}{\nu_0}\sqrt{\frac{\Delta\nu_0}{2\pi\nu_0}} \tag{2.8}$$

Hereby, ν_0 denotes the RR. This equation is valid for a free-running MLL only. The $\mathrm{TJ}_{\mathrm{ptp}}$ measure is not common for stationary noise like actively MLL. For an exemplary stationary noise characteristic of $\Delta t_k = \Gamma(k)$ a value of $\sqrt{2}\Gamma$ is obtained if a white noise source is assumed thus also showing the usability of the measure $\mathrm{TJ}_{\mathrm{ptp}}$ for an actively MLL. However, to be correct, for stationary noise characteristics the TPN PSD has to be evaluated to obtain the $\mathrm{TJ}_{\mathrm{ptp}}$ [98, Eq. (2)]. This evaluation of the TPN PSD is also valid for a free-running MLL but more laborious as compared to the evaluation of the RR line-width. For a free-running MLL the $\mathrm{TJ}_{\mathrm{ptp}}$ and the TPN PSD can be calculated from the RR line-width. Rearranging Eq. (2.8) leads to $\Delta\nu = \sigma_{\mathrm{ptp}}^2 \nu_0^3 2\pi$ which allows to deduce an interesting principle. Assuming a linear dependence of σ_{ptp} on active medium length as suggested in [103, equation B8] and varying the active medium length leads to a linear dependence of the RR line-width $\Delta\nu$ on the RR. Therefore, to achieve narrow RR line-widths long monolithic MLLs are adequate.

- Using Eq. (2.8) in the case of feedback (FB) yields a different meaning of σ_{ptp}. In that case the obtained value characterizes only the **long term drift or the long term timing jitter ($\mathrm{TJ}_{\mathrm{lt}}$)** of the TJ and not the noise source strength any more which will be shown in chapter 5 and was initially reported in [5].

- The **repetition rate (RR) line-width** also represents a measure for TJ for a non-stationary TJ characteristics which is the case for a free-running passively MLL. Based on Eq. (2.8) it is directly related to the $\mathrm{TJ}_{\mathrm{ptp}}$. It is also quite intuitive, that a large line-width of the RR corresponds to a high TJ. This measure is not meaningful for an actively MLL because it only specifies the noise stemming from the driving oscillator and disregards the other noise contributions. It is noteworthy, that the ratio of RR and its line-width can be also used to quantify RR stability. This ratio would correspond to the **quality factor** of a generic resonator.

- The **equivalent pulse-to-pulse timing jitter ($\mathrm{TJ}_{\mathrm{ptp}}^{\mathrm{eq}}$)**, only found in this work, represents a scalar measure for TJ for a free-running passively MLL. It bases on the calculation of the $\mathrm{TJ}_{\mathrm{int}}^{(f_1,f_2)}$ from the TPN PSD and subsequent conversion to a corresponding $\mathrm{TJ}_{\mathrm{ptp}}$ by assuming an ideal Lorentzian or f^{-2} shape. It accounts for the total TJ magnitude but disregards the spectral distribution. Therefore $\mathrm{TJ}_{\mathrm{ptp}}^{\mathrm{eq}}$ equals $\mathrm{TJ}_{\mathrm{ptp}}$ for an ideal Lorentzian or f^{-2} shaped TPN PSD but it has the experimental advantage to account for *irregularities* of the TPN PSD in contrast to a $\mathrm{TJ}_{\mathrm{ptp}}$ obtained from the FWHM of the RR line-width. In detail, $\mathrm{TJ}_{\mathrm{ptp}}^{\mathrm{eq}}$ is obtained by using Eq. (2.7) to obtain $\mathrm{TJ}_{\mathrm{int}}^{(f_1,f_2)}$ and using Eq. (2.22) to obtain $\mathrm{TJ}_{\mathrm{ptp}}$ which is $\mathrm{TJ}_{\mathrm{ptp}}^{\mathrm{eq}}$. Hereby both integration frequencies must coincide. The $\mathrm{TJ}_{\mathrm{ptp}}^{\mathrm{eq}}$ is basically derived from the $\mathrm{TJ}_{\mathrm{int}}^{(f_1,f_2)}$ but has the property to fully coincide with the useful $\mathrm{TJ}_{\mathrm{ptp}}$ for a stably running passively MLL.

In summary, depending on the type of TJ different measures are suitable for quantification. The TPN PSD is valuable for all types of TJ, contains most information and all other measures of TJ can be derived from it. The $\mathrm{TJ}_{\mathrm{int}}^{(f_1,f_2)}$ is a single value measure of TJ useful for comparison of different types of TJ if an identical frequency range is selected. It also takes into account irregular shapes of the TPN PSD. The $\mathrm{TJ}_{\mathrm{ptp}}$ is ideally suited for stably and free-running MLL because it is the only measure necessary. The proposed TJ_{ptp}^{eq} is like TJ_{ptp} but in addition accounts for irregular shapes of the TPN PSD. In the following subsection the inter-dependencies of selected measures of TJ will be derived and the limitation of the useful method for the estimation of TPN PSD by von der Linde for free-running MLL will be presented.

2.4.2 Interconnection and derivation of parameters of timing jitter

In numerical or analytical models of mode-locked lasers (MLLs) describing timing jitter (TJ), including the simple model presented in this work, microscopic timing-jitter parameters like the pulse-to-pulse timing jitter (TJ_{ptp}) are used which directly reflect the noise source [103, eq. 10]. However, in measurements, directly obtainable parameters like the line-width or the power spectrum (PS) of the repetition rate (RR) are a common base for estimation of TJ. In order to allow to compare results obtained by experiment and simulation a mathematical accurate connection of these microscopic TJ parameters with parameters obtained in measurements is derived here specifically addressing the dominant kind of TJ of a passively MLL. Full featured models which describe all aspects of a MLL [69] provide the optical field of an optical pulse as a function of time for each round trip. In such a way timing phase noise power spectral density (TPN PSD) can be also extracted by means of the PS of the fully simulated optical pulse train [99]. Here, in the simulation part of this work, only the timing phase deviations of corresponding pulses are considered and evaluated. Therefore it will be shown that the *evaluation* of the optical pulse train and the direct *evaluation* of the timing phase yield the same result in terms of TPN PSD. A schematic overview of this latter aspect is given by Fig. 2.6. In addition, the limitation of the method by von der Linde for estimating the TPN PSD of passively MLL will be explicitly shown. These derivations and interconnections for the TJ also represent a useful reference work.

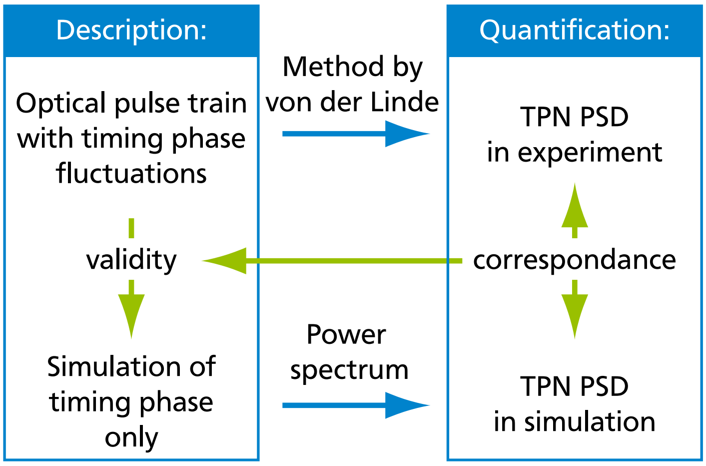

Figure 2.6: Schematic showing estimation and correspondence of TPN PSD in experiment and simulation in this work.

The derivation of a PS and the corresponding TPN PSD is complex. General derivations found in literature are not directly applicable because they are derived for continuous optical frequency noise under influence of observation time [104] or are highly general and thus highly complex but also need further adaption of the parameters [105]. Therefore, the aim here is to provide the most straightforward derivation of the connection by exploiting the statistical properties of the timing noise as early as possible within the derivation and only concentrate on the most fundamental noise source. The statistics of the TJ follow a random walk (RW) and the dominant noise source is amplified spontaneous emission (ASE) [106]. Unfortunately, a most straightforward derivation does not mean simple derivation, because some non-easy but mandatory steps are still required. It is potentially not easily possible to provide a simpler derivation. One peculiarity of the derivation approach presented here is to translate the discrete noise process which is utilized in the simulation into a continuous noise process to allow for easier subsequent analytical calculations.

The idealized pulse train emitted from a MLL can be described in frequency domain as a multitude of phase-locked oscillations with frequencies being multiple integers of the RR. To keep the derivation simple a MLL is not regarded as a pulse emitter here but as a single oscillator subject to phase-noise. This does not restrict the validity of the derivation because these harmonic oscillations are regarded as fully phase locked to the fundamental oscillation frequency which is the RR. This simplification also holds true in the time-domain because a simple oscillation corresponds to an optical pulse train with a pulse width of half the repetition period. To account for TJ additional phase fluctuations are introduced.

In the following the derivation of the PS and TPN PSD is given. The PS can be obtained by the Wiener-Chintschin-Theorem [107, p. 17] which states, that the power spectrum of wide-sense-stationary random process corresponds to the Fourier-transform of the auto-correlation (AC) function of this process. Assuming an ideal oscillation with a frequency of ν_0 and with phase fluctuations $\psi(t)$ the PS is given by Eq. (2.9).

$$\mathrm{PS}(\nu) = \mathrm{FT}\left\{\mathrm{AC}\left\{\exp(i2\pi\nu_0 t + i\psi(t))\right\}\right\} \tag{2.9}$$

Hereby, AC$\{\}$ and FT$\{\}$ denote the AC and Fourier-transform operation, respectively. To account for the phase fluctuations $\psi(t)$ a discrete random-walk process $\psi(N)$ is used as a basis [106] as it represents the dominant source of noise in semiconductor MLLs. A timing phase deviation $\psi(N)$ as a function of the pulse number N and a root mean square (RMS) timing phase difference $\Delta\psi_0$ per step or pulse can be described by Eq. (2.10).

$$\psi(N) = \sum_{n=0}^{N} \Delta\psi_0 \Gamma(n) \tag{2.10}$$

Hereby, $\Gamma(n)$ denotes a white-noise process with a RMS value of 1. The phase deviation $\psi(N)$ has an expectation value of zero. The widely reported pulse-to-pulse timing jitter ($\mathrm{TJ}_{\mathrm{ptp}}$) is naturally defined by Eq. (2.11).

$$\sigma_{ptp} = \frac{\Delta\psi_0}{2\pi\nu_0} \tag{2.11}$$

The most important characteristic of the RW is the non-zero and non-constant variance $\left\langle \psi^2(N) \right\rangle$ and is defined in the first row of Eq. (2.12).

$$\begin{aligned} \left\langle \psi^2(N) \right\rangle &= \Delta\psi_0^2 \left\langle \left(\sum_{n=0}^{N} \Gamma(n) \right)^2 \right\rangle \\ &= \Delta\psi_0^2 N \\ &= \Delta\psi_0^2 \frac{t}{T_0} \\ \left\langle \psi^2(t) \right\rangle &= \Delta\psi_0^2 \nu_0 t \ \text{ and } \ t \geqslant 0 \end{aligned} \tag{2.12}$$

Hereby, $\langle\rangle$ denotes the averaging operation. The variance of a standard RW is the pulse number N which can be substituted by the quotient of continuous time variable t and the repetition period T_0 thus finally leading to the variance as a function of continuous time which can be processed further. Hereby, ν_0 corresponds to the inverse repetition period and thus the RR. The AC used here is defined as the limit of a time average to allow for convergence leading to two multiplicative terms as shown in Eq. (2.13).

$$\begin{aligned} \text{AC}\left\{\exp(i2\pi\nu_0 t + i\psi(t))\right\} &= \lim_{T\to\text{inf}} \frac{1}{T} \int_0^T \exp(-i2\pi\nu_0 t - i\psi(t) + i2\pi\nu_0(t+\tau) + i\psi(t+\tau))dt \\ &= \exp(i2\pi\nu_0\tau)\left\langle \exp(i\psi(t+\tau) - i\psi(t)) \right\rangle_t \end{aligned} \tag{2.13}$$

The first term corresponds to the undisturbed oscillation and the second term represents the time average of the phase fluctuations. The whole expression is still valid for all kind of phase-noise statistics. At this stage the statistical properties of the RW can be exploited to simplify this second term by using the *Gaussian moment theorem* [108] which is applied in the first row of Eq. (2.14).

$$\begin{aligned} \left\langle \exp(i\psi(t+\tau) - i\psi(t)) \right\rangle_t &= \exp(-\frac{1}{2}\left\langle (\psi(\tau+t) - \psi(t))^2 \right\rangle_t) \\ &= \exp(-\frac{1}{2}\left\langle \psi^2(\tau) \right\rangle) \\ &= \exp(-\frac{1}{2}\Delta\psi_0^2\nu_0\tau) \ \text{ and } \ \tau \geqslant 0 \\ &= \exp(-\frac{1}{2}\Delta\psi_0^2\nu_0|\tau|) \end{aligned} \tag{2.14}$$

It can be understood as follows. For a *drift-free*[7] RW process of the phase $\psi(t+\tau)$ for a fixed delay τ on the complex unit circle which is given by the argument of the exponential function, only even moments of the distribution $\langle\rangle_t$ with respect to t are non-zero thus leading to a symmetrical distribution with respect to zero. In such a way all the imaginary parts of the noise term on the complex unit circle cancel out leading to a real valued distribution, only depending on the variance. Furthermore, the RW does not

---

[7] Drift-free means that the first moment, namely the expectation value, is zero.

depend on the absolute time but only on the time difference with respect to a reference point leading to the simplification in Eq (2.14) (first line to second line). The remaining variance as a function of the time delay τ is replaced by means of Eq. (2.12). As the variance is only defined for positive values of τ and the AC has always to be symmetric with respect to zero delay τ is substituted by $|\tau|$.

Having found the complete AC function in accordance with the ansatz in Eq (2.9) the Fourier-transform can be applied to estimate the PS as depicted in Eq. (2.15).

$$\begin{aligned}\mathrm{PSD}(\nu) &= \mathrm{FT}\left\{\exp(i2\pi\nu_0\tau)\cdot\exp(-\frac{1}{2}\Delta\psi_0^2\nu_0|\tau|)\right\}\\ &= \delta(\nu-\nu_0) * \frac{\Delta\psi_0^2\nu_0}{(\frac{1}{2}\Delta\psi_0^2\nu_0)^2+(2\pi)^2\nu^2}\\ &= \frac{\Delta\psi_0^2\nu_0}{(\frac{1}{2}\Delta\psi_0^2\nu_0)^2+(2\pi)^2(\nu-\nu_0)^2}\end{aligned} \tag{2.15}$$

According to the convolution theorem of the Fourier-transform the oscillatory part and the noise part in line one of the equation can be converted separately leading to a convolution of a Dirac-delta-function at the oscillation frequency ν_0 and a Lorentzian shaped function centered at a frequency of zero. Therefore, the final PS corresponds to a Lorentzian shaped function centered at a frequency corresponding to the RR of the MLL. It is evident, that the full-width at half-maximum (FWHM) $\Delta\nu$ of the Lorentzian shaped PS directly depends on the RMS timing phase difference $\Delta\psi_0$ per pulse and on the RR ν_0 if the noise source is represented by a RW process leading to a FWHM of $\Delta\nu = (2\pi)^{-1}\Delta\psi_0^2\nu_0$. This FWHM together with Eq. (2.11) (on page 31) successfully yields the Eq 2.8 (on page 28) which is used to estimate the $\mathrm{TJ}_{\mathrm{ptp}}$ from the RR line-width.

The PS given by Eq. (2.15) can be used to estimate the TPN PSD $\mathrm{L}_\psi(f)$ as a function of offset frequency by implementing the approach by von der Linde [99] as shown in Eq. (2.16)[8].

$$\begin{aligned}\mathrm{L}_\psi(f) &= \lim_{(\nu-\nu_0)^2 \gg (\Delta\psi_0^2\nu_0)^2} \frac{\mathrm{PSD}(\nu-\nu_0)}{\int_{-\inf}^{+\inf}\mathrm{PSD}(\nu-\nu_0)d\nu}\\ &= \frac{\Delta\psi_0^2\nu_0}{(2\pi)^2(\nu-\nu_0)^2}\\ &= \frac{\Delta\psi_0^2\nu_0}{(2\pi)^2\left|f\right|^2}\end{aligned} \tag{2.16}$$

The required noise-power of the carrier-signal which does not exist for a free-running oscillator is consequently replaced here by the total integrated noise-power. A limit towards large offset frequencies

---

[8] Resolving the PS $P_F(\omega)$ in [99, Eq. (13)] to the timing noise power spectral density (TN PSD) $P_J(\omega_\mu)$, omitting amplitude-jitter $P_A(\omega_\mu)$ and only regarding the fundamental RR line ($\mu = 1$) yields $P_J(\omega) = P_F(\omega)/[(2\pi)^2\omega_0^2|\tilde{f}(\omega)|^2]$. Hereby, $|\tilde{f}(\omega)|^2$ defines the carrier power envelope. This TN PSD $P_F(\omega)$ corresponds to a TPN PSD of $L_\psi(\omega) = P_F(\omega)/|\tilde{f}(\omega)|^2$

has to be used to adapt this approach for a free running oscillator as pointed out in [98] and as will be evident at the end of this sub-section. Despite the necessary limit term, it is evident, that the TPN PSD is just a normalized PS. In such a way a f^{-2} dependence of the TPN PSD is obtained. According to the definition in Eq. (2.10) this formula allows to deduce the RMS timing phase noise $\Delta\psi_0$ per pulse from the measured TPN PSD $\mathrm{L}_\psi(f)$. Alternatively the widely used $\mathrm{TJ}_{\mathrm{ptp}}$ can also be obtained by means of Eq (2.11).

Now, referring to the schematic shown in Fig. 2.6, the direct connection of the intrinsic TJ parameter $\Delta\psi_0$ and the experimentally accessible TPN PSD will be derived. The simulations in this work model the phase only, therefore in the following the experimentally accessible TPN PSD is directly derived from the phase evolution according to Eq. (2.17) without the detour over the RR.

$$\mathrm{L}_\psi(f) = \mathrm{FT}\left\{\mathrm{AC}\left\{\psi(t)\right\}\right\} \tag{2.17}$$

Hereby, by definition, the TPN PSD is *directly* the Fourier-transform of the AC of the timing phase evolution in contrast to Eq. (2.9) where the PS of the optical pulse train is used.

Using the discrete RW term of Eq. (2.10) the AC is calculated *numerically* leading to the result shown in Eq. (2.18).

$$\mathrm{AC}\left\{\psi(N)\right\} = \Delta\psi_0^2 N - \Delta\psi_0^2 |n| \tag{2.18}$$

Obligatory, the AC has to be unbiased[9] to be able to identify the function and properly normalized[10]. Substituting the discrete variables record length N and the delay n in terms of pulse numbers by the corresponding continuous time variables T and τ leads to the AC shown in Eq. (2.19).

$$\mathrm{AC}\left\{\psi(\tau)\right\} = \Delta\psi_0^2 \nu_0 T - \Delta\psi_0^2 \nu_0 |\tau| \tag{2.19}$$

Finally, to obtain the TPN PSD this AC is Fourier transformed leading to the expression given in Eq. (2.20).

$$\begin{aligned}\mathrm{L}_\psi(f) &= \mathrm{FT}\left\{\mathrm{AC}\left\{\psi(\tau)\right\}\right\}\\ &= \frac{\Delta\psi_0^2 \nu_0}{(2\pi)^2 \left|f\right|^2} + \Delta\psi_0^2 \nu_0 T \delta(f)\\ &= \frac{\Delta\psi_0^2 \nu_0}{(2\pi)^2 \left|f\right|^2} \text{ for } f > 0\end{aligned} \tag{2.20}$$

---

[9] Unbiased means, that the numerical AC is modified not to decrease with increasing delay due to the finite length of input data and due to the non-decaying phase $\psi(N)$ with increasing N. Although the validity reduces with increasing delay the AC *function* can be accurately obtained. For other cases and if the highest precision in delay and amplitude is required biasing must be on.

[10] The normalization factor is 2 in order to yield the expected value of $\Delta\psi_0^2 N$ at zero delay.

Hereby, the Dirac-delta term may be neglected for the TPN PSD because the frequency dependent term diverges to infinity for a frequency of zero anyway. This expression represents the direct power spectral density (PSD) of a RW which is equivalent to a TPN PSD.

Eq. (2.20) allows now to give specific interconnections of the TJ measures listed in sub-section 2.4.1. Combining the connection of $\Delta\psi_0$ and $\mathrm{TJ}_{\mathrm{ptp}}$ in Eq. (2.11) with the TPN PSD from Eq. (2.20) yields the TPN PSD for a free-running MLL as a function of $\mathrm{TJ}_{\mathrm{ptp}}$ as shown in the following Eq. (2.21).

$$\begin{aligned} \mathrm{L}_{\psi}(f) &= \frac{\sigma_{\mathrm{ptp}}^2\,\nu_0^3}{f^2} \\ &= \frac{\Delta\nu}{2\pi f^2} \end{aligned} \tag{2.21}$$

Furthermore, $\mathrm{TJ}_{\mathrm{ptp}}$ can be substituted by the line-width $\Delta\nu$ of the RR line by means of Eq. (2.8).

This Eq. (2.21) now allows to specify the integrated timing jitter ($\mathrm{TJ}_{\mathrm{int}}^{(f_1,f_2)}$) as a function of $\mathrm{TJ}_{\mathrm{ptp}}$ for a free-running MLL by insertion of Eq. (2.21) into Eq. (2.7) (on page 27) leading to the following Eq. (2.22).

$$\begin{aligned} \sigma_{\mathrm{int}} &= \frac{\sigma_{\mathrm{ptp}}\sqrt{\nu_0}}{\sqrt{2}\pi}\sqrt{\frac{1}{f_1}-\frac{1}{f_2}} \\ &= \frac{\sqrt{\Delta\nu}}{2\pi^{3/2}\nu_0}\sqrt{\frac{1}{f_1}-\frac{1}{f_2}} \end{aligned} \tag{2.22}$$

Hereby, $\mathrm{TJ}_{\mathrm{ptp}}$ can be substituted by the line-width $\Delta\nu$ of the RR line by means of Eq. (2.8). It is evident that using the full frequency range by using $f_1 = 0$ anf $f_2 = \infty$ the value of $\mathrm{TJ}_{\mathrm{int}}^{(f_1,f_2)}$ diverges thus showing the unbounded phase on long time-scales.

Finally, comparing the PSD of the timing phase as shown in Eq. (2.20) with the TPN PSD of the optical pulse train as shown in Eq. (2.16) yields full correspondence and therefore verifies that the TJ of a passively MLL driven by a RW may be correspondingly treated on a timing-phase level. Therefore the connection shown in Fig. 2.6 is verified.

Furthermore, the applied limit in Eq. (2.16) directly represents the limitation of the method of von der Linde for passively MLL because Eq. (2.20) represents the correct and also intuitively reasonable solution. Thus, the TPN PSD obtained by the method of von der Linde is valid for offset frequencies above the FWHM of the RR line only. This limitation can be understood via the fact, that the phase noise is applied to an oscillation and thus is not accessible directly, or in other words full information of the phase is lost.

This derivation shows that the ideal shape of the RR signal is Lorentzian. Thus any deviation from a Lorentzian shape or any additional signals in the PS indicate additional uncommon instabilities. Hereby the word uncommon is used to highlight that the TJ represents an expected inherent timing instability. In addition, using the direct PS of the phase in simulations to obtain the TPN PSD yields validity over the whole obtained frequency range without limitations as compared to the TPN PSD obtained from the PS of the optical pulse train.

2.4.3 Source of timing jitter

In the previous sub-section the experimental measures of estimation of timing jitter (TJ) were derived based on the sole assumption of a random walk (RW) process for the timing phase evolution. Hereby, it was anticipated that the dominant type of TJ is the direct projection of amplified spontaneous emission (ASE) on the intra-cavity pulse-timing. Nevertheless, there is a multitude of types and sources of TJ. Hereby, different types of TJ may originate from the same noise source. Therefore in the following, the most relevant types of TJ will be introduced which are also relevant for this work. Various noise sources and types were initially investigated theoretically in [106] and revised in [44]. TJ can be introduced amongst others by fluctuations of gain, fluctuations of the refractive index, mechanical vibrations, coupling of intensity noise to timing noise, coupling of vacuum fluctuations reflected at the laser facet to timing noise, direct projection of ASE onto the intra-cavity pulse and fluctuations of the optical center frequency [44]. All these noise sources and types are significant for mode-locked lasers (MLLs) which exhibit extremely low TJ such as the solid-state laser (SSL) reported in [64].

However, only two TJ types are dominant for monolithic semiconductor MLLs which depend on various laser parameters and the spontaneous emission [44]. They will be discussed in the following. Such fundamental origins of TJ are sometimes referred to as *quantum-limited* TJ [44, 64].

The contribution of **direct projection of ASE** on the pulse timing can be described by Eq. (2.23) which defines the timing noise power spectral density (TN PSD) for this type of noise. This equation is valid for Gaussian shaped pulses and is an adapted version of [109, Eq. (1)] by using [44, Eq. (6)].

$$L_t^{\mathrm{ASE}}(f) = 2\left(\frac{1}{2\sqrt{2\ln 2}}\right)^2 \frac{h\nu\theta g \tau_p^2}{E_p T_0} \frac{1}{(2\pi f)^2} \tag{2.23}$$

Hereby, h is the Planck constant, ν is the optical frequency, θ is the inversion parameter or spontaneous emission factor[11], g is the gain per round-trip or equivalently the loss per round-trip, τ_p is the full-width at half-maximum (FWHM) pulse-width, E_p is the pulse energy and T_0 is the round-trip period. The numerical factor mainly accounts for the conversion of the FWHM based pulse width to an standard deviation (SD) based pulse width. The inversion parameter θ is a measure for the impact of ASE and amounts to 1 for an ideal four-level gain media. It was assumed to be 3 for a semiconductor laser (SCL) modeled in [110] and was even assumed to be 18 for the SSL reported in [64]. Eq. (2.23) allows to specify and partially to understand why TJ originating from direct ASE projection is magnitudes of orders higher for typical monolithic SCLs as compared to SSLs. The round-trip gain g mainly has to compensate

---

[11] Also denoted as n_{sp}. It is not the *spontaneous emission coupling factor* which is denoted as β.

for mirror losses. Hereby, anti-reflection coated edge-emitters exhibit output losses of 90 % per round-trip whereby SSLs exhibit output losses below 1 %. The highest impact on noise originates from the squared pulse width τ_p which lies in the 1 ps and 100 fs range for SCLs and SSLs, respectively. Longer pulses accumulate more ASE. Assuming similar average power levels the intra-cavity pulse Energy E_p correspondingly depends on pulse-width as well. Finally the repetition rate (RR) represented by T_0 lies in the 10 GHz and 100 MHz range for SCLs and SSLs, respectively. In conclusion, taking into account all the mentioned parameter differences between typical SSLs and SCLs a typical SSL should exhibit a TN PSD which is by a factor of $\approx 10^7$ lower than a TN PSD of a SCL while considering only the direct ASE contribution.

Interestingly, the contribution of T_0 is only a mathematical reason for the TN PSD but has no physical meaning. Recapitulating, pulse-to-pulse timing jitter ($\mathrm{TJ}_{\mathrm{ptp}}$) is a measure for the per-round-trip jitter which ideally quantifies the noise source strength. Therefore, calculating $\mathrm{TJ}_{\mathrm{ptp}}$ from Eq. (2.23) yields no RR or T_0 dependence as given by Eq. (2.24).

$$\sigma_{\mathrm{ptp}}^{\mathrm{ASE}} = \sqrt{\frac{h\nu\theta g\tau_p^2}{E_p}} \tag{2.24}$$

This novel fact is easily understood because the contribution of the cavity length on the noise strength is contained within the round-trip gain g.

Using this information leads directly to the narrow RR line-widths of external-cavity semiconductor MLL. Extending a monolithic MLL by a passive external cavity and assuming identical operating conditions leads to an unchanged $\mathrm{TJ}_{\mathrm{ptp}}$ due to the unchanged gain. Now, using Eq. (2.8) (on page 28) leads to a f^3 dependence of the RR line-width on RR. In [111] a RR line-width of 30 Hz was reported at a RR of 281 MHz. However, this narrow line-width corresponds to a high $\mathrm{TJ}_{\mathrm{ptp}}$ of 460 fs which is ≈30 times higher than the lowest $\mathrm{TJ}_{\mathrm{ptp}}$ of monolithic MLLs based on the same gain medium. According to Eq. (2.8) a RR line-width of 150 mHz is expected.

Another significant source of TJ is caused by fluctuations of the optical center frequency which causes timing fluctuations mediated by intra-cavity dispersion. This type of TJ is also known as **Gordon-Haus jitter**. A MLL exhibits a comb of optical-modes. Uncorrelated frequency fluctuations of each mode are covered by the direct ASE contribution. A collective fluctuation of all modes causes a timing fluctuation by dispersion. The effect of this type of noise on the pulse timing can be described by Eq. (2.25) taken from [109] and adapted for Gaussian shaped optical spectra.

$$L_t(f) = 2\left(\frac{1}{2\sqrt{2\ln 2}}\right)^2 \left(\frac{D_2}{f\,T_0}\right)^2 \frac{1}{(2\pi f)^2 + \tau_\nu^{-2}} \frac{\theta h \nu g \Delta\nu_p^2}{E_p T_0} \qquad \text{with } \tau_\nu = T_0 \left(\frac{\Delta\nu_g}{\Delta\nu_p}\right)^2 \tag{2.25}$$

Hereby, D_2 is the group delay dispersion (GDD) in units of s/Hz, $\Delta\nu_p$ is the FWHM spectral bandwidth of the pulse and $\Delta\nu_g$ is the FWHM spectral gain bandwidth of the medium. The equation consists of four main parts. The last part accounts for the strength of the noise source which is described as a projection of ASE on the pulse spectrum similar to Eq. (2.23). The first part converts the FWHM based spectral width to a SD based width. The third part, which has a Lorentzian shape, confines the frequency drift due to the limited spectral width of the gain $\Delta\nu_g$. Finally, the second part converts the optical frequency noise to timing noise by means of dispersion. No round-trip gain g is used here in τ_ν in contrast to [109]. There, no gain is only assumed for passive bandwidth filtering effects. This full equation also allows to specify why TJ originating from dispersion-mediated center-frequency fluctuations is higher for typical monolithic SCLs as compared to SSLs. The same parameter dependence also applies here as reported above for the direct ASE projection. Here, in addition, the GDD of SSLs lies in the 1000 fs^2 range whereas the GDD of SCLs may even lie in the 1 ps^2 range [61] thus further increasing the TJ of a SCL as compared to an SSL. For high frequencies ($(2\pi f)^2 > \tau_\nu^{-2}$) the Gordon-Haus jitter exhibits a f^{-4} slope. However, for low frequencies a f^{-2} slope is obtained which is indistinguishable from the f^{-2} slope of the TJ caused by direct ASE projection which may prevent a simple identification of this type of TJ.

To summarize, the fundamental or quantum TJ limits may be deduced by means of Eq. (2.23) and Eq. (2.25) if the required parameters are well known. However, some parameters have to be arbitrarily assumed including the inversion parameter θ and the round-trip gain g. Also the GDD D_2 is unknown. The accuracy of prediction is quite good for SSLs which exhibit nearly constant parameters including the intra-cavity pulse energy. In contrast, the intra-cavity pulse energy of a SCL undergoes high variations due to the relatively low reflectivity at the output facet. This pulse energy variation also represents an additional source of mismatch with respect to both equations which require constant parameters. Nevertheless it will be shown in the experimental part of this work that with thorough approximations good accordances of experiment and theory can be obtained.

2.4.4 Summary

In the previous sub-sections the timing jitter (TJ) was introduced and explained, the most important measures of TJ were given, an ideal power spectrum (PS) and an ideal timing phase noise power spectral density (TPN PSD) were derived to allow deducing the interconnections of the various parameters and finally the most important sources of TJ for a mode-locked semiconductor laser (SCL) were introduced.

This overview is useful to understand the results obtained in the experimental part of this work in particluar in chapter 5. The most important findings of this section can be given as:

- Free-running passively mode-locked lasers (MLLs) exhibit non-stationary noise-characteristics whereas actively MLLs exhibit stationary noise characteristics which have to be treated differently in terms of evaluation and quantification.
- The TPN PSD and the simply related power spectral densities (PSDs) including the timing noise power spectral density (TN PSD) and the frequency noise power spectral density (FN PSD) contain most of the information on TJ and all other measures of TJ including the integrated timing jitter ($\mathrm{TJ}_{\mathrm{int}}^{(f_1,f_2)}$) and the pulse-to-pulse timing jitter ($\mathrm{TJ}_{\mathrm{ptp}}$) can be derived from them. If obtained without experimental limitations the TPN PSD is valid over the whole frequency range for all types of MLL.
- The TPN PSD for passively MLL obtained from the PS of the optical pulse train by the method of von der Linde is valid for a frequency range starting at a frequency offset well above half the repetition rate (RR) line-width and up to a frequency offset of half the RR being the Nyquist-frequency.
- The $\mathrm{TJ}_{\mathrm{ptp}}$ or equivalently the line-width of the RR are the only necessary measure of TJ for a stable and free-running MLL.
- The $\mathrm{TJ}_{\mathrm{ptp}}$ is also a direct measure for the strength of the noise source of a MLL.

2.5 Global summary

Having presented the fundamentals of mode locking (ML) and the peculiar and beneficial properties of quantum-dot (QD) based active media, having highlighted some less known particularities of the measurement methods and their impact on applications and having provided an wide and profound treatment of timing jitter (TJ) of semiconductor mode-locked laser (MLL) has set the basis which now allows to present, evaluate and discuss the experimental and simulation results of this work.

3 Suppression of amplitude instabilities of mode-locking

> Resistance is futile.
>
> The Borg, species from Star Trek (Science fiction television and movie series)

The optical pulse train emitted by a passively mode-locked laser (MLL) may be affected by undesired fluctuations, whereby the pulses experience amplitude modulations by Q-switching (QS) at frequencies from the MHz to the GHz range related to undamped relaxation oscillations [72, 73]. The saturable absorber required for mode locking (ML) operation can assist these QS modulations by providing saturable absorption on timescales of multiples of the pulse repetition period (PRP) thus potentially favoring emission of an envelope modulated pulse train. In [112] it is stated that the physical effect needed for short-pulse generation, typically nonlinear losses or gain, is also responsible for QS instabilities. Hereby, ML operation influenced by QS is denoted as Q-switched mode-locking (QS ML). Unfortunately, QS or QS ML often occur at lower gain currents where the shortest pulses are found which are desirable for many applications. Another source of such amplitude instabilities could originate from trailing edge instability (TEI) or leading edge instability (LEI) as numerically identified and demonstrated in [69, Fig. 7]. In real devices such broadband amplitude modulations (20 MHz to 250 MHz, approximated from [69, Fig. 7]) may excite any system-based frequency resonance manifesting in distinct sharp frequencies. Such resonances can for example be formed by electrical parasitics or electrical cable resonances.

Lasers based on quantum-dots (QDs) exhibit strong damping of relaxation oscillations (ROs) [13]. Straight QD based MLL are not found to exhibit QS ML but the tapered MLLs investigated in the context of this work can exhibit QS ML and amplitude instabilities. The difference of both types of lasers is the geometry of the tapered MLL. In [72, Eq. (7)] a condition for stable ML operation was derived and is given by Eq. (3.1)[1].

$$E_P \left| \frac{dq_P}{dE_P} \right|_{\bar{E}_P} < \frac{T_0}{\tau_L} + \frac{E_P}{E_{\mathrm{sat,g}}} \quad \text{with} \quad E_{\mathrm{sat,g}} = \frac{h\nu A}{\Gamma dg/dn} \tag{3.1}$$

Hereby, E_P denotes the pulse energy, $\bar{E}_P$ the mean pulse energy, q_P the round-trip loss of the absorber, T_0 the repetition rate (RR), τ_L the carrier lifetime, $E_{\mathrm{sat,g}}$ the saturation energy of the gain, ν the light frequency, A the modal area, Γ the confinement factor and dg/dn the differential gain. T_0 lies in the 50 ps range and τ_L lies in the 1 ns range. The large modal area A and the low differential gain dg/dn of the tapered section [76, Fig. 1] resulting in a high saturation energy $E_{\mathrm{sat,g}}$ of the gain section may lead to a low value on the right hand side of Eq. (3.1) whereas a high differential loss dq_P/dE_P of the absorber required for ML operation leads to a high value on the left hand side of Eq. (3.1). Therefore it may be

---

[1] In [72] all subsequent simplified equations are given for semiconductor saturable absorber mirrors (SESAMs) only.

assumed that the inequality is not always fulfilled thus suggesting that the tapered MLL exhibits QS ML more easily as compared to straight MLL.

As mentioned above, in [69] new kinds of amplitude instabilities are numerically demonstrated for straight section MLL which are also found for tapered MLL in [71]. These TEI and LEI originate from a gain and absorption imbalance at different operation conditions and lead to broad-band amplitude instabilities of the simulated pulse train. The occurrence of such proposed instabilities could not be specified by a simple equation so far.

Preventive approaches for avoiding QS ML or amplitude instabilities in mode-locked semiconductor lasers (SCLs) rely on a specific active region design [114, 115] or on the concept of the inverse saturable absorption [116, 117]. Hereby, the normally required saturable absorption is still present allowing for ML operation by absorbing low power levels[2] and transmitting high power levels but in addition the absorption is increasing again above a certain power threshold. This power threshold is tailored to lie above the expected steady state power level of the MLL [116, Fig. 2] thus suppressing the build-up of pulsed RO. Inverse saturable absorption reduces or nullifies the differential loss dq_P/dE_P in Eq. (3.1) for high values of $\bar{E}_P$. Alternatively, subsequent suppression of QS ML can be achieved by means of an active opto-electrical feedback loop realized by means of an intra-cavity loss modulator or control of the pump parameter [38, 47, 118, 119].

In this chapter a simple method to suppress amplitude instabilities in mode-locked two-section SCLs is demonstrated by only utilizing frequency-selective passive electrical components connected to the absorber section. The basic idea of the presented stabilization approach originates from the fact that QS, QS ML or any amplitude instability represent a strong amplitude modulation of the optical pulses in the low-frequency range leading to modulation of the optical average power. The optical power is directly related to the carrier density and thus the laser voltage which is exploited in self-mixing experiments [120]. Thus, amplitude instabilities are expected to cause modulation of the voltage of the absorber section of a MLL which in turn can be influenced for example by a common opto-electrical feedback (FB) loop. Here, in contrast an all-passive electrical approach is presented. Hereby, the absorber section is exploited both as a photo-diode and a control element of the MLL by grounding the absorber AC photo-current in the MHz frequency range. A suppression of amplitude instabilities is achieved and additionally an extension of the ML operation range towards lower gain currents is presented.

Extending this passive electrical control acting on the MHz timescale towards higher control frequencies while still keeping it a passive approach leads to short-delay all-optical feedback (AO FB). It will be shown that such short AO FB allows reduction of QS ML operation towards clean ML for a specific operation range.

---

[2] In pulsed operation the fluence represents the correct measure.

3.1 Stabilization schemes

In the following *two* different specifically selected tapered mode-locked laser (MLL) will be used for demonstration and investigation of the presented stabilization approach. They exhibit features in the power spectrum (PS) which suggest different types of amplitude instabilities. Both different quantum-dot (QD) wafers (do 2584, do 1790) of the two MLLs were grown on a GaAs substrate by molecular beam epitaxy (MBE) incorporating 10 layers of InAs QDs separated by GaAs barriers. The *first* fully gain-guided tapered structure (do 2584 s1b a6) consists of a straight absorber section with a length of 400 μm and a tapered gain section with a full taper angle of 2° and a length of 2100 μm resulting in a total length of 2500 μm which corresponds to a repetition rate (RR) of 16 GHz. The *second* fully gain-guided tapered structure (do 1790 gg2 a400 E3) consists of a straight absorber section with a length of 400 μm and a tapered gain section with a full taper angle of 2° and a length of 2380 μm resulting in a total length of 2780 μm which corresponds to a RR of 14.6 GHz. The investigated structures base on wafers fabricated by *Innolume GmbH, Germany* and are initially proposed and processed by *III-V Lab, France*.

In Fig. 3.1a the electrical contacting layout for the laser is shown. For mode locking (ML) operation the gain section is pumped with a DC current and a negative voltage is applied to the absorber section. To achieve the desired suppression of instabilities the absorber is grounded by a high-frequency DC-block and a high-frequency 50Ω resistor[3] in series and is connected to a voltage source[4] by a inductor. This DC-Block which is a capacitor and the resistor represent an electrical high pass filter. The inductor represents an electrical low-pass filter. The DC-Block and the inductor are incorporated in a bias-T[5]. Hereby, the 50 Ω resistor is connected to the AC-port of the bias-T. To achieve variable resistance the 50 Ω resistor is replaced by a high-frequency variable electrical attenuator[6] while either grounding the other port of this electrical attenuator by a short-circuit element or leaving it open. The absorber is connected to the bias-T by a high-frequency SMA-cable with a length of 0.3 m. Measurements were carried out by means of an optical power meter, an auto-correlator and a fast photo detector connected to an electrical spectrum analyzer (ESA). It is noted, that such electrical configuration for the absorber was used in literature [121], however, the reason or motivation for such a configuration was neither given nor motivated.

The short all-optical feedback (AO FB) is implemented in free-space configuration by splitting the main beam, attenuating it and reflecting it back into the MLL by a mirror as schematically shown in Fig. 3.1b. Hereby the delay-length of the AO FB initially amounts to ≈50 cm which corresponds to a frequency of 300 MHz. The total ratio of output power to back-reflected power amounts to $1.7 \cdot 10^{-3}$ while disregarding input-coupling losses.

---

[3] Huber & Suhner, SMA, 50Ω, 18 GHz

[4] Rohde & Schwarz, NGT20

[5] Picosecond Pulse Labs, Bias-T 5590, external inductor not used

[6] JFW Industries, 50DR-060, DC - 2 GHz

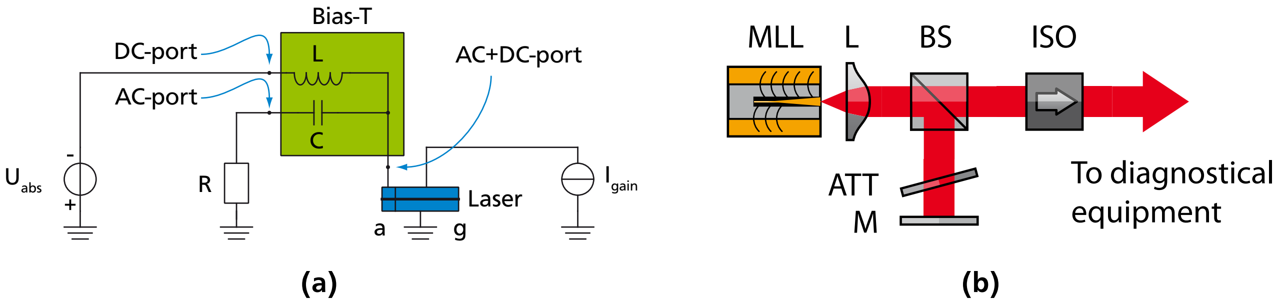

Figure 3.1: (a) Schematic of electrical stabilization configuration of the two-section laser (U_{abs}: DC voltage source, I_{gain}: DC current source, L: low-pass filter, C: DC-block, R: resistor, a: absorber section, g: gain section. (b) Schematic of experimental realization of AO FB stabilization (L: collimation lens, BS: beam splitter, ATT: optical attenuator, M: mirror, ISO: optical isolator).

3.2 Passive electrical stabilization

Because amplitude instabilities or Q-switching (QS) are primarily observable in the radio-frequency (RF) domain, in Fig. 3.2 the RF power spectra (PS) are shown **for the first mode-locked laser (MLL) (do 2584 s1b a6)** as a function of gain current for an absorber voltage of −6.0 V. The PS on top (Fig. 3.2a, Fig. 3.2b) depict the *low-frequency band* up to 200 MHz which generally can be used to identify amplitude modulations of a signal and is thus necessary for estimation of QS. The PS on the bottom (Fig. 3.2c, Fig. 3.2d) depict the *high-frequency band* around the repetition rate (RR) frequency which allows for determination of existence of mode locking (ML). The PS on the left side are obtained without and on the right side with the suppression circuit.

Without the suppression circuit, lasing starts at a current of 500 mA and is immediately accompanied by a form of QS. This is indicated by the pronounced frequency comb in the low-frequency band at multiples of ≈17 MHz and a barely pronounced RR signal exhibiting a line-width of large 37 MHz in the high-frequency band. At a current of 615 mA the number of frequency peaks in the low-frequency comb reduces and a distinct RR signal accompanied by severe modulation side-bands at multiples of 19 MHz is observable in the high-frequency band indicating Q-switched mode-locking (QS ML). At a gain current of 730 mA the side-bands at an offset of 19 MHz disappear and the RR exhibits a narrow line-width of 32 kHz. However, strong side-bands at multiples of ≈500 MHz appear (not shown) which indicate a different regime of QS ML. Stable ML is not recognizable in the observed current range. Such low QS frequencies were also observed in [23] where three regimes of QS were found with a lowest frequency of 33 MHz. In [122] pseudo-periodic switches between a ML regime and a non-lasing state were observed down to frequencies of 1 MHz.

With the suppression circuit connected, the lasing threshold is slightly increased by ≈5 mA which is evident from the absence of any signal. However, now, no modulation comb in the low-frequency range is visible in the whole current range. In addition, the sidebands of the RR frequency at multiples of 19 MHz also fully disappear. However, the side-bands at a frequency offset of ≈500 MHz persist (not shown) and now start at a current of 725 mA which is 5 mA lower as compared to the free-running case. This shows clearly the absence of QS or amplitude modulations up to a current of 725 mA. Furthermore, ML starts at a significantly reduced gain current which amounts to 570 mA as obvious from the existence of the narrow RR signal. Now, stable ML without instabilities is obtained in the current range from 570 mA to 625 mA and from 675 mA to 720 mA. The current range in between these two ranges and the small current range around 605 mA correspond to a change in RR frequency representing a so called supermode-transition as reported in [122].

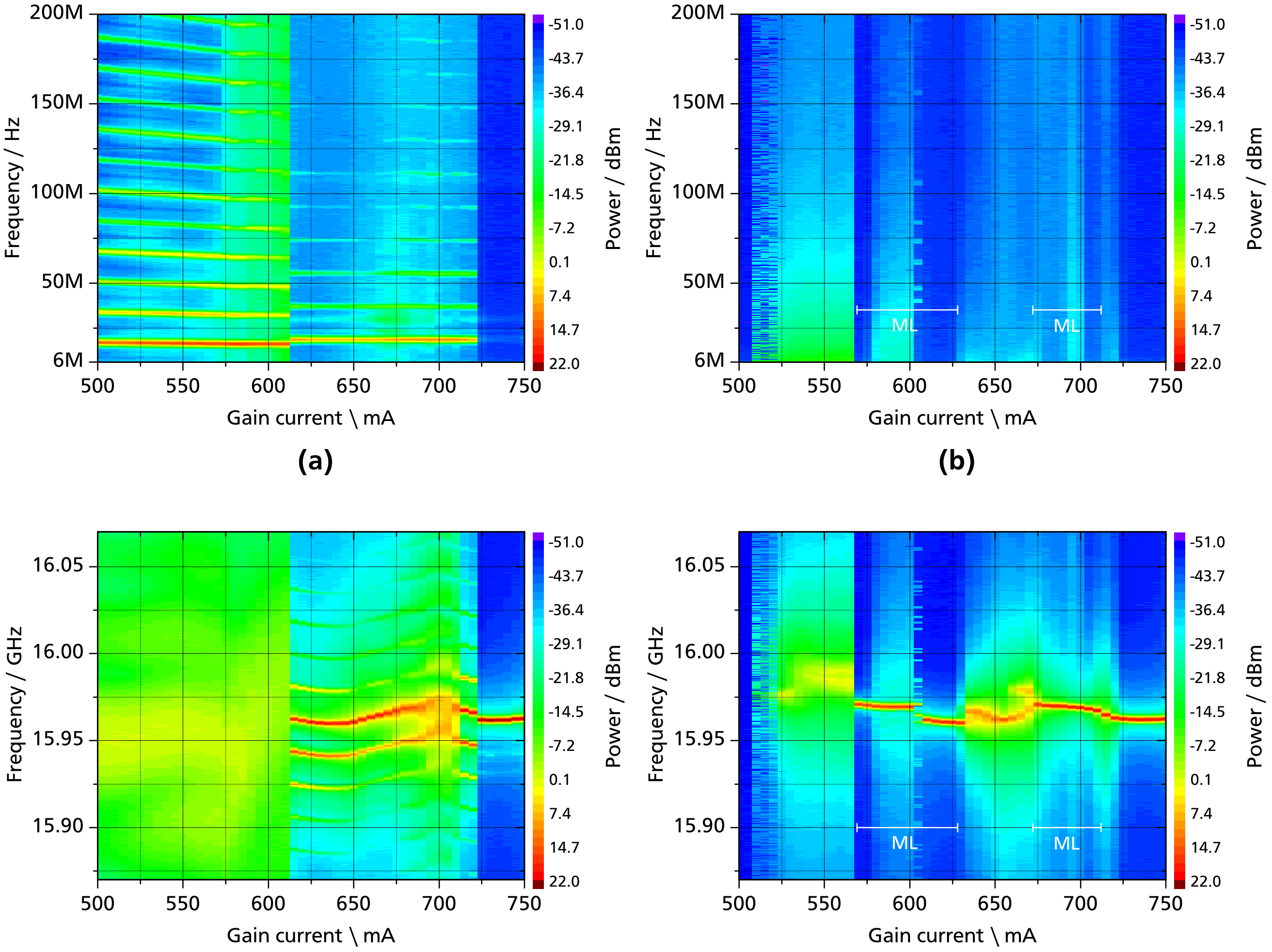

(a) **(b)**

(c) **(d)**

Figure 3.2: PS for the first of the two investigated MLL as a function of gain current at an absorber voltage of −6.0 V depicting (a) the low-frequency region without stabilization (b) the low-frequency region with stabilization (c) the RR frequency region without stabilization and (d) the RR frequency region with stabilization. The white bars denote stable ML operation.

To exclude any destabilizing or stabilizing role of the used voltage source, other voltage sources including a battery are investigated always showing QS or QS ML for this laser. Also variations of electrical contacting and cables do not change the laser characteristics but the type of electrical cables has an influence on the frequency of the amplitude modulations by altering it by a few MHz. This observation supports the assumption, that the broadband amplitude modulations originating from trailing-edge-instabilities [69, Fig. 7] excite an existing electrical frequency resonance manifesting in distinct sharp frequencies in addition to the RR frequency. This electrical resonance may originate from a parasitic capacitance or inductance of the MLL or of the electrical contacting. It it emphasized that these potential resonances have no influence on stable ML because stable ML can not excite these low-frequency resonances. The only noise-source of a stably running MLL is the RR itself which lies in a completely different frequency range as compared to any possible resonance. It is found that in experiment, QS at frequencies in the MHz range may disturb the constant current operation of the current source indicated by a fluctuating gain current or absorber voltage value.

Interestingly, as an alternative to the passive stabilization, an actively stabilizing voltage source[7] used to provide the absorber voltage is able to stabilize another MLL (do 2584 s3 a3 in chapter 4) at low gain currents but destabilizes this MLL at high gain currents. The feedback-loop reaction time of this voltage source is specified to be 70 μs[8] and is measured to be ≈3 μs (≈333 kHz) to recover to ≈10 % of the initial voltage for a load change from 2 kΩ to 1 MΩ. This demonstrates that closed-loop based active absorber voltage control allows for stabilization of a MLL too and that stabilization in the low-frequency range (<333 kHz) can be sufficient for stabilization of ML operation. Nevertheless, the broad-band passive stabilization is also successful for the mentioned laser and in contrast does not destabilize it.

Having described the qualitative differences of the PS introduced by the stabilization circuit, now, the changes are quantified to allow for a precise statement of effectivity. Fig. 3.3a shows the integrated power spectral densities (PSDs)[9] in a low-frequency range from 6 MHz to 200 MHz (open symbols) and the integrated PSDs in a high-frequency range from 200 MHz to 8 GHz (closed symbols) as a function of gain current for an absorber voltage of 6.0 V. If a RR signal exists any signal component from 0 Hz to half of the RR represents an amplitude modulation which is the case for QS or QS ML. Frequency modulations do not appear in this frequency range. An integration of this frequency range thus represents a measure for the total magnitude of amplitude modulations or an absolute noise-power. These two frequency ranges are investigated separately in Fig. 3.3a to allow to separate the two different QS ML regions (no. 1 and no. 2) starting at a current range of 610 mA and 725 mA which can be well identified in Fig. 3.2. To give an comparable impression of the noise power, it is noted here, that the power of the RR line in stabilized operation above a current of 570 mA amounts to a nearly constant value of $+(18 \pm 2)$ dBm. In addition, the instrument noise power contributes by a value of -10 dBm in the high frequency range and by a value of -26 dBm in the low frequency range indicated by the dashed and dotted horizontal lines respectively.

Without stabilization the three regimes (QS, QS ML no. 1 and QS ML no. 2) are well separable by means of both integration ranges. QS is indicated by a high value of low-frequency noise-power (+20 dBm) and a high value of high-frequency noise-power (+10 dBm) indicating the general instability. In the least worst case at a current of 645 mA the dominant low frequency noise power is only -10 dB lower as compared to the expected power of the RR signal of 17.5 dBm. The QS ML region no. 1 is characterized by a high value of low-frequency noise power (≈ +10 dBm) and a lower value of high-frequency noise-

---

[7] Keithley, Source meter 2600

[8] Transient response time <70 μs for the output to recover to 0.1 % for a 10 % to 90 % step change in load.

[9] The PSD is obtained by dividing the PS by the resolution bandwidth (RBW).

power ($\approx$-3 dBm) indicating the dominance of noise on the MHz timescale. The QS ML region no. 2 is characterized by a very low value of low-frequency noise power (−25 dBm, close to the detection limit) and a high value of high-frequency noise-power (+13 dBm) indicating the dominance of noise on the GHz timescale. The sum of noise-power of both frequency ranges is roughly constant ($\approx$+10 dBm) in a current range above 615 mA thus suggesting a redistribution of amplitude noise at the transition from the first to the second QS ML region at a current above 725 mA.

With electrical stabilization the two stable ML ranges are obtained as already noted and indicated by the bars in Fig. 3.3a. The low-frequency noise power is highly reduced in the whole current range up to 725 mA with a maximum suppression of −35 dB at a current of 570 mA being only +1 dB higher than the instrument noise contribution of −26 dBm. Above a current of 720 mA the low-frequency noise power is unchanged and low. Also the high-frequency noise-power is strongly reduced with a maximum suppression of −28 dB being only +3 dB higher than the instrument noise contribution of −10 dBm up to a current of 615 mA. In the most efficient case at a current of 575 mA the dominant high frequency noise power is −27 dB lower as compared to the expected power of the RR signal of +18.0 dBm. Above a current of 615 mA and in particular above a current of 720 mA the high-frequency noise-power is roughly unchanged. Therefore the low-frequency instabilities QS up to a current of 615 mA and QS ML no. 1 up to a current of 720 mA can be effectively suppressed, however, the high-frequency instability QS ML no. 2 above a current of 720 mA is not affected by the electrical circuit thus suggesting that the circuit cannot suppress amplitude instabilities at frequencies higher than 200 MHz.

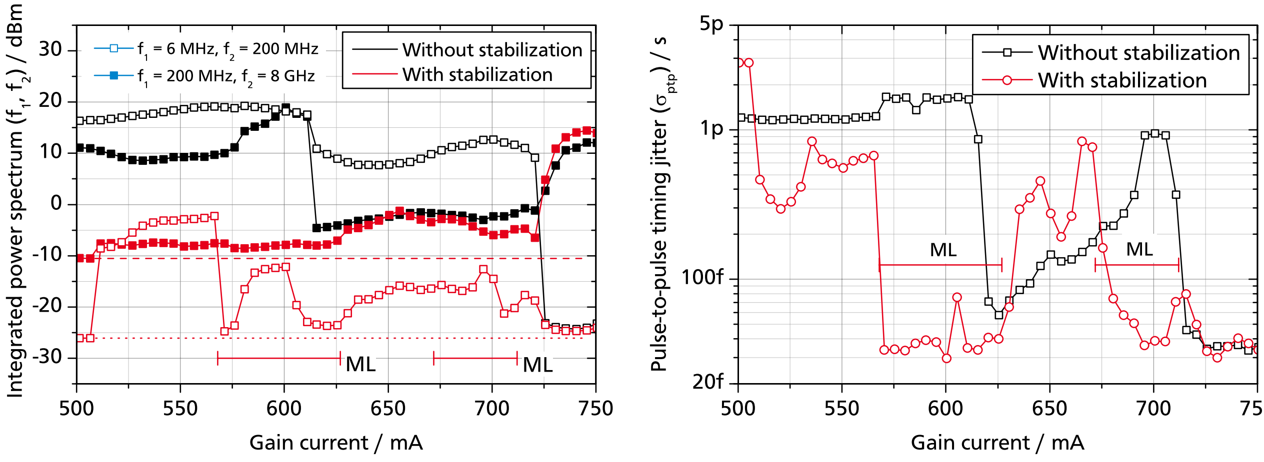

(a) (b)

Figure 3.3: (a) Integrated PS for the first MLL in a low (6 MHz to 200 MHz) and a high-frequency range (200 MHz to 8 GHz) as a function of gain current for both configurations. Instrument noise power contributes to a value of −10 dBm in the high frequency range and to −26 dBm in the low frequency range. (b) TJ$_{\text{ptp}}$ for the first MLL as a function of gain current for both configurations.

Having presented quantitative results on amplitude instabilities, now, consequently the influence of the stabilizing scheme on the timing jitter (TJ) will be investigated. Fig. 3.3b shows the TJ$_{\text{ptp}}$ (see subsection 2.4.1) as a function of gain current.

Without stabilization the calculated TJ_{ptp} amounts to a high value of up to 1.6 ps in the QS regime up to a current of 615 mA which amounts to ≈3 % of the pulse repetition period (PRP) or to a RR line width of 66 MHz. This gives an impression which values correspond to highly unstable ML operation. In the first QS ML regime starting at a current of 620 mA the TJ_{ptp} amounts to 70 fs and subsequently increases steadily from 60 fs to ≈1 ps from a current of 625 mA to 700 mA. This high value of ≈1 ps results from a dual RR comb around a current of 700 mA as shown in Fig. 3.2c. Interestingly, in the second QS ML region starting at a current of 730 mA the TJ_{ptp} amounts to a low value of 35 fs indicating a very regular optical pulse train exhibiting periodic amplitude modulations.

With stabilization the TJ_{ptp} is strongly reduced in the former QS region in a gain current range of 570 mA to 625 mA to very low values of down to 30 fs which is limited by the selected instrument setting[10] and therefore may be lower. Also in the second ML range the TJ_{ptp} is reduced to a low value of 36 fs. Hereby, the two ML regimes can be clearly identified by the low value of TJ_{ptp}. In between, a RR transition occurs as evident in Fig. 3.2d. The TJ_{ptp} is unchanged in the second persisting QS ML range starting at a gain current of 725 mA showing that the circuit is not effective for this operation regime but also does not degrade it.

Having shown the improvement of timing and amplitude stability of the pulse train with the suppression circuit now the influence on the pulse generation will be investigated in the time domain by using an optical auto-correlator. Fig. 3.4a shows the measured pulse-width assuming a sech^2 shaped pulse-shape as a function of gain current at a absorber voltage of −6.0 V with and without suppression circuit. Without stabilization only weak pulses with a high continuous-wave (CW) background exist up to a current of 610 mA. Clear pulses exist only above this current which is the transition from QS to the first QS ML region. The pulses exhibit pulse-widths of down to 815 fs at a gain current of 700 mA. In the second QS ML regime the pulse-width amounts to more than 1.05 ps. With stabilization clear mode-locked pulses are already observable at a reduced gain current of 570 mA with a significantly reduced pulse-width of 700 fs. In the second ML regime the minimum pulse-width amounts to 710 fs. In the second QS ML range above a current of 720 mA the pulse-width is unchanged. The pulse-train is not only stabilized in time and amplitude but also the pulse-width is reduced thanks to stabilized ML operation.

The influence of the stabilizing circuit can also be observed in the output power of the laser. Fig. 3.4b shows the output power as function of gain current with an absorber voltage of −6.0 V for both configurations. With suppressing circuit the threshold is slightly increased by +5 mA. Most importantly, the optical power is strongly reduced up to the first ML region and is still lower for the first ML region and up to the beginning of the second QS ML region. This power reduction clearly indicates additional losses caused by the suppressing circuit which reflect the stabilizing activity of the circuit.

The stabilizing influence of the suppressing circuit can also be observed in the optical spectrum of the laser. Fig. 3.5a shows the optical spectrum at a gain current of 600 mA and an absorber voltage of −6.0 V for both configurations. Without suppressing circuit the spectrum is highly irregular. Do to the strong amplitude modulations in this QS range the inversion of the inhomogeneously broadened gain in

---

[10] TJ_{ptp} is derived from the measured RR line-width which is limited by the chosen minimum RBW of 30 kHz here.

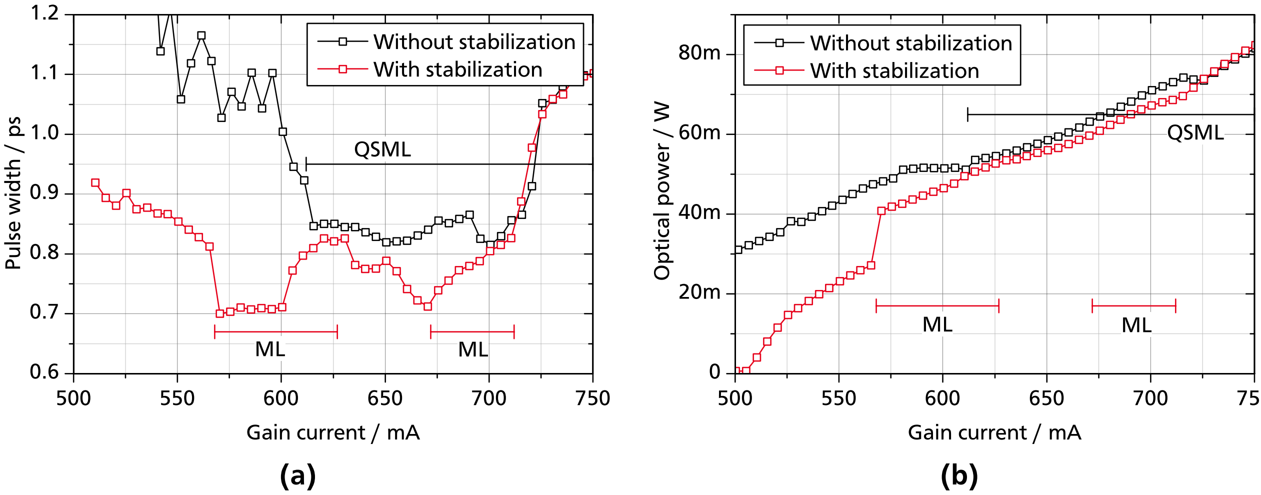

Figure 3.4: (a) Pulse-width (assuming a sech^2 shape) as a function of gain current for the first MLL for both configurations. (b) Optical power as a function of gain current for the first MLL for both configurations.

the gain section is expected to be highly modulated thus periodically changing the emission wavelengths resulting in a mean spectral broadening. With the suppressing circuit the spectral envelope has nearly a parabolic shape (in logarithmic representation) which is an indication of ML and is accompanied by a reduction of the spectral width. This change of spectral width is quantified in Fig 3.5b. There the spectral width is estimated by an integrative approach from [96]. Without stabilization the spectrum stays irregular up to a current of 615 mA indicated by the local maximum in width. The maximum of the width in a current range from 650 mA to 725 mA is related to the mentioned dual RR comb evident in Fig. 3.2c and results from an overlap of two offset spectral envelopes. With stabilization the spectral width is highly reduced and has nearly a parabolic shape in the two ML ranges. The local maximum at 665 mA reflects the mentioned RR super-mode transition by a gradual alternation of the two correspoding spectral envelopes.

To demonstrate the feasibility of the stabilizing approach the **second MLL (do 1790 gg2 a400 E3)** is now investigated. Fig. 3.6a shows the integrated PSDs in a low-frequency range from 6 MHz to 200 MHz (open symbols) and the integrated PSDs in a high-frequency range from 200 MHz to 8 GHz (closed symbols) as a function of gain current. Without stabilization no stable ML is observed. Up to a current of 750 mA the PS exhibits narrow-spaced multiple peaks in the RR region as shown in Fig. 3.6b which are also reflected in the low-frequency noise power in Fig. 3.6a. In the current range from 770 mA to 830 mA QS ML is existent with modulation side-bands at an offset frequency of ≈700 MHz and its harmonics resulting in a large high-frequency noise-power. Above a current of 830 mA the PS exhibit various irregularities. With stabilization the multiple peaks in the RR region disappear as shown in Fig. 3.6b which is also well reflected in the low frequency range in Fig. 3.6a. Hereby stable ML is achieved in a current range from 590 mA to 750 mA. The QS ML region exhibiting the modulation at ≈700 MHz is not improved. Nevertheless, these results show the capability of the stabilization circuit to suppress low-frequency instabilities.

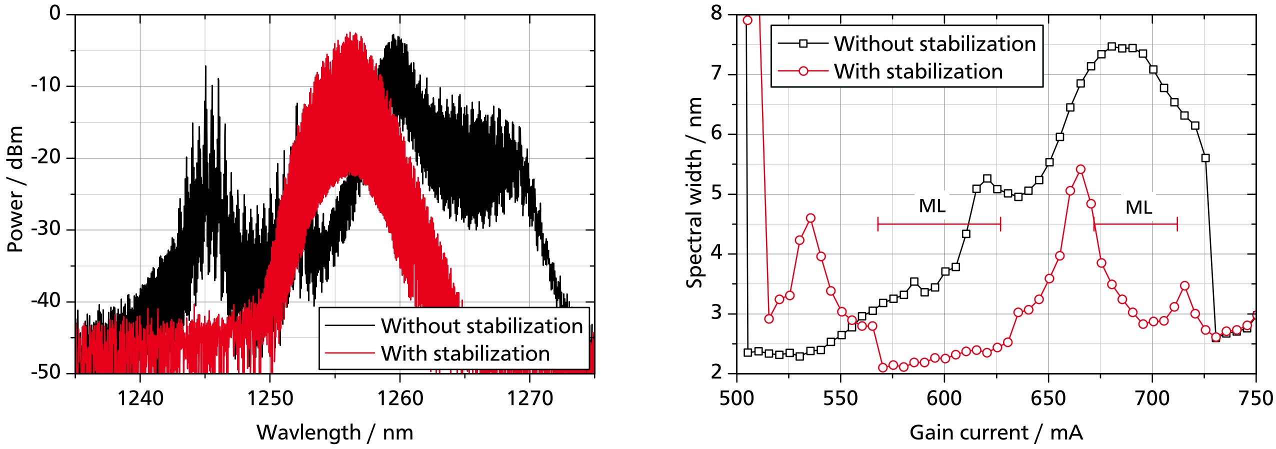

(a) (b)

Figure 3.5: (b) Optical spectrum at a gain current of 600 mA for both configurations. (a) Width of optical spectra as a function of gain current for both configurations. Both figure represent results for the first MLL and an absorber voltage of −6.0 V.

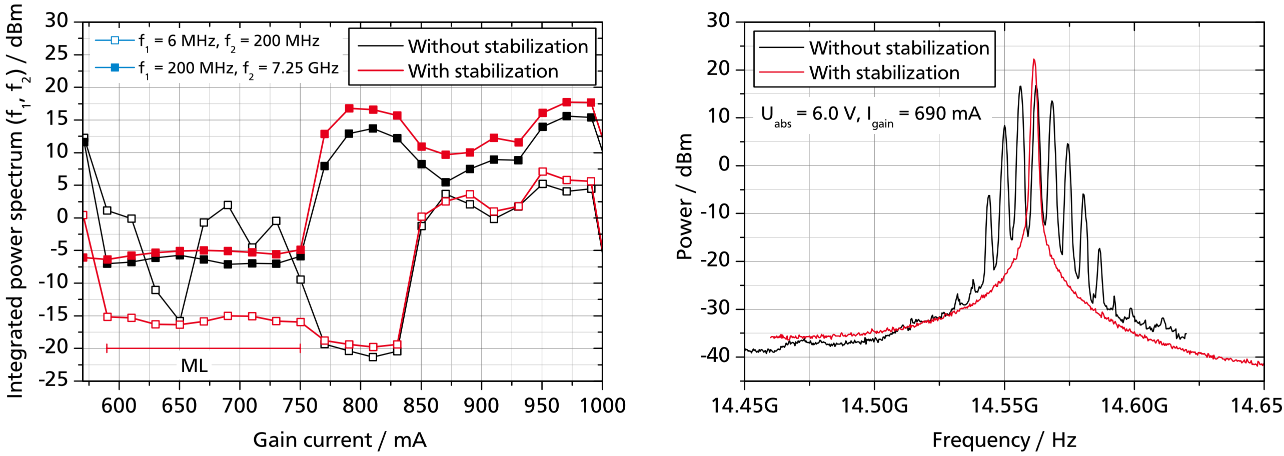

(a) (b)

Figure 3.6: (a) Integrated PS for the second MLL in a low (6 MHz to 200 MHz) and a high-frequency range (200 MHz to 8 GHz) as a function of gain current for both configurations. Instrument noise power contributes to a value of −10 dBm in the high frequency range and to −24 dBm in the low frequency range. (b) The PS at a absorber voltage of 6.0 V and a gain current of 690 mA for both configurations.

Having demonstrated the stabilizing effect of the passive electrical approach on the laser dynamics, now the principle of operation will be discussed. As already mentioned in the introduction, QS or QS ML represent a strong amplitude modulation of the optical power or the power envelope of the optical pulse train, respectively. This modulates the carrier density and induces a modulated photo-voltage in the absorber section as shown in Fig. 3.7a (on page 52) for the second MLL. Depicted is the root mean square (RMS) AC voltage of the absorber within a bandwidth of $f_1^a = 50$ Hz to $f_2^a = 62.5$ kHz measured with a high-impedance oscilloscope (1 MΩ) in parallel connected to the absorber as a function of gain current and for an absorber voltage of −6.5 V *without* stabilization. In addition, the integrated low-frequency (6 MHz to 200 MHz) noise-power for this absorber voltage is also given. Threshold current amounts to 495 mA. The QS operation is evident up to a current of 585 mA by the high value of RMS voltage of 3.2 V. Hereby, the lowest and highest measured instantaneous absorber voltage amounts to −1 V and −12 V, respectively which is a high deviation from the mean voltage of −6.5 V. At currents above 585 mA QS ML takes place still exhibiting a RMS voltage of around 80 mV still above the instrument-noise value of 40 mV. This instrument-noise limited value is also found for stable ML operation where no modulations occur. The RMS absorber voltage well reflects the low-frequency noise-power fluctuations of the optical output power depicted in the same figure thus indicating the important connection of absorber voltage and output power. Furthermore, both variations are measured within different frequency ranges but they well correspond. A direct connection of absorption bleaching which influences optical power and absorber voltage is given in [70, Fig. 4(a)] showing a high dependence of both quantities. The increase of the absorber voltage is a direct consequence of varying carrier accumulation in the absorber. Such a high carrier accumulation increases absorber transparency which favors high intra-cavity power which increases until the gain saturates. Because the absorption regenerates faster than the gain the intra-cavity power reduces after saturation of the gain and the cycle starts again.

The proposed passive electrical stabilization by the high-pass circuit provides a grounding of these these accumulated carriers or reduces their dynamic accumulation for high frequencies while not altering the mean absorber voltage. It therefore represents a damping of these modulations. This carrier grounding is supported by the light-current characteristic, which is shown in Fig. 3.4b. With the circuit connected the optical output power is significantly reduced up to a current of 570 mA corresponding to the new ML threshold. This reduction in optical power is attributed to an increased AC photo-current or carrier-escape-current caused by the circuit resulting in an increased absorption of the absorber. This required damping is not possible by the non-stabilizing voltage source, furthermore it is found experimentally to have a very low transmission bandwidth of roughly 4 MHz. The high frequency damping is possible by using high-frequency components with an bandwidth of 18 GHz. However, contacting and electrical properties of the laser are expected to allow for transmission of signals below a frequency of 1 GHz only. In fact, a small-signal-modulation response of the first homogeneously pumped tapered laser yields a −3 dB cut-off frequency of roughly 300 MHz by modulation of the absorber and operating the laser at a homogenous gain current of 450 mA. A small signal response analysis performed *during* stable ML operation has an irregular shape but exhibits a similar cut-off frequency. Therefore the circuit is technically not able to influence the RR of the laser and keeps stable ML operation unaltered as also observed in various experiments. This upper bandwidth limitation of 300 MHz is also expected to explain, that the second QS ML region of the first and second MLL is not stabilized or influenced because the QS modulation occurs at frequencies above 500 MHz and 700 MHz, respectively. In fact in [38, 112] it is stated that reliable control is found to require a bandwidth that is at least comparable to the frequency of QS but also has to be lower than the RR.

Having explained the basic idea of stabilization, now, at this point it is reasonable to briefly summarize the bandwidth of each part of the stabilized MLL system individually including the active medium as outlined in Fig. 3.8 to allow for a better understanding of the functionality of the approach. The pulse-width and the corresponding carrier dynamics in quantum-dot (QD) media occur in the 1 ps range as

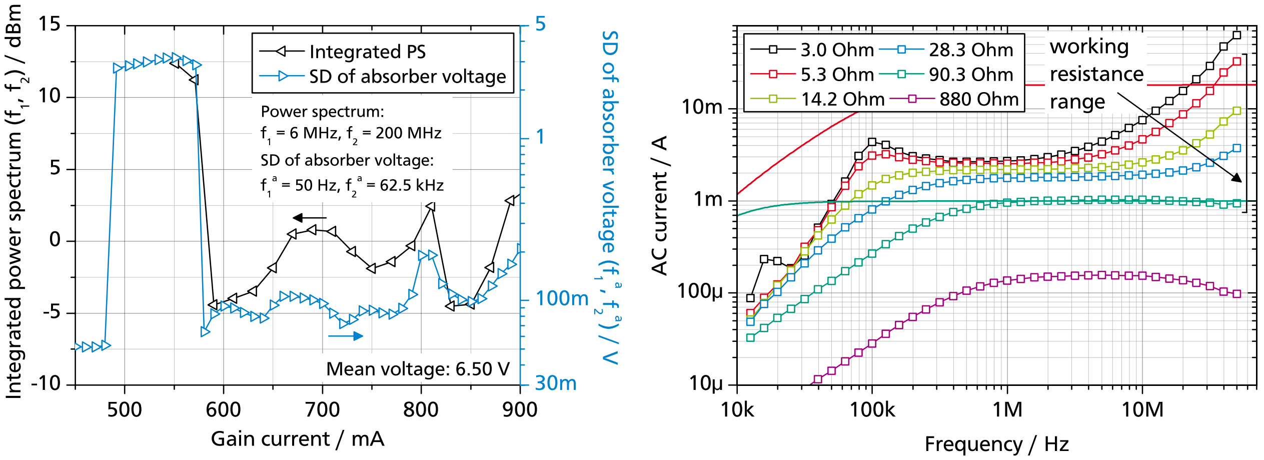

(a) **(b)**

Figure 3.7: (a) Integrated PS for the second MLL in a low (6 MHz to 200 MHz) frequency range and the RMS voltage of the absorber ($f_1^a = 50$ Hz to $f_2^a = 62.5$ kHz) as a function of gain current at a absorber voltage of −6.5 V *without* stabilization. (b) Current transmittance of the bias-T used for stabilization as a function of frequency for various grounding resistances according to Fig. 3.1a. Solid lines show two simulated responses for the corresponding resistance.

shown by pump-and-probe experiments [62]. This high frequency range is only practically accessible and capable of being influenced in the optical domain for example by all-optical feedback (AO FB). The RRs amount to frequencies in the 10 GHz range and are well accessible electrically as shown in [123] where a MLL is used as an electrical RF signal generator which is made possible by using a high-frequency capable contacting allowing to extract the GHz-modulated photo-current.[11] Here, the cut-off frequency amounts to 300 MHz which only allows to extract an averaged photo-current. However, this is beneficial for ML operation because contacting capable of transmission of the RR would create electrical resonators which can influence ML operation.[12] Now, QS and QS ML frequencies are found to be in the 10 MHz to the 1 GHz range. This frequency range can be partially transmitted by the contacting (< 300 MHz) and the high-pass filter (< 18 GHz) thus allowing the desired stabilization. Finally, the voltage source has only a frequency range from DC to the 1 MHz range and thus only provides the required reverse voltage. The inductor of the bias-T also shown in Fig. 3.8 and Fig. 3.1a is beneficial to isolate electrical resonances which can be excited by a unstable MLL.

In experiment, it is found, that the stabilization works for grounding resistances of 5 Ω to 100 Ω. The cut-off frequency and the current transmittance of this specific high pass filter both are important for stabilization and depend on the selected resistance. An increase of resistance while keeping the voltage modulation by the absorber constant is expected to result in a decrease of maximum current flow and a decrease of the cut-off frequency. This reduction of current-transmittance is expected to disable the stabilizing operation. Using the given capacity from the bias-T data-sheet (C = 220 nF) and calculating the frequency response of an ideal high pass filter for a resistance of 5 Ω and 100 Ω the cut-off frequency

---

[11] In the context of this work, it is found that a 5 GHz and 20 GHz RR is measurable directly from the absorber with a power of −41 dBm and −82 dBm, respectively.

[12] In chapter 5 an semi-electrical resonator will be exploited to reduce the TJ of the MLL by means of an long opto-electrical feedback (OE FB) resonator.

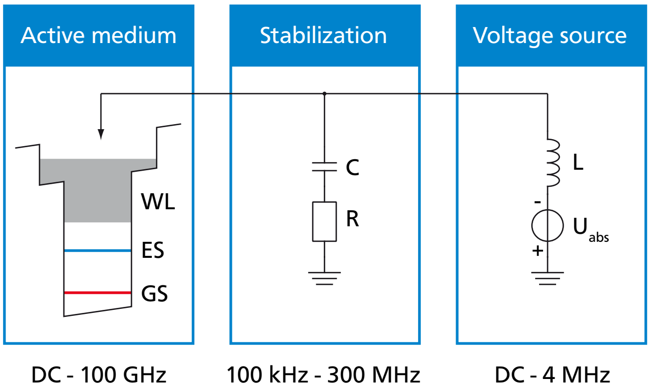

Figure 3.8: Schematic and bandwidths of specific parts of the stabilized MLL system.

should correspond to 145 kHz and 7.2 kHz, respectively and the current reduction from 5 Ω to 100 Ω should amount to a factor of 20. However, this simplification is not expected to be valid in experiment due to the complexity of the whole system, therefore the frequency response has to be measured.

To quantify this frequency response of the used bias-T experimentally for different resistance settings, the absorber is replaced by a signal generator and the voltage parallel to the variable high frequency resistor is measured with an oscilloscope allowing to calculate the current flowing though the resistor. The absorber voltage source is kept at the DC port of the bias-T. The modulation voltage amounts to 100 mV. Such a voltage modulation represents an approximation of absorber voltage fluctuations. The resulting frequency responses *of the current* are shown in Fig. 3.7b and the vertical bracket on the right side shows the responses belonging to the range of stabilizing resistance values. Current was chosen as a measure instead of electrical power because the photo-current is the physically relevant measure. For a resistance range from 28Ω to 90Ω which is close to the design-resistance of the bias-T of 50 Ω the response represents an ideal shape of a response of an high-pass filter. Increasing the resistance within the working range from 5.3 Ω to 90.3 Ω results in an *increase* of the cut-off frequency[13] from 71 kHz to 370 kHz and an decrease of the current (at 2 MHz) by a factor of only 2.5. The expected cut-off frequency trend is reversed and the current reduction is much smaller. In addition, at a frequency of 100 kHz a resonance is observed and at frequencies above 10 MHz an strong increase of current with reducing resistance is observed.

A corresponding simulation of the full experimental circuit reproduces the experimentally obtained frequency response with good agreement up to a frequency of ≈10 MHz (not shown). It is found that the reversed cut-off frequency trend, the reduced current decrease factor and the resonance at 100 kHz originate mostly from the not avoidable inner resistance of 50 Ω of the signal generator. This shows, that such a series resistance has a strong impact on the circuit characteristics. The series resistance of the absorber is not known but is expected to be in the single digit Ω range. Therefore also a calculated frequency-response of the whole circuit without the 50 Ω series resistance is shown for 5.3 Ω and 90.3 Ω in Fig. 3.7b which represent the borders of the stabilizing resistance range. The deviation from experimental reults above ≈10 MHz might result from not considered parasitic elements.

---

[13] Engineering conventions which are used here state that the −3 dB criterion always refers to power which corresponds to only ≈ 1.41 times the corresponding voltage or current.

These frequency response results do not answer the question which minimum frequency is required for stabilization because all the cut-off frequencies do not vary much and all lie in the sub-MHz range. However, simulated results allow to deduce, that the AC resistance has to be within a range of $100\ \mathrm{mV}/20\ \mathrm{mA} = 5\ \Omega$ and $100\ \mathrm{mV}/1\ \mathrm{mA} = 100\ \Omega$ which represents a damping strength. The high-resistance limit is obvious, because it eliminates current flow, but the low-resistance limit suggests that a high AC current flow is deteriorating the ML operation. A potential qualitative explanation is the instantaneous reduction of optical absorption induced by the AC current flow through a series resistor. The absorber section, the contacting and the cables provide a small series resistance. A current flow results in an instantaneous voltage drop across the resistance which results in a lowered total voltage across the absorber. This reduced voltage reduces the electric field across the absorber and thus the absorption which in turn increases intra-cavity power leading to a counter-acting of the stabilization. This resistance related phenomenon was exploited to create a self-electro-optic effect device used as an optical bistable switch [124] and was even used to switch between emission states of a QD laser in [4, 125]. In fact, it is found experimentally that using a $\approx 50\Omega$ resistor between voltage source and the absorber can prevent ML operation. The onset of ML is found to be accompanied by an increase in absorber current which reduces absorber voltage by the said effect and thus can prevent ML operation.

Having specified the operation limits of the stabilization circuit, now, statements from other works are provided which are useful for further explanation of the presented passive electrical approach. The elimination of QS instabilities by active loss or gain control or inverse saturable absorption was investigated theoretically in [127] in the framework of Laplace-transform based control theory. Despite the fact that only active loss control is investigated and the parameters for calculation of bandwidth requirements for the investigated MLLs are not known here still some qualitative statements can be drawn. It was found in [127] that in order to prevent QS instabilities active control of the losses requires much lower relative loss modulation than relative gain modulation which is expected to be valid for the passive loss control presented here. It was highlighted that a quite low lower cut-off frequency of the active loss control in the sub-kHz range may be required for stabilization. It was argued that the response of the controller to a QS cycle changes the loss balance for long time-scales if the lower cut-off frequency is too high [127, Fig. 5(b)] thus preventing stabilization of the system. This represents an alternative explanation for the observed lower resistance limit of $5\ \Omega$ in experiments where decreasing resistance values increase the lower cut-off frequency into the kHz range. It was also stated that high RR and high steady state differential loss (A_{11} in [127]) require high loss-control-bandwidth and low control-phase-delay. For example an Er-Yb:glass MLL with a RR of 40 GHz was found to require a bandwidth of 10 MHz and a maximum delay of 13 ns. The tapered MLL investigated here exhibits a similar RR of 16 GHz therefore it might be comparable. Hereby, both conditions are easily met by the proposed circuit.

Finally, worth mentioning is, that an adiabatic current increase starting at threshold with activated gain control was found to be easily able to prevent QS instabilities while a switch-on of the active gain control during already occuring QS operation was not successful in stabilization [127]. In fact, a third tapered MLL (do 2584 s4 d2) which could be also successfully stabilized with the passive circuit exhibits a pronounced hysteresis behavior in terms of the resistance value. Starting from unstable QS operation at a fixed gain current and a fixed absorber voltage the transition to stable ML occurs for a resistance range of 28 Ω to 90 Ω, but starting in already stabilized ML operation (inside the stabilizing resistance range) the transition to unstable QS occurs for an increased resistance range from 19 Ω to 132 Ω. This hysteresis behavior in terms of control parameter corresponds to the previous statement of adiabatic laser state change: Prevention of instabilities requires less control magnitude than an elimination of already existing instabilities.

3.3 Stabilization by short optical feedback

In the previous section the useful passive electrical stabilization of Q-switching (QS) leading to stable mode locking (ML) was demonstrated and qualitatively explained. However, potentially due to the limited bandwidth of the realized electrical contacting the QS oscillations at a frequency of 700 MHz in Q-switched mode-locking (QS ML) operation could not be eliminated. This bandwidth limitation can be partially overcome by optical detection and *amplified* electrical modulation but would represent a well known active approach [38, 47, 118, 119]. Full signal bandwidth as well as an all-passive approach is accessible by an all-optical approach only. Therefore, in the following short all-optical feedback (AO FB) is investigated in terms of QS reduction. This approach is demonstrated in [16] and was also reported in [129].

The mode-locked laser (MLL) used for investigation is the second laser (do 1790 gg2 a400 E3). Fig 3.9 shows the power spectra (PS) for three selected currents (670 mA, 810 mA and 870 mA) and an absorber voltage of −6.0 V exhibiting qualitatively different characteristics. For all three conditions optical pulses are existent amounting to a pulse width of 1.25 ps, 1.59 ps and 1.51 ps, respectively. Fig. 3.9a and Fig. 3.9c show the PS of the free-running MLL around the repetition rate (RR) with a span of 200 MHz and the PS of the free-running MLL from 0 Hz to 1.5 times the RR, respectively. Both frequency ranges are essential for classification of operation condition of the laser. Starting at a current of 670 mA the RR exhibits multiple peaks with a close spacing of 6 MHz which are also existent at multiples of 6 MHz (in the low-frequency range) thus indicating amplitude modulations. In the wide-span PS (Fig. 3.9c) only a weak pedestal with −50 dB suppression with respect to the RR signal is observed. In the narrow-span PS (Fig. 3.9a) the weak peaks with an offset of multiples of 45 MHz with respect to the RR are expected to stem from weak electrical setup resonances namely from a current-meter measuring the absorber current because they disappear if the current meter is removed. At a current of 810 mA a single RR Lorentzian-shaped line is observed and the 6 MHz side-peaks exhibit a high suppression of −40 dB. However, in the wide-span PS strong amplitude modulations at multiples of 740 MHz can be observed indicating QS ML. At a current of 870 mA the 6 MHz side peaks re-appear with an irregular shape of the whole RR signal. In addition, the wide-span PS shows amplitude modulations at multiples of 500 MHz.

Applying short (0.5 m) AO FB corresponding to a feedback (FB) frequency of 300 MHz with a FB ratio[14] of $1.7 \cdot 10^{-3}$ yields the results shown in Fig. 3.9b and Fig. 3.9d. Hereby, the FB length is adjusted to only nearly match the pulse repetition period (PRP) of the optical pulse train: Interestingly, if the FB

---

[14] The FB ratio is defined as the ratio of free-space output power to back-reflected power while disregarding unknown coupling losses.

is not adjusted to ensure a red-shift of the RR of 8 MHz the lasing threshold current increases from 580 mA to 605 mA. The FB length is kept constant for the whole current range. In the narrow-span PS it can be observed, that AO FB eliminates the 6 MHz side-peaks for all currents thus ensuring a distinct RR. However, amplitude noise in the vicinity of the RR is increased as is clearly evident for a current of 870 mA . The origin of the additional amplitude-modulation peaks at multiples of 15 MHz is unknown. In the wide-span PS the prominent periodic QS modulations are eliminated and replaced by a amplitude-noise plateau exhibiting a weak comb modulation with a period of 300 MHz for all currents indicating the FB frequency. Amplitude noise is increased for a current of 670 mA. The pulse widths amount to 1.04 ps, 1.67 ps and 1.89 ps, respectively. Although an qualitative improvement in terms of noise is evident a quantification of noise-power for both configurations like in section 3.2 is required.

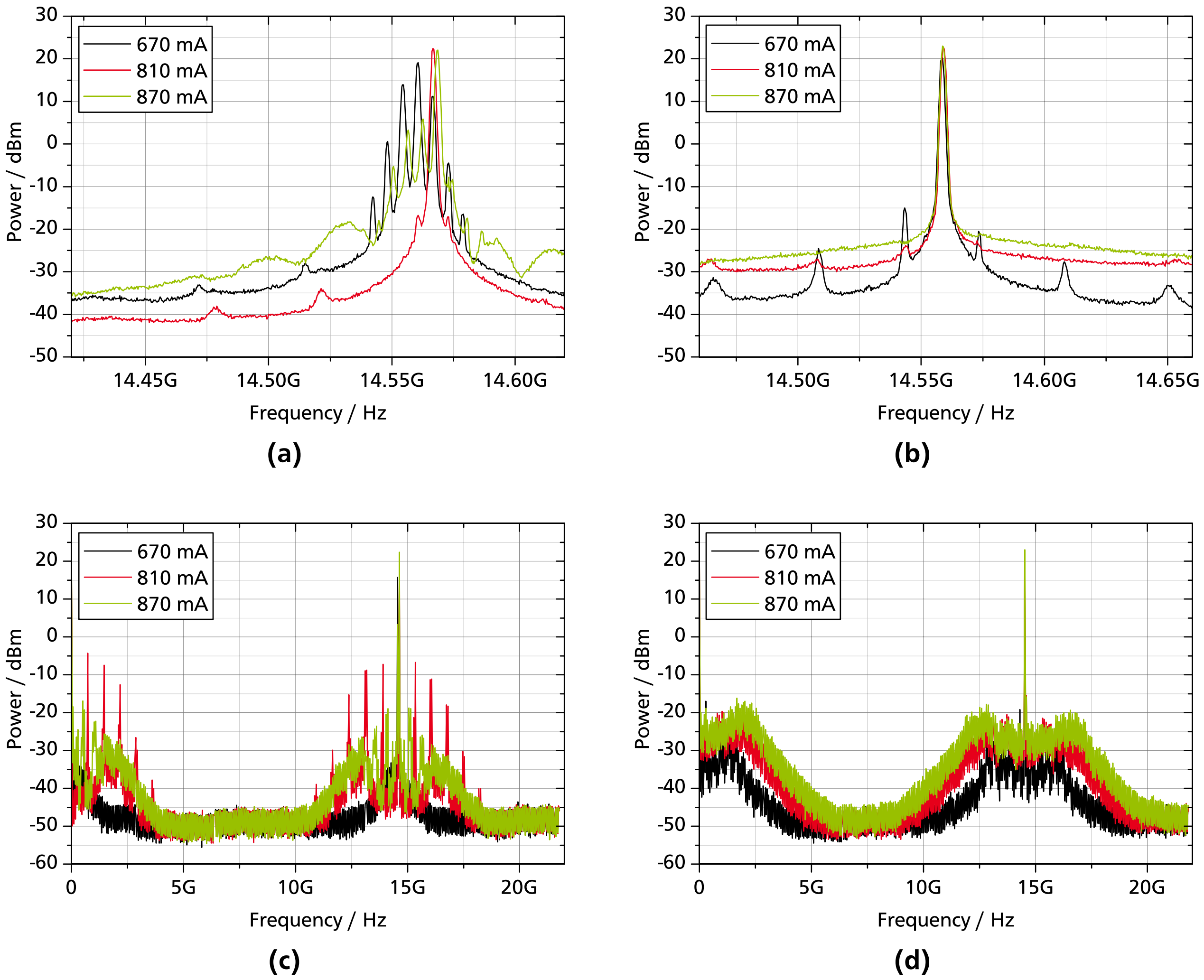

Figure 3.9: PS for the second MLL at a absorber voltage of 6.0 V and three selected gain currents showing (a) the RR frequency range in free-running condition, (b) the RR frequency range with AO FB, (c) a frequency range from 0 Hz to 1.5 times the RR in free-running condition and (d) a frequency range from 0 Hz to 1.5 times the RR with AO FB.

To quantify the noise-power Fig. 3.10a and Fig. 3.10b show the integrated power spectral densities (PSDs) in a low-frequency range from 6 MHz to 200 MHz and in a high-frequency range from 200 MHz to 7.25 GHz as a function of gain current, respectively. In the low-frequency range the noise-power is reduced by −10 dB for a current of 670 mA, increased by +17 dB for a current of 810 mA and reduced by −6 dB for a current of 870 mA as indicated by the black arrows. In the high-frequency range the noise-power is increased by +11 dB for a current of 670 mA, reduced by −4 dB for a current of 810 mA and increased by +7 dB for a current of 870 mA as indicated by the black arrows. This quantification allows to deduce that although qualitative improvement exist short AO FB can not reduce noise power in both domains simultaneously.

The AO FB configuration can be combined with the passive electrical stabilization which results are also shown in Fig. 3.10a and Fig. 3.10b. This double configuration is beneficial in the low-frequency range for currents between 610 mA and 670 as expected but it is surprisingly beneficial in the high frequency range. This can be explained by the noise induced by AO FB at multiples of the FB frequency of 300 MHz for currents below 770 mA as shown in Fig 3.9d. This noise at a frequency of 300 MHz can be compensated by the passive electrical stabilization which is expected to have an upper cut-off frequency of 300 MHz as stated in section 3.2 thus showing that optically induced amplitude noise can be also reduced by the circuit. Results for sole passive electrical stabilization are also plotted in both frequency ranges again showing the effectivity of the electrical approach. Fig. 3.11a shows the frequency and power of the dominant amplitude modulation signal as a function of gain current. Hereby only frequencies above 50 MHz can be evaluated. Passive electrical stabilization is achieved in a current range between 590 mA and 750 mA where dominantly low-frequency amplitude modulations are observed.

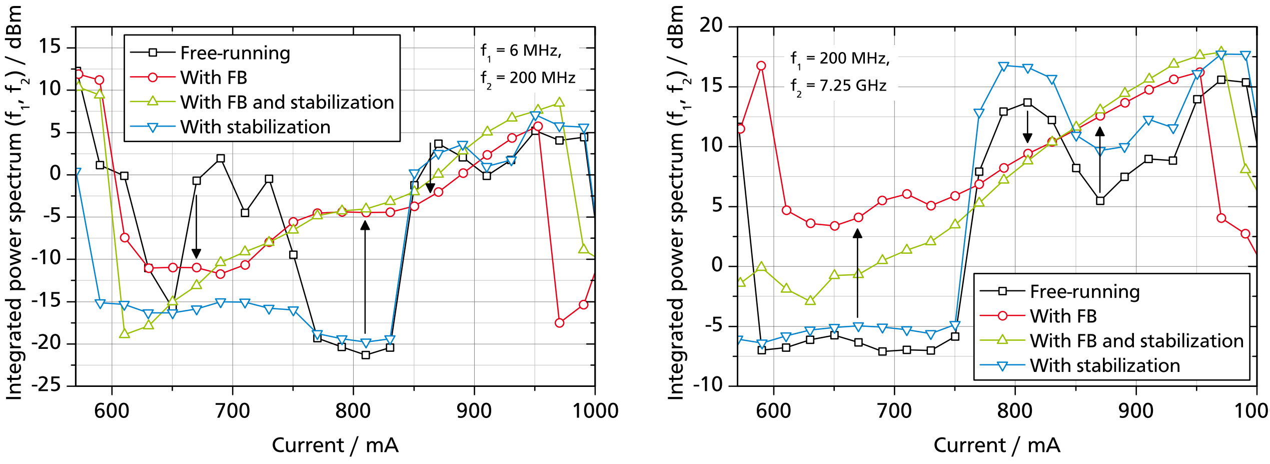

(a) (b)

Figure 3.10: Integrated PS for the second MLL as a function of gain current at an absorber voltage of −6.0 V for the free-running condition, for AO FB only, for simultaneous AO FB and passive electrical stabilization and for sole passive electrical stabilization (a) in a low-frequency range (6 MHz to 200 MHz) and (b) in a high-frequency range (200 MHz to 7.25 GHz). Instrument noise power contributes with a value of −24 dBm in the low frequency range and with −10 dBm in the high frequency range.

Having demonstrated and quantified the effects of short AO FB on QS modulations the possible reason for these effects will be discussed. In [129] it was suggested, that QS effects tend to occur close to lasing threshold and that AO FB significantly lowers lasing threshold and enhances stimulated emission thus damping relaxation oscillation (RO) and QS. However, there, the MLL is operated at 2.2 times the threshold and AO FB ratio amounts to $5.0 \cdot 10^{-4}$ and here the MLL is operated at 1.4 times the threshold and the FB ratio amounts to $1.7 \cdot 10^{-3}$. Both conditions are far above threshold and AO FB is weak, therefore an alternative explanation is suggested here. QS ML represents an amplitude modulated pulse train. An optical re-injection of this pulse train with a phase delay of 180° with respect to the frequency of this *amplitude modulation*[15] results in the filling of the gaps where only weak pulses are existent. These also amplitude modulated FB pulses experience gain and are expected to counteract the modulation. In analogy to the electric field this counteracting effect is denoted as destructive intensity interference. The effect of this phase is quantified by constructive or destructive intensity interference defined by Eq. (3.2).

$$A = \cos(f_{\mathrm{QS}}/f_{\mathrm{FB}} \cdot 2\pi) \tag{3.2}$$

Hereby, A denotes the magnitude and sign of the intensity interference effect, f_{QS} denotes the QS frequency, f_{FB} denotes the AO FB frequency and the ratio of both frequencies represents the AO FB phase. A number of $+1$ and -1 for A represents constructive and destructive intensity interference, respectively. Hereby, according to the explanation given above, a destructive intensity interference of -1 represents a stabilizing effect.

Normally, to study a variation of the AO FB phase, a fixed operation point of the MLL would be selected and the AO FB would be varied but the varying frequency of the QS offers the possibility to keep a fixed length or AO FB frequency (300 MHz) and just change the current to change the AO FB phase. Furthermore, it is experimentally difficult to keep the AO FB ratio constant over two periods of the corresponding QS wavelength which corresponds to 43 cm. To investigate the hypothesis of intensity interference the free-running modulation or QS frequency is required. Thus, Fig. 3.11a shows the frequency and the power of the QS signal above a frequency of 50 MHz as a function of the gain current. In a current range from from 590 mA to 750 mA the QS peak frequency varies from 70 MHz to 800 MHz and the power stays below −30 dBm. Above a current of 750 mA the QS peak frequency varies from 350 MHz to 1.5 GHz. The red line indicates the transition from domination of integrated low-frequency noise to integrated high-frequency noise in accordance with Fig. 3.10a and Fig. 3.10b. Based on this QS frequency and the fixed AO FB length Fig. 3.11b shows the calculated and dimensionless intensity interference as a function of the gain current. Also the power difference of the integrated PS (200 MHz to 7.25 GHz) between the free-running case and AO FB configuration is given thus indicating an increase or decrease of amplitude noise by AO FB. The power difference of the peak power of the QS signal between the free-running case and AO FB configuration highlights the effect on the QS signal itself. The integrated power difference exhibits a global decreasing trend which may be related to the increasing optical power with increasing current but a modulation of this power difference can be well observed. This modulation is even more pronounced by regarding the QS signal power difference which is strongly correlated to the integrated difference. As can be observed the minima of both power differences correlate with the minima of the intensity interference thus indicating a locally stabilizing effect of the AO FB if the intensity interference is destructive. Therefore it is deduced that AO FB may be regarded as an all-optical control loop with high control bandwidth. The required phase of −180° corresponds to the −90° phase for a

---

[15] It is emphasized, that this phase is not referred to the *optical* frequency but to the frequency of the *amplitude modulation* of the pulse train.

common differential active opto-electrical approach like in [112]. The maximum of the derivative of the optical power already has a phase difference of −90° which, together with the stated −90°, sums up to the demonstrated value of −180°.

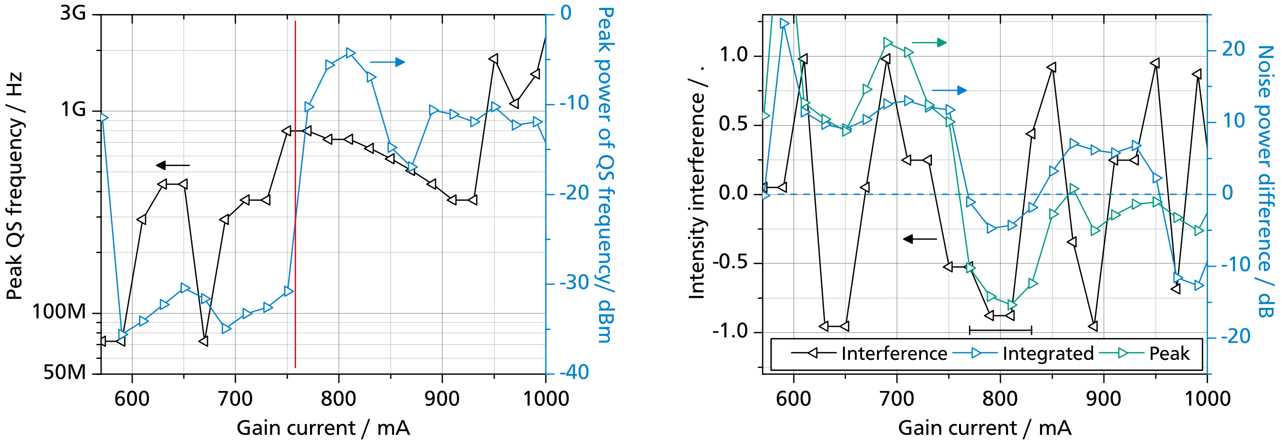

(a) (b)

Figure 3.11: (a) QS frequency and QS signal peak power as a function of gain current at an absorber voltage of −6.0 V for the free-running condition. The red line indicates the transition from domination of low-frequency noise to high-frequency noise in accordance with Fig. 3.10a and Fig. 3.10b. (b) Dimensionless intensity interference of AO FB in terms of the QS frequency and power difference of integrated PS (200 MHz to 7.25 GHz) or peak power of the QS signal between the free-running case and the AO FB configuration.

The PS of the RR for the second MLL is quite peculiar exhibiting a narrow spaced comb of RR components which difference frequency is also evident in the PS at a frequency of 6 MHz thus indicating amplitude modulation. However, the PS at the second harmonic RR frequency indicates additional effects. Fig. 3.12a shows the PS at the first (i.e. fundamental) and second harmonic RR at a absorber voltage of −6.0 V and a gain current of 610 mA. Hereby the frequency axis has an offset with respect to the corresponding RR. If sole amplitude-modulation was existent the second harmonic PS should be similar to the first harmonic PS. Here, a split of the RR mode group is observable which suggests two different but closely spaced RR with a frequency difference of 6.2 MHz which consequently doubles for the second harmonic PS and is indicated by the arrows. Thus, a dual pulse train can be expected. It is noted, that the optical spectrum exhibits no irregularities. To prove this assumption of a dual pulse train a time-domain investigation is required which is accessible by an optical cross-correlation. The optical output is coupled into a fiber, split by a fiber-splitter whereby one path is delayed by an additional optical fiber with a length of 4.5 m which corresponds to a delay of 22.0 ns using the refractive group index of 1.465 for the used SMF-28 fibers. This delay corresponds to 318 pulses using the RR of 14.5 GHz. The corresponding cross-correlation is shown in Fig. 3.12b where the square root of the cross-correlation signal was taken to represent a value being proportional to the pulse intensity. Indeed, in free running condition a double-peak structure is evident with a large spacing corresponding to the PRP of 69 ps. The structure stems from two different RR at 14.5 GHz and a difference of 6.2 MHz resulting in a timing difference of $69\text{ ps} \cdot 6.2\text{ MHz}/14.5\text{ GHz} \cdot 318 = 9.4\text{ ps}$ which corresponds well to the measured value of 8.5 ps thus validating the dual pulse train assumption. Hereby it is noted, that in this case a symmetrical cross-correlation (i.e. a three-peak structure) is not expected because these are not satellite pulses with a fixed delay and identical RR but two independent pulse trains which do not cross-correlate with each other because of the different RR. It is just a superposition of two independent cross-correlations. The double-peak structure is wider at non-zero delay, because the delay is not fully linear close to the turning points of the auto-correlator delay. Also the noise floor stems mostly from stray light. Such a dual pulse train generation was reported in [85], where two spectrally and spatially distinct pulse trains with a RR separation of 55 MHz and a spectral separation of 7.5 nm were observed. But here, no spatial dependence of optical spectra or PS are observed.

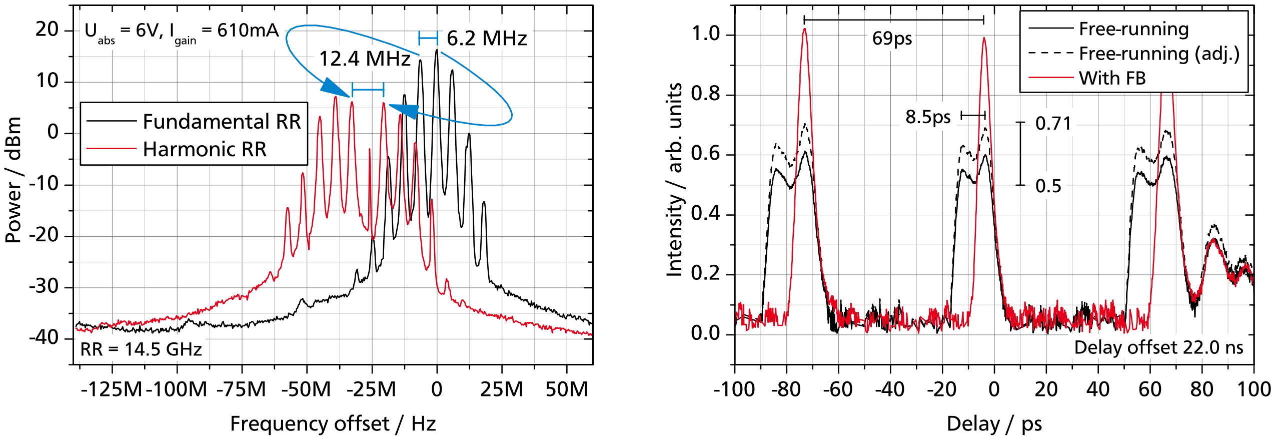

(a) **(b)**

Figure 3.12: Fundamental and harmonic PS for the second MLL for a gain current of 610 mA and a absorber voltage of -6.0 V for the free-running condition. (b) Optical cross-correlation of the optical pulse train with an delay of ≈318 pulses for the free-running condition and AO FB.

Applying AO FB eliminates the multi-peak RR structure as shown in Fig. 3.9b which consequently eliminates the dual pulse train as evident in Fig. 3.12b. Hereby, it can be observed that the optical power is redistributed into one single pulse train evident from the similar area corresponding to the pulse energy. Still one question cannot be answered easily from the cross-correlation, namely if both pulse trains coexist simultaneously with half of the total optical power for each or if the pulse trains switch from one to the other at high frequency while having full optical power. The nonlinear effect of the auto-correlator allows to distinguish between these two cases because for example a doubled RR or a doubled power results in a doubled but quadrupled auto-correlator signal strength, respectively. Hereby, the single pulse train under AO FB is used as a reference and a redistribution of power from the AO FB case to the free running case is assumed. A *binary* alternating dual pulse train corresponds to a full peak power but a halved *mean* RR resulting in a signal factor of 0.5 or intensity factor of $\sqrt{0.5} \approx 0.71$ for each of the two pulse trains. A simultaneous dual pulse train corresponds to a halved peak power but a full RR thus resulting in a signal factor of 0.25 or an intensity factor of $\sqrt{0.25} = 0.5$. Both numbers are indicated in the figure. Hereby, the dashed free-running plot in Fig. 3.12b compensates the increased pulse-width and reduced optical power of the free-running case to allow for a direct comparison with the AO FB configuration. Due to the observation, that the free-running peak-power is closer to the upper value but still below it can be deduced that the dual pulse train is at least partially switching. In the low-frequency range a 6 MHz amplitude modulation signal is evident, which potentially defines the switching frequency. The reason for the switching of the dual RR may lie in the slow (6 MHz) but strong amplitude modulation which periodically alters the optical cavity length by variation of the carrier density in the tapered section allowing the MLL to switch between different super-modes defined in [122]. In contrast to fast (700 MHz) amplitude modulations a slow modulation allows the RR to relax to the new steady state. Fast modulations may prevent relaxation to a steady state thus preventing ML operation and causing a broad RR signal. Eliminating the (6 MHz) amplitude modulations by the passive electrical stabilization thus eliminates the assumed source of the switching dual RR. In contrast, the AO FB just selects one RR due to the required integer matching of internal cavity length and FB cavity length eliminating the other RR. Hereby, it is highlighted, that this RR oscillation is an additional effect to the AO FB induced damping of QS modulations at higher frequencies which is evident in Fig. 3.9a where no multiple RR are observed but AO FB still reduces the noise-power.

3.4 Summary and conclusion

Monolithic tapered mode-locked laser (MLL) are found to be subject to different kinds of amplitude instabilities. This chapter focused on suppression of such amplitude instabilities which result from undamped relaxation oscillations (ROs) [72], trailing edge instabilities (TEIs) or leading edge instabilities (LEIs) [69, Fig. 7]. These amplitude instabilities can result in Q-switching (QS) or Q-switched mode-locking (QS ML) and are found to even manifest in a dual pulse train with different repetition rates (RRs). The frequencies of these instabilities are defined by the RO frequency but are also attributed to any (external) resonance of the MLL system which can be excited by the amplitude noise.

The developed passive electrical approach stabilizes these amplitude-modulations up to a frequency of 300 MHz thus eliminating QS and stabilizing QS ML in this frequency range. The also observed dual pulse train emission can also be eliminated because it is expected to originate from low-frequency amplitude-modulations which are eliminated by the approach. Suppression or elimination of these instabilities for the investigated lasers was presented and additionally an increased mode locking (ML) range available for the generation of ultra-short pulses was achieved.

The electrical approach consists of a high-pass filter grounding the absorber section therefore representing a differential photo-current detector and control element. The observed suppression is attributed to the reduction of dynamic accumulation of photo generated carriers and thus effectively damps low-frequency fluctuations. Hereby, the absorber section is exploited both as a photo-diode and a control element of the MLL by grounding the absorber AC photo-current in the MHz frequency range. This circuit may also be understood as a differential passive control loop suppressing changes of the photo-current thus preventing strong oscillations. It represents an additional AC branch for the photo-current to flow off and therefore no deterioration of already stable ML performance is observed because in practice stable ML results in a DC photo-current only.

Complementary it was found that all-optical feedback (AO FB) is able to influence and reduce QS ML which is expected to result from anti-phase AO FB with respect to the frequency of the QS modulation thus representing an all optical passive control loop.

The AO FB was also found to eliminate amplitude-modulated dual pulse train emission. Hereby, in contrast to the electrical stabilization which eliminates the source of the dual pulse train, namely the amplitude modulation, the AO FB requires integer matching of internal cavity length and feedback (FB) cavity length leading to a selection of one of these pulse trains thus representing a different stabilization approach. Therefore AO FB has two independent effects on the ML properties of a MLL.

Passive semiconductor saturable absorber mirrors (SESAMs) are commonly used for ML of solid-state lasers (SSLs). The presented passive electrical approach may be applied to active electrically controllable SESAMs [130] to stabilize these systems in terms of QS instabilities. Furthermore, a high-frequency capable contacting commonly used for MLL in telecommunications is expected to enhance the stabilization regime beyond 300 MHz.

Having developed a highly efficient but simple way to eliminate or reduce amplitude instabilities of MLLs now the increased potential of the tapered MLLs with respect to pulse-width and peak power generation can be used which is one part of the topic of the following chapter.

4 Pulse generation and amplification

> The Force is strong with this one.
>
> Darth Vader, character in Star Wars (Cinema movie series)

One of the targets of quantum-dot (QD) based optical pulse emitters is to access applications that are currently serviced by conventional, expensive, ultra-fast solid-state laser (SSL). One such application range is bio-medical nonlinear microscopy where cheap, compact and robust pulsed sources are beneficial for widespread use of such techniques. The use of femto-second SSLs as excitation sources has allowed to improve the resolution of microscopy by multi-photon excitation or by exploiting non-linear excitation effects including second harmonic generation [39, 40]. The basic principle of these techniques is that for focused ultra-short pulses the photon density is high enough to induce multi-photon absorption or other nonlinear coherent processes only within a confined focal volume. Bio-medical fluorophores whose excitation wavelength covers the visible red spectral range [131] can be excited by two infrared photons. Since nonlinear absorption and thus induced fluorescence occurs solely within the focal volume of the laser beam, a high axial and lateral resolution can be attained. Furthermore, there is no undesired fluorescence from the surrounding medium as compared to single photon excitation. Imaging depth depends on absorption and scattering both being dependent on wavelength. Hereby the emission wavelength of QDs of around 1270 nm offers minimal total losses in biological tissue [25] thus accessing very high imaging depths of 1.6 mm at a wavelength of 1280 nm [132] and minimizing photo-damage [133] and thermal load. Based on Eq. (2.4) imaging intensity, and thus the figure of merit (FOM), depends quadratically on the peak power and linearly on the duty cycle. Thus, high (peak) power and short pulses are desirable for nonlinear imaging for a given average power.

First, novel fully gain-guided monolithic mode-locked lasers (MLLs) are investigated, which have a tapered gain section to enhance the pulse peak power and to deliver a stable pulse-train with sub-pico-second pulse-widths. Hereby a focus lies on the thorough quantification of stability ranges of mode locking (ML) operation in terms of timing jitter (TJ) and amplitude jitter (AJ) not considered for semiconductor laser (SCL) in literature so far. Subsequently novel gain-guided tapered semiconductor optical amplifiers (SOAs) with weak index-guiding are investigated allowing to increase the pulse peak power of pico-second pulses to the two-digit Watt range thus exhibiting characteristics which access non-linear imaging capabilities which was *successfully* demonstrated for a QD based system with a stated usable[1] peak power of 25.8 W and a duty cycle of $6.9 \cdot 10^{-3}$ leading to a stated usable FOM of 4.56 W^2 [134].

---

[1] Collimation losses are re-included.

Initial studies of straight two-section passively mode-locked lasers (MLLs) with cavity lengths from 1 mm to 3 mm and no anti-reflective (AR) coating and a absorber section length of 10 % of the total length show a minimum pulse width of 2 ps and a maximum peak power of 160 mW. Multi-section MLLs with cavity lengths from 2 mm to 4 mm and a high-reflective (HR) and AR coating exhibited pulse-widths above 1.3 ps and a peak power of 750 mW [135]. The highest performance for straight monolithic quantum-dot (QD) based MLLs was reported in [86] where a very low pulse width of 400 fs and a peak power of 3 W was observed for a repetition rate (RR) of 21 GHz, however, leading to a insignificant figure of merit (FOM) of 0.08 W^2.

Thus, to improve the pulse peak power the approach presented in [136] is followed by using a tapered gain section. Those tapered MLLs typically consist of a straight ridge-waveguide section coupled to a tapered gain section. In [136] it was demonstrated for a quantum-well (QW) active medium emitting at a wavelength of 980 nm, that a tapered gain section allows to increase the peak power from 0.5 W to 2 W while keeping the pulse-width unchanged. The tapered gain section has the effect of increasing the average modal area A in the gain section which leads to an increase of the gain saturation energy $E_{\text{sat,g}}$ as shown in Eq. (4.1).

$$E_{\text{sat,g}} = \frac{h\nu A}{\Gamma dg/dn} \tag{4.1}$$

Hereby, ν denotes the light frequency, A the modal area, Γ the the confinement factor and dg/dn the differential gain. This high saturation energy $E_{\text{sat,g}}$ reduces pulse broadening originating from gain saturation and allows the generation of pulses with increased power that can more effectively saturate the narrow waveguide absorber section. This required narrow absorber section acts as a lateral mode filter forcing fundamental lateral mode operation while also keeping a good beam quality [41].

The development and state-of-the-art of ultra-short pulse generation by semiconductor lasers (SCLs) with considerable pulse peak power is briefly outlined in the following while focusing on *monolithic* pulse sources without any post-processing thus leading to a simple robust system. As already mentioned, in [136] a peak power of 2 W with a pulse width of 3.3 ps, a RR of 2.5 GHz and a wavelength of 940 nm was reported for a QW based tapered MLL. In [85] a record pulse-width of 360 fs with a peak power of 2.25 W and a RR of 17 GHz at a wavelength of 1280 nm was reported for an index-guided QD based tapered MLL. In [137] a pulse-width of 3.3 ps with a peak power of 3.6 W, a RR of 14.6 GHz and a wavelength of 1250 nm was reported for a gain-guided QD based tapered MLL. A similar MLL is also investigated in this work. Furthermore, some other high power mode locking (ML) configurations can be also used for example a slab-coupled optical waveguide MLL demonstrated in [138] which exhibits a pulse-width of 10 ps with a peak power of 5.8 W and a RR of 4.29 GHz at a wavelength of 1500 nm. In a completely different wavelength range at a wavelength of 405 nm a record peak power of 20 W with a pulse width of 1.6 ps and a RR of 1 GHz was reported for a tapered MLL [139]. However, taking into account the different photon energy as compared to 1270 nm and the assumption that one electron can only excite one photon, this peak power of 20 W corresponds to 6.3 W for a wavelength of 1270 nm. Finally, in [9] a record peak-power of 17.7 W with a pulse-width of 1.26 ps (Lorentzian shape), a RR of 10 GHz and a FOM of 3.8 W^2 was reported for a gain-guided and tapered QD based MLL. A similar MLL is also investigated in this work. All these reported values are directly adapted from literature.

4.1.1 Tapered quantum-dot mode-locked lasers

The different investigated tapered MLLs which are summarized in Table 4.1 are arranged in two groups or generations indicated and separated by the horizontal line. Initially a variation of different geometries, guiding types and the QD active medium type is investigated. The most powerful device from the 1st generation is selected and numerical models are developed and adapted to allow for a reproduction of the experimentally obtained results. A successful reproduction allows to deduce design rules and to suggest variations of geometry which lead to an improvement of performance for the 2nd generation of MLL. Modeling is carried out by the *Semiconductor Integrated Optoelectronics and Photonics Group, Department of Electronics and Telecommunications, Politecnico di Torino, Italy*. The investigated structures base on wafers fabricated by *Innolume GmbH, Germany* and are initially proposed and processed by *III-V Lab, France*.

The QD epitaxial structures used for the tapered MLLs were grown on a GaAs substrate using molecular beam epitaxy (MBE). The active region consists of five or ten identical layers of InAs QDs separated by 33 nm GaAs barriers and incorporated into an AlGaAs waveguide with 35 % Al content. The MLLs consist of two separate electrically insulated sections namely the narrow straight absorber section and a tapered gain section. Proton implantation has been performed outside the electrode or desired waveguide area to achieve lateral gain guiding and to improve the electrical isolation between the two sections, resulting in a fully gain-guided geometry which allows for a simpler fabrication process without any etching of a ridge. The gain guiding effect confines the optical field within the border of the active region by absorbing photons outside and amplifying photons inside. Furthermore, the carrier-induced refractive index variation enhances the guiding. All MLLs are fully gain guided except device (C3) which is index guided. All MLLs have an AR coating on the tapered output facet and a HR coating on the absorber facet side amounting to a reflection of 3 % and 95 %, respectively and have an absorber section waveguide width of 14 μm. Some MLLs (a3, d2) have two straight sections and a taper section. Hereby, the straight sections can be either independently used as an absorber or as an amplifying section. All other device parameters including taper full angles, section lengths and the important absorber section length to gain section length ratio (AGLR) are summarized in Table 4.1. Unfortunately, the tapered MLL always differ by at least two structural properties which prevents a standard side-by-side comparison.

Laser (Chip ID)	QD layers	Sections	Total length /mm	Absorber length /mm	AGLR	Taper angle /°
do 1791 gg6 a400 (A5)	5	2	2.77	0.40	0.17	6
do 1791 gg2 a740 (D1)	5	2	3.86	0.74	0.24	2
do 1790 gg2 a400 (E3)	10	2	2.78	0.40	0.17	2
do 1790 ig0.6 a600 (C3)	10	2	2.97	0.58	0.24	0.6
do 2584 s1b a6 (a6)	10	2	2.50	0.40	0.19	2
do 2584 s1b a8 (a8)	10	2	2.50	0.40	0.19	2
do 2584 s3 a3 (a3)	10	3	3.00	0.50 / 0.50	0.20 / 0.20	2
do 2584 s2b b3 (b3)	10	2	4.00	0.80	0.25	2
do 2584 s4 d2 (d2)	10	3	3.00	0.70 / 0.70	0.44 / 0.44	2

Table 4.1: Overview of geometries and structures of all the investigated tapered MLL.

4.1.2 Measurement methods

According to section 2.3 characterization of the tapered MLL is carried out in parallel by means of a power meter, an optical intensity-auto-correlator, an optical spectrum analyzer (OSA) and an electrical spectrum analyzer (ESA) which allow to measure and deduce important parameters. These include amongst others the pulse-width, the emission wavelength, the spectral width, the time-bandwidth-product (TBP), the RR, the pulse-peak power, the timing jitter (TJ) and the amplitude jitter (AJ). The pulse-width is estimated assuming different pulse shapes which are chosen depending on the minimal residual error of the fit function.

The AJ is given as a relative standard deviation (SD) of the pulse intensity variations. It is experimentally obtained from the signal-to-noise ratio (SNR) being the ratio of the integrated power spectral density (PSD) of the RR signal up to an offset frequency of ±100 MHz and the integrated PSD of the noise from 6 MHz to half of the RR thus representing almost the full evaluable frequency range for amplitude noise. Noise integration is performed separately in a low-frequency range from 6 MHz to 200 MHz and a high frequency range from 200 MHz to half of the RR because the high frequency range cannot resolve the important frequencies below 100 MHz due to the limited amount of data points of the ESA. Hereby, the noise floor of the ESA lies −55 dB below a typical stable RR signal for a resolution bandwidth (RBW) of 1 MHz. A tolerant threshold for pulse-to-pulse timing jitter ($\mathrm{TJ}_{\mathrm{ptp}}$) of 10 % is selected for amplitude stability classification for the following results.

The TJ is given either as $\mathrm{TJ}_{\mathrm{ptp}}$ or as the equivalent pulse-to-pulse timing jitter ($\mathrm{TJ}_{\mathrm{ptp}}^{\mathrm{eq}}$). Hereby $\mathrm{TJ}_{\mathrm{ptp}}$ represents the ideal choice of measure for a stably running passively MLL from which all other measures can be derived. The $\mathrm{TJ}_{\mathrm{ptp}}^{\mathrm{eq}}$ represents a possibility to quantify the TJ for a not ideally running passively MLL as stated in sub-section 2.4.1. It is reminded, that the $\mathrm{TJ}_{\mathrm{ptp}}^{\mathrm{eq}}$ is basically derived from the integrated timing jitter ($\mathrm{TJ}_{\mathrm{int}}^{(f_1,f_2)}$) but has the property to coincide with $\mathrm{TJ}_{\mathrm{ptp}}$ for a stably running passively MLL thus allowing to compare stable and unstable regimes. For calculation of the $\mathrm{TJ}_{\mathrm{ptp}}^{\mathrm{eq}}$ an evaluation frequency range from 5 MHz to 50 MHz is chosen. Both measures have a lower evaluation limit lying in the 20 fs range either given by the selected RBW for the estimation of $\mathrm{TJ}_{\mathrm{ptp}}$ or by the selected evaluation frequency range for the estimation of $\mathrm{TJ}_{\mathrm{ptp}}^{\mathrm{eq}}$. A more accurate quantification requires the measurement of the timing phase noise power spectral density (TPN PSD). However, this would increase the measurement duration by a factor of at least 4 and the detection limit of 20 fs is sufficient in this chapter but will be dropped in the following chapter. Further details and peculiarities of measurement and evaluation can be found in section 2.3. A tolerant threshold is defined for timing stability classification amounting to $3.3 \cdot 10^{-3}$ of the pulse repetition period (PRP). Such a PRP related relative measure for classification of timing-stability is regarded the most reasonable one because it is independent of the cavity length which has an impact on the TJ.

Pulse-width is estimated by identifying the optimal fit function for the measured auto-correlation signal which leads to an assumed pulse-shape. From the full-width at half-maximum (FWHM) of the fit the FWHM pulse-width can be estimated by using a deconvolution factor given in Table 2.1. The peak power is calculated by using Eq. (2.2) (on page 18) *and* the appropriate peak-power correction factor f_{pk}.

All tapered MLLs are operated at a mount temperature of 20°C. The gain section is driven by a constant current source[2] and the absorber section is negatively biased by a constant voltage source[3]. With respect to optical power, collimation optics losses[4] due to the high $1/e^2$ divergence angle of ±45° of the tapered MLLs which are measured to be −12.4 % are not removed in the presented data because they are not avoidable.

Due to the tapered gain section the focuses of fast and slow beam-axis do not coincide which is denoted as astigmatism for lasers. The fast axis focus is located at the physical facet. The slow axis focus is experimentally found to be located −1.0 mm inside the MLL. This was done by extrapolation of the measured slow-axis beam-width as a function of facet distance. Hereby, the facet distance is found by the extrapolated fast-axis beam-width as a function of relative distance. To allow for complete collimation, first the fast-axis beam is collimated with a collimation lens with a focal distance of ≈2.75 mm. Subsequently the intermediate focus for the slow-axis which is calculated to be located at ≈14.0 mm with respect to the facet position is collimated with an AR coated cylindrical lens with an focal distance of 60 mm. After collimation an optical isolator is used to prevent undesired feedback. Subsequently the diagnosis equipment is used for detection and analysis.

4.1.3 Results and discussion

Initially, the performance of the 1st generation tapered MLLs lasers as given in Table 4.1 will be briefly outlined and discussed with a focus on the MLL which exhibits optimal performance in terms of pulse-width, and peak power.

---

[2] ILX Lightwave, LDC-3742B

[3] Rohde & Schwarz, NGT20

[4] Thorlabs, C390TM-C

4.1.3.1 Results for 1^{st} generation tapered lasers

The laser **do 1791 gg6 a400** exhibits an AGLR of 0.17, a total length of 2.77 mm, has 5 layers of QDs and a large taper full-angle of 6°. This laser does not mode-lock in monolithic condition and only emits in continuous-wave (CW) operation. Using a planar semi-reflective mirror with a reflectivity of 30 % located at a distance of 28 cm allows to induce ML operation at the *monolithic* RR of 14.85 GHz. In such a way the highest estimated peak power amounts to 228 mW with a pulse width of 7.3 ps (Gaussian), a TJ_{ptp} of 39 fs and an average power of 26.3 mW at an absorber voltage of −6.0 V and a gain current of 640 mA. The absence of ML operation in monolithic configuration can be explained by the large taper angle of 6° which hinders efficient light field propagation in backward direction. Indeed, in [71] it was pointed out for index guided tapered MLL that the field profile does not transform adiabatically when traveling back through the tapered section and significant radiation of the field into the non-pumped substrate occurs which leads to a large decrease in the overlap between the field profile and the absorber section, reducing therefore the effectiveness of the saturable absorber but not preventing CW emission. This deteriorating effect is expected to be even higher for a gain-guided structure reported here. Following this explanation additional optical feedback (FB) increases the power in the absorber section thus eventually allowing ML operation.

The MLL **do 1791 gg2 a740** exhibits an AGLR of 0.24, a total length of 3.86 mm, has 5 layers of QDs and a taper full-angle of 2°. The highest estimated peak power amounts to 1.78 W with a pulse width of 9.7 ps (Gaussian), a TJ_{ptp} of 196 fs, a RR of 12.95 GHz and an average power of 238 mW at an absorber voltage of −3.0 V and a gain current of 1195 mA. These values are potentially limited by the suggested safe range of the bias conditions of 1 A at −4 V for this device. Furthermore, a tapered MLL with 5 QD layers exhibits a reduced MLL range as compared to a 10 layer MLL as reported in [137]. Therefore a 5 layer MLL yields worse performance as compared to a 10 layer MLL.

The MLL **do 1790 ig0.6 a600** exhibits a AGLR of 0.24, a total length of 2.97, has 10 layers of QDs, a small taper full-angle of 0.6° and is index-guided. The highest estimated peak power amounts to 1.78 W with a pulse width of 3.6 ps (Gaussian), a TJ_{ptp} of 103 fs, a RR of 13.6 GHz and an average power of 95 mW at an absorber voltage of −4.5 V and a gain current of 750 mA. Although such low taper angle should be beneficial according to [71] the index-guiding might be responsible for the non-existing improvement in pulse-width and peak power because the slow-axis can not be collimated in experiment and the near-field distribution measured by *III-V Lab* strongly exhibits a higher order lateral mode (not shown) potentially preventing proper bleaching of the absorber. Concluding, these three tapered MLL show relatively large pulse-widths and insignificant pulse peak power therefore no graphical representation of the results is presented.

Finally, the MLL **do 1790 gg2 a400** which exhibits an AGLR of 0.17, a total length of 2.78 mm, has 10 layers of QDs, a taper full-angle of 2° and is gain-guided shows significantly improved performance and a well defined stability region the latter being demonstrated by in Fig. 4.1a and Fig. 4.1b. These figures show the relative SD of AJ within a bandwidth of 50 MHz to 2.5 GHz and the TJ_{ptp}, respectively as a function of absorber voltage and gain current *offset*. The offset is related to the corresponding different threshold currents $I_{thr}(U_{abs})$ which vary as a function of the absorber voltage. This uncommon depiction is used to allow for a comparison with simulation results. The shown operation range represents only a part of the investigated range (0.0 V to 7.0 V and 300 mA to 1050 mA) and is focusing on the region where stability is observed.

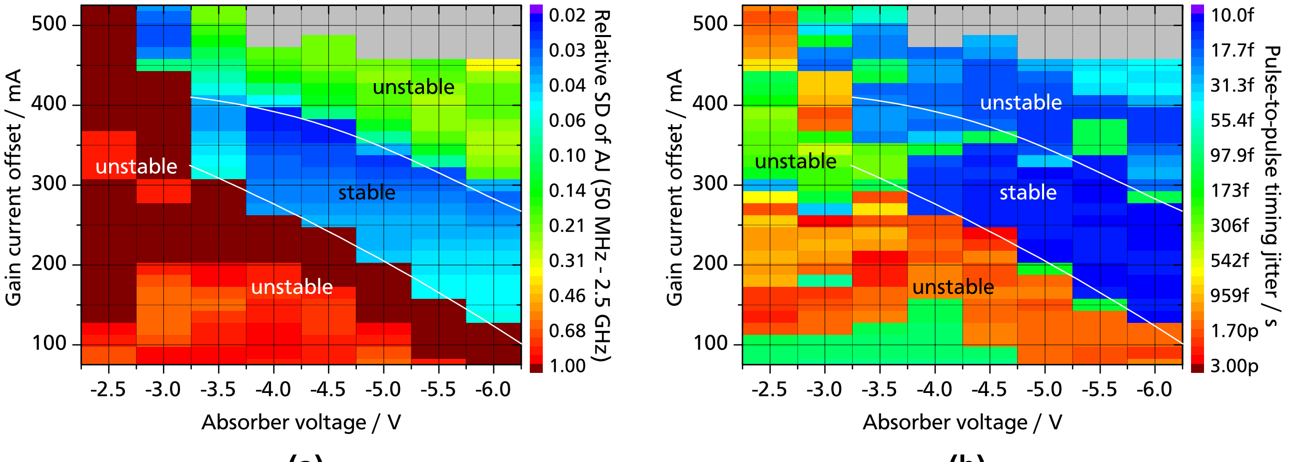

(a) **(b)**

Figure 4.1: Experimentally obtained depiction of (a) relative SD of AJ and (b) TJ_{ptp} as a function of absorber voltage and gain current offset with respect to the corresponding different threshold currents $I_{thr}(U_{abs})$. White lines indicate the borders between stable and unstable regions. (Laser: do 1790 gg2 a400)

The existence of a RR signal is in general no sign of timing or amplitude stability. The measured AJ shown in Fig. 4.1a exhibits three different and clearly separated regions. The first region, located at low gain current offsets exhibits broad-band amplitude modulation up to a frequency offset of ≈2 GHz while exhibiting a low power of the RR signal. This results in AJ values of even higher than 1 thus denoting this region as highly unstable. Hereby, the optical spectrum is also irregular (not shown). The second region, located at intermediate gain current offsets exhibits a narrow RR signal and only weak amplitude modulations leading to a low AJ of below 6 % thus representing a stable train of pulses while exhibiting a regular Gaussian shaped spectrum. Finally, at high gain currents amplitude modulations at multiples of 1.8 GHz to 400 MHz appear depending on absorber voltage. These quite sharp amplitude modulations with a −3 dB width of down to 4 MHz indicate Q-switched mode-locking (QS ML) and result in a periodic modulation of the optical pulse train. Hereby, the AJ lies in a range of 4 % to 34 %. The transition from the first to the second region is discrete whereas the transition from the second to the third region is continuous as also evident in the depiction. Hereby, a stability threshold with respect to AJ is defined amounting to 10 % and is also indicated as the two white lines in the figure.

The stability criterion with respect to AJ is also partially reflected in the distribution of the TJ which is depicted in Fig. 4.1b using the measure TJ_{ptp}. The unstable region at low gain current offsets exhibits a huge TJ_{ptp} of up to 2 ps which corresponds to 3 % of the PRP. In contrast, the stable region exhibits a low TJ_{ptp} of down to 11 fs which corresponds to a narrow RR line-width of 2.4 kHz or to $1.6 \cdot 10^{-4}$ of the PRP. Interestingly, the unstable region at high gain current offsets which represents QS ML can also exhibit low TJ values thus demonstrating a strongly and periodically modulated but *equidistant* pulse train. Hereby, a stability threshold is defined amounting to $3.3 \cdot 10^{-3}$ of the PRP which corresponds to 230 fs for the presented MLL and is also indicated by the white lines in the figure.

Knowing the stable region, now, the other parameters of the MLL can be presented including the pulse-width and peak-power which are shown in Fig. 4.2a and Fig. 4.2b, respectively. It can be observed, that the pulse-width amounts to at least 6 ps in the unstable region and is below 2 ps in the stable region. Interestingly also in the QS ML region the pulse width is as short as in the stable region which is also reflected in the continuous increase of the peak power value from stable to the QS ML region. Now, the optimal stable operation points can be identified. The highest obtained peak power amounts to 3.8 W with a pulse width of 1.29 ps (Gaussian), a $\mathrm{TJ}_{\mathrm{ptp}}$ of 12 fs, a RR of 14.6 GHz, an average power of 77 mW and a TBP of 1.96 at an absorber voltage of −6 V and a gain current of 740 mA (current offset of 290 mA). The shortest pulse-width amounts to 0.94 ps with a peak power of 3.1 W, a $\mathrm{TJ}_{\mathrm{ptp}}$ of 11 fs, an optical average power of 46 mW and a TBP of 0.98 at a absorber voltage of −6.0 V and a gain current of 580 mA (current offset of 130 mA).

Having shown these competitive results it is concluded, that the combination of a taper angle of 2°, 10 layers of QDs and gain-guiding leads to a starting point for further optimizations. To allow for improving suggestions by simulation results, first, the numerical model must be able to reproduce the experimentally observed behavior of the gain-guided tapered MLL. Simulations base on a multi-section delayed differential equation (DDE) numerical model which was verified by comparison with a finite-difference traveling-wave (FDTW) numerical model [69]. This DDE model was extended towards simulation of tapered MLLs [71]. By using a beam propagation method (BPM) model [140] which uses pre-calculated results obtained from multi-population rate-equations (MPREs) [67] the gain-guiding properties can be accounted for. The obtained simulation results for a similar gain-guided tapered MLL are shown in Fig. 4.2c and Fig. 4.2d depicting the pulse-width and peak power, respectively as a function of absorber voltage and gain current offset.

Regarding Fig. 4.2c it can be observed that the shape of the regions as well as the pulse-width values are in good qualitative and quantitative agreement. Regarding Fig. 4.2d it can be observed that the peak power is also reproduced with good agreement. Also the unstable QS ML region can be identified and is confirmed to originate from leading edge instabilities (LEIs) which were introduced in sub-section 2.1. These LEIs occur for high gain currents. However, the unstable region at lower gain currents, possibly originating from trailing edge instabilities (TEIs) is not identified. Also the sharp transition is not evident. This can be explained by the difficulty to decide whether an undesired net gain window which can be identified in simulations is significant enough to induce an actual instability. Indeed, in [70, section 6] it is stated, that a critical noise level exists within the net gain window of a TEI below which the ML stability is preserved.

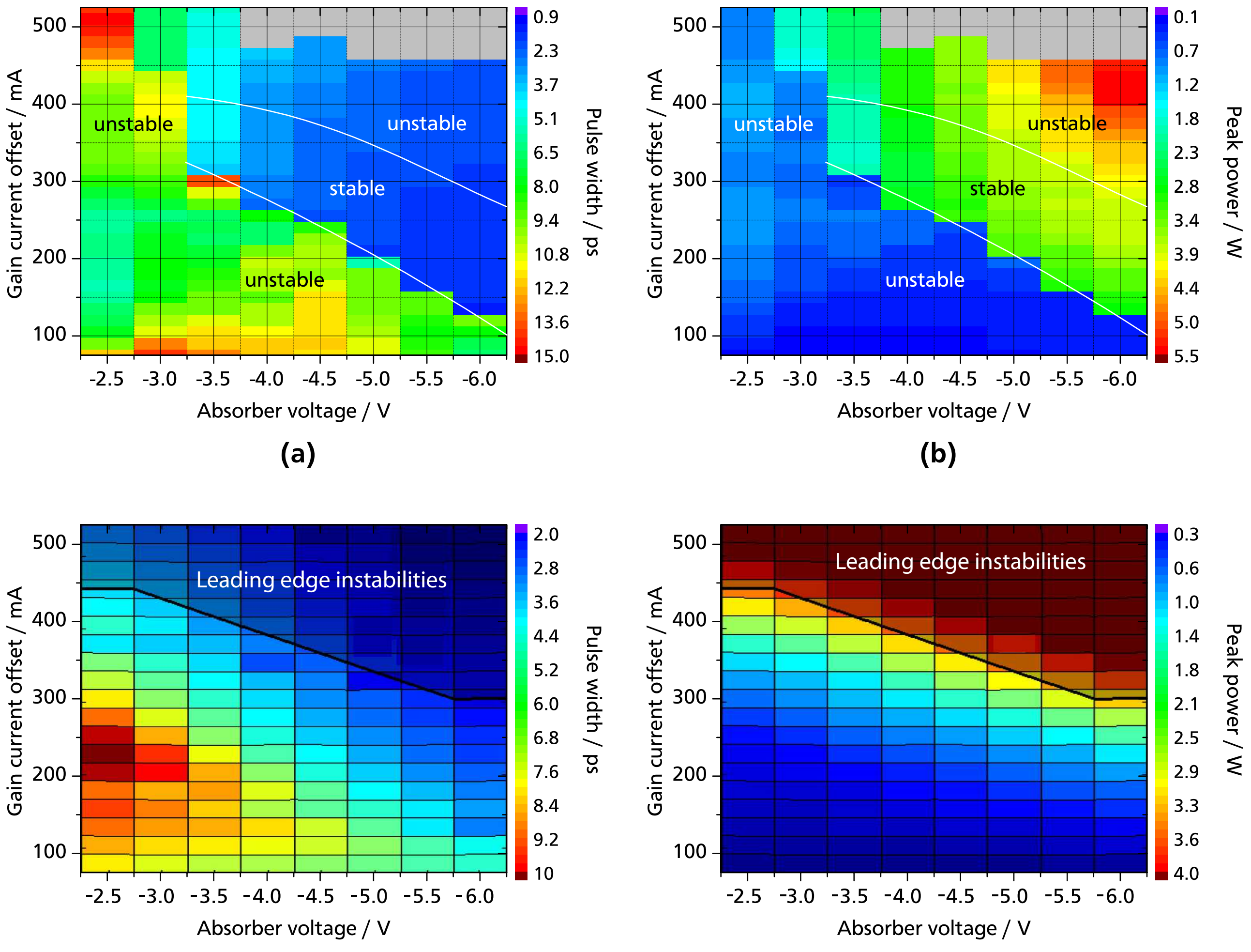

(a) **(b)**

(c) **(d)**

Figure 4.2: Experimentally obtained depiction of (a) pulse-width and (b) peak-power as a function of absorber voltage and gain current offset with respect to the corresponding different threshold currents $I_{\mathrm{thr}}(U_{\mathrm{abs}})$. Depiction of (c) pulse-width and (d) peak power obtained from simulations [141]. (Laser: do 1790 gg2 a400)

4.1.3.2 Design considerations for 2$^{\mathrm{nd}}$ generation tapered lasers

Having demonstrated the good agreement of experimental and simulation results, now, possible design suggestions can be discussed. Motivated by [142, 143] a variation of the total MLL length as well as a variation of the AGLR is investigated by simulations. In [143] it was observed for a straight index guided MLL that an increase of the AGLR from 1/14 to 1/3 resulted in a pulse-width decrease from 2.3 ps to 800 fs and a peak power increase from 19 mW to 260 mW. This was attributed to an increased amount of saturable absorption leading to an increased amount of pulse shortening per cavity round-rip. The increased threshold current for high AGLR forces the MLL to operate at elevated gain current leading to increased output power. Now, the simulations reveal the following observations which are also partially reported in [63, 70].

- Considering a fixed MLL length of 1.5 mm and increasing the absorber length, an increase in the threshold current density is obtained leading to a decrease in the differential gain which increases further the saturation energy in the gain section and therefore leads to a further improvement of the ML quality. However, for absorber lengths above 0.3 mm (AGLR $>$ 0.2), at low injected current density, a low frequency amplitude instability starts to appear. This can be justified since the main cause of instability is the bleaching of the absorber which is enhanced when the absorber length is increased [34]. Moreover, the magnitude of the instability is larger near threshold due to the fact that the gain recovery is too slow with respect to the photon lifetime in the cavity and therefore gain dynamics cannot properly compensate the absorption changes [34].

- Furthermore assuming different total lengths the following is observed. For long tapered MLLs (3.7 mm) with increasing absorber lengths improved stability is observed at high currents, leading to higher power. Also for short tapered MLLs (2.5 mm) by increasing the absorber length the region of stability shifts towards higher gain currents leading to higher power. However, the region of stability decreases in size and TEIs may appear at lower gain currents thus forming a stability corridor which shifts to higher gain currents for increasing absorber section lengths.

- It is found that introducing an additional straight forward-biased section between the absorber and the tapered section for a 2.5 mm tapered MLLs (3 sections in total), leads to a higher coupling of the optical field with the absorber section but at the same time to a reduction of the coupling between the optical field and the gain section. Thus, the region of stability shifts towards larger currents, similarly to the behavior obtained when the absorber length is increased. Applying different current densities in the straight and tapered gain sections does not lead to a significant improvement of MLLs performance.

These guidelines were used to specify the geometry of the 2nd generation tapered MLL as given in Table 4.1 below the horizontal line. The experimental investigation of these MLLs is given in the following.

4.1.3.3 Results for 2nd generation tapered lasers

Having outlined initial results for the 1st generation of tapered MLL and introduced design considerations, now, the experimental characterization of the 2nd generation tapered MLL as given in Table 4.1 will be briefly outlined and discussed with a final focus on a specific MLL which exhibits most optimal performance in terms of pulse-width and peak power.

The MLL **do 2584 s1b a6** exhibits an AGLR of 0.19, a total length of 2.5 mm, a taper full-angle of 2° and has 10 layers of QDs. The RR amounts to 16 GHz. The MLL **do 2584 s1b a8** exhibits identical structural parameters and is found to exhibit almost identical performance. Thus results of only the first MLL will be shown. The following results are obtained by using the passive stabilization introduced in chapter 3 which allows for an extension of the stability range towards lower gain currents.

First, the stability regions in terms of AJ are identified. Fig 4.3a shows the relative SD of AJ obtained in a frequency range from 6 MHz to half of the RR thus covering almost the whole relevant range as a function of gain current and absorber voltage. Stability is defined by an AJ of below 10 %. At low gain currents no lasing occurs indicated by a gray area and at low absorber voltages together with high gain currents CW emission is dominant also indicated by a gray area. In the remaining region a highly inhomogeneous distribution of AJ can be observed. No simple trends are evident. The most unstable region with an AJ higher than 1 is characterized by broad-band amplitude noise up to a frequency offset of 2 GHz to 3 GHz. All other regions exhibit various different shapes of the AJ spectrum. Interestingly *two* stable regions can be recognized, one expected region, similar to the region of the 1^{st} generation MLL, is located from −4.0 V and 775 mA to −6.5 V and 650 mA exhibiting an AJ below 10 % and the other region is located around −0.5 V and 450 mA. This second region is surprising, because for such low absorber voltages only thermionic carrier escape but no tunneling escape occurs in the absorber therefore inefficient absorption and thus no ML is expected. This weak absorption is reflected by the high pulse-widths of around 10 ps. Nevertheless this indicates that the balance of gain and absorption is achieved for two independent and not interconnected operation regimes.

Both stable regions are also well reflected by the low TJ_{ptp}^{eq} amounting to a low value of below 200 fs as shown in Fig. 4.3b. Hereby, stability with respect to TJ is again defined as $3.3 \cdot 10^{-3}$ of the PRP and amounts to 200 fs. In particular, a corridor of TJ stability from around −3 V and 1 A to −6.5 V and 650 mA can be observed similar to the results of the first generation MLL shown in Fig. 4.1b. Also here, for high currents or low absorber voltages inside this corridor, the low TJ is accompanied by a high amount of AJ which can manifest in QS ML and originates from LEIs. The unstable range below this corridor possibly originates from TEIs as denoted in sub-section 4.1.3.2.

Having identified the stable regions, the pulse-width and peak-power can be presented which are shown in Fig. 4.3c and Fig. 4.3d. Hereby, the defined stability in terms of both AJ and TJ from Fig. 4.3a and Fig. 4.3b is represented as a outline. In the whole displayed range pulses exist starting from threshold current and a pulse-width could always be determined. Thus, the existence of pulses does not indicate stable ML at all. Typically, the shortest pulse durations are observed at high reverse-bias voltages around −6.0 V and low driving currents close to threshold. Deviations from these optimum driving conditions lead to pulse broadening. Hereby, the stable region around −6.0 V and 650 mA is well reflected by pulse-widths well below 2 ps. However, the unstable QS ML region around −6.0 V and 800 mA which also exhibits a short pulse-width of 1.2 ps and an TJ of 62 fs can only be quantitatively identified by the AJ which amounts to a high value of 25 %. This means, that QS ML can be quite stable in terms of TJ and can exhibit short pulse widths while being modulated by an envelope with a frequency ranging from 500 MHz to 1.5 GHz. It is well known, that for regular non-tapered MLL the pulse-width generally increases with increasing gain current and decreases with increasing absorber voltage for stable ML operation. Despite the region exhibiting high pulse-widths around −3.5 V and 700 mA this statement is also fully valid here for the absorber voltage but the gain current dependence is more complex. In [70] it was noted, that maximum absorption bleaching and maximum gain compression are almost independent on absorber voltage and gain current for a given pulse-width and pulse energy. This statement is supported by the large sub-picosecond pulse-width region around an absorber voltage of −6.0 V and a gain current of

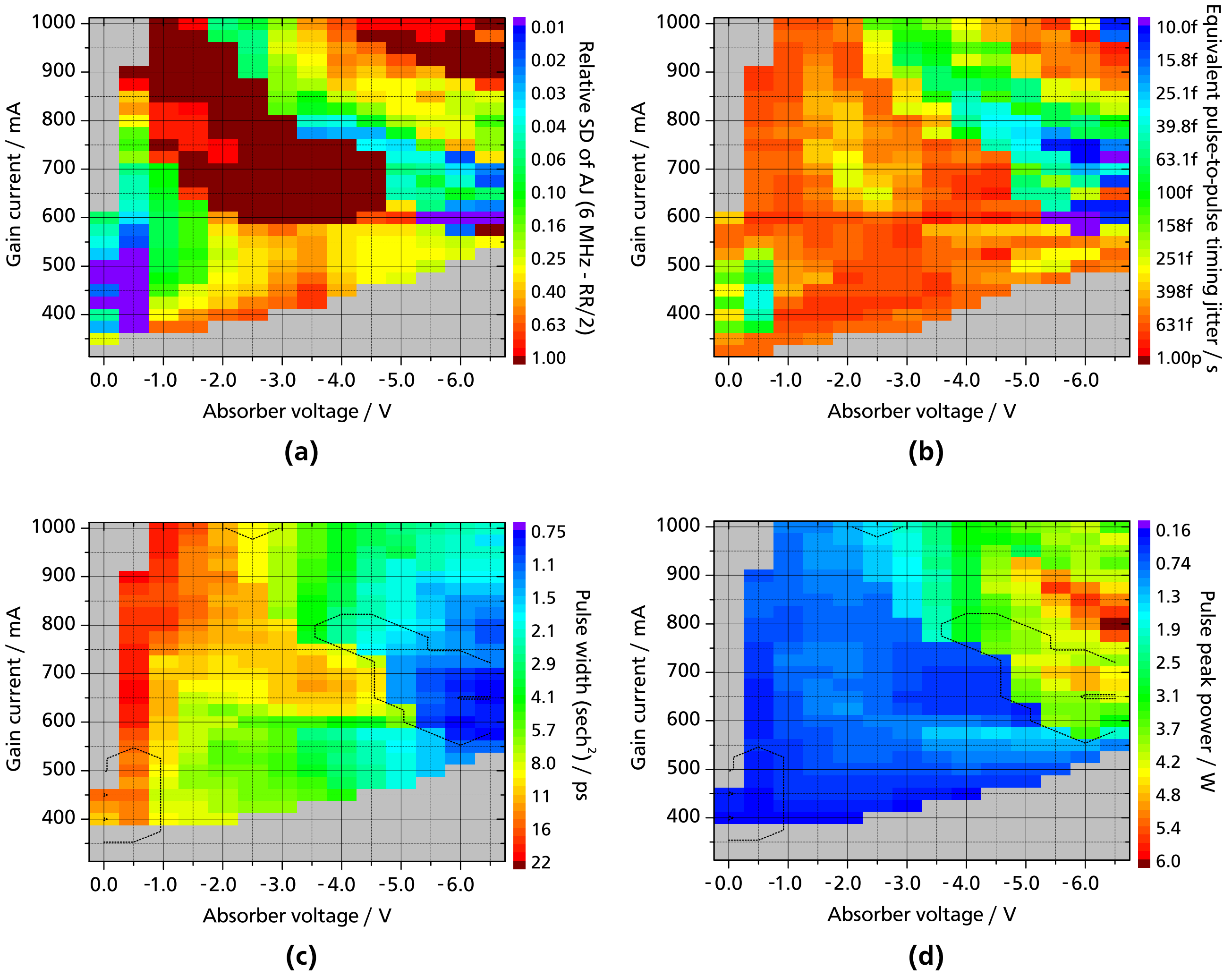

Figure 4.3: Experimentally obtained depiction of (a) relative SD of AJ (b) TJ_{ptp}^{eq} (c) pulse-width ($sech^2$) and (d) peak-power as a function of absorber voltage and gain current. The outlines indicate regions of stability. (Laser: do 2584 s1b a6)

650 mA. The pulse-width has also a dominant impact on the calculated pulse-peak power as shown in Fig. 4.3d. There, only for high gain currents and high absorber voltages a significant peak power can be obtained resulting from the low pulse-width and the high average power which generally increases with gain current. Two regions of local maxima of the peak power can be observed. One region is located around −6.0 V and 700 mA being stable and the other is located around −6.5 V and 800 mA offering a higher peak power but being unstable. Hereby, at a absorber voltage of −6.0 V the peak power increases from 3.8 W to 4.2 W within the displayed current range of 575 mA to 1000 mA demonstrating, that an increase of the pulse-width is more than compensated by an increase of the average power. The peak power within the stable region at an absorber voltage of −0.5 V and a gain current of 525 mA amounts to 0.45 W and is therefore insignificant.

Having identified the regions of stability as well as the regions of short-pulses and high peak power within these stable regions now the most relevant operation points are presented which exhibit the highest peak power or the shortest pulse-width. For identification, a smaller current step size is chosen for a voltage of

−6.0 V. Thus, the highest peak power of 5.48 W is observed together with a pulse width of 757 fs, a TBP of 0.630 being 2.0 times the Fourier limit for a sech^2 shaped pulse, an AJ of 2.9 % and a TJ_{ptp}^{eq} of 23 fs at an absorber voltage of −6.0 V and gain current of 695 mA. Hereby, the pulse-width is always below 1 ps at an absorber voltage of −6.0 V and within the stable regions. The shortest pulse-width of 672 fs (sech^2 shape) is observed together with a peak power of 3.8 W, a TBP of 0.355 being 1.12 times the Fourier limit for a sech^2 shaped pulse, an AJ of 1.7 % and a TJ_{ptp}^{eq} of 10 fs at an absorber voltage of −6.0 V and gain current of 570 mA. This close to Fourier-limited pulse-width is remarkable and is found to be often attributed to a balancing of the pulse dispersion in the gain and absorber sections [76]. But also the low carrier density near threshold current thus minimizing the magnitude of chromatic dispersion or the insignificant pulse broadening due to low gain saturation are expected to support Fourier-limited pulse generation.

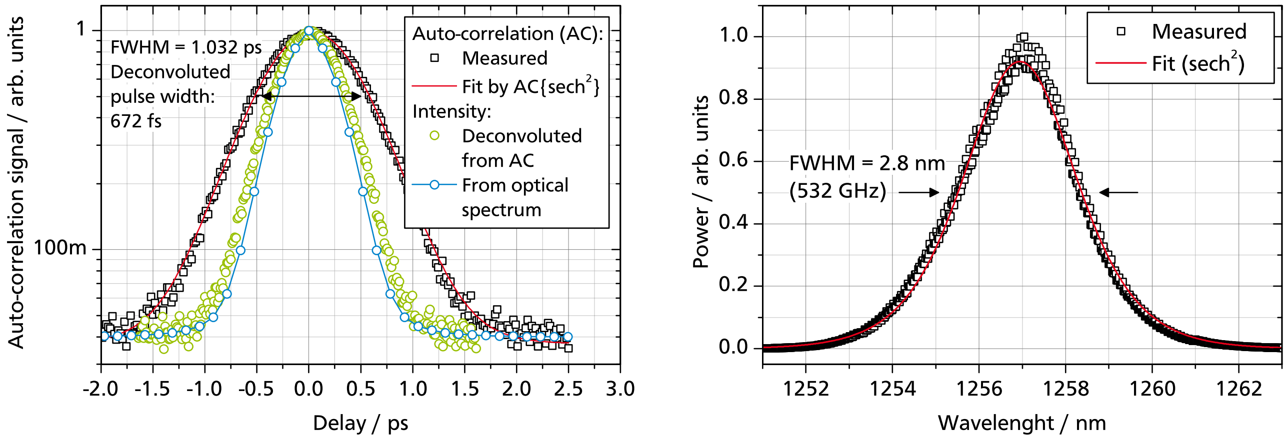

(a) (b)

Figure 4.4: Experimentally obtained (a) auto-correlation signal and calculated intensity profiles and (b) corresponding optical spectrum at an absorber voltage of −6.00 V and a gain current of 570 mA. (Laser: do 2584 s1b a6)

The experimentally obtained auto-correlation (AC) trace for this condition and the corresponding optical spectrum are shown in Fig. 4.4a and Fig. 4.4b, respectively. The measured AC trace as well as the matching fit by a $\text{AC}\left\{\text{sech}^2\right\}$ function[5] are shown. Hereby, $\text{AC}\left\{\right\}$ denotes the auto-correlation operation. The also shown deconvoluted intensity profile is simply obtained by rescaling of the time-axis of the auto-correlation trace by a factor of 0.65 according to Table 2.1 because a sech-function is an eigenfunction of the Fourier-transform. The shown intensity profile obtained from the optical spectrum is calculated by taking the square root of the power of the optical spectrum shown in Fig. 4.4b to obtain electric-field magnitudes, then performing the Fourier-transform while using a flat phase profile and finally squaring the result to obtain the intensity. Comparing the intensity profiles in Fig. 4.4a obtained from the auto-correlation and the optical spectrum yields correspondence of the shape as well as the slightly increased FWHM of the intensity profile obtained from the auto-correlation by a factor of 1.12. This factor being close to 1 comprehensively demonstrates the almost Fourier-limited TBP of the sub-pico-second optical pulse reported in [9].

---

[5] See [87] for full numerical expression.

The MLL **do 2584 s3 a3** exhibits an AGLR of 0.20, a total length of 3.0 mm, a taper full-angle of 2° and has 10 layers of QDs. This MLL has three geometrical sections: One absorber section with a length of 0.5 mm, one straight gain section with a length of 0.5 mm and a tapered gain section length of 2.0 mm. Both gain sections are electrically not insulated from each other. The RR amounts to 13.4 GHz. This tapered MLL exhibits a higher length (+20 %) and a slightly higher AGLR (+5 %) as compared to the previous MLL do 2584 s1b a6. The following results are obtained by using the passive stabilization introduced in chapter 3 which allows for an extension of the stability range towards lower gain currents for this MLL.

Again, first the stability regions in terms of AJ and TJ are identified. Fig 4.5a shows the relative SD of AJ obtained in a frequency range from 6 MHz to half of the RR as a function of gain current and absorber voltage. Stability is defined by an AJ below 10 %. Hereby, the span of the displayed gain current is higher by 200 mA as compared to the previously discussed MLL. Similar to the previous MLL do 2584 s1b a6 again two pronounced regions with low AJ can be identified. One is around an absorber voltage of −6.0 V and a gain current of 750 mA and the other around an absorber voltage of −0.5 V and a gain current of 550 mA. The previously mentioned stability corridor from around −3.5 V and 1000 mA to −6.5 V and 775 mA is not existent any more and is only weakly hinted. All other regions exhibit highly irregular shapes of the radio-frequency (RF) spectra indicating severe instabilities. Nevertheless, a large amplitude stability region emerges from ≈ 0 V to ≈ −6 V and ≈450 mA to ≈700 mA. However, the TJ_{ptp}^{eq} imposes a severe constrain on TJ stability as shown in Fig. 4.5b. Hereby, stability with respect to TJ is again defined as $3.3 \cdot 10^{-3}$ of the PRP and amounts to 250 fs. Two relevant stable regions are evident. One is around an absorber voltage of −4.0 V and a gain current of 600 mA and the other is around an absorber voltage of −6.0 V and a gain current of 650 mA and is highly fragmented. Such an abrupt and fragmented parameter dependence is unexpected and the reason for its occurrence is unknown. The region around an absorber voltage of −4.0 V and a gain current of 1150 mA exhibits high timing stability but shows for example broad-band amplitude noise within a frequency offset range from ≈1 GHz to ≈6 GHz or QS ML at frequencies from ≈1 GHz to ≈3 GHz.

The strong fragmentation of the TJ with respect to the driving conditions is also reflected in the pulse width as shown in Fig. 4.5c. The shortest pulses are obtained at high absorber voltages and close to threshold. Consequently, the peak power also exhibits highest values in this region as shown in Fig. 4.5d. For identification of most of the relevant operation points, a smaller current step size is chosen for a voltage of −6.0 V. Thus, the shortest pulse-width of 955 fs is observed together with also the highest peak power of 4.85 W, a TBP of 0.68 being 1.43 times the Fourier limit for a Gaussian shaped pulse, an AJ of 1.6 % and a TJ_{ptp}^{eq} of 16 fs at an absorber voltage of −6.0 V and gain current of 630 mA. Although this tapered MLL exhibits a higher length (+20 %) and a slightly higher AGLR (+5 %) as compared to the previous MLL do 2584 s1b a6 it does not exhibit an improvement in terms of pulse-width and pulse-peak power. The slightly increased AGLR leads just to an increased threshold (≈+75 mA) but the optical average power is similar and in addition does not increase monotonically like for all the other lasers leading to a limited peak power.

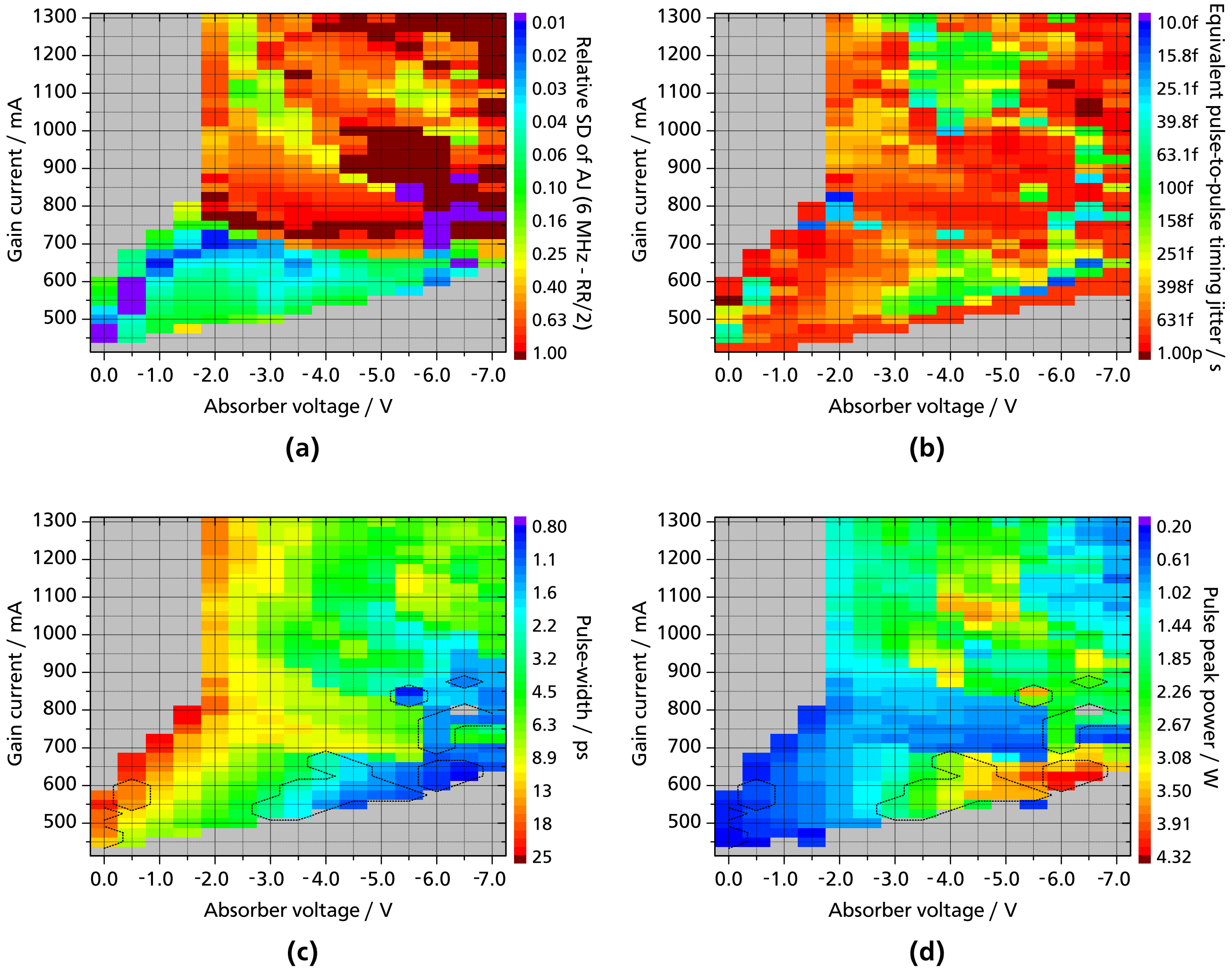

Figure 4.5: Experimentally obtained depiction of (a) relative SD of AJ (b) $\mathrm{TJ}^{\mathrm{eq}}_{\mathrm{ptp}}$ (c) pulse-width (Gaussian) and (d) peak-power as a function of absorber voltage and gain current. The outlines indicate regions of stability. (Laser: do 2584 s3 a3)

The MLL do 2584 s2b b3 exhibits an AGLR of 0.25, a total length of 4.0 mm, a taper full-angle of 2° and has 10 layers of QDs. The RR amounts to 10.0 GHz. This tapered MLL exhibits a higher length (+60 %) as well as a significantly higher AGLR (+32 %) as compared to the MLL do 2584 s1b a6. The following results are obtained by using the passive stabilization introduced in chapter 3 which allows for an extension of the stability range towards lower gain currents as well as towards higher absorber voltages for this MLL. The stabilization influences the pulse-width, the average power and stability for high absorber voltages and low gain currents. A detailed but brief comparison is presented below to highlight the effectiveness of the stabilization. Stability with respect to TJ is defined as $3.3 \cdot 10^{-3}$ of the PRP and amounts to 330 fs and stability with respect to AJ is defined as 10 % of the relative SD of AJ.

To demonstrate the general behavior of the MLL Fig. 4.6a and Fig. 4.6b show the pulse-width (Gaussian or single sided exponential shape) and corresponding peak power, respectively as a function of gain current and absorber voltage. The outlines indicate regions of stability defined by the values stated above. Hereby, the span of the displayed gain current range is higher by 400 mA and the displayed absorber voltage starts at a higher value as compared to the results of the MLL do 2584 s1b a6. At an absorber voltage of −6.5 V the threshold current amounts to 950 mA but no pulses can be observed up to a gain current of 1450 mA. In this region no RR signal can be observed or the power of the RR is insignificant and is always at least lower by −40 dB as compared to a typical power. Thus, dominant CW emission can be assumed which is attributed to the high AGLR and high absorber voltage. The pulse-width exhibits two regions of low pulse-width around a minimum value of 0.9 ps. The first region around an absorber voltage of −4.0 V and a gain current of 950 mA exhibits low TJ and low AJ whereas the second region around an absorber voltage of −4.0 V and a gain current of 1550 mA exhibits a low TJ but a high AJ around a value of 30 %. All other regions exhibit instability in terms of AJ and TJ. For this MLL the shortest pulses and the highest peak power as shown in Fig. 4.6b is obtained for a relatively low absorber voltage of −4.0 V as compared to the MLL do 2584 s1b a6 which offers optimum performance at an absorber voltage of −6.0 V. This could originate in the higher AGLR which requires a lower absorber voltage in order to not to degrade the balance of gain and loss. The pulse-width approximately dominates the peak power as shown in Fig. 4.6b. The peak power reflects both mentioned regions which both are defined by low TJ. Unfortunately the region of high peak power in the 10 W range around an absorber voltage of −4.5 V and a gain current of 1550 mA exhibits a broad-band AJ up to a frequency of 3 GHz. It is found that this instability can not be reduced by the passive electrical stabilization which is also demonstrated in the following for an absorber voltage of −4.0 V. Both figures (Fig. 4.5c and Fig. 4.5d) allow to identify an absorber voltage of −4.0 V which offers low pulse width and high peak power for further investigations with a smaller current step size.

First, stability is precisely quantified in terms of AJ and TJ at an absorber voltage of −4.0 V as a function of gain current as shown in Fig. 4.6c. Hereby, also a comparison of both quantities is given for the free running condition and the stabilized condition. The red line indicates the mentioned stability threshold for both AJ and TJ. Without the stabilization, TJ and AJ are both above stability threshold up to a current of 1500 mA. For higher currents the TJ is below stability threshold but the AJ amounts to at least 30 %. Hereby, the stabilization can not influence this high-bandwidth AJ. However, starting from threshold current up to a current of 1100 mA the stabilization massively reduces AJ and consequently allows ML operation leading also to a low TJ. At a gain current of 890 mA the AJ reduces from above 1 down to a value of 4 % and the TJ reduces from 930 fs to 63 fs. Stable ML is obtained in a current range of 821 mA to 914 mA and 961 mA to 1000 mA also indicated by the green bars in the figure. In between these current ranges a RR transition takes place whereby at 930 mA both RR signals coexist with a RR difference of 9 MHz. The difference amounts to 18 MHz at the second harmonic RR which indicates a dual pulse train. Hereby, in contrast to the temporal dual pulse train reported in section 3.3 no amplitude modulation is observed. Thus, a permanent simultaneous dual pulse train can be assumed. Also here the optical spectrum exhibits a superposition of two spectral envelopes with a width of 3.5 nm each and a separation of 4 nm supporting the dual pulse train assumption.

Precisely knowing the stability range, now the evolution of the pulse-width and peak power as a function of gain current can be presented as shown in Fig 4.6d. Hereby the green bars indicate stable ML and the red dashed line indicates a transition from a Gaussian pulse shape to a single-sided exponential pulse shape dictated by the measured auto-correlation shape and a corresponding ideally matching fit function.

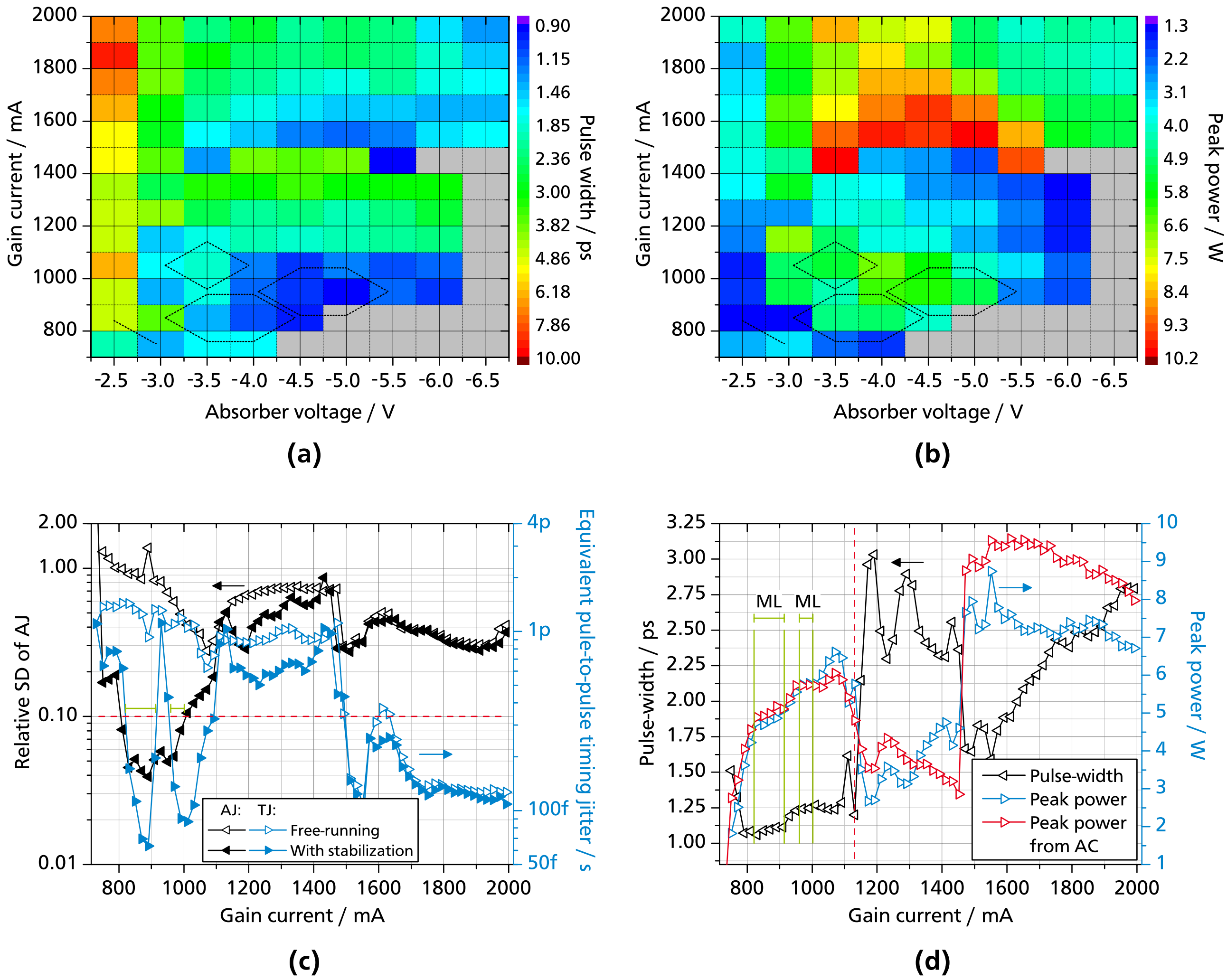

Figure 4.6: Experimentally obtained depiction of (a) pulse-width (Gaussian or single sided exponential) and (b) peak-power as a function of absorber voltage and gain current. Dotted outlines indicate regions of stability. (c) Depiction of relative SD of AJ and $\mathrm{TJ}_{\mathrm{ptp}}^{\mathrm{eq}}$ with and without passive electrical stabilization. (d) Pulse-width (Gaussian or single sided exponential) and corresponding peak power as a function of gain current at an absorber voltage of −4.0 V. Green bars indicate stability. (Laser: do 2584 s2b b3)

This single-sided exponential pulse shape indicates a strong pulse-asymmetry. Due to the high AJ this asymmetry may result from a LEI. The shortest pulse-width of 1.06 ps (Gaussian shape) is observed at a gain current of 830 mA with a peak-power of 4.75 W, a TBP of 0.64 being 1.45 times the Fourier-limit, an AJ of 5 % and a TJ of 170 fs. The highest peak power amounts to 5.78 W with a pulse-width of 1.25 ps (Gaussian shape) and a TBP of 0.82 which is 1.86 times the Fourier-limit, an AJ of 8 % and a TJ of 90 fs. This highest peak power of 5.78 W is higher by +5 % as compared to the MLL do 2584 s1b a6 and the shortest pulse-width of 1.06 ps is higher by +58 % as compared to the MLL do 2584 s1b a6. The highest peak-power in the unstable AJ dominated regime at a gain current of 1551 mA amounts to 8.74 W with a pulse-width of 1.6 ps (single-sided exponential shape), a TBP of 1.72 being 15.6 times the Fourier-limit, a TJ of 85 fs and a high AJ of 32 %. The AJ results from a broad amplitude modulation from a frequency of 500 MHz to 3 GHz which extends up to the Nyquist frequency of 5 GHz. The high timing stability and high *calculated* peak power motivates to investigate the output of a nonlinear optical detection system which is insensitive to AJ. Such a system is the used intensity auto-correlator. Thus, Fig 4.6d also shows the square root of the maximum amplitude of the AC signal which should ideally represent the pulse peak power. Hereby, the obtained values are scaled by a constant factor. Indeed, for the low current range up to a value of 1130 mA which exhibits the Gaussian pulse shape a perfect correlation exists thus demonstrating the feasibility of estimation of the relative peak power directly from the AC signal. Above a current of 1460 mA, the AC based peak power roughly matches the calculated peak-power thus demonstrating that the amplitude instability does not prevent the existence of pulses.

The last investigated MLL **do 2584 s4 d2** consists of three sections. An tapered gain section, a straight intermediate section and a straight back section with lengths of 1.6 mm, 0.7 mm and 0.7 mm, respectively. Thus the MLL exhibits an AGLR of 0.44 for the last and intermediate section. The total length amounts to 3.0 mm, the taper full-angle amounts to 2° and the MLL has 10 layers of QDs. The RR amounts to 13.4 GHz. This tapered MLL exhibits a higher length (+20 %) as well as a much higher AGLR (+130 %) as compared to the MLL do 2584 s1b a6.

In experiments it is found that using the back-facet section as absorber (AGLR of 0.44) does not allow stable ML operation for an investigated absorber voltage range of 0.0 V to −6.0 V and a current rage of up to 2.5 A. Although the passive stabilization is able to strongly reduce the amplitude instabilities it does not allow stable ML. In this case the highest power of the RR signal is observed for an absorber voltage of −4.0 V. Although a high AGLR is expected to be in principle beneficial in terms of pulse-width and peak-power it does not allow ML in the experiments. Using the middle section as absorber (AGLR of 0.44) does not allow stable ML operation either in the stated operation rage. However, in this case the stabilization is successfully capable to provide stable ML operation at an absorber voltage of −6.0 V. Hereby threshold current amounts to a value of 635 mA.

In [143] it was found experimentally that for a straight two section MLL and for configurations with an AGLR of more than 0.33 the gain is insufficient to overcome the absorber losses and thus lasing operation could not be achieved. Here, in contrast ML operation *is* achieved for an even higher AGLR of 0.44. It is assumed, that the taper gain section allows for much higher values of AGLR due to the higher gain as compared to a straight gain section. Furthermore, using the middle section as the absorber represents a different scheme. Indeed, not only the AGLR but also the absorber location is important. In [63, 144] the effect of the location of the absorber section on ML characteristics was investigated by numerical simulations for QD based MLL. It was found, that placing the absorber at the output facet instead of at the back facet reduces the pulse-width significantly and increases the stability range. The front facet saturable absorber location resulted in a higher pulse energy arriving at the absorber due to the longer connected gain length. This higher intra-absorber pulse energy was found to result in shorter pulses and thus also in a higher peak power. Following this finding, however, this would rather favor the last section as absorber instead of the middle section in terms of performance. Another reason for the difference in operation could be the transient time of the pulse within the absorber which is shorter for the configuration using the middle section as absorber. However, the regeneration time of the absorber seems not to be related to the transient time of the pulse within the absorber because the pump and probe response of a QD based absorber in [78, Fig. 2(a)] does not show any change in regeneration rate after the transient time of 13.6 ps of the pump pulse. However, it is known, that a self-colliding pulse effect occurs in the absorber by reflection of the pulse at the facet. The two mentioned absorber configurations in [63,144] always exhibit a self colliding pulse effect. But for the configuration used here no self colliding pulse effect can occur because the absorber is located in the middle of the cavity. Indeed in [66] it is stated, that a self colliding pulse effect in a Fabry-Pérot MLL provides increased effectiveness of the saturable absorber as compared to an equivalent ring MLL. Therefore, using the middle section as absorber instead of the last section prevents colliding pulse effects and reduces absorption which corresponds to a reduction of the AGLR finally allowing ML operation.

First, the quantification of stability in terms of AJ and TJ is shown in Fig. 4.7a which displays the relative SD of AJ and the $\mathrm{TJ}_{\mathrm{ptp}}^{\mathrm{eq}}$ at an absorber voltage of −6.0 V as a function of gain current. Stability is defined as an AJ of below 10 % and a $\mathrm{TJ}_{\mathrm{ptp}}^{\mathrm{eq}}$ of below 250 fs which amounts to $3.3 \cdot 10^{-3}$ of the PRP. Stable ML is obtained in a current range from 790 mA to 870 mA. For not shown currents below 785 mA and not shown currents above 985 mA 3rd harmonic ML occurs. The reason for their occurrence will be addressed later. The hatched region indicates a continuous transition from fundamental to 3rd harmonic ML. In the stable range the minimum AJ amounts to $4 \cdot 10^{-4}$ and the lowest TJ amounts to 33 fs. Within this stable region the discontinuous increase of AJ at a current of 820 mA from $7 \cdot 10^{-4}$ to $1.4 \cdot 10^{-2}$ is also accompanied by a discontinuous drop of RR by a frequency difference of 9 MHz. For currents higher than 825 mA a gradual degradation of stability occurs. The local maximum of TJ at a current of 890 mA results from a dual RR signal.

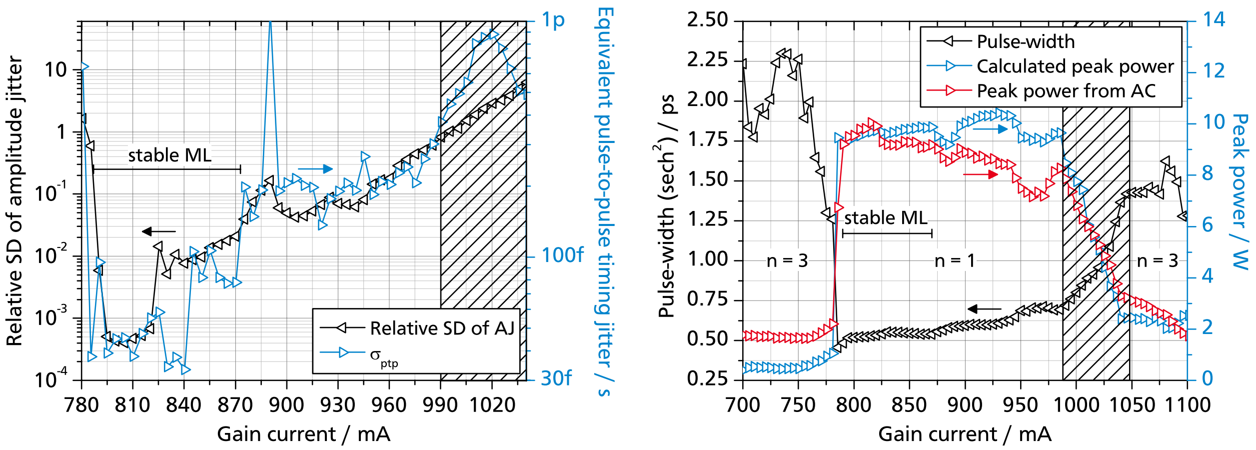

(a)

(b)

Figure 4.7: Experimentally obtained (a) relative SD of AJ and $\mathrm{TJ}_{\mathrm{ptp}}^{\mathrm{eq}}$ and (b) pulse-width (sech^2) and pulse peak power as an function of total gain current at an absorber voltage of −6.0 V. Hatched areas indicate a transition from fundamental ($n = 1$) to 3rd harmonic ML ($n = 3$). (Laser: do 2584 s4 d2)

Having quantified the stability of this MLL now the evolution of the pulse-width and peak power as a function of gain current can be presented and is shown in Fig. 4.7b. Hereby, an increased current span is displayed as compared to Figure 4.7a. For currents below 780 mA 3rd harmonic QS ML occurs with Q-switching (QS) frequencies at multiples of 1.3 GHz. Hereby, in the figure the letter n denotes the harmonic number of ML. At a current above 790 mA the reduction of AJ and TJ is also accompanied by a decrease of pulse-width down to a minimal value of 492 fs at a current value of 790 mA. In the current range from 790 mA to 985 mA fundamental ML occurs and the pulse-width stays below 540 fs within the stable regime up to 870 mA and only increases slightly at higher currents. The sub-pico-second pulse-width results in a high calculated peak power close to 10 W within the stable regime. The scaled relative peak power obtained from the auto-correlation signal well reflects the calculated peak power in the stable regime and is also satisfactory at higher currents. The decrease above 870 mA could be attributed to a systematic change in the beam shape or beam quality. Between 990 mA and 1045 mA a continuous transition from fundamental to unstable 3rd harmonic ML occurs indicated by the hatched area in the figure. Although the average power steadily increases with current, the peak power in the unstable 3rd harmonic ML regime amounts to less than a third of the fundamental peak power due to the redistribution of pulse energy. The mismatch of calculated and auto-correlation based relative peak power below a current of 780 mA can be attributed to QS. The calculated peak power represents a mean value whereby the modulated pulse envelope results in temporary higher pulse peak power which leads to a higher nonlinear efficiency of the second harmonic generation (SHG) process of the auto-correlator leading to a higher measured peak power.

The shortest pulse width is observed at a current of 790 mA and amounts to 492 fs with a peak power of 9.22 W, a TBP of 0.38 being 1.2 times the Fourier limit, an AJ of 0.6 % and a TJ_{ptp} of 95 fs. Fig. 4.8a shows the corresponding auto-correlation trace and the corresponding fit. The highest peak power is observed at a current of 870 mA and amounts to 9.87 W with a pulse-width of 540 fs, a TBP of 0.46 being 1.5 times the Fourier-Limit, an AJ of 2 % and a TJ_{ptp} of 78 fs.

Now the question is briefly addressed, why the MLL exhibits 3rd harmonic ML at currents above 1010 mA and below 790 mA. Harmonic ML is not observed for all the other tapered lasers. This can be understood by considering the peculiar geometry and biasing scheme as shown in Fig. 4.8b which shows a snapshot of 3rd harmonic ML. The delay or distance between subsequent pulses is equal. It is evident that counter propagating pulses meet exactly within the absorber and exhibit a colliding pulse effect. This increases bleaching of the absorber which further reduces losses. Therefore existence of 3 pulses instead of 2 is energetically favored for appropriate biasing conditions. This is possible because 2 pulses would not meet *exactly* within the absorber but in the middle of the cavity which is part of the tapered gain section. A multi section configuration was demonstrated in [145] which allows 7th harmonic ML by use of only one specifically located absorber.

Having presented the outstanding performance of this peculiar MLL one aspect needs verification. Both gain sections are electrically connected by means of an external electrical wire-bridge and driven by a single constant current source which should ideally apply the same voltage across both sections which theoretically leads to an identical current density. The resistance of the back section and the taper section for a total current of 790 mA and an identical voltage of 1.42 V yield values of 7.9 Ω and 2.3 Ω, respectively. Because this resistance is low the contacting and cable resistance can significantly influence the ratio of the current flowing through both sections. Therefore an identical current density through both section can *not* be guaranteed in the experiments. Using two separate current sources would be

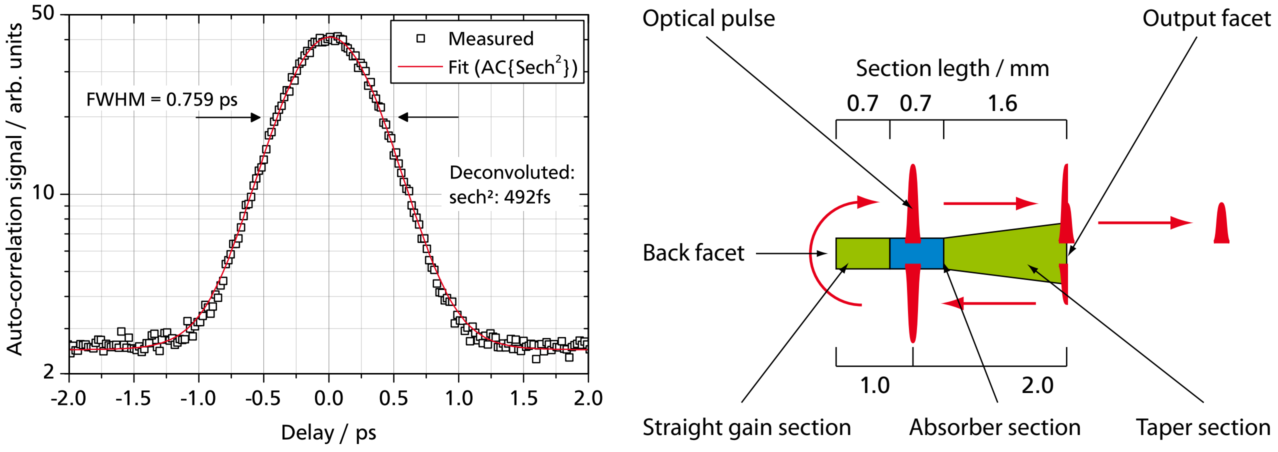

(a) (b)

Figure 4.8: (a) Experimentally obtained auto-correlation signal at a total gain current of 790 mA and an absorber voltage of −6.00 V. (b) Schematic representation of colliding-pulse assisted RR transition. (Laser: do 2584 s4 d2)

ideal in terms of precision of control but is practically not possible, because it is found that the active *area*, which must be known to be able to apply the correct current, does not correspond to the area defined by the mask. This may originate from the gain-guiding properties of the structure.

Thus, to exclude that such short pulse-width of below 500 fs is obtained by accident also inhomogeneous electrical pumping of both sections is investigated by using two separate current sources to identify the range of currents which allows stable ML operation. Fig 4.9 shows the minimum and maximum allowed taper current as a function of straight section current. Hereby a fixed straight section current was adjusted and the taper section current is increased. At straight section currents of 180 mA and below no stability is obtained. It can be observed, that a variety of current combinations allows for stable operation. Furthermore, the pulse-width for the lowest applied taper current is also given demonstrating that up to a straight section current of 190 mA the pulse-width stays below the reported value of 492 fs. Thus, the MLL is tolerant for deviating pumping conditions with respect to short pulse generation. In the figure the green bars indicate possible current combinations leading to a total current of 790 mA and 870 mA which define stability for single current source pumping according to Fig. 4.7b. Hereby the green arrow represents a possible single current source pumping path for results reported in Fig. 4.7b.

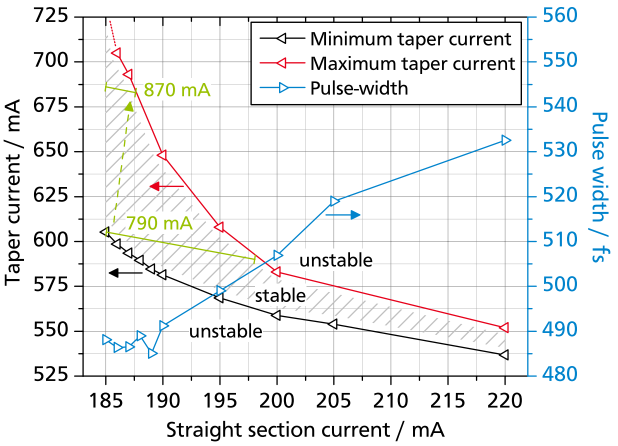

Figure 4.9: Lowest and highest possible taper current for a given straight section current allowing stable ML and the experimentally obtained pulse-width (sech^2) for the lowest taper current, both at an absorber voltage of −6.0 V. Green lines indicate possible combinations for a total current of 790 mA and 870 mA. Green arrow represents a possible single source pumping path for results reported in Fig. 4.7b. (Laser: do 2584 s4 d2)

4.2 Pulse amplification

In the previous section quantum-dot (QD) based tapered mode-locked laser (MLL) have been investigated yielding an highest peak power of almost 10 W at a repetition rate (RR) of 13.4 GHz, with a sub-picosecond pulse-width and excellent timing and amplitude stability for the MLL do 2584 s4 d2. However, the figure of merit (FOM) for the targeted 2$^{\text{nd}}$ order nonlinear imaging applications amounted to a low value of 0.64 W^2. Thus, in this section the amplification properties of tapered semiconductor optical amplifiers (SOAs) are investigated with a focus on improvements of peak power by amplification. Hereby, the target is to investigate the most simple and thus robust configuration namely a direct amplification setup without any dispersion management.

Indeed, the net output power of highly sophisticated semiconductor based systems is outstanding. The values in brackets given in the following take into account the corresponding correction factor to allow for a comparison of the results reported for different pulse shapes. In [21] at a wavelength of 975 nm a pulse width of 590 fs (sech^2 shape) and a peak power of 1.4 kW (1.23 kW) at a RR of 95 MHz was reported resulting in a FOM of 110 W^2 (85 W^2). This result was achieved by using an external cavity MLL, a preamplifier, a chirped pulse amplification scheme with an tapered amplifier realized by a tailored chirped Bragg grating and pulse compression. In [146] at a wavelength of 830 nm a pulse width of 660 fs (Lorentzian shape) and a peak power of 2.5 kW (1.59 kW) at a RR of 330 MHz is reported resulting in a FOM of 1361 W^2 (552 W^2). This result was achieved by a grating based chirped pulse amplification scheme. Although the performance of such all-semiconductor based systems is comparable to solid state based systems the complexity is also similar.

Simple and robust systems without dispersion management consequently offer reduced but significant output power characteristics. In [147] at a wavelength of 940 nm a pulse width of 4.2 ps (sech^2 shape) and a peak power of 28.1 W (24.8 W) at a RR of 2.5 GHz was reported leading to a FOM for 2nd order nonlinear imaging of 8.3 W^2 (6.5 W^2). This system just consists of a straight section external cavity MLL and a tapered SOA. In [134] at a wavelength of 1260 nm a pulse width of 10.6 ps (Lorentzian shape) and a usable peak power of 25.5 W (16.32 W) at a RR of 648 MHz was reported leading to a FOM of 4.6 W^2 (1.86 W^2). This system consists of a straight section bent waveguide external-cavity MLL and a tapered SOA. In this section an improvement of peak power and especially of the FOM is presented with respect to these reported results.

4.2.1 Tapered quantum-dot optical amplifiers

Tapered semiconductor optical amplifiers (SOAs) offer the same advantages as the tapered gain section of mode-locked laser (MLL). The tapered SOA shape has the effect of increasing the average modal area which leads to an increase of the gain saturation energy. This high saturation energy reduces pulse broadening originating from gain saturation and allows the amplification of pulses with increased power as compared to straight section SOAs. A narrow input section acts as a lateral mode filter forcing fundamental lateral mode amplification thus supporting good beam quality.

In order to determine the optimum tapered SOA geometry to achieve high amplification together with good beam quality, extensive simulations have been performed. The optimization included the investigation of various tapered waveguide shapes as well as the variation of the dimensions of these shapes. Modeling and optimization was carried out by *Semiconductor Integrated Optoelectronics and Photonics Group, Department of Electronics and Telecommunications, Politecnico di Torino, Italy* and *Optical Communications & Photonics Technology Group, Division of Communications and Signal Processing, National and Kapodistrian University of Athens, Greece* by means of a finite-difference beam propagation method (BPM) model. Hereby, combining the finite-difference BPM model with pre-calculated results obtained from multi-population rate-equation (MPRE) allows for consideration of saturation effects for gain and weakly index-guided SOA structures [140]. Hereby, approximations are made to reduce the computational cost of the model by considering amplification of continuous-wave (CW) emission with high input power leading to high gain saturation. Although using this approximation neglects the dynamical effects occurring for pulse amplification this approach still allows to evaluate the different geometries because dynamical effects do not depend on the geometry of the active medium. The most promising three geometries resulting from this numerical optimization process are depicted in Fig. 4.10.

Assuming an high CW input power of 32 mW it was found that structure (A) should exhibit a gain of 14.7 dB with a beam quality factor of 2.0, structure (F) should exhibit a gain of 16.4 dB with a beam quality factor of 1.8 and structure (G) should exhibit a gain of 15.2 dB with a beam quality factor of 1.4 at gain currents of 1.4 A, 2.1 A and 1.6 A, respectively. These different currents result from an identical applied current density and different active areas. These values correspond to a gain increase of +50 % for structure (F) and +12 % for structure (G) as compared to structure (A). The realized structures base on wafers fabricated by *Innolume GmbH, Germany* and are processed by *III-V Lab, France*. Eight working structures were fabricated and base on two different wafers. The structures composed of 10 layers of

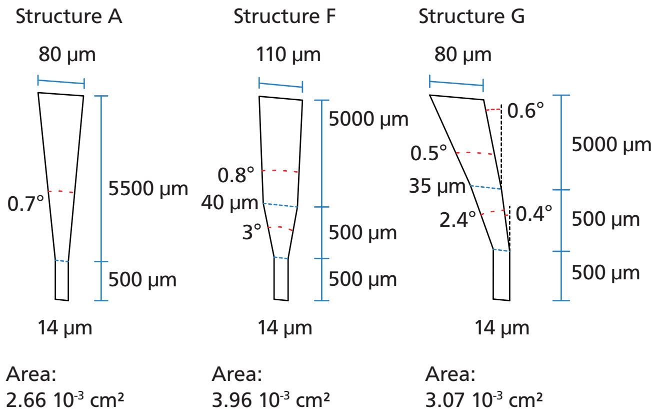

Figure 4.10: Schematics of the three proposed and realized geometries of the investigated SOAs. The shown geometries are not true to scale for sake of visibility. Blue dashed lines denote section borders. Red dashed curved lines denote full angles.

quantum-dots (QDs) (wafer do 2584) are denoted with A-318, A-108, A-133, F-216, F-85 and G-106. The structures composed of 15 layers of QDs (wafer do 1792) are denoted with F-452* and G-968*. In addition, weak index guiding has been introduced by etching in order to increase the lateral guiding for improving beam quality and amounts to an index difference of $\Delta n = 1 \cdot 10^{-4}$.

4.2.2 Measurement methods

For investigations of the amplification properties of the tapered semiconductor optical amplifiers (SOAs) the accurate estimation of the amplified output is essential. Hereby, the amount of the amplified spontaneous emission (ASE) in the SOA output stemming from the SOA itself has to be estimated. It is found and well known, that during amplification of continuous-wave (CW) emission by a SOA the ASE from the SOA decreases strongly with increasing input power. In this case for a significantly high input power all output power can be considered stemming from the amplified input power. This may not be the case for tapered SOAs due to a reduced confinement factor denoted by Γ in literature [71]. This non-ideal overlap of pumped regions of the SOA and the amplified electric field may result in residual ASE generated by pumped but not stimulated regions. Nevertheless, for the SOAs investigated here ASE during CW amplification is negligible. However, for amplification of optical pulses the non-existence of optical input power between pulses may allow the build-up of ASE which depends on the carrier dynamics and the corresponding time constants. In literature, in the case of pulse amplification most often the free-running ASE power of the SOA without input power is subtracted from the amplified output to obtain the usable amplified power [134]. However, this approximation may lead to a high underestimation of the amplified output power. For straight section SOAs an simple approach is initially suggested here for estimation of the ASE. Measuring the power of the ASE during amplification stemming from the *input* facet corresponds to the power of the ASE within the output of the SOA because of symmetry of emission. However, tapered SOA have spatially dependent gain due to the tapered section as well as beam direction dependent losses due to the refraction of the tapered section. Both effects break the symmetry and result in different ASE power from both facets in free-running operation as well as during amplification which prevents this simple evaluation method. Therefore, this convenient method for estimation of ASE can not be applied for tapered SOAs.

In [148] an estimation method was proposed which uses a narrow-band band-pass-filter to filter the amplified output of the SOA. It was found, that the mentioned approximation of subtracting the free-running ASE is indeed a huge underestimation and that the amplified output amounts to ≈90 % of the total output power which can be deduced from [148, Fig. 3]. Following this approach, in this work the optical spectrum of the SOA output is used as a basis to estimate the amplified output power as indicated in Fig. 4.11a. The figure shows the output spectrum of the SOA with a mode-locked laser (MLL) as input and with no input. Already here it is evident that not only CW input but also pulsed input significantly reduces the ASE.

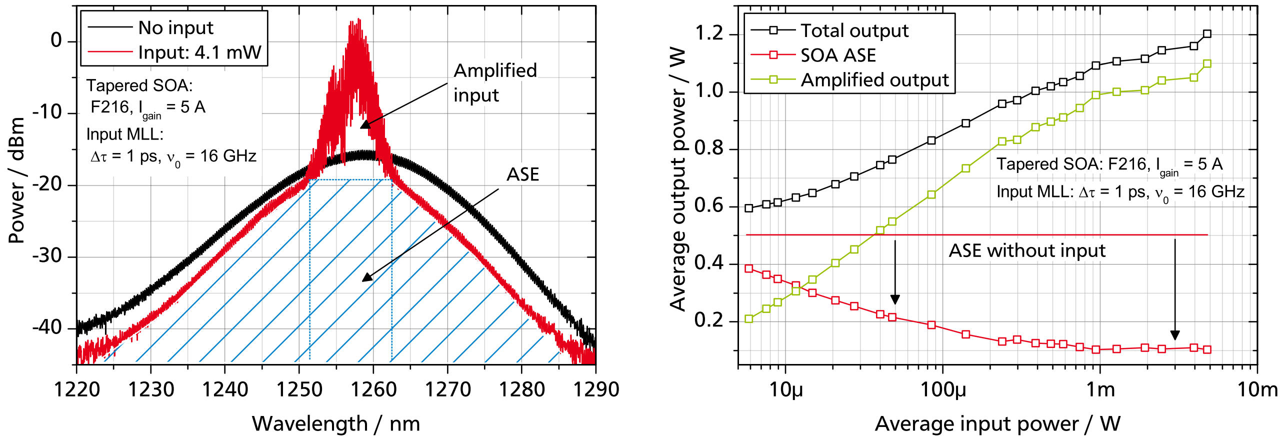

(a) (b)

Figure 4.11: Typical output characteristics of a tapered SOA (F-216) with a MLL as an input source. (a) Output spectrum used for evaluation of amplified output ratio. The blue hatched area indicates the assumed ASE part. (b) Composition of output power estimated by the spectral evaluation as a function of input power. Shown are the total output power, the ASE power stemming from the SOA and the amplified output power. Parameters are given in the figures.

To estimate the desired amplified output power the following approach is applied [12]. Hereby, the spectral parts which stem from the ASE are integrated outside the amplified part of the spectrum. The ASE which is underneath the amplified part is approximated by a linear trend defined by the values of the ASE power just outside the amplified part of the spectrum. The ratio of the total integral minus the sum of all ASE parts divided by the the total integral represents the ratio of amplified output power with respect to the total output power. This approach is verified by coupling a known value of power of a laser in one fiber and a known value of power of a free-running SOA, combining them by a 2x2 fiber splitter and performing the mentioned spectral evaluation on one of the output ports.

Additionally, Fig 4.11b shows the ASE power as well as the estimated usable amplified output as a function of average input power (free-space power, collimation losses not considered) with a MLL as input. The free-running ASE of the SOA is also given. It can be observed that the pulsed input significantly reduces the ASE power for high input power. This results from depletion of inversion within the SOA by stimulated emission used for amplification. This decrease of ASE is supported by the high repetition rate (RR) of the MLL. Anytime there is at least one or two pulses within the SOA. This prevents the SOA from full gain regeneration and thus the build-up of ASE. From this figure it is evident, that at the highest input power the usable amplified output power amounts to 92 % of the total output.

Also the estimation of input coupling efficiency is important. The following approach can be used for straight SOAs basing on mode matching considerations. Hereby a fiber, a collimation lens and a focusing lens to couple light into the SOA are necessary. First the input coupling has to be optimized by means of maximizing the amplified output power of the SOA. Subsequently, light has to be coupled in at the output facet and amplified in reverse direction, back into the used fiber. The ratio of power in the fiber and the power of the reversely collimated beam corresponds to the input coupling efficiency of the SOA in forward direction. Assuming Gaussian beams this is possible because the beam overlap integral, which is used for calculations of coupling efficiency, is symmetric with respect to a focal diameter ratio of 1-to-1 and amounts to an magnitude of 1 at this ratio. This means that for example as shown in Fig. 4.12 a ratio of 2 in forward direction has an identical coupling efficiency as compared to a ratio of 0.5 in reverse direction. However, due to the tapered section and the gain guiding properties of the tapered SOAs the resulting astigmatism and potentially non-ideal beam quality in reverse direction is expected to deteriorate this method. Thus, an exact number for input coupling can not be given.

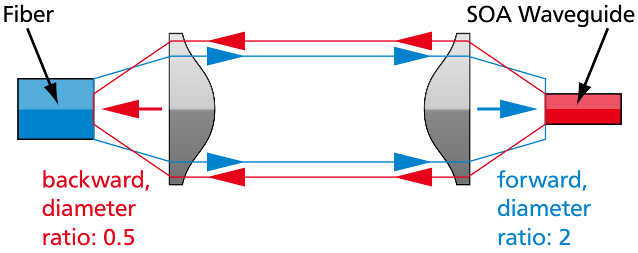

Figure 4.12: Schematic representation of the basic idea of coupling efficiency estimation by fiber coupling and reverse direction amplification.

The experimental setup for characterization of amplification properties is shown in Fig. 4.13a. The beam of the MLL used for amplification is collimated as reported in detail in section 2.3, passed through an optical isolator, variably attenuated, coupled into a single-mode fiber (6 m of smf-28), polarization adjusted, coupled out, passed through an optical isolator and coupled into the SOA by an aspherical lens. The output of the SOA has to be collimated by an aspherical lens and a cylindrical lens comparably to the MLL due to the tapered geometry. The output is passed through an isolator and to the diagnostics equipment.

Collimation of the beam of the SOAs comprises a peculiarity. The SOAs output facets are tilted with respect to the waveguide by 7° to reduce facet feedback resulting in a beam output angle of 17° with respect to the waveguide as indicated in Fig. 4.13b. The required cylindrical lens for slow axis collimation after the aspherical collimation lens is omitted in the figure. In the upper part of the figure the common collimation configuration is depicted whereby the axis of the divergent output beam coincides with the

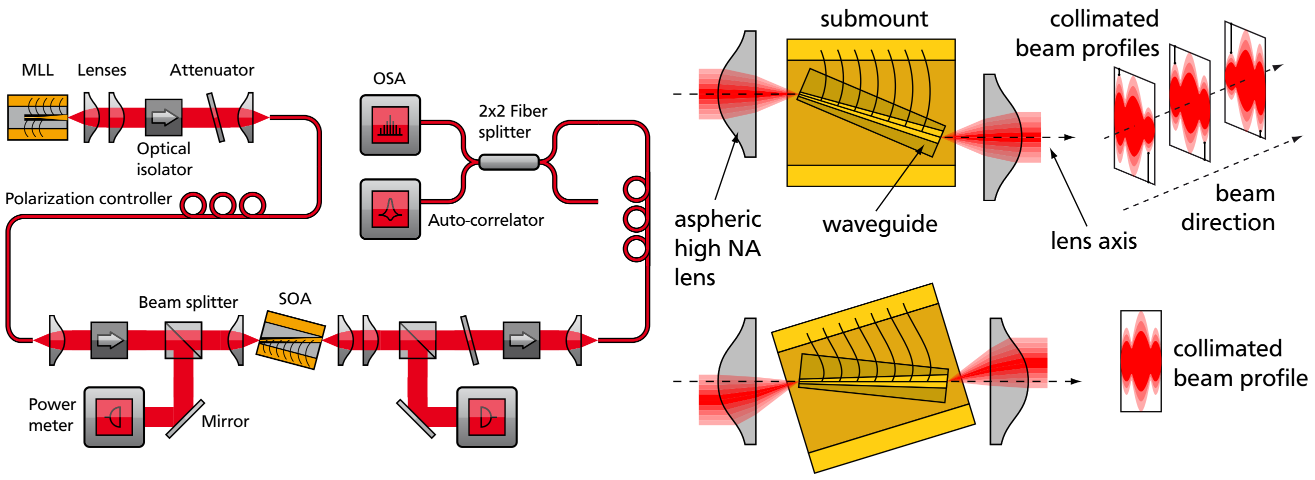

(a) (b)

Figure 4.13: (a) Scheme of experimental characterization setup. (b) Output beam collimation schemes. The upper part shows the common configuration, which however does not allow complete collimation here. Hereby, the lens axis coincides with the output beam axis. The lower part shows a configuration which allows complete collimation. Hereby, the lens axis coincides with the waveguide axis [12].

collimation lens axis. Hereby, no complete collimation can be achieved. If the vertical slice of the center of the beam profile is collimated the left vertical slice exhibits a focus while the right vertical slice diverges as shown in the figure. In [150] calculations for straight tilted SOAs were performed by vector wave optics and could reproduce the far-field beam distortions observed in experiment originating from phase distortions. It was suggested that using an off-axis ball lens could reduce beam distortions. Following this suggestion for tapered SOAs, the geometry in the lower part of Fig. 4.13b is implemented. Hereby, the lens axis coincides with the waveguide axis and not with the output beam axis. This configuration allows for a complete beam collimation [12]. The remaining exemplary three-lobe beam profile is expected to stem from the gain guiding properties of the SOA [151].

4.2.3 Results and discussion

For investigations of amplification properties and demonstration of high peak power amplification a monolithic tapered mode-locked laser (MLL) with a high repetition rate (RR) is selected. This offers two advantages. First, the tapered MLL offers the potential of a high output power, thus no preamplifier is necessary and input coupling optimization is not vital. Second, the high RR of a monolithic MLL offers the potential for a large figure of merit (FOM) according to Eq. (2.4). The source MLL is do 2584 s1b a6 and is operated at an absorber voltage of −6.0 V and a gain current of 590 mA. Due to fiber dispersion the pulse width increases from 0.8 ps to 1.0 ps. The RR amounts to 16 GHz and the average optical power amounts to 6 mW leading to an input peak power of 353 mW. As evident from Fig. 4.11b the semiconductor optical amplifier (SOA) is already strongly saturated. From this figure the corresponding free-space gain[6] of this SOA (F-216) at a gain current of 5 A amounts to 44.5 dB, 38.3 dB, 30 dB and 20 dB for an average free-space input power of 10 μW, 100 μW, 1 mW and 10 mW respectively. Thus further increase of input power is not that beneficial any more.

The experimentally obtained amplification results for the eight investigated different tapered SOAs are shown in Fig. 4.14. First, Fig. 4.14a displays the average amplified output power as a function of SOA gain current. Structures (A) show the highest output power for currents below 2.5 A but they exhibit a strong output power saturation as a function of gain current. The results of the three structures exhibit some spread. Structures (F) show the lowest output power at currents below 2.5 A but show a steady and nearly unsaturated power increase. The results of these three structures exhibit low spread. The output power trend for structures (G) lies in between the two other structures. As mentioned in subsection 4.2.1 simulations predicted a continuous-wave (CW) gain increase of +50 % for structure (F) and +12 % for structure (G) as compared to structure (A) which holds true for a high current of 5 A. Structures (A) exhibit the highest free-space average power gain of 21.8 dB leading to an average power of 0.9 W.

Fig. 4.14b shows the output pulse-width as a function of SOA gain current. Prominently, the pulse width increases as a function of gain current which is attributed to pulse broadening due to gain saturation or due to increasing spectral broadening by self phase modulation (SPM) [152] together with material dispersion. Indeed, the typical SPM characteristics are evident in the optical spectrum shown in Fig. 4.11a. Here, a clear statement of structure-dependent trends is difficult to be given. All structures show similar trends but also some minor spread. Extrapolating all the pulse-widths towards a gain current of 0 A leads to a value above 1.1 ps which is higher than the input pulse width of 1.0 ps. This constant broadening is attributed to material dispersion.

Fig. 4.14c shows the output peak power as a function of SOA gain current. The pulse-width has a minor impact on the peak power. The average power and thus the gain properties of the structures dominate the peak power. Structures (F) demonstrate a peak power around 35 W at the highest applied gain current [12]. Furthermore, structures (A) exhibit the strongest and structures (F) show the lowest saturation trend. Indeed, the latter allow higher values of peak power of up to 42 W at an elevated gain current of 7 A [10].

Finally, Fig. 4.14d shows the FOM for 2nd order nonlinear imaging as a function of SOA gain current. The square dependence of the FOM on the peak power results in a stronger separation of the results at higher gain currents. Hereby, structures (F) offer the highest FOM of 30 W^2 for the targeted application.

---

[6] Free-space gain is defined as the ratio of amplified output power to input power while disregarding coupling losses.

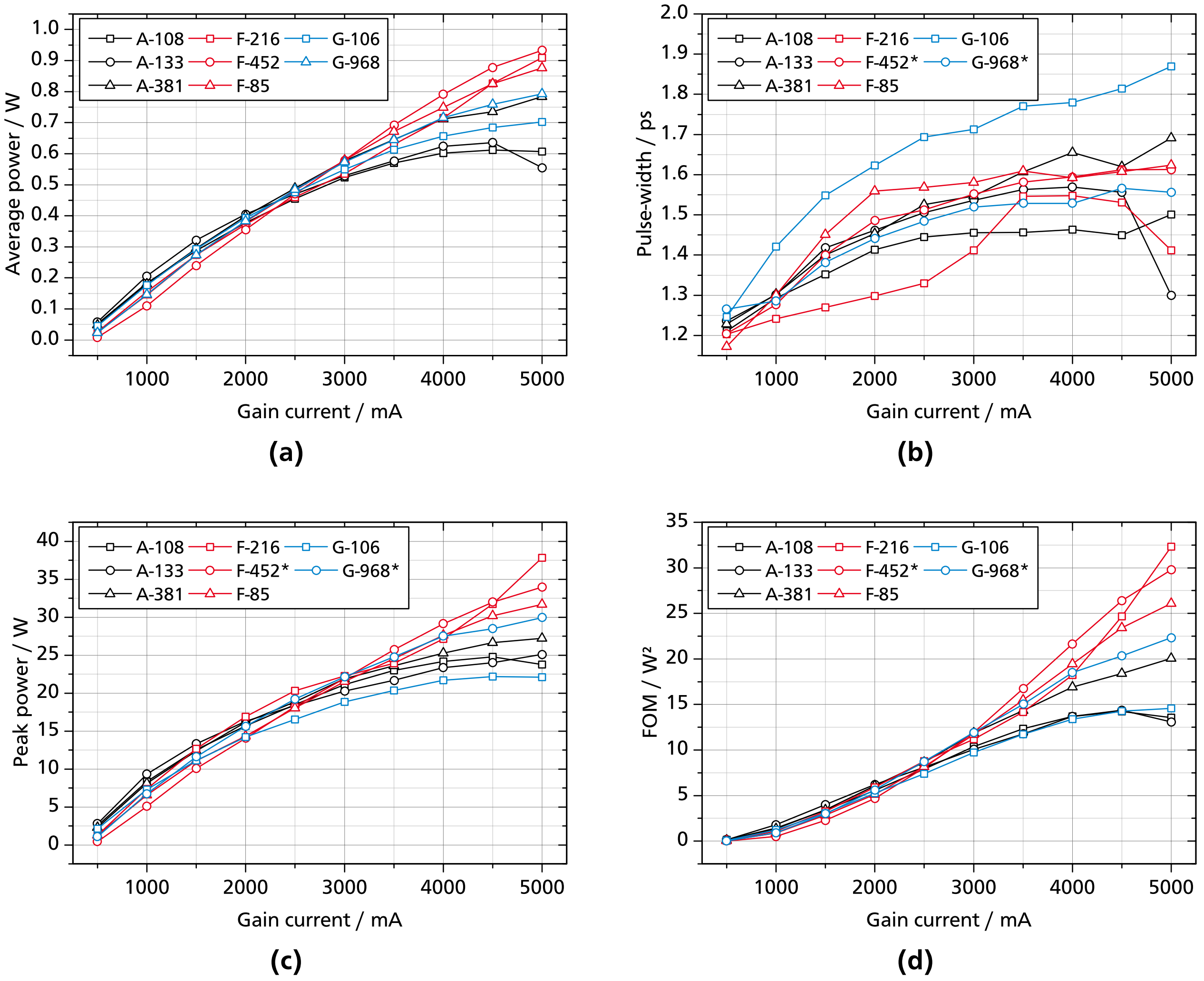

Figure 4.14: (a) Amplified average output power (b) pulse-width (Gaussian shape) (c) peak power and (d) FOM for all investigated tapered SOAs as a function of SOA gain current. Correction factor for peak power and FOM are considered.

4.3 Conclusion

In summary, tapered mode-locked laser (MLL) have been extensively investigated with an emphasis on mode locking (ML) stability regions with respect to timing jitter (TJ) and amplitude jitter (AJ) which is hardly addressed in literature. Although it can be said that the investigated MLL exhibit ML operation in a very wide range of gain currents and absorber voltages *stable* ML is obtained in a significantly reduced operation range only.

Here, it is found that the passive electrical stabilization demonstrated in chapter 3 is beneficial with respect to ML stability with various extent for all the investigated MLL. The most powerful MLL does not show any ML operation without the stabilization.

The shortest pulse width of 492 fs ($sech^2$ shape) and the highest peak power of 9.87 W, which corresponds to 11.2 W without correction (see Eq. (2.2)), are observed for a tapered MLL which exhibits an absorber section length to gain section length ratio (AGLR) of 0.44 and a total length of 3 mm (laser: do 2584 s4 d2). Hereby, not the back-facet section is used as an absorber but an intermediate section in the middle of the laser. In this configuration pulse generation is not assisted by colliding pulse effects at the back facet thus allowing for an increased AGLR. Such high AGLR does does not allow ML operation if the back-facet section is used as an absorber. This lowest observed pulse width is attributed to this elevated AGLR.

Although an excellent peak-power of almost 10 W is observed for a monolithic tapered MLL, to access high figure of merit (FOM) for the targeted 2nd order nonlinear imaging applications subsequent amplification is necessary which is pursued by investigations of amplification properties of tapered semiconductor optical amplifiers (SOAs). Hereby, a simple reliable method is presented to estimate the usable amplified power within the total output power which also contains amplified spontaneous emission (ASE) stemming from the SOA itself. It is found that not only for amplification of continuous-wave (CW) input but also for pulsed input the ASE stemming from the SOA is strongly reduced for sufficiently high input power.

Using a tapered MLL with 1 ps pulse-width and a repetition rate (RR) of 16 GHz as input, these novel tapered quantum-dot (QD) based SOAs offer high amplification leading to a peak power in the 35 W range as well as a FOM of 30 W^2 for immediate application potential in the targeted applications.

Having investigated and demonstrated the excellent performance of QD based MLLs and SOAs now, in the following chapter additional all-optical methods for reduction of TJ are investigated and in particular a simple but capable model is developed which unveils a common physical mechanism of all these different investigated techniques.

5 Timing jitter control of mode-locked lasers: Experiment and simulation

> Remember kids, the only difference between screwing around and science is writing it down.
>
> Adam Savage, host in Mythbusters (Science entertainment television program)

Ultra-fast mode-locked laser (MLL) oscillators are very capable low-noise optical and microwave signal sources and important for various time-critical applications including optical sampling, clock recovery and optical comb generation [42, 154–156]. The timing stability of the optical pulse train of a MLL is highly important for these applications. Solid-state and fiber MLL with pulse-widths in the femtosecond range offer ultra-low timing jitter (TJ) [157] enabling most demanding applications including ultra-low sampling-jitter photonic analog-to-digital converters [158]. Semiconductor based monolithic passively MLL operating at high repetition rates (RRs) and with pulse-widths in the pico-second and sub-pico-second range are promising candidates for these applications by offering multiple advantages including compact size, simple fabrication and the ability for hybrid integration to silicon substrates. Hereby, quantum-dot (QD) based MLL offer low threshold current density and reduced spontaneous emission rates due to higher efficiency of population inversion as compared to semiconductor lasers (SCLs) with a bulk or quantum-well (QW) based active medium leading to reduced noise [77]. However, the high TJ of the optical pulse-train as compared to solid-state lasers (SSLs) is the main drawback of such monolithic semiconductor passively MLLs. It results from a non-stationary origin but is in particular highly dependent on various laser parameters including pulse width, pulse energy and repetition rate which was the subject of theoretical investigations in [105, 106, 110, 159]. For a semiconductor MLL without additional instabilities the TJ is dominant and amplitude jitter (AJ) can be neglected [51].

To circumvent the negative issue of the high TJ of monolithic semiconductor passively MLL, different schemes for TJ reduction have been proposed in literature. These cover synchronization to an electric reference oscillator by direct electric modulation [160–162], by exploitation of a phase-locked loop [154, 163, 164] or by exploitation of an opto-electrical feedback (OE FB) approach [6, 50, 166]. An alternative all-optical approach was demonstrated by means of a long delay all-optical feedback (AO FB) scheme in [51–54, 167, 168]. The AO FB scheme was also subject of theoretical investigations for short delays in [169, 170] and subject of numerical simulation for long delays in [57]. Hereby, long delay AO FB is in principle substantially different as compared to short delay AO FB. However, an explanation of the origin of the TJ reduction for AO FB and its theoretical understanding is still pending.

In fact, investigations of TJ of semiconductor MLLs and various schemes of stabilization are of constant interest in very recent scientific research [171, 172]. Thus, in this chapter the TJ of a pulse train of a semiconductor MLL is explored and various schemes for timing stabilization are systematically and consecutively investigated in experiments. In particular a numerical model is presented which allows for a comprehensive understanding of the TJ. With respect to modeling of mode locking (ML) A. G. Vladimirov stated [173]: '*Although the direct numerical simulations are, in principle, capable to reproduce experimental data, they give only little insight into the physical mechanisms involved.*' This is circumvented in the presented model here because it only includes one single proposed mechanism. One important objective of this chapter is to identify and quantify the mechanism responsible for TJ reduction of a passively MLL in the case of self and external pulse train injection, namely for the widespread AO FB and the optical pulse train injection (OPTI) configuration.

To develop an understanding a consecutive approach of experiments together with simulations is chosen. First, a free-running passively MLL is investigated allowing to give an impression of typical free-running behavior. Then, a hybrid mode-locking (HML) configuration will be investigated because it represents the most direct way to control the TJ and the underlying mechanism responsible for TJ control is known [174]. In addition the comparison of experimental and simulation results of HML is used to allow for a calibration of the parameters used for subsequent simulation of the OE FB configuration. This OE FB scheme represents a hybrid approach of TJ control by using optical detection and electrical interaction. The OE FB configuration is selected for investigation for two reasons: On the one hand, it is a feedback (FB) scheme like the targeted AO FB configuration but on the other hand it shares the known physical TJ control mechanism with the HML configuration because it bases on electrical modulation [174]. In fact, it will be shown, that the OE FB configuration and the AO FB configuration exhibit almost identical TJ characteristics thus indicating a common origin of the TJ reduction. Then, the AO FB configuration which can be regarded as *self* pulse train injection is consequently replaced by *external* pulse train injection (OPTI) by means of a master MLL. Here the term OPTI is used to emphasize the role of the timing interaction of the pulses of master and slave MLL and to distinguish from common continuous-wave (CW) injection. In such a way locking of the TJ characteristics of the slave MLL to the master MLL is achieved. Simulation results of the TJ are in good agreement with the measurement results for all investigated configurations and finally allow to identify and quantify the mechanism responsible for TJ reduction [5]. Based on this knowledge the AO FB is then extended towards a *dual* AO FB scheme in simulations and further numerical studies are preformed allowing to predict parameter dependencies. These results of these studies suggest a novel way to investigate dynamical properties of a MLL.

First, in section 5.1 the MLL under investigation is described and the experimental setups are introduced including the HML configuration, the OE FB configuration, the AO FB configuration and the OPTI configuration by means of a master MLL. Then, in section 5.2 the methods of experimental estimation of TJ are briefly outlined. In section 5.3 the simple model for description of TJ for all the investigated configurations is presented. In section 5.4 the obtained experimental measurement results and simulation results are presented, discussed and explanations for these results are given. Finally in section 5.5 the summary is presented and conclusions are drawn.

5.1 Devices and experimental setups

The passively mode-locked laser (MLL) under investigation (do 1791 e1) is a multi-section quantum-dot (QD) based semiconductor laser consisting of 5 InGaAs QD layers separated by GaAs barriers with a total cavity length of 8 mm resulting in a repetition rate (RR) of 5.06 GHz which allows to estimate a group velocity index of 3.70. The waveguide consists of a sequence of absorber and gain sections. This peculiar multi-section configuration does not play a role for the investigations conducted here because the widespread two-section configuration is also investigated here and is not found to exhibit different behavior. The gain sections are pumped by a DC current and a reverse bias voltage is applied to the absorber sections. The total absorber length amounts to 11 % of the total length. The output facet is anti-reflection coated with a reflectivity of 10 % whereas the back facet is high-reflection coated with a reflectivity of 99 %. The waveguide has a width of 4 μm and a height of 1 μm. For all timing jitter (TJ) control experiments identical driving conditions of the MLL were maintained resulting in an optical average power (P_{opt}) of 2.5 mW, a pulse width of 4 ps, a spectral width of 3.5 nm and an output pulse energy of 0.49 pJ. According to the dependence of quantum limited TJ on pulse width, pulse energy and RR as explained in sub-section 2.4.3 a relatively high value of TJ is expected for the investigated MLL and amounts to a pulse-to-pulse timing jitter (TJ_{ptp}) of 152 fs for this selected condition according to Eq. (2.8) (on page 28) and using the measured RR line-width of 18.8 kHz.

The following four experimental schemes including hybrid mode-locking (HML), mode locking (ML) subject to opto-electrical feedback (OE FB), ML subject to all-optical feedback (AO FB), and ML subject to optical pulse train injection (OPTI) were implemented for investigations as already mentioned in the previous section.

- HML is commonly implemented by modulating the absorber with a frequency corresponding to the RR of the MLL by means of a bias-T and a frequency synthesizer as shown in the left part of Fig. 5.1 (c). Here, no impedance matching measures of the MLL and the electrical system were taken.

- To implement the OE FB shown in Fig. 5.1 (a), a part of the output beam of the MLL is coupled into a fast photo-detector via a long optical fiber, is amplified, delayed and subsequently applied to the absorber section by means of a bias-T. The total round-trip delay length of the OE FB amounts to 28.1 m (in vacuum) which corresponds to a frequency of 10.7 MHz. The bandwidth of the electrical system covers only the RR of the MLL.

- The AO FB configuration is implemented as shown in Fig. 5.1 (b). There, a part of the output beam is coupled into a long fiber, reflected back by means of a mirror, polarization aligned, and redirected into the MLL. Hereby, the AO FB delay length is treated as a sum of a *macroscopic* delay length in the meter range realized by long optical fibers and a *microscopic* fine-delay length in the micrometer range realized by the mirror mounted on a translation stage. This microscopic delay is used to match the total AO FB delay and multiples of the pulse repetition period (PRP).

The macroscopic round-trip length of the AO FB external-cavity amounts to 31.8 m (in vacuum) corresponding to a frequency of 9.4 MHz or 538 pulses. The optical feedback (FB) ratio is defined as the inverse ratio of P_{opt} to the returning optical power excluding coupling losses.

- The OPTI setup is depicted in Fig. 5.1 (c). The output beam of the master MLL is coupled into a fiber, polarization aligned, variably attenuated and coupled into the slave MLL. The master MLL is identical to the slave MLL in terms of specifications, however it does not exhibit sufficiently similar RR and is therefore hybridly mode-locked to match the RR of the slave MLL.

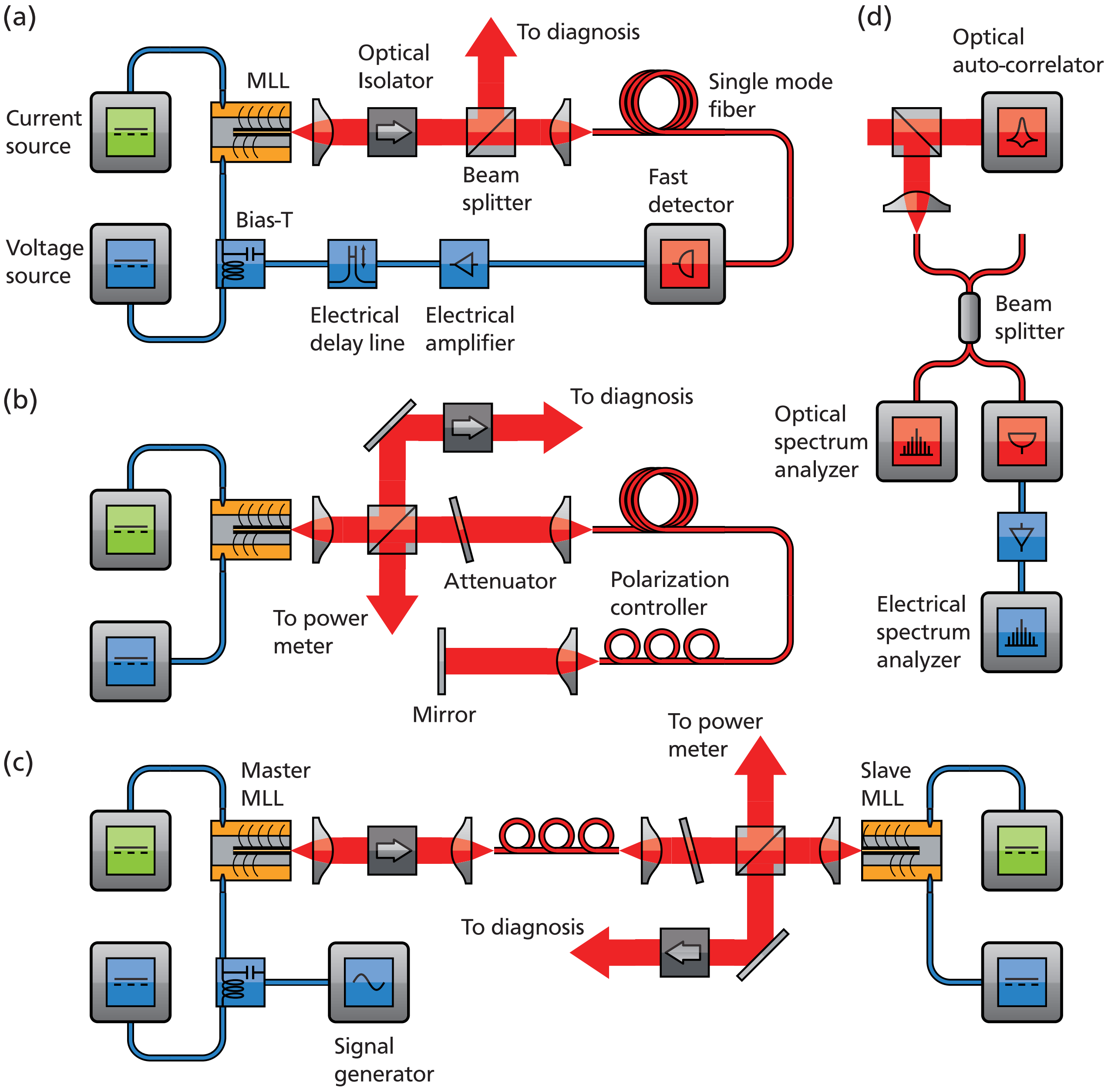

Figure 5.1: Schematics of experimental setups depicting (a) the OE FB, (b) the AO FB and (c) the OPTI scheme including HML of the master laser. (d) Emission diagnosis equipment.

The frequency-domain distribution of timing jitter (TJ) is represented by the corresponding timing phase noise power spectral density (TPN PSD) and the experimental estimation of TPN PSD bases on a well-known method by von der Linde developed for actively mode-locked laser (MLL) [99] which has been also described in sub-section 2.4.2. The power spectrum $P(f)$ of the instantaneous optical output power of the MLL is measured by means of an optical high-frequency detector and a high-frequency electrical spectrum analyzer (ESA) and evaluated. The method is well applicable to MLL exhibiting a significant amount of TJ. However, ultra-low noise MLLs require a different method which is not limited by the noise of the electrical components [175]. According to [99, 100] and assuming only timing fluctuations the (single-sided) TPN PSD $L_\psi(f)$ is then given in experiment by

$$L_\psi(f) = \frac{P(f-\nu_0)}{RBW \cdot P_{\text{tot}}} \quad \text{with} \quad P_{\text{tot}} = \int P(f)/RBW\,df \tag{5.1}$$

with ν_0 being the frequency of the repetition rate (RR) line, P_{tot} the total integrated power of the RR line [176] and RBW the used resolution bandwidth. It is evident, that $L_\psi(f)$ is a normalized power spectrum $P(f)$. Instead of integration of the power spectral density (PSD) to obtain P_{tot}, alternatively, the peak power obtained using a resolution bandwidth (RBW) much wider than the RR line-width could also be used. This integrated P_{tot} corresponds to the so called carrier power of an actively driven oscillating system. In the measurements, the total TPN PSD is composed of multiple separately measured aligned spectra each covering one order of frequency offset range. The final spectrum is obtained by averaging 10 measured spectra in linear space with the detection mode of the ESA set to sample-mode. The widely reported integrated timing jitter ($\text{TJ}_{\text{int}}^{(f_1,f_2)}$) (also called root mean square (RMS) TJ) can be obtained from the TPN PSD $L_\psi(f)$ by Eq. (2.7) (on page 27).

However, this TPN PSD estimation method is only partially valid for passively MLL as pointed out by [105, 106] and shown in sub-section 2.4.2. The so measured TPN PSD has a finite value at zero Hz, however an infinite value is expected because for low frequencies, which correspond to long time-scales, a free-running oscillator tends to accumulate unbounded timing deviation [105]. However, calculating $\text{TJ}_{\text{int}}^{(f_1,f_2)}$ for a frequency offset from zero to half of the RR (also called the Nyquist frequency) from the measured TPN PSD yields a finite and constant value for $\text{TJ}_{\text{int}}^{(f_1,f_2)}$ which is independent of the RR line-width or independent of the equivalent TJ. Using these integration limits demonstrates the limitation of equation (5.1) for passively MLL.

Intuitively, the RR line-width represents a measure of the TJ for passively MLL. Therefore a tailored measure of TJ namely the pulse-to-pulse timing jitter (TJ_{ptp}) and the corresponding estimation method was proposed specifically addressing free-running passively MLL [98]. The parameter TJ_{ptp} describes the

RMS pulse-to-pulse timing deviation from the mean timing period. There, the TPN PSD $L_{\psi}(f)$ and the TJ_{ptp} are obtained by

$$L_{\psi}(f) = \frac{\Delta \nu}{2\pi f^2} \tag{5.2}$$

$$\sigma_{ptp} = \frac{1}{\nu_0}\left[\frac{\Delta \nu}{2\pi \nu_0}\right]^{0.5} \tag{5.3}$$

with $\Delta \nu$ being the RR line-width. These equations have also been derived in sub-section 2.4.2. Based on this relation it is emphasized, that for passively MLL the TJ_{ptp} and the RR line-width are equivalent and a fully sufficient measures for TJ if no additional instabilities are existent. Fig. 5.2 shows calculated TPN PSDs for various RR line-widths and thus TJ magnitudes. Plots (A) are obtained using equation (5.1) and a Lorentzian shaped RR line and plots (B) using equation (5.2). As plots (B) represent the correct TPN PSD for a passively MLL it can be seen that the evaluation based on equation (5.1) is only valid for frequency offsets well above the RR line-width. It is essential to be aware of this limitation when performing TPN PSD measurements of passively MLL, because calculating $\text{TJ}_{\text{int}}^{(f_1,f_2)}$ for a frequency integration range starting below the RR-line width would lead to a significant underestimation of the TJ. It must be noted, that the evaluation based on [99] additionally allows to estimate the amplitude jitter (AJ) PSD but only if AJ and TJ are uncorrelated.

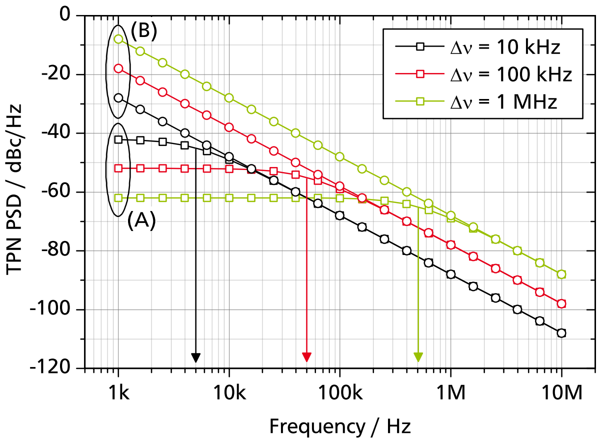

Figure 5.2: Calculated TPN PSD for different RR line-widths. Plots (A) are obtained by equation (5.1) and (B) obtained by equation (5.2). The arrows indicate the corresponding width of the RR.

5.3 Model description

In the following a simple model will be presented which in particular addresses the dynamics of timing jitter (TJ) subject to time-delayed feedback (FB) and synchronization to an external modulation or external pulse-train injection. It is meant to provide a simplified insight into the mechanisms governing the external control of TJ. Up to now, several specialized models were developed covering the dynamics of monolithic passively mode-locked laser (MLL) [69, 93, 159, 173, 177]. The effects of all-optical feedback (AO FB) on dynamics of MLL were numerically studied for short delay times in [169, 170, 178].

Long delay AO FB, which is substantially different from short delay FB, was numerically studied in [57] but still offers room for numerical and experimental investigations. Here, a simple model is presented specifically addressing TJ for all the presented different configurations which allows to reproduce the experimentally obtained timing phase noise power spectral density (TPN PSD) with good agreement.

It is advantageous to utilize a reduced and problem-oriented description of the investigated system in contrast to a highly complex and powerful modeling approach. A reduced description allows to clearly identify origins for observed effects and to understand the system behavior more easily. In the worst case, a highly sophisticated model perfectly reproducing experimental results does not guarantee a gain of understanding. Even a significant mismatch of experimental and simulation results might be beneficial as it allows to exclude the origins of effects only observed in experiment. Hereby, a numerical approach was chosen. Compared to an analytical approach it offers the advantage of high flexibility and easy extensibility as well as a simple implementation. Due to its simplicity it is able to access very long delays in the AO FB configuration. Indeed, simulated timescales in the order of 10 μs and more still require a high amount of computation time for sophisticated models.

The basic idea is to consider a MLL as a free-running oscillator subject to uncorrelated timing noise, namely the optical pulse oscillating in the laser cavity and exhibiting timing deviations within each round trip. One of the main sources of timing noise is amplified spontaneous emission (ASE) directly coupling to the optical pulse [105, 106, 174, 177] which was also discussed in sub-section 2.4.3. This spontaneous emission is uncorrelated and thus white in frequency. After each round-trip the timing deviation is accumulated leading to a random walk or if regarded continuously to a Wiener process. Numerically [44, 159] or analytically [105] applying such a series of accumulated timing deviations to an ideal equidistant optical pulse train directly leads to a repetition rate (RR) mode comb, Lorentzian shaped RR lines (see also sub-section 2.4.2) and the well-known dependence of the experimentally obtained TPN PSD on the squared harmonic-number of the investigated RR line in the case of absence of amplitude jitter as experimentally shown in [54]. This dependence is valid for all kinds of timing noise or frequency modulation. Not only MLLs but also free-running optoelectronic microwave oscillators are subject to a random walk [179]. In the presented model only the timing of the pulses is considered as a variable. Changes of optical power, pulse width or shape are not considered and are regarded as constant. Therefore this modeling may be regarded as a linearization around the free running condition for small perturbations.

Now, the hypothesis of the **mechanism responsible for the TJ reduction** will be outlined. A convenient form of controlling TJ is possible by hybrid mode-locking (HML). It affects the timing of the intra-cavity pulse directly by modulation of the absorber section [174] with a frequency corresponding to the RR. This modulation may be viewed as a continuous gating of the intra-cavity pulse. Also for the opto-electrical feedback (OE FB) configuration the optically detected pulse train is transformed to an electrical signal which in turn modulates the absorber section. This time-delayed self-modulation influences the timing of the intra-cavity pulse. It therefore represents an interaction of the timing of intra-cavity pulse and delayed FB pulse. Based on these two schemes now for the AO FB configuration an interaction of the timing of intra-cavity pulse and the returning FB pulse is assumed and could be explained by means of the MLL gain and absorption dynamics. Another possibility would be an interaction based on interference [180]. Such an timing interaction is expected to lead to an averaged timing per round-trip which was initially proposed in [53]. It is assumed, that purely statistical effects are responsible for reduction of TJ in the case of AO FB.

Despite the assumed timing-interaction the **basic idea of the statistical effect** is outlined by the following inequalities. Assuming $\Gamma_i(N)$ is a sequence of random numbers and $\langle\rangle_N$ denotes the averaging with respect to the index N Eq. (5.4) shows that the average of two independent sequences of random numbers has a smaller variance than one single sequence of random numbers.

$$\left\langle \left(\Gamma_i(N)\right)^2 \right\rangle_N > \left\langle \left(\frac{\Gamma_1(N) + \Gamma_2(N)}{2} \right)^2 \right\rangle_N \tag{5.4}$$

Hereby the left term represents a free-running MLL and the right term represents a locking of one MLL laser to another *independent* MLL. The averaging operation represents the timing interactions. The idea of the statistical influence of FB has to be described by one single sequence of random numbers as shown in Eq. (5.4).

$$\left\langle \left(\Gamma_i(N)\right)^2 \right\rangle_N \geq \left\langle \left(\frac{\Gamma_i(N) + \Gamma_i(N - N_d)}{2} \right)^2 \right\rangle_N \geq \left\langle \left(\frac{\Gamma_1(N) + \Gamma_2(N)}{2} \right)^2 \right\rangle_N \tag{5.5}$$

The middle term represents the system under FB operation. Hereby, $\Gamma_i(N - N_d)$ belongs to the same ensemble or sequence as $\Gamma_i(N)$ but is only delayed by N_d with respect to N. If N_d is zero then the middle term trivially equals the left term. Depending on the statistical properties of $\Gamma_i(N)$ and the value of N_d the value of the middle term may be equal to the left term or the right term or lie in between. Assuming $\Gamma_i(N)$ represents white noise then the middle term will be equal to the right term for $N_d > 0$ because the auto-correlation of white noise is only non-zero for $N = 0$. Now, assuming that an auto-correlation of $\Gamma_i(N)$ exists for $N_d > 0$ and decreases for increasing N_d, which is the case for a random walk, the middle term will converge to the right term for increasing N_d. The middle term will be equal to the right term for $N_d = \infty$ because $\Gamma_i(N)$ and $\Gamma_i(N - N_d)$ will be completely uncorrelated. Therefore increasing N_d increases the statistical independence of $\Gamma_i(N)$ and $\Gamma_i(N - N_d)$. Already here it is evident, that a high value of N_d corresponding to a high delay time is desirable to minimize the variance. In addition, it is evident, that a fundamental limit exists which is represented by the right term. However, it is emphasized, that these equations just represent statistical approximations and do not represent differential-equations of a real dynamical closed-loop system because all $\Gamma_i(N)$ do not depend on each other, therefore such a limit might not be observed in experiment or in simulations.

For numerical investigations a time-domain approach is chosen instead of a frequency-domain approach because it is more comprehensive. The timing dynamics of the pulse of the MLL is implemented by a numerical finite-difference approach with the time interval corresponding to the inverse mean RR of the MLL [103] or in other words by discretized differential equations. The time variable utilized for numerical modeling is the timing *deviation* $T(n)$ of a pulse n with respect to an ideal pulse train with an period corresponding to the inverse RR. The timing deviation $T(n)$ is therefore defined as

$$T(n) = t_n - n \cdot \frac{1}{\nu_0} \tag{5.6}$$

with t_n being the absolute timing of the pulse n and ν_0 being the RR. The choice of the timing deviation $T(n)$ for a fixed time but variable pulse number n allows for a convenient and direct formulation of discrete difference equations of the timing evolution of a pulse train. A numerical approach was chosen instead of an analytical approach for two reasons. First, a numerical approach is easily extendible and second, in the case of FB a delay-term is required which complicates the determination of an analytical solution.

Now, the **discretized differential equations** for each investigated configuration will be introduced. These phenomenologically defined equations describe the discretized time evolution of the timing deviations $T(n)$ of the optical pulses with respect to the inverse RR.

- The timing of a free-running MLL is described by a random walk process with white noise being the noise source and is represented by Eq. (5.7).

  $$T(n+1) = T(n) + \sigma_{\mathrm{ptp}}\Gamma \tag{5.7}$$

  Hereby, σ_{ptp} denotes directly the pulse-to-pulse TJ value and is also the direct representation of the noise source strength. Γ is a normally distributed normalized noise term.

- The timing of a hybridly MLL is incorporated by an additional linearized timing-restoring term as compared to the free-running case [181] and is represented by Eq. (5.8).

  $$T(n+1) = T(n) + \sigma_{\mathrm{ptp}}\Gamma - \gamma T(n) \tag{5.8}$$

- The timing of a MLL in a AO FB or OE FB configuration is incorporated by an additional weighted time-delayed term as compared to the free running case and is represented by Eq. (5.9).

  $$T(n+1) = \frac{T(n) + \sigma_{\mathrm{ptp}}\Gamma + \gamma W(T(n) - T(n-n_d))T(n-n_d)}{1 + \gamma W(T(n) - T(n-n_d))} \tag{5.9}$$

  Hereby, γ denotes the timing interaction strength (TIS) which reflects the experimental FB ratio. A TIS of 1 corresponds to a FB ratio of 100 %. A TIS of > 1 can be experimentally achieved by using an optical amplifier in the AO FB loop. n_d denotes the discretized time delay of the FB in terms of number of pulses. $W(\Delta T)$ is a weighting function which decreases with increasing

$|\Delta T|$. If not stated otherwise the weighting function is a Gaussian function with a full-width at half-maximum (FWHM) of $\Delta\tau$ for the AO FB to account for the assumption that pulses cannot interact if their timing deviation ΔT is larger then their pulse width. This assumption is essential to explain the limited locking properties of the MLL with respect to the external FB cavity. For OE FB $W(\Delta T)$ is set to a constant value of 1 due to the large period of the electrical modulation frequency corresponding to the inverse RR which is much larger than the pulse width. Most importantly, the denominator is obligatory for the assumed statistical timing-averaging effect and also reflects the interaction of the timing deviations. In experiments a reflection of FB pulses on the facet of the MLL takes place leading to additional round-trips of these secondary FB pulses. However, the already highest applied experimental FB ratio amounts to $2 \cdot 10^{-3}$ which results in a relatively low second round-trip FB ratio of $4 \cdot 10^{-6}$ and can therefore be neglected in experiments and simulation.

- The timing of a MLL subject to optical pulse train injection (OPTI) is implemented by an independent and weighted random walk (Eq. (5.7)) as additional source of timing noise and is represented by Eq. (5.10).

$$T(n+1) = \frac{T(n) + \sigma_{\text{ptp}}\Gamma + \gamma W(T_2(n) - T(n))T_2(n)}{1 + \gamma W(T_2(n) - T(n))} \tag{5.10}$$

  Hereby, $T_2(n)$ denotes the absolute timing deviation of an independent master MLL.

As a consequence of the finite-difference approach and the chosen time-step of the inverse RR, integer matching of the inverse RR and external-delay time is always fulfilled leading to a constant and unchanged RR in the first instance. This integer matching is often denoted as the main resonance condition. However, implementation of a detuning of the FB delay time is possible by adding a constant timing offset to the timing of the returning FB pulses. Such a constant offset leads to a systematic increase or decrease of the timing deviation which reflects the change of the RR of a MLL with non-matching FB delay time. This allows to study detuned non-resonant AO FB which is covered in section 5.4.5.

In the simulations these equations are solved numerically and iteratively. Because FB is switched on at $t = 0\ s$ the evaluation is performed after a sufficient waiting time to guarantee a relaxation of the system. It was found that a relaxation time of 50 times the external FB round-trip time ($\approx 2.5 \cdot 10^3$ pulses) is sufficient as indicated by the relaxation of the TPN PSD. To obtain a quantitatively correct TPN PSD which matches the experimentally obtained TPN PSD a few careful steps have to be done. The timing-deviation-series obtained from the discretized differential equations is Fourier transformed by a fast Fourier transform algorithm (FFT) using a Hanning window and squared subsequently to obtain the timing noise power spectral density (TN PSD) $L_t(f)$. The inverse RR was used as the sampling interval. In general, the term power spectrum roughly denotes the squared Fourier-transform of an arbitrary quantity which is also the case for the experimentally measured electrical spectrum analyzer (ESA) power spectrum $P(f)$. The TPN PSD $L_\psi(f)$ can then be obtained from the TN PSD by $L_\psi(f) = (2\pi\nu_0)^2 L_t(f)$ [159, equation (2)]. It is essential to use a windowing function for the FFT. A properly normalized [1]

---

[1] Normalization was chosen to ensure an identical area of the Hanning window as compared to a rectangular window.

Hanning window has proven to provide error-free results.[2] In addition, as a FFT of a non-periodic broadband signal is performed, namely a random walk process, the obtained power spectrum must be scaled by a factor proportional to the length of the time-series to obtain correct spectral amplitudes. In our case the scaling factor for the power spectrum, which also depends on the implementation of the FFT, is $N/(\nu_0\pi)$ with N being the number of the pulses in the time-series. This factor represents the resolution bandwidth (RBW) of the FFT and converts the power spectrum to a power spectral density (PSD). The presented calculated spectra are obtained by averaging the spectra of 10 independent simulation runs each containing a series of $6.4 \cdot 10^5$ pulses only limited by the used computer system or the MATLAB software. A noise floor was added to the calculated spectra to account for the noise floor of the whole experimental setup and to allow for a visual correspondence of experiment and simulation.

5.4 Results and discussion

First the evolution of the timing phase noise power spectral density (TPN PSD) of the free-running mode-locked laser (MLL) as a function of gain current will be shown. This allows to show typical trends of timing jitter (TJ). Subsequently, the influence of external electrical modulation on the TPN PSD of the free-running MLL which represents hybrid mode-locking (HML) will be investigated. This external oscillator is then substituted by the time delayed repetition rate (RR) signal of the MLL itself leading to an opto-electrical feedback (OE FB) configuration. Subsequently this OE FB will be replaced by all-optical feedback (AO FB) and the correspondence of both feedback (FB) schemes in terms of TPN PSD characteristics will be shown. Consecutively non-resonant detuned AO FB will be investigated. This optical self-injection (AO FB) is then changed to external optical pulse train injection (OPTI) by a master MLL leading to the effect of TJ locking. Finally, results of a dual AO FB scheme reported in literature will be successfully reproduced by simulations.

For the following investigations a monolithic MLL with a total cavity length of 8 mm is used as described in section 5.1 leading to a relatively low RR of 5.06 GHz to allow for an effective electrical modulation. For all experiments the applied reverse bias voltage of the absorber amounts to −6.00 V and the gain current is set to 165.4 mA. The measured optical pulse-width is 4.0 ps, the spectral width amounts to 3.4 nm and the free-running RR line-width amounts to 19 kHz which corresponds to a pulse-to-pulse timing jitter ($\mathrm{TJ}_{\mathrm{ptp}}$) of 152 fs according to Eq. (2.8) (on page 28). On the one hand these biasing conditions are intentionally chosen to ensure a weak local minimum of the TJ but on the other hand still provide a relatively high TPN PSD not being limited by the setup noise floor. In particular it is essential to ensure that the MLL does not exhibit non-regular mode-locking operation or any sort of instabilities. An evaluation of the TPN PSDs of different harmonics of the RR yields the expected quadratic dependence of TPN PSD on harmonic number leading to the statement that amplitude jitter (AJ) is below the detection limit or in other words is insignificant as compared to the TJ.

---

[2] Without a correct windowing function the TPN PSD of a HML configuration did not match the TPN PSD of a corresponding free-running MLL for high frequency offsets as required.

At the beginning, the TJ of the free-running MLL is investigated to know the reference operation condition for the following investigations. At high reverse voltages the broadest range of mode locking (ML) operation can be achieved in terms of gain current for most quantum-dot (QD) based MLL. Therefore the investigations are focused on a reverse voltage of −6.0 V. The threshold current at this voltage amounts to ≈150 mA. An overview of experimental TPN PSDs in the current range from 155 mA to 215 mA is shown in Fig. 5.3a. Already slightly above threshold the MLL starts ML operation and exhibits a high TPN PSD. With increasing gain current the TPN PSD decreases, remains low and finally increases again. This is more clearly illustrated in the experimental results shown in Fig. 5.3b. There the TPN PSD at a frequency of 1 MHz is selected as experimental measure for TJ because it always allows a direct comparison with results in literature in contrast to the integrated timing jitter ($\mathrm{TJ}_{\mathrm{int}}^{(f_1,f_2)}$) which is not comparable without an identical frequency range. The trend of the experimental TPN PSD at 1 MHz exhibits an exponential decrease from a gain current of 155 mA to 180 mA, a nearly constant value at a gain current from 180 mA to 210 mA and a sudden increase above a gain current of 215 mA. The lowest observed TJ at a frequency of 1 MHz amounts to −106.6 dBc/Hz which corresponds to a $\mathrm{TJ}_{\mathrm{ptp}}$ of 13.0 fs and a RR line width of 137 Hz.

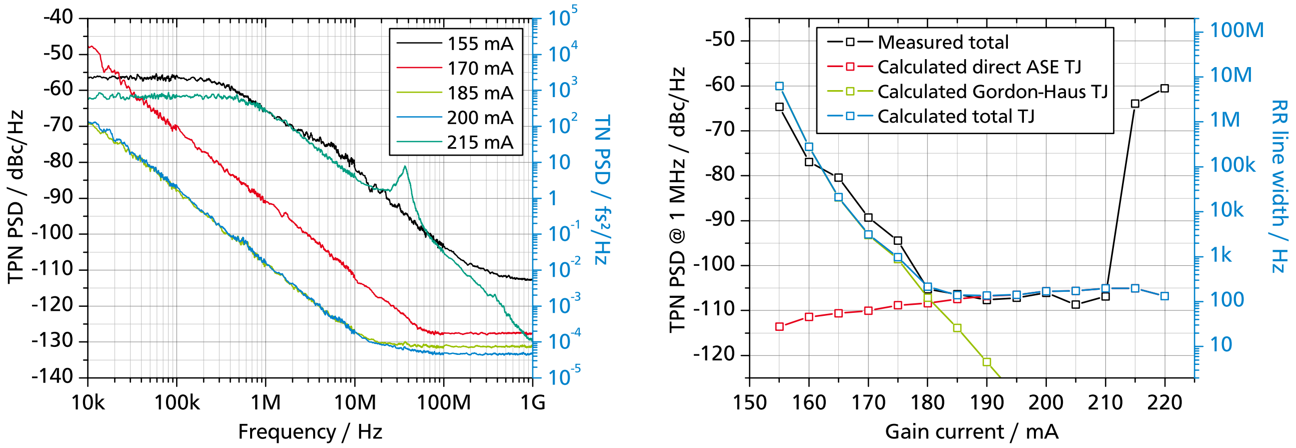

(a) **(b)**

Figure 5.3: (a) Experimental TPN PSDs for various gain currents at a reverse voltage of −6.0 V. A corresponding TN PSD axis is also given. (b) Experimental and calculated TPN PSD components at a frequency offset of 1 MHz of the free-running MLL at a reverse voltage of −6.0 V and a gain current of 165 mA. A corresponding RR line-width axis is also given.

In Fig. 5.3a all shown TPN PSDs exhibit the expected Lorentzian shape and the only visible deviation occurs at a gain current of 215 mA. There, some kind of resonance at a frequency of around 340 MHz occurs. The high TPN PSD at a gain current above 215 mA originates from a transition region to harmonic ML which persists up to a current of 230 mA. From this current on stable harmonic ML occurs exhibiting a doubled RR of 10.12 GHz and very similar $\mathrm{TJ}_{\mathrm{ptp}}$. Although the setup is identical for all shown TPN PSDs in Fig. 5.3a it might seem surprising that the instrument noise floor exhibits very different values. This can be easily explained by means of Eq. (5.1). There, a normalization of $L_{\psi}(f)$ by P_{tot} is performed. Hereby, P_{tot} depends on signal power which changes with gain current. In addition $L_{\psi}(f)$ obtained with the method by von der Linde always contains a constant integrated area or energy thus the noise floor rises with increasing RR line-width.

One single unique TPN PSD measured at a gain current of 165 mA shown in Fig. 5.4a (on page 106) shows a slight deviation from the expected Lorentzian shape which indicates the origin of the high TPN PSD at gain currents below 180 mA. Above a frequency of 10 MHz the slope decreases stronger than the expected f^{-2} dependence. In sub-section 2.4.3 (on page 36) the theoretical shapes of the TPN PSDs for two dominant TJ sources were demonstrated. There, an increased slope indicated the f^{-4} slope for the Gordon-Haus TJ accuring at high frequencies. The transition from the f^{-2} to the f^{-4} slope starts at a frequency which depends on various MLL parameters and amounts to 200 kHz for the solid-state laser (SSL) reported in [64] which facilitates the visibility of the transition because low frequencies are located far above the noise floor. Here, the visibility of this transition is limited to a very small current range because it starts at a high frequency of 10 MHz and is therefore easily camouflaged by the *variable* noise floor for lower and higher gain currents. Finally all types of relative intensity noise (RIN) induced TJ [44] can be most likely excluded. For example using [44, Eq. (29)] and assuming a flat RIN power spectral density (PSD) up to the relaxation oscillation (RO) and a subsequent decrease with a f^{-2} slope a transition of the TPN PSD from a f^{-2} slope to a f^{-4} slope is expected around the RO frequency. This RO frequency which amounts to around a GHz [13, 182] is an order of magnitude higher than the observed transition frequency in Fig. 5.4a therefore eliminating RIN induced TJ as an explanation.

In the following, this experimentally determined TPN PSD will be compared by calculated TPN PSD for this MLL by using Eq. (2.23) (on page 36), Eq. (2.25) (on page 38), measured parameters and parameters taken from literature. The parameters obtained from experiment are the pulse repetition period (PRP) T_0, the pulse-width τ_p, the average power P_{avg}, the optical frequency ν and the spectral width of the optical pulse $\Delta\nu_p$. Parameters taken from literature are the inversion parameter $\theta = 3$ [110], the adjusted round-trip gain $g = 9$ [110] and the gain bandwidth $\nu_g = 3$ THz (16 nm) obtained from the spectral width of the amplified spontaneous emission (ASE) of the used MLL. The round-trip gain has to be reduced with respect to [110] to keep the theoretical ASE induced TJ limit *below* the experimentally obtained value at gain currents ranging from 185 mA to 220 mA which will be shown below. An experimental value cannot be lower than a fundamental limit. As already mentioned in sub-section 2.4.3 the required pulse energy is not constant for a mode-locked semiconductor laser (SCL) which is shown in simulations in [144, Fig 4(a)]. However, the pulse evolution shown in this reference shows, that a linear approximation should be satisfactory. Therefore a linear pulse energy evolution is assumed using the facet reflectivities (100 % and $R = 10$ %) as boundary conditions leading to an average pulse energy given by Eq. (5.11).

$$E_p \approx (1+R)/(2(1-R)) \cdot P_{\text{avg}}/\nu_0 \approx 0.6 \cdot P_{\text{avg}}/\nu_0 \tag{5.11}$$

The only remaining parameter, namely the group delay dispersion (GDD) is extracted by fitting the theoretical TPN PSD to the experimental TPN PSD and amounts to a value of 1.45 ps^2 for a gain current of 165 mA. Hereby, the matching of the theoretical and experimental TPN PSD is good as shown in Fig. 5.4a. This allows a separation of the two dominant TJ components. At this gain current the Gordon-Haus TJ is dominant and the TJ resulting from direct projection of ASE on the optical pulse is insignificant.

Having identified these two different sources of TJ allows to estimate the strength of these TJ sources. The direct ASE induced TJ is well defined by the known parameters. Using the measured total TJ and the calculated direct ASE TJ allows to identify the unknown GDD for other gain currents not showing the required transition from the f^{-2} slope to the f^{-4} slope. The GDD is obtained from the experimental TPN PSD by Eq. (2.25) and is plotted in Fig. 5.4b. The trend of the GDD suggests an exponential decrease. Therefore an exponential fit of the GDD is used to calculate the Gordon-Haus TJ and the total TJ as shown in Fig. 5.3b. Most importantly, it can be observed, that the direct ASE TJ represents a fundamental limit in the current range from 185 mA to 210 mA. In Fig. 5.4b also the pulse-width is plotted which strongly influences the direct ASE TJ. The increase of the pulse-width thus results in an increase of the direct ASE TJ as evident in Fig 5.3b.

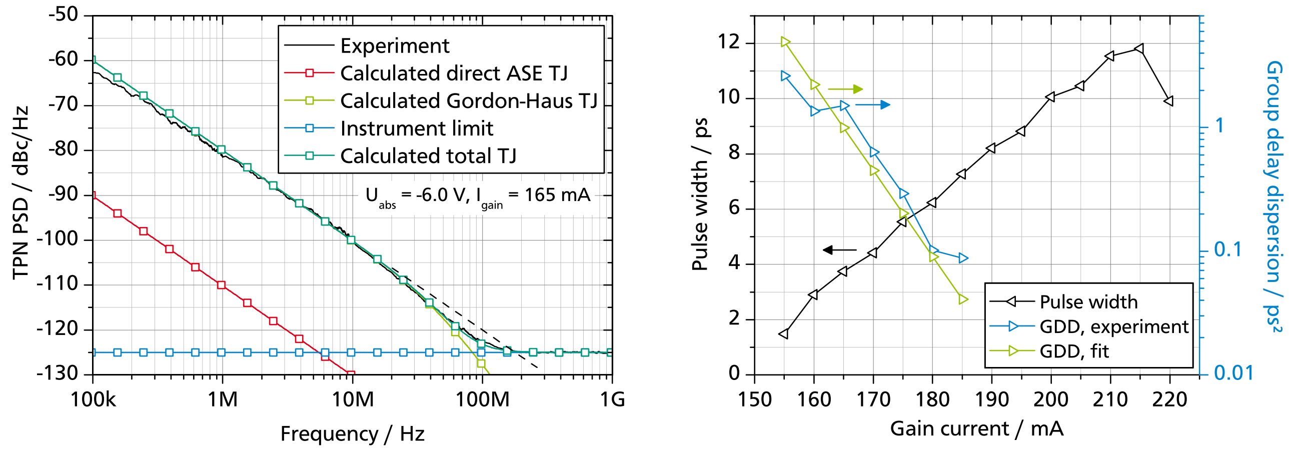

(a) **(b)**

Figure 5.4: (a) Experimental and calculated TPN PSDs components for a reverse voltage of −6.0 V and a gain current of 165 mA. (b) Measured pulse width and estimated GDD as a function of the gain current of the free-running MLL for a reverse voltage of −6.0 V.

Summing up, the free running MLL exhibits three different regions of TJ. The first region stating at threshold current and exhibiting an exponential decrease as a function of gain current potentially represents the Gordon-Haus TJ. The second region exhibiting almost an unchanged TJ originates from the direct ASE contribution on the TJ. Finally at higher currents a high TJ is existent originating from a transition region from fundamental to harmonic ML. Knowing the existence of these different regions which represent different and fundamental TJ limits allows to investigate if these limits may be brought down by various experimental schemes and in particular positively influenced and controlled by AO FB.

A common approach to influence TJ of a semiconductor MLL is HML [160]. Here the absorber section is modulated electrically with a low-noise frequency signal matching the RR of the free-running MLL thus effectively providing a continuous gating of the pulse timing in the absorber section. Experimental and corresponding simulated TPN PSD for the hybridly MLL are shown in Fig. 5.5 for different electrical modulation power (P_{mod}) and corresponding timing interaction strength (TIS), respectively. In experiment, already for the weakest applied modulation power of $+12.2$ dBm a RR locking is achieved together with a broad-band TPN PSD reduction up to a frequency of around 100 kHz. With increasing modulation power the TPN PSD plateau decreases thus also extending to higher frequencies of up to around 1 MHz for a modulation power of $+31.2$ dBm. Above this frequency the free-running TPN PSD is unchanged. Therefore HML significantly reduces timing fluctuations on slow time-scales but due to the wide electric gating window which generally amounts to multiples of the optical pulse-width the high-frequency TPN PSD is not affected. In accordance with [162] also a inversely proportional dependence of TPN PSD plateau level on P_{mod} is found. Identical TPN PSD characteristics can also be achieved by utilizing a phase locked loop (PLL) configuration [163] which was also found in experiment but is not shown here. It is emphasized that these TPN PSD plateaus are no artifacts in contrast to the plateau of the TPN PSD at a gain current of 155 mA and 215 mA shown in Fig. 5.3a (on page 104).

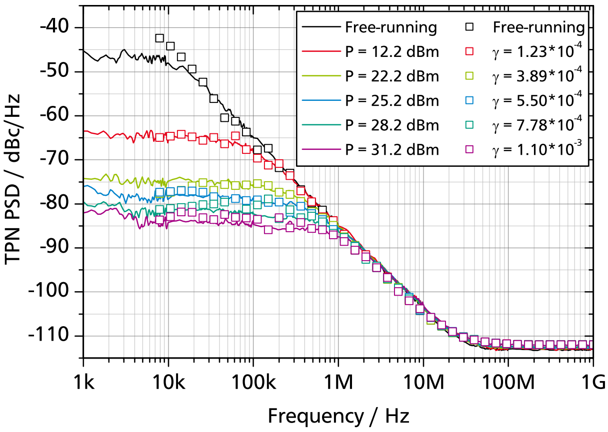

Figure 5.5: Measured (solid lines) and corresponding calculated (open symbols) TPN PSDs of the hybridly MLL for different values of P_{mod} and corresponding TISs, respectively. The TPN PSD for the free-running MLL is also given as a reference.

By properly selecting TIS in the simulations based on equation (5.8) the numerically obtained TPN PSD results accord with the experimental results in the whole frequency range. A comparison of P_{mod} in experiment and corresponding TIS in the simulations is shown in Fig. 5.6 and yields a square-root dependence of TIS on P_{mod}. The exponent amounting to 0.5 is expected to be valid for HML in general while the scaling factor of $9.6 \cdot 10^{-4}$ results from the realized electrical setup and is also expected to strongly depend on the impedance matching of MLL and electrical setup. This estimated dependence is necessary in the following to obtain the correct calibrated TIS for a known value of P_{mod} in the OE FB configuration simulation. It also represents a connection of experiment and simulation.

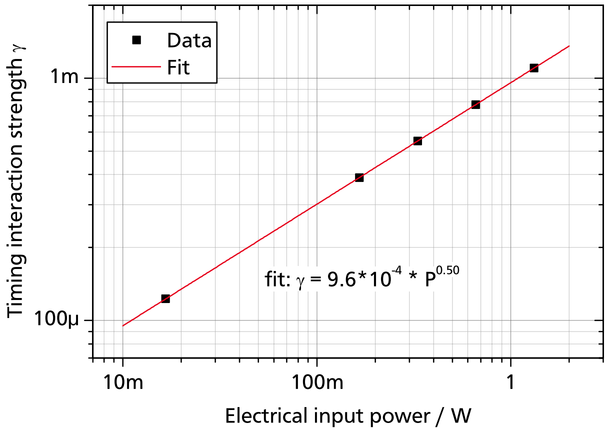

Figure 5.6: TIS in the simulation as a function of the corresponding experimental P_{mod} in the realized setup for HML operation .

Besides exploiting the HML configuration for TJ reduction and RR locking also a corresponding all-optical dual-mode injection approach is established. In [183, 184] two optical modes are injected into a passively MLL. These modes are locked by means of a fixed modulation frequency which matches the RR of the passively MLL thus allowing to transfer this fixed modulation frequency onto the optical mode comb of the passively MLL. This approach may be regarded as optical HML.

5.4.3 Opto-electrical feedback

To realize the proposed idea of statistical interaction of the timing of the optical pulses now the OE FB configuration is implemented [6, 50, 53, 166]. The electrical modulation of the absorber represents a continuous time domain gating of the timing of the intra-cavity pulse. In relation to HML now the external reference oscillator is replaced by the time-delayed RR signal of the laser output itself. The OE FB configuration is closely related to the widely reported coupled opto-electronic oscillators [185]. However, the latter stops pulsed operation without the opto-electric loop because it effectively bases on ML of a continuous-wave (CW) laser by regenerative electrical feedback [46, 47]. It therefore only consists of one single oscillation loop whereas the OE FB configuration presented here represents a main oscillator with an additional FB loop.

The experimental and corresponding simulated TPN PSD for the MLL in OE FB configuration are shown in Fig. 5.7 for different values of P_{mod} and corresponding TISs, respectively. The electrical delay is fine-tuned to match the free running RR of the MLL. In the experiment a broadband TPN PSD reduction of −5 dB is achieved up to a frequency of around 3 MHz for the maximum applied P_{mod} of +31.2 dBm. At around 6 MHz and its harmonics *weak and broad* peaks are evident which originate from the OE FB delay-time. These peaks are noise resonances which are in fact related to super-mode noise peaks in harmonically mode-locked external cavity lasers [103]. The OE FB configuration presented here is able to successfully reduce the TPN PSD without the use of a stable reference oscillator. In comparison to HML (Fig. 5.5) the TPN PSD reduction of the OE FB configuration is inferior at low frequencies below

800 kHz as expected but surprisingly the reduction at higher frequencies between 800 kHz and 4.5 MHz is superior. This OE FB scheme shows a dependence of TPN PSD on frequency following a f^{-2} law at frequencies below the noise resonance peak frequency which indicates that this configuration is still subject to a random walk.

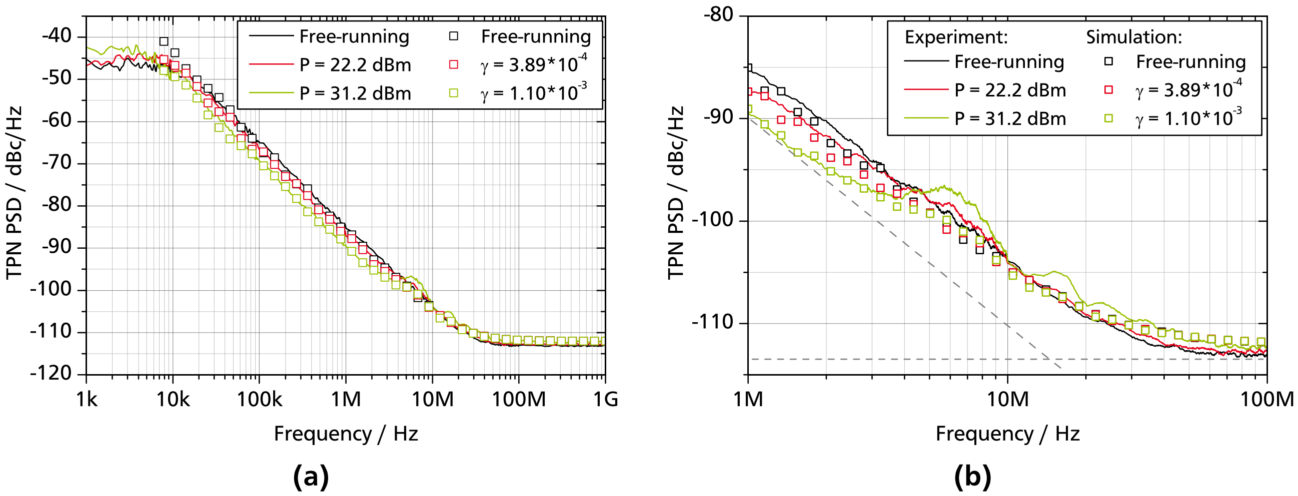

Figure 5.7: (a) Measured (solid lines) and corresponding calculated (open symbols) TPN PSDs of the laser in OE FB configuration for different values of P_{mod} and corresponding TISs, respectively. The TPN PSD for the free-running MLL is given as a reference. (b) Same as (a) but with a different view. The gray dashed lines serve as a guide for the eye.

The simulation results based on Eq. (5.9) (on page 101) with a constant weighting function $W(\Delta T) = 1$ and using the estimated parameters from the HML simulation (Fig. 5.6) coincide with the experimental results very well except for the significantly lower noise resonance peaks as shown in Fig. 5.7b. A time-domain representation of these noise peaks will be given later. Due to the good accordance between experiment and simulation the assumption of a timing interaction of intra-cavity pulse and time-delayed absorption gating is validated. The reduction of TPN PSD or TJ can be attributed to a statistical averaging of the nearly independent timing deviations of the intra-cavity pulse timing and the timing of the time-delayed absorption gating leading to a reduced TJ [53]. This statistical averaging is directly modeled by Eq. (5.9) in section 5.3.

5.4.4 All-optical feedback - Resonant delay

In the previous section the statistical part of the idea of the timing-interaction was validated by a well defined OE FB configuration. Now this timing interaction which is based on absorption gating by delayed electrical self-modulation is transferred to the all-optical domain. For the AO FB configuration also timing interaction of intra-cavity pulse and the returning time-delayed pulse is assumed and could be explained by means of the MLL gain dynamics. For example a weak injected Gaussian-shaped FB pulse preceding the main intra-cavity Gaussian shaped pulse experiences higher gain than the main pulse due to the non-linearity of the dynamical gain and thus increases in intensity. This FB pulse first traverses the gain section of the MLL and *subsequently* the absorber section. This changes the center of mass of the total optical pulse forwards in direction of motion. Finally after one or a few round-trips the gain and absorber sections reshape this pulse back to a stable Gaussian shape while keeping the changed timing. Despite the all-optical interaction a limited timing interaction range which amounts to the optical pulse width is assumed and is represented by the weighting term $W(\Delta T)$.

Such an AO FB configuration is widely exploited to reduce TPN PSD and consequently the RR line-with of passively MLL by means of reflecting a small fraction of the optical output power back into the MLL [51, 53, 54, 171]. Here a combined free-space and fiber based setup is chosen to allow for a convenient and precise control of both FB ratio and large delay length, repectively. It was found that in order to obtain the highest TPN PSD reduction the external delay length had to be slightly detuned resulting in a change of $\approx +0.1$ MHz of the RR with respect to the free-running RR. Despite this slight RR detuning this AO FB configuration is denoted as integer resonant FB to emphasize the required integer matching of external delay time with respect to the pulse period of the MLL. An explanation for the slight detuning will be given in the sub-section 5.4.5.

Experimental and simulated TPN PSD for the MLL in the realized AO FB configuration are shown in Fig. 5.9 for different values of FB ratios and corresponding TIS, respectively. In the experiment a broad-band TPN PSD reduction of -15 dB is achieved up to a frequency of around 3 MHz for the maximum applied FB ratio of $1.6 \cdot 10^{-3}$. At 8.7 MHz and its harmonics distinct noise resonance peaks are evident which originate from the AO FB delay. The calculated frequency of the delay of the FB corresponds to a value of 9.4 MHz. For a high FB ratio of $1.6 \cdot 10^{-3}$ the frequency of these observed narrow resonance peaks corresponds quite well to the delay length whereas for a weak FB ratio of $4 \cdot 10^{-4}$ these peaks are located at a lower frequency of 8.4 MHz and are strongly broadened.

In addition it is found that the dependence of the spectral amplitude of the resonance peaks on harmonic number of the RR lines follows a square-law thus proving that these peaks are pure timing fluctuations [99]. This statement can be verified by comparison of the PSDs of the TJ and the AJ. Both can be obtained from evaluation of the power spectra (PS) around different harmonics of the RR. In contrast, evaluating only one single harmonic of the RR yields a total jitter being a sum of AJ and TJ. In general, TJ dominates the jitter of mode-locked SCLs. Specific steps to obtain these two jitter components from the PS are given in [100]. Fig. 5.8 shows the experimentally obtained TPN PSD and the PSD of the AJ for the MLL subject to AO FB. The jitter components are extracted from the 1st and 8th harmonic of the RR. It can be observed, that the PSD of the TJ well coincides with the PSD of the total jitter. Thus, the difference of both, namely the AJ is below the detection limit as indicated by the many missing data points. This shows, that AO FB influences the timing properties of a MLL but does not induce AJ. Finally, at very high FB ratios instabilities or a coherence collapse is expected [186].

To estimate the correct values of TIS for this AO FB configuration this parameter is varied to obtain a matching of the TPN PSD in the low frequency regime up to 1 MHz while keeping the full-width at half maximum $\Delta\tau$ of the Gaussian shaped timing weighting function $W(\Delta\tau)$ in equation (5.9) at 4 ps corresponding to the measured pulse-width of 4 ps of the measured Gaussian shaped optical pulses. This variation is performed for FB ratios higher than $1 \cdot 10^{-4}$. As can be seen in Fig. 5.9 the simulation results

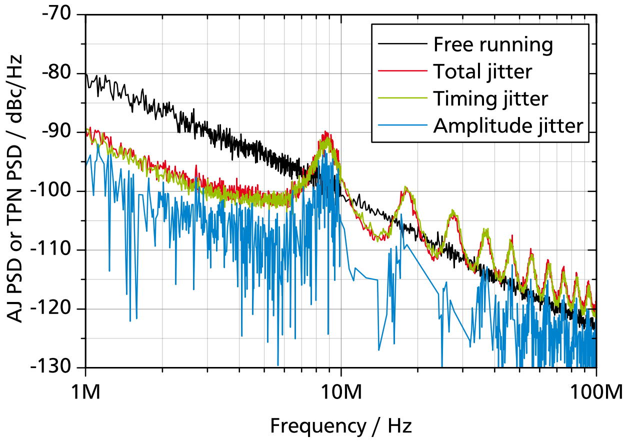

Figure 5.8: Experimentally obtained PSDs of TJ, AJ and the total jitter of the MLL in AO FB configuration represented as TPN PSDs and relative AJ PSD. The TPN PSD for the free-running MLL is given as a reference.

coincide with the experimental results very well except for the significantly lower noise resonance peaks which is more clearly shown in Fig. 5.10. In addition, it is found that the dependence of TIS on FB ratio yields a simple power-law with an power of around $a = +0.45$. This found relation represents the connection of model and experiment.

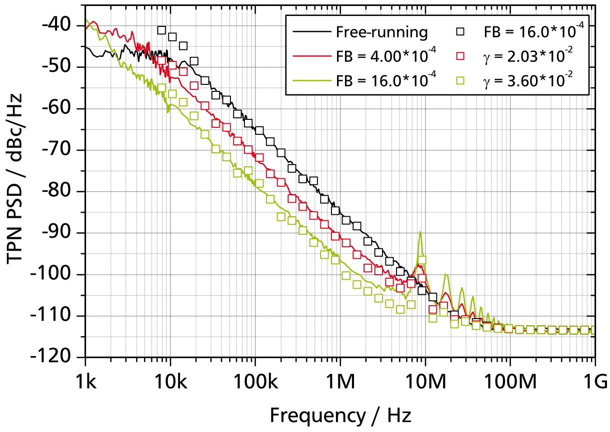

Figure 5.9: Measured (solid lines) and simulated (open symbols) TPN PSDs of the laser in AO FB configuration for different values of FB ratios and corresponding TISs, respectively. The TPN PSD for the free-running MLL is also given as a reference.

The maximum identified TIS for the AO FB configuration amounts to $3.0 \cdot 10^{-2}$ whereas the maximum identified TIS for the OE FB configuration amounts to $1.1 \cdot 10^{-3}$ which results in a ratio of 27. Given the experimental limitation of electrical modulation power for the OE FB configuration and the FB ratio of the AO FB configuration this ratio of the TIS values reflects the internal efficiency difference of both mechanisms. The higher effectivity of the AO FB configuration can be attributed to the gain provided by the active medium which amplifies the FB pulse.

To highlight the role of the weighting function $W(\Delta T)$ defined in Eq. (5.9) a detailed depiction of the first noise resonance peak for a FB ratio of $1.6 \cdot 10^{-3}$ in experiment and two corresponding simulated

TPN PSD are shown in Fig. 5.10. In the presented simulation results two combinations of TIS and interaction widths $\Delta\tau$ are chosen which both match the TPN PSD reduction up to 3 MHz. The parameter combination $\gamma = 3.0 \cdot 10^{-2}$ and $\Delta\tau = 4$ ps match the measured noise resonance peak frequency of 8.7 MHz exactly and the amplitude much better than the parameter combination $\gamma = 4.8 \cdot 10^{-3}$ and $\Delta\tau = \infty$. This better accordance implies that a timing interaction width is indeed necessary to well reproduce the experimentally obtained results and substantiates the chosen timing-interaction approach. The deviation of measured and simulated noise resonance frequency of 8.7 MHz from the realized delay-frequency of 9.4 MHz is a direct consequence of the timing-mechanism because with increasing TIS in simulation or increasing FB ratio in experiment the resonance-peak frequency converges towards the realized delay-frequency. Also like the OE FB scheme the AO FB scheme shows a dependence of TPN PSD on frequency following a f^{-2} law at frequencies below the resonance peak frequency which indicates that this configuration is still subject to a random walk.

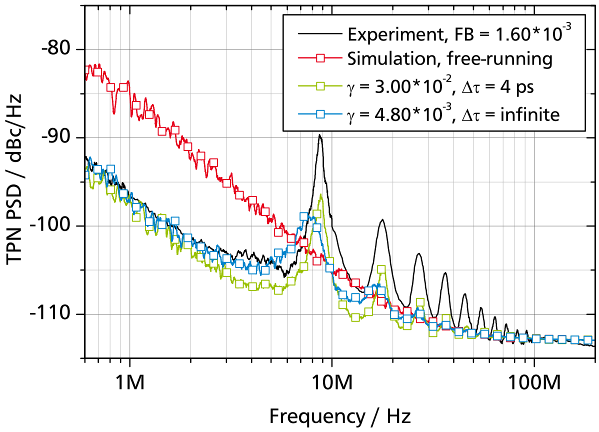

Figure 5.10: Measured TPN PSD for a FB ratio of $1.6 \cdot 10^{-3}$ (black line) and calculated (solid line with open symbols) TPN PSD of the laser in AO FB configuration for different values of TIS and interaction widths $\Delta\tau$. The simulated TPN PSD for the free-running MLL is also given as a reference.

From the overall accordance of TPN PSD and resonance-peak frequency in experiment and simulation it can be deduced that the assumption of an *optical* timing interaction between intra-cavity pulse and returning time-delayed FB pulse is valid similar to the OE FB case. It is emphasized, that the FB pulses still carry the timing noise generated inside the cavity and are still able to reduce the TJ of the intra-cavity pulses. To depict the efficiency of the AO FB it is pointed out that the returning delayed pulse with a power of much less (due to unknown coupling losses) then $1.6 \cdot 10^{-3}$ times the intra-cavity pulse power influences the timing of the intra-cavity pulse by significant 3 % per round-trip which is more than one order of magnitude higher than the FB ratio of $1.6 \cdot 10^{-3}$ itself.

This picture of the timing-interaction of intra-cavity pulse and FB pulse is supported by the influence of an intra-cavity Fabry-Perot etalon on the TJ of harmonically MLL [187, 188]. There, the intra-cavity etalon reduces the so-called super-mode-noise which occurs in harmonically MLL. Such a harmonically MLL exhibits multiple pulses inside the long optical cavity. Each of these pulses is approximately uncorrelated with respect to the preceding or subsequent pulses. In the time-domain representation an optical pulse exiting the etalon represents a weighted average of many input pulses thus leading to reduced AJ and TJ as suggested by [189]. Thereby, a high finesse is required because it represents many round-trips of an optical pulse inside the etalon cavity.

Furthermore, the effect of RR line-width reduction by AO FB is sometimes related in literature to the higher Q-factor of the FB loop resonator [50]. A high Q-factor, mainly defined for single frequency oscillators and CW lasers, results in a narrow optical line-width of an optical resonator and requires interferometric precision. In contrast, for the widespread AO FB configurations used for TJ reduction interferometric precision is not given. However, using the Q-factor formalism with respect to the RR and not the optical frequency leads to the frequency-domain picture of coupled oscillators which represents an alternative approach for theoretical investigations. Nevertheless, in this work the time-domain approach for investigations and simulations is chosen to account for the existence of optical pulses and the interaction of their timing.

Another important optical line-width related aspect of the timing interaction mechanism can be indicated at this point. The optical line-widths of an optical mode comb of a QD based MLL were estimated to lie in the 20 MHz range as reported in [97]. Therefore the coherence length amounts to 15 m which is shorter than the FB length of 31 m (in vacuum) used here and which resulted in a significant TJ reduction. This indicates, that an interference-based pulse-to-pulse interaction might be excluded and solely relies on the incoherent interaction of FB pulse and intra-cavity pulse by means of the active medium. This assumption is supported by results from [171] where a CW injected MLL with optical line-widths of around 10 MHz and thus a coherence length of up to 30 m also exhibited high TJ reduction if exposed to AO FB with a FB length of around 350 m (in vacuum). Thus, the exclusion of a coherence based interaction which was also assumed in [53, 190] can be assumed. Furthermore, results covering OPTI which will be shown in sub-section 5.4.6 will substantiate this assumption.

To show the quantitative dependence of TPN PSD reduction on optical FB ratio Fig. 5.11 shows the TPN PSD at a frequency of 120 kHz as a function FB ratio in experiment and simulation. The frequency of 120 kHz is selected because it is well below the frequency of the noise-resonance peaks. In the experiment, with increasing FB ratio the TPN PSD is steadily reducing. Based on equation 5.2 (on page 98) the TPN PSD is proportional to the RR line-width. Therefore, the presented dependence applies for the RR line-with in the same way. Below a FB ratio of $1 \cdot 10^{-4}$ the TPN PSD should be sufficiently spaced from the free running TPN PSD to allow for meaningful evaluation. Hereby a power-law-fit describing the dependence of TPN PSD L_ψ on experimental FB ratio κ yields $L_\psi(\kappa) = 3.9 \cdot 10^{-11} \kappa^{-0.90}$ and thus an power of -0.90 which also corresponds to other reported experimental results covering AO FB in [52, 55, Fig. 4 (b)]. Furthermore, no threshold-behavior is evident. The simulated TPN PSD corresponds to the measured data quite well yielding the dependence of TIS γ on FB ratio κ given by Eq. (5.12).

$$\gamma(\kappa) = 0.523\kappa^{0.446} \tag{5.12}$$

Combing these both dependencies $L_{\psi}(\kappa)$ and $\gamma(\kappa)$ leads to the dependence of TPN PSD L_{ψ} on TIS γ which yields a power-law with an power of −2.1 which matches quite well the expected exponent of 2 which directly stems from simulations.

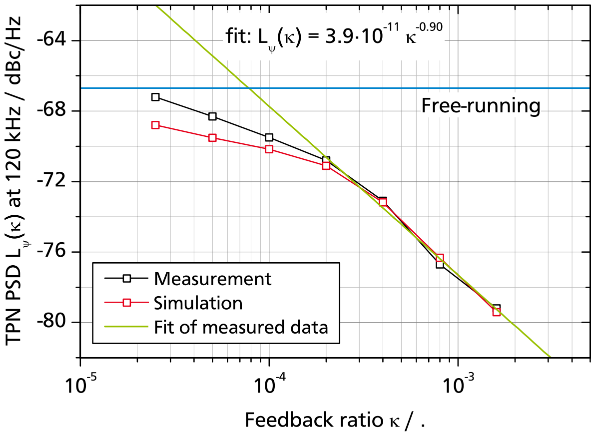

Figure 5.11: Measured and calculated TPN PSD L_{ψ} at 120 kHz for the AO FB configuration as a function of FB ratio κ. The solid horizontal line denotes the TPN PSD of the free running MLL.

It is emphasized, that the given experimental FB ratio κ contains coupling losses. Thus, a TIS γ of 1 which corresponds to a interaction strength of 100 % leads to a corresponding FB ratio κ of 4.3 according to Eq. (5.12). In contrast, excluding coupling losses a TIS γ of 1 should correspond to a FB ratio of 1. Thus, the inverse of 4.3 amounting to 23 % should reflect these coupling losses. This value of 23 % lies in an experimentally reasonable range if laser to fiber coupling is regarded which is the case for the realized setup.

To demonstrate the general effectiveness of AO FB, this scheme was also investigated for two other MLLs with the result, that also other MLLs exhibit a TPN PSD reduction by AO FB but with different extent. Results covering these two other lasers are given in the following.

The MLL do 1790 c2 consisting of 10 layers of QDs and having a total length of 4 mm resulting in a RR of 10.1 GHz is operated at a gain current of 96 mA and a reverse absorber voltage of −5.0 V to ensure ML operation. In free-running operation it exhibits a narrow RR line width of 614 Hz which corresponds to a $\mathrm{TJ}_{\mathrm{ptp}}$ of 9.7 fs. The already investigated MLL in previous sub-section 5.4.1 has a gain section length of 8 mm and exhibits a $\mathrm{TJ}_{\mathrm{ptp}}$ of 13.0 fs, a RR line-width of 137 Hz and a pulse-width of 5.6 ps. Due to the shorter active medium length a halved $\mathrm{TJ}_{\mathrm{ptp}}$ value and a doubled RR line-width is approximately expected for the shorter laser assuming identical gain medium conditions as explained in sub-section 2.4.1 (on page 25) which is approximately fulfilled. Now, using the AO FB scheme with a FB frequency of ≈8 MHz[3] corresponding to a total delay length of 37 m (or 18.5 m in dual-pass notation) and adjusting ideal delay yields a reduction of TPN PSD of −17 dB for low frequencies as shown in Fig. 5.12a. There, only the first and second noise resonance peak can be observed in experiment for the AO FB configuration due to unavoidable instrument noise. From the low frequency part of the TPN PSD a long term timing jitter ($\mathrm{TJ}_{\mathrm{lt}}$) of 1.4 fs and a RR line width of 12.5 Hz can be calculated. The simulated

---

[3] The FB Frequency is different as compared to the previous MLL because the experimental setup is different.

TPN PSDs in Fig. 5.12a are obtained by using the RR of 10.1 GHz, the FB frequency of 8 MHz the pulse width of 5.6 ps for the full-width at half-maximum (FWHM) of $W(\Delta T)$ and a TIS of $8.0 \cdot 10^{-3}$. Hereby, a simulated TPN PSD with and without instrument noise floor is shown to allow to highlight the loss of information for the experimentally obtained TPN PSD. In general a good matching of simulation and experiment is obtained thus showing the validity of the model for different MLLs and thus different parameter sets.

The MLL do 2584 s1b a8, which has a tapered geometry of the gain section, consisting of 10 layers of QDs and having a total length of 2.5 mm resulting in a RR of 16.0 GHz is operated at a gain current of 737 mA and a reverse absorber voltage of −6.5 V to ensure ML operation. In free-running operation it exhibits a RR line width of 1.58 kHz which corresponds to a TJ_{ptp} of 7.8 fs. Such a low TJ was also reported in [191] where a TJ_{ptp} of 6 fs was demonstrated for a QD based free running MLL with a RR of 19.4 GHz. The TPN PSD for the free-running case is displayed in Fig. 5.12b. Despite the f^{-2} slope for frequencies higher than 100 kHz a flat pedestal can be observed below this frequency. This pedestal represents a slow drift of the RR during the measurement of the TPN PSD. The *tapered* MLL is found to be prone to additional very weak optical FB from a short distanced vibrating surface namely a commercial beam blocker made of a black steel sheet. This unwanted FB shows the potential to tune the RR in a narrow range without influencing the TPN PSD or TJ (as expected, due to the short FB length) and might be attributed to changes of the optical frequency originating from a three-mirror cavity description [8]. Other non-tapered MLLs do not show this effect. Now, using the AO FB scheme with a FB frequency of ≈8 MHz and adjusting ideal delay yields a high reduction of TPN PSD of −26 dB for low frequencies as shown in Fig. 5.12b. From the low frequency part of the TPN PSD a very low TJ_{lt} of 0.36 fs and a RR line width of very low 3.3 Hz can be calculated. However, due to the FB vibrations the RR envelope amounts to 4 kHz as evident from Fig. 5.12b. The simulated TPN PSDs in Fig. 5.12b are obtained by using the RR of 16.0 GHz, the FB frequency of 8 MHz the pulse width of 1.1 ps for the FWHM of $W(\Delta T)$ and a TIS of $7.0 \cdot 10^{-3}$ according to the calibration function (5.12) and a FB ratio of $6.5 \cdot 10^{-5}$. Although the magnitude of the noise resonance peaks is significantly lower for the simulation the reduction of TPN PSD for low frequencies is satisfactory matched. It is highlighted, that all the parameters required for the simulation are obtained from experiment only thus proving the wide validity of the developed picture. Despite this, the tapered MLL exhibits a more symmetric beam profile[4] as compared to the straight MLL. This results in a higher coupling efficiency which increases the factor in the calibration function (5.12) leading to an higher TIS. This would further reduce the TPN PSD for low frequencies and increase the magnitude of the noise resonance peaks thus improving the matching of experiment and simulation.

Interestingly such quite low TISs of $8.0 \cdot 10^{-3}$ and $7.0 \cdot 10^{-3}$ result in a high TJ reduction of −17 dB and −26 dB as compared to the 8 mm long laser which exhibits almost no TPN PSD reduction for a TIS of $8.0 \cdot 10^{-3}$ which can be extrapolated from Fig. 5.9. This arises from from two reasons. First, a short pulse-width together with an high TJ_{ptp} (154 fs as compared to 9.7 fs and 7.8 fs) results in an temporary

---

[4] Straight MLL exhibit roughly a 4 to 1 ratio of fast-axis to slow-axis beam diameter, whereas tapered MLL exhibit roughly a 4 to 2 ratio due to the required 2 collimation lenses which leads to a better coupling efficiency into the fiber and thus provides higher FB.

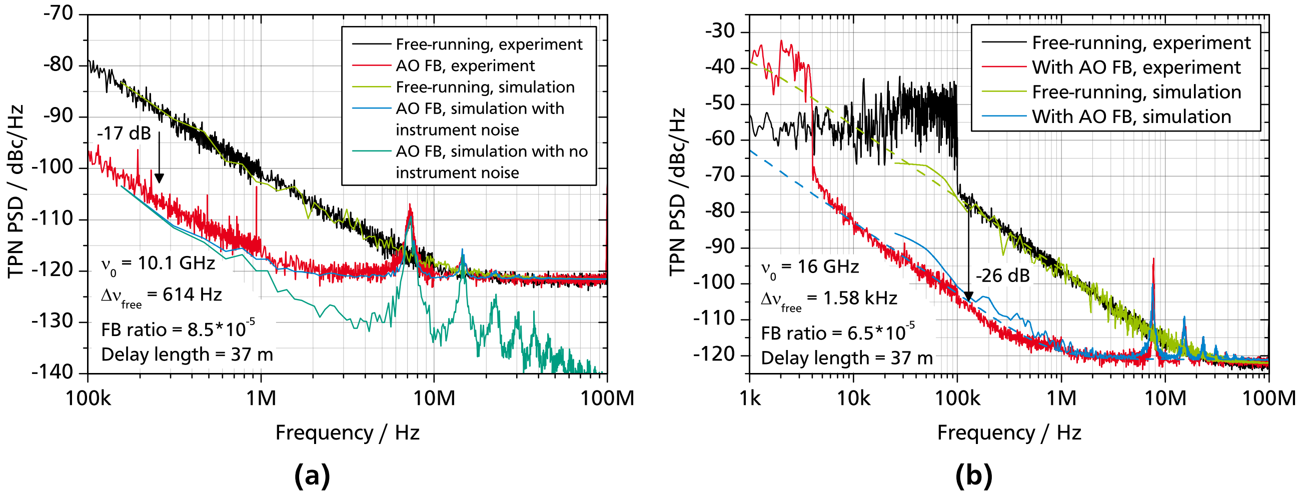

Figure 5.12: (a) Experimental and simulated TPN PSD for a 4 mm long laser exhibiting a RR of 10.1 GHz, a pulse-width of 5.5 ps and a TJ_{ptp} of 9.7 fs for free-running operation and AO FB configuration with a TIS of $8.0 \cdot 10^{-3}$. (b) Experimental and simulated TPN PSD for a 2.5 mm long *tapered* laser exhibiting a RR of 16.0 GHz, a pulse-width of 1.1 ps and a TJ_{ptp} of 7.8 fs for free-running operation and AO FB configuration with a TIS of $4.0 \cdot 10^{-3}$.

and recurring loss of temporal overlap of intra-cavity pulse and FB pulse due to the still present random walk of intra-cavity pulse during one AO FB round-trip time together with a fixed timing deviation of the returning FB pulse. This leads to a lower TJ reduction which will be discussed in detail in subsection 5.4.5. Second, the doubled and tripled RR as compared to the 8 mm laser while keeping the FB delay or frequency almost identical results in a doubled and tripled FB length in terms of number of pulses or in other words in a doubled or tripled memory time which is the second reason for a reduced TJ.

Due to this increased equivalent FB length the effect of FB delay on the TPN PSD is studied in simulations because in experiment it is not possible to guarantee identical integer matching of FB length and PRP for different macroscopic delay lengths from 10 m to a few 100 m. Fig. 5.13a shows the simulated TPN PSDs for different FB delay lengths. It can be observed, that with increasing FB length the TPN PSD at low frequencies and the width of the noise resonance peaks decreases. The envelope of the magnitude of this noise resonance peaks stays below a maximum slope. This behavior of TPN PSD reduction is quantified in Fig. 5.13b which shows the calculated TPN PSD at 100 kHz and the corresponding RR line-width as a function of the FB delay length. Here, a frequency of 100 kHz is chosen for analysis in order to not be limited by the low FB frequency of 500 kHz. It can be observed that the TPN PSD reduces with FB length. A double-logarithmic plot (not shown) reveals a clear f^{-2} behavior of TPN PSD with FB length; therefore a corresponding fit is also given. The deviation of the simulated value at a FB length of 300 m can be attributed to the influence of the 1^{st} noise resonance peak pedestal on the PSD at the chosen frequency of 100 kHz as evident from Fig. 5.13a. Despite the usefulness of the double-logarithmic plot a semi-logarithmic plot is chosen to allow for a comparison with recent results reported in literature. Indeed in [171, Fig. 5] the RR line-width is plotted a function of FB length offset with respect to reference length of 14.6 m and shows a qualitative agreement. However, unfortunately a quantitative agreement is not possible because in [171, Fig. 5] not only the FB length was varied but also the FB strength was changed for each length. There, it can be concluded, that additional fibers or longer fibers introduce increased optical losses which were not accounted for thus resulting in weaker FB with increasing FB length and consequently in a disturbed and reduced RR line-width finally resulting in a reduced slope as compared to the ideal case. Comparing the results shown in Fig. 5.13b yielding no saturation behavior as a function of delay length with the basic idea of timing-interaction outlined by Eq. (5.5) (on page 100) which proposes a limit of TJ reduction for infinite delay length yields a contradiction. However, this contradiction can be resolved because the input terms $\Gamma_i(N)$ are predefined and fixed and do not represent a required closed-loop system. Thus, these terms only indicate the idea of AO FB and only represent an approximation. In contrast, the dynamics of a MLL subject to AO FB are well represented by the discretized differential equations (Eq. (5.9) on page 101).

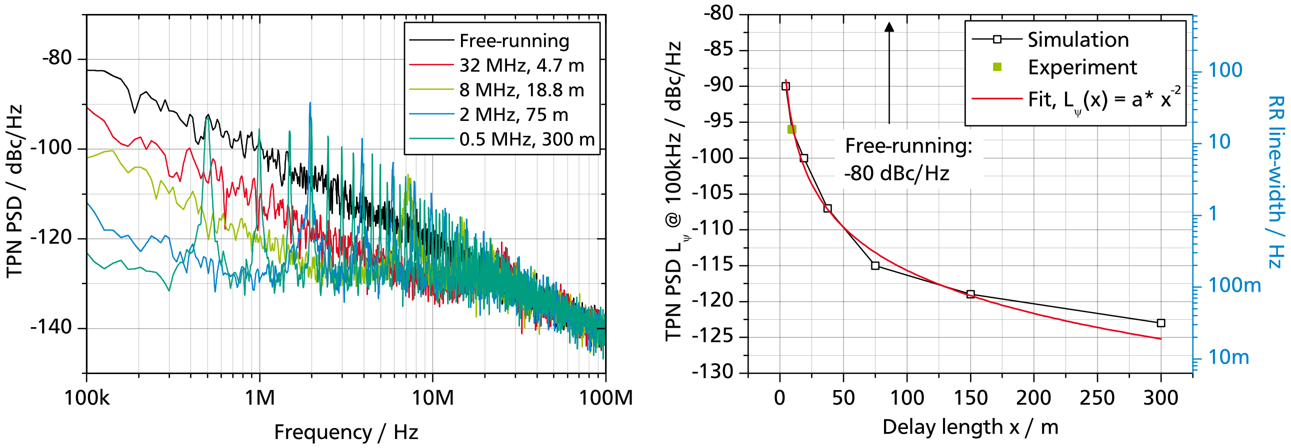

(a) **(b)**

Figure 5.13: (a) Simulated TPN PSDs for various FB lengths. (b) Simulated TPN PSD at 100 kHz (left axis) and corresponding RR line-width (right axis) as a function of FB length. The MLL parameters used for simulations are the same as in Fig. 5.12a

In conclusion, the correspondence of OE FB and AO FB in terms of TJ reduction has been demonstrated as evident from comparison of Fig. 5.7 and Fig. 5.9, respectively, as it was published in [6] and in particular by the fact, that the TJ dynamics of both schemes can be described by the same discretized differential equation (Eq. (5.9)). This underlying common mechanism of TJ reduction thus cannot be of solely optical origin because in the OE FB case the modulation is only electrical and its bandwidth contains solely the RR. Thus, the statistical part of the proposed idea of the timing-interaction as well as the timing-interaction itself has been validated. A direct comparison of the corresponding TPN PSDs has been also given in Fig. 5.14 additionally showing a further reduced TPN PSD of a combined OE FB AO FB scheme. It is evident, that a simultaneous application of these two different FB schemes is possible without disturbances and in addition beneficial. The additionally applied OE FB is capable to reduce the TPN PSD by additional $\approx$2 dB with respect to the sole but dominant AO FB scheme. Another interesting aspect of the OE FB scheme is an improved TJ reduction in a narrow frequency range from 800 kHz to 4 MHz as compared to an HML configuration which is marked with (A) in Fig. 5.14. Hereby, the same modulation power $P_{\text{mod,el}}$ is applied. This shows, that the timing-interaction in a FB scheme results in a lower TJ in a narrow frequency range as compared to an active modulation by an superior low-noise electrical oscillator.

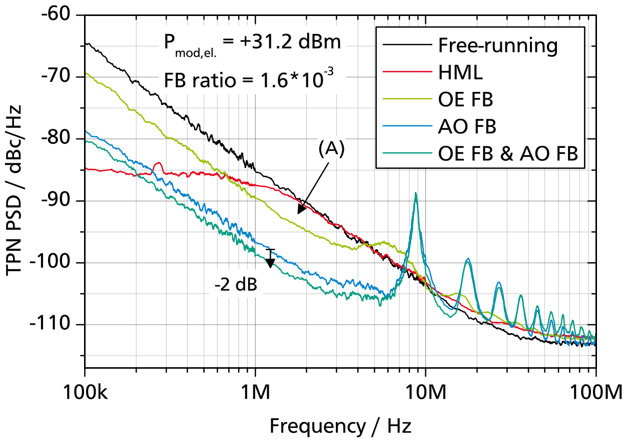

Figure 5.14: Experimentally obtained TPN PSDs for the OE FB, the AO FB and the combined configuration. The TPN PSD of the free-running MLL and the laser in HML configuration are given as a reference.

5.4.5 All-optical feedback - Non-resonant delay

Having experimentally verified the model for a MLL in resonant AO FB configuration in terms of TPN PSD or TJ reduction for integer resonant matching of the FB delay time and the PRP, it is consequent to investigate the effects of detuned or non-resonant FB delay. Delay detuning is realized by a fixed macroscopic delay in the meter range together with an additional tunable fine-delay in the micrometer range. Hereby, the dependence of delay detuning on the TPN PSD and the RR will be investigated. Having verified the timing interaction of intra-cavity pulse and FB pulse, a change of RR is naturally expected if the delay time is detuned due to a systematic timing offset of the FB pulses. The influence of detuning on TJ and RR was experimentally presented in [167, 168, 193] always showing a repetitive sawtooth-shaped dependence of RR on FB delay detuning. The observed effect of RR locking to the external FB cavity is a direct consequence of the RR manipulation by detuned FB. Here, novel TJ and RR dependencies will be reported and the numerical model is utilized to validate and explain these characteristics. In addition, the model also allows to investigate the role of pulse-width on the locking properties of a MLL subject to detuned FB which is not accessible in experiments.

The experimental setup corresponds to the setup depicted in Fig. 5.1 (b). A motorized translation stage is used to control the optical delay with the required sub-mm-scale precision and cm-scale tuning range. The MLL used for the following investigations is the same as the device used in the previous sections (do 1791 e1). The driving conditions are slightly different as compared to the conditions in the previous sections. The TJ_{ptp} now amounts to 263 fs, the optical average power (P_{opt}) and pulse width of the free running MLL amounts to around 2.6 mW and 4.1 ps, respectively. The experimental FB ratio amounts to $1.8 \cdot 10^{-3}$. The RR amounts to 5.06 GHz corresponding to a PRP of 198 ps. The experimentally realized macroscopic FB delay amounts to a FB frequency of ≈9.3 MHz which corresponds to ≈108 ns or ≈544 pulses in the external cavity. It is emphasized that the given fine-delay values in the ps range have to be understood as an offset to the macroscopic and fixed delay of ≈108 ns.

The experimental results on RR deviation as compared to the free running RR, the TPN PSD at a frequency of 1 MHz and the TPN PSD of the first noise peak at around 9 MHz as a function of the FB delay are shown in Fig. 5.15a and exhibit a highly complex behavior. Because the offset of the given fine-delay with respect to the integer matching condition is unknown, a value of zero does not correspond to the integer matching condition. The TPN PSD at 1 MHz allows to conveniently classify the different observed features because it is directly related to the RR line-width or the $\mathrm{TJ}_{\mathrm{ptp}}$ according to the relations given in section 2.4. For the free running MLL the TPN PSD at 1 MHz amounts to around −80 dBc/Hz. The plotted TPN PSD does not differ from the TPN PSD of the free running MLL for a FB delay from 0 ps up to 30 ps as well as above 175 ps up to the end of the PRP at 198 ps. In these mentioned ranges the MLL is hardly affected by the AO FB. Also five TPN PSD minima can be observed which exhibit very different values of TPN PSD reduction and are located at a FB delay of 44 ps (-4 dBc/Hz), 67 ps (+1 dBc/Hz), 94 ps (-12 dBc/Hz), 123 ps (-3 dBc/Hz) and 148 ps (-11 dBc/Hz). The delay differences of these minima amount to 23 ps, 27 ps, 26 ps and 25 ps, respectively and are obviously very similar. The minima with the highest TPN PSD reduction are located at 94 ps and 148 ps and are also accompanied by the existence of significant noise peaks which magnitude is also plotted in the figure. Such a TPN PSD reduction is *always* accompanied by the existence of noise peaks for an AO FB configuration. Both main minima exhibit a width of around 26 ps which is much wider then the measured pulse width of 4.1 ps. A very remarkable aspect is the high increase of TPN PSD around each of these main minima which amounts up to +16 dBc/Hz and relaxes down to the free running TPN PSD at larger delays away from these minima. This increased TPN PSD suggests that AO FB can induce additional TJ.

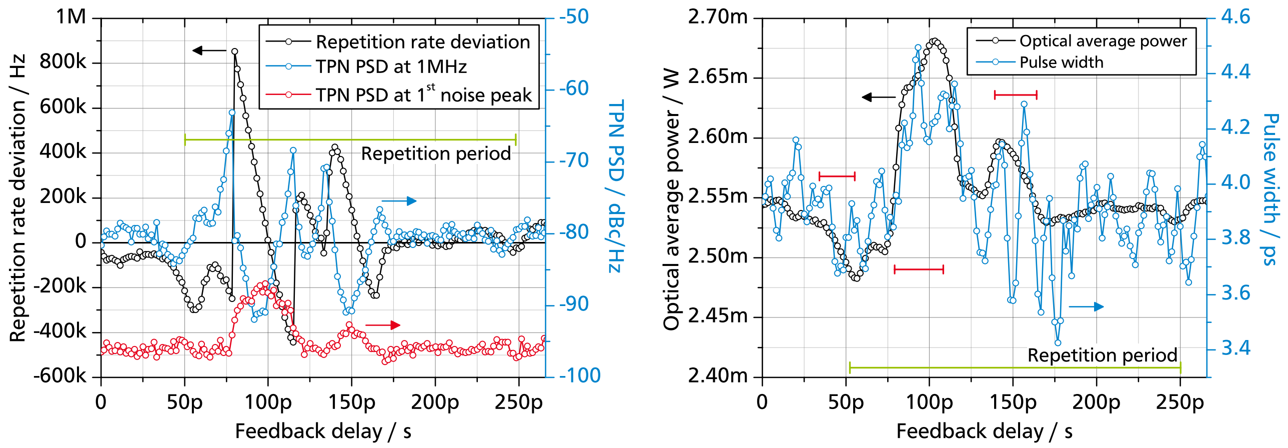

(a) (b)

Figure 5.15: (a) Measured RR deviation, TPN PSD at 1 MHz and TPN PSD at the first noise peak frequency as a function of FB delay. (b) Measured P_{opt} and pulse-width as a function of FB delay. The red horizontal bars denote the main regions of TPN PSD reduction. Operating conditions: Gain current of 165.4 mA, reverse bias of 6.00 V and FB of $1.8 \cdot 10^{-3}$.

The observed RR deviation evolution depicted in Fig. 5.15a (black plot) also shows a complex behavior over the whole PRP of 198 ps. The usual repetitive sawtooth-shaped dependence of RR deviation on

FB delay with a period corresponding to the PRP [167] is not observed here. To begin with, it must be noted, that the RR must be identical between delay points separated by the PRP. The unexpected mismatch of the RR at 0 ps and 198 ps, which should not exist, is attributed to a long-term RR drift of the free running passively MLL during the whole measurement. In addition the unexpected mismatch of the RR deviation minimum at 56 ps and 254 ps is attributed to a reduction of the FB ratio due to a slight length-dependent angle-deviation of the translation stage and thus the FB mirror. The plotted RR deviation from the RR of the free running MLL is mostly zero for a FB delay from 0 ps up to 40 ps as well as above 175 ps up to the end of the PRP at 198 ps. Again, in these ranges the MLL is hardly affected by the AO FB. Also five distinct RR deviation features can be observed. At a FB delay of 56 ps a local minimum, at a delay of 67 ps a local maximum, at a delay of 100 ps a N-shaped crossing, at a delay of 120 ps a local maximum and finally at a delay of 154 ps a sine-shaped crossing can be observed. In accordance with the TPN PSD evolution the most significant RR deviation occurs around delays of 100 ps and 150 ps. Interestingly, in both main cases the local minimum of the TPN PSD does not occur at an unchanged but clearly increased RR. This offset holds also true for the weaker feature at 120 ps. In addition, in both cases the magnitude of the positive RR deviation is higher than the magnitude of the negative RR deviation. In both cases the ratio of positive to negative RR deviation amounts to a large value of 1.9 and 1.8. In other words the speed-up of the RR is higher than the slow-down of the RR.

Experimental results on the P_{opt} and the pulse-width as a function of the FB delay are shown in Fig. 5.15b. The horizontal bars denote the ranges of highest TPN PSD reduction. Assuming a P_{opt} of 2.55 mW of the free running MLL three main features can be observed. At a delay of 56 ps a decrease of power of −2.6 %, at a delay of 103 ps an increase of power of +5.1 % and at a delay of 142 ps an increase of power of +1.8 % is observed. Although the regions of increased optical power around 103 ps and 142 ps match well with the two main regions of reduced TPN PSD a clear offset or discrepancy of the minimum of TPN PSD and maximum of P_{opt} is evident from the stated delays. The increase in optical power for these two regions can be explained by the FB pulse filling a net gain window which is not used by coherent emission [59] and thus contributes to the P_{opt}.

The measured pulse width also shows a complex behavior but significant features are evident. In general, around 50 ps the pulse width is reduced, around 100 ps the pulse width is increased and around 150 ps the pulse width does not show an overall trend. However at a delay of 45 ps a narrow minimum of pulse width, at a delay of 94 ps a narrow maximum of pulse width and at a delay of 149 ps a narrow minimum of pulse width can be observed. In fact, the delays of the pulse width extrema perfectly match the mentioned delays of the TPN PSD minima. Therefore the pulse width is a more precise indicator for the highest TPN PSD reduction than the optical power or the RR deviation. An influence of FB delay on pulse-width was also recently reported in [57]. All the mentioned delay times of the various observed parameter extrema are summarized in table 5.1. The general pulse width increase around a delay of 94 ps can be explained by the pulse reshaping mechanism under influence of a delay detuned FB pulse. The intra-cavity pulse and the added detuned FB pulse result in a combined broadened pulse via the gain and absorption dynamics (see subsection 5.4.4 on page 109). Even if the mean delay detuning of intra-cavity pulse and FB pulse is zero the timing fluctuations accumulated over the duration of one

Delay region	Minimum of TPN PSD	Zero crossing of RR	Extremum of P_{opt}	Minimum of pulse width
50 ps	44 ps	56 ps	56 ps	45 ps
100 ps	94 ps	100 ps	103 ps	94 ps
150 ps	148 ps	154 ps	142 ps	149 ps

Table 5.1: Summarized characteristics of the three main TPN PSD reduction delay regions shown in Fig 5.15a and Fig. 5.15b.

external FB delay time still result in a distribution of timing deviation with a mean of zero but with a standard deviation which is not zero thus always resulting in an increased pulse width.

As already stated, from other experimental [167, 168, 193] or numerical [169] results in literature a repetitive sawtooth-shaped or repetitive N-shaped RR trend is expected, respectively. The observed complex behavior of the RR and TPN PSD may be explained by the existence of at least two additional weak satellite pulses or satellite net-gain windows. The delay ratios of the satellite features at a delay of 148 ps and 120 ps with respect to the main feature at a delay of 94 ps and the PRP amount to 1/4 and 1/8, respectively. These ratios suggest locking dynamics of externally driven dynamical systems described by a Farey-tree used in the context of an electrically modulated SCL [194] or for the classification of a MLL subject to AO FB in [169]. Interestingly, both explanations do not contradict each other. The satellite pulses represent a physical explanation whereas the Farey-tree allows for a classification of the system dynamics as in [169].

Under the assumption of the proposed pulse-interaction between the main pulse and satellite pulse, a total of two pulses will have three possible combinations of interaction similar to an optical auto correlation. Already three pulses will have five possible combinations of interaction which matches the number of observed minima of TPN PSD in Fig. 5.15a. However, due to the low P_{opt} of the MLL no additional output pulses could be observed by means of an optical auto correlation at the investigated bias condition. But, at a increased gain current of 220 mA and an identical absorber voltage of −6.0 V satellite pulses are existent as shown in Fig. 5.16a. There, the main pulse with highest power as well as the two weaker satellite pulses all exhibit a pulse width of around 9 ps. More importantly, the delay between the pulses amounts to around 28 ps which is very close to the mean delay difference of the TPN PSD minima of 25 ps shown in Fig. 5.15a. Although the conditions at these two bias conditions are not comparable the existence of satellite pulses may be assumed. One reason for the existence of these satellite pulses might be the peculiar MLL device geometry where the first absorber section is located 2 mm away from the back facet. In such a way colliding pulse ML effects [145] could open a net gain window 4 mm after the main pulse which corresponds to the observed delay offset of 50 ps assuming a group velocity index of 3.7. In fact, the very long monolithic MLL cavity with a length of 8 mm was found to be prone to harmonic ML at different bias conditions. This is especially true for external cavity semiconductor MLL [111]. It may be helpful to note that satellite pulses have a constant delay offset with respect to the main pulse and do no oscillate independently with a different velocity.

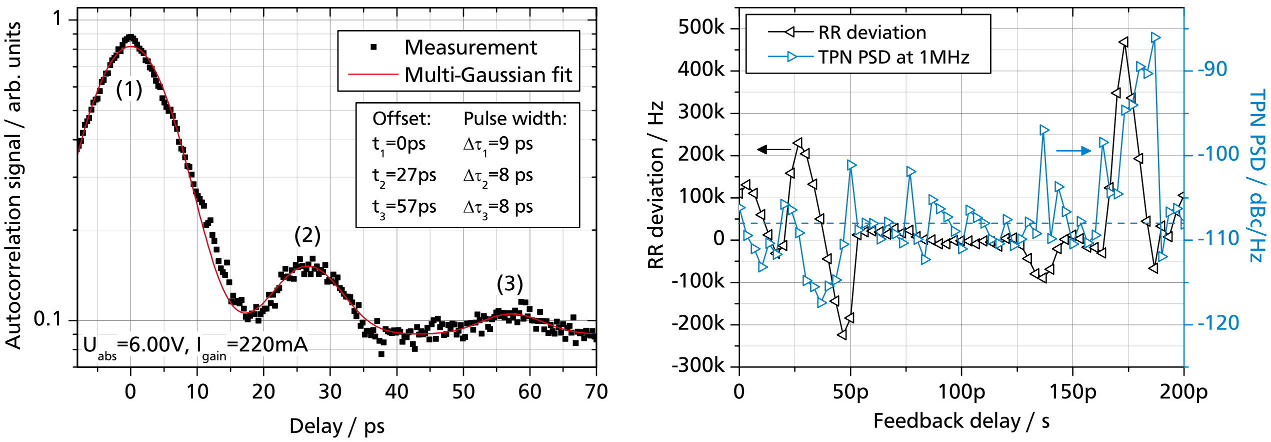

(a) **(b)**

Figure 5.16: (a) Measured optical auto-correlation signal at a increased gain current of 220 mA and an absorber voltage of −6.00 V. The given fit values denote the timing-offsets and deconvoluted pulse widths of the three optical pulses. (b) Measured TPN PSD and RR of the MLL at a gain current of 195 mA.

Such a combined measurement of TPN PSD, RR, optical average power and pulse-width was also performed at higher gain currents which exhibited lower TJ according to the results shown in Fig. 5.3b in sub-section 5.4.1 (on page 104). For example at a gain current of 195 mA (see Fig. 5.3b) TJ reduction by AO FB is also possible. Fig. 5.16b shows the experimentally obtained TPN PSD and RR as a function of the delay and they exhibit similar complex features as a function of FB delay. The free-running TPN PSD amounts to ≈-107 dBc/Hz. A TPN PSD reduction of −7 dB can be achieved with a FB ratio of $1.3 \cdot 10^{-3}$ and the correct FB delay of 37 ps. However, a massive increase of TJ is also possible which occurs at a FB delay of 187 ps. Here, the TPN PSD increase amounts to +25 dB accompanied by a small decrease of optical power in contrast to the decrease shown in Fig. 5.15b. Simulation results are not performed because the narrow RR line-width of ≈160 Hz leads to a TPN PSD below the instrument noise level for high offset frequencies which prevents the visibility of noise resonance peaks which are required for fitting. At first glance, it seems that AO FB is able to reduce the TPN PSD below the value dictated by the quantum-limited direct ASE TJ (see sub-section 2.4.3 on page 36 and sub-section 5.4.1 on page 104). However, it is noted that the source of the TJ is still unchanged and that only the TJ statistics are changed which will be explained in detail in sub-section 5.4.7.

Having described the observed experimental results, now simulation results will be presented, compared and discussed. To allow to reproduce the experimental results some minor extensions to the model have to be applied. As already pointed out in section 5.3, a detuning of the FB delay is implemented by adding a constant timing offset to the FB pulse in Eq. (5.9). This represents a change of the delay length in experiment as shown in figure 5.1 (on page 96). The changed RR (ν_{FB}) can be extracted from the simulated timing deviation evolution $T(n)$ by equation (5.13).

$$\nu_{\text{FB}} = \frac{1}{\left\langle T(n+1) - T(n) + 1/\nu_0 \right\rangle_n} \tag{5.13}$$

Hereby, $\langle\rangle_n$ denotes the average with respect to pulse number n. This Eq. (5.13) is derived from Eq. (5.6) (on page 101).

Numerical investigations will be intentionally restricted to FB delays covering two main TPN PSD minima at 94 ps and 148 ps because they are the only ones exhibiting significant TPN PSD reduction which allow an unambiguous matching of the TPN PSD in experiment and simulation. Initial simulations revealed that assuming an interaction width $\Delta\tau$ of 4 ps used in equation (5.9) which corresponds to the measured pulse width allows for good matching of experiment and simulation for a FB delay of 94 ps. However, this assumed pulse-width did not allow to reproduce the specific features of the measured TPN PSD at a delay of 148 ps. Only an interaction width of 10 ps allowed a good matching of the TPN PSD in experiment and simulation. This interaction width could be explained by an assumed temporal overlap of a 4 ps FB pulse with a 10 ps intra cavity satellite pulse[5]. Therefore the delay around 148 ps does not represent the resonant integer matching condition defined in sub-section 5.4.4 where integer multiples of the PRP match the external FB delay time. With this knowledge the other main TPN PSD minimum at 94 ps must represent the resonant integer matching condition for the main optical pulse and thus the satellite pulse. Therefore a dual timing-interaction is used in simulations for matching the TPN PSD at a delay of 94 ps. Hereby the main interaction occurs between the main intra cavity pulse with a pulse width of 4 ps and its corresponding FB pulse which was used in sub-section 5.4.4. The additional second weaker interaction occurs between the satellite intra-cavity pulse with a pulse width of 10 ps and its corresponding FB pulse. This assumed dual interaction approach is described in simulations by Eq. (5.14).

$$T(n+1)=\frac{T(n)+\sigma_{ptp}\Gamma+[\gamma_1 W_1(T(n)-T(n-n_d))+\gamma_2 W_2(T(n)-T(n-n_d))]T(n-n_d)}{1+\gamma_1 W_1(T(n)-T(n-n_d))+\gamma_2 W_2(T(n)-T(n-n_d))} \tag{5.14}$$

This Eq. (5.14) is derived from Eq. (5.9) (on page 101) which is used to model AO FB by adding a second timing term with identical delay n_d but different TIS γ_2 and different width of the weighting function W_2. Both FB pulses represented by the index 1 and 2 are locked to each other and do not represent independent FB cavities. Although the TPN PSD suggests the existence of a total of three optical pulses, only the two dominant pulses are used in simulations for simplicity.

Furthermore, to be able to reproduce the asymmetry of the RR deviation with respect to the unchanged RR as shown in Fig. 5.15a (on page 119) the Gaussian-shaped weighting interaction function $W(\Delta T)$ has to be made asymmetric with respect to the timing difference variable ΔT. Hereby, the half-width of $W(\Delta T)$ for negative ΔT is increased while the half-width of $W(\Delta T)$ for positive ΔT is decreased. In Fig. 5.17 the weighting interaction function $W(\Delta T)$ multiplied with the corresponding TIS is shown for single pulse interaction and the sum of the weighting interaction functions $W_{1,2}(\Delta T)$ multiplied with the corresponding TISs is shown for dual pulse interaction represented by the part in square brackets in equation (5.14). In simulations the increase and decrease of the mentioned half-widths is chosen to

---

[5] A Pythagorean sum in principle represents an accurate operation to calculate pulse overlapping effects and is used in the context of intensity auto-correlation [92]. However, it is not used here, because the precise relation of pulse width and interaction width is unknown.

be ±12 %. In such a way, the strength of the interaction is increased if the FB pulse is injected before the intra cavity pulse and decreased if the FB pulse is injected after the intra cavity pulse while keeping the maximum interaction strength at zero delay. This asymmetry of the weighting interaction function $W(\Delta T)$ is motivated by the non-symmetrical shape of the net-gain in the vicinity of the optical intra-cavity pulse. It is assumed, that $W(\Delta T)$ results from an overlap between the temporal intra-cavity gain shape in the vicinity of the intra-cavity pulse and the FB pulse. In such a way the main difference of the pulse-shape and the shape of $W(\Delta T)$ lies in the allowed asymmetry for $W(\Delta T)$ with respect to time which is not explainable by an cross correlation of intra-cavity pulse and FB pulse which is always symmetric with respect to time. Therefore it is unlikely that the reason of the RR asymmetry is an asymmetry of the optical pulse-shape. The impact of the AO FB on the pulse asymmetry (skewness) was recently reported in [57].

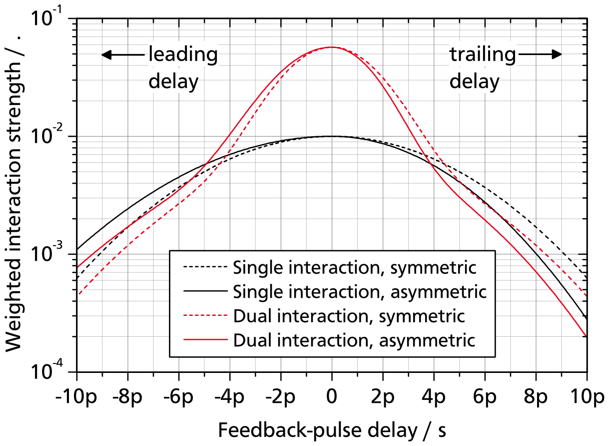

Figure 5.17: Plots of the weighting functions $W(\Delta T)$ multiplied with the corresponding TIS used in the simulations of the delay detuning.

Having introduced the necessary model changes by including a systematic timing delay to the FB pulses, by including the dual or cross interaction of the two main pulses and by including the asymmetry of the timing interaction weighting function finally a good matching of TPN PSD for the two main resonances is obtained in experiment and simulation as shown in Fig. 5.18a and Fig. 5.18b for the two main TPN PSD minima. The parameter values used for the simulation for an experimental delay of 94 ps are $\Delta\tau_1 = 4$ ps, $\gamma_1 = 5 \cdot 10^{-2}$, $\Delta\tau_2 = 10$ ps, $\gamma_2 = 7 \cdot 10^{-3}$ and a delay detuning of -3 ps with respect to the integer matching of both cavities. For an experimental delay of 148 ps the values are $\Delta\tau = 10$ ps, $\gamma = 1 \cdot 10^{-2}$ and a delay detuning of -3 ps with respect to the integer matching of both cavities.

In both cases not only the low-frequency slope up to a frequency of 3 MHz but also the magnitude and width of the noise peaks at multiples of 9 MHz are well reproduced by the simulation results. The inconsistency in noise peak amplitude in the experimental TPN PSD previous to and after 100 MHz arises from the combination of nearest neighbor averaging applied to the spectra together with a logarithmic data-point density per each decade. The resolution bandwidth (RBW) of the electrical spectrum analyzer (ESA) which is different for each decade also contributes to this deviation. As can be directly seen from the simulation results the TPN PSD of the AO FB scheme converges to the TPN PSD of the free running MLL for high frequencies. This convergence for high frequencies therefore still represents the internal TJ_{ptp}. Despite the good accordance of experiment and simulation, the experimentally obtained TPN PSD for the free-running MLL is slightly lower as compared to the expected simulated TPN PSD at frequencies above 20 MHz. This is attributed to the Gordon Haus jitter as mentioned in sub-section 5.4.1. Nevertheless, despite the different TPN PSD suppression at low frequencies and different noise peak magnitudes for the two presented FB delays an inconspicuous difference can be also observed. For the FB delay of 94 ps the TPN PSD converges to a value which is roughly 4 dB higher than the TPN PSD of the free running MLL for high frequencies and for the FB delay of 148 ps the TPN PSD converges to a value which is roughly 1.5 dB lower than the TPN PSD of the free running MLL for high frequencies. This is a sign that for the FB delay of 94 ps the internal TJ_{ptp} is increased by the AO FB and for the delay of 148 ps the internal TJ_{ptp} is decreased by the AO FB. Due to these two oppositional effects of AO FB on TJ_{ptp} by the two different delays it can be assumed, that they are independent of the proposed timing-interaction mechanism and just represent an additional and optional effect of AO FB.

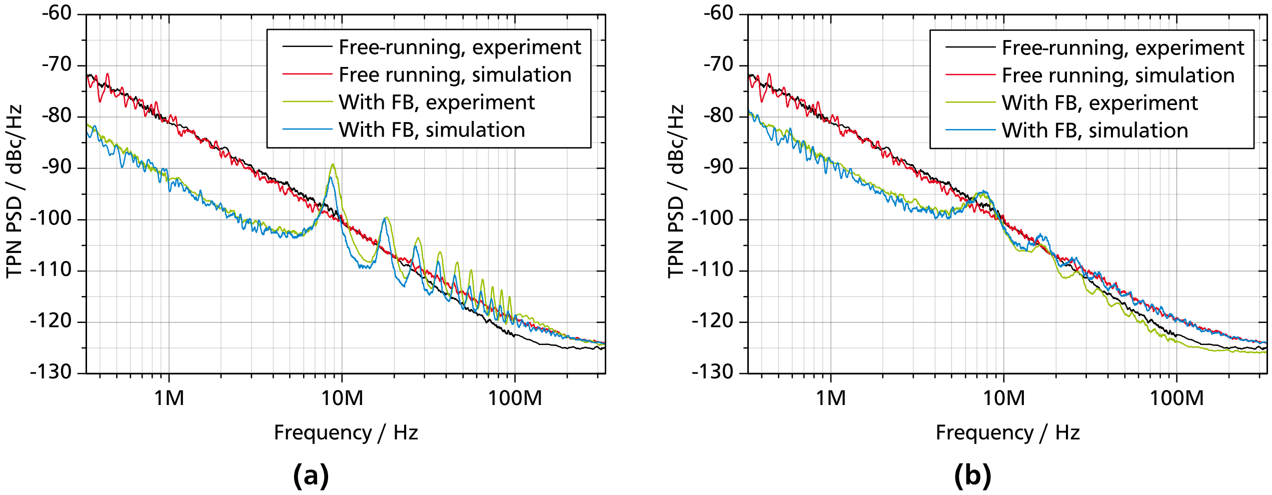

Figure 5.18: Measured and simulated TPN PSDs for an experimental FB delay of (a) 94 ps and (b) 148 ps which is defined in Fig. 5.15a and exhibits the highest TPN PSD reduction at 1 MHz.

Having presented the good accordance of the TPN PSD for the two main TPN PSD minima in experiment and simulation, now the whole delay detuning range will be investigated covering the whole PRP. In Fig. 5.19a the RR deviation as a function of FB delay is shown in experiment and simulation. Again, the two TPN PSD minima denoted by (A) and (B) are treated separately in simulation and the parameters used are identical to the ones used for calculation of the TPN PSD in Fig. 5.18a and Fig. 5.18b except for the variable delay detuning. Hereby it is emphasized, that the experimental absolute delay values are arbitrary but the delay detuning values in simulations are related to the ideal integer resonance condition at 0 ps. Alignment of experiment and simulation results in terms of delay is done by matching the RR evolution and not the TPN PSD. An unchanged RR represents integer matching of cavity length and external FB length. Therefore the experimentally realized delay of 100 ps can now be set in relation to the zero delay detuning of the simulations the latter representing the correct reference. Regarding the experimental delay range around 148 ps all observable RR deviation features including shape, magnitude, slope, asymmetry and in particular the locking range are well reproduced. Unfortunately, within the delay range around 94 ps the maximum observed RR deviations of +850 kHz and −450 kHz could not be reproduced and amount only to +432 kHz and −247 kHz in simulation, respectively. This might result from the overall complexity of the behavior of the investigated MLL. Nevertheless, the slope and the asymmetry of the RR deviation and in particular the locking range are well reproduced. The RR deviation around 130 ps was not considered in the investigations as already mentioned before and is attributed to a very weak satellite pulse. The same applies for the delay ranges around 40 ps and 60 ps.

Having shown the RR trends now in Fig. 5.19b the TPN PSD at 1 MHz as a function of FB delay is shown in experiment and simulation. Again, the two TPN PSD minima are treated separately in simulation and denoted by (A) and (B) in the figure. First of all, quite prominent is the delay offset between the results of experiment and simulation which amounts to roughly 4 ps and 2 ps for the 94 ps and 148 ps range, respectively. This offset can be conveniently explained in the picture of timing interaction and gain and absorption dynamics. The strongest pulse interaction and thus the highest TPN PSD reduction is expected to occur if the FB pulse experiences highest round-trip gain. This is mostly the case if the FB pulse overlaps the leading edge of the intra cavity pulse because this edge offers the highest gain for the chosen biasing conditions [71, 110, Fig. 6(a)]. This preceding FB pulse thus directly results in an increase of the RR. Therefore the highest TPN PSD reduction is observed in experiment for an increased RR as compared to the free-running MLL as shown in Fig. 5.15a. In simulations such a leading edge interaction offset is not considered, therefore the highest TPN PSD reduction always occurs close to the unchanged RR in simulations.

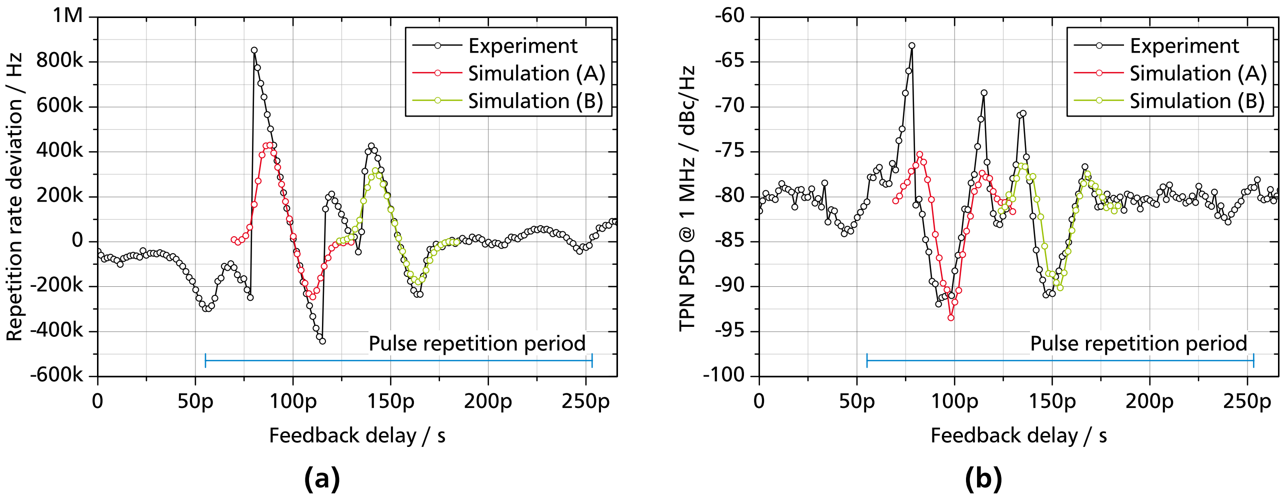

(a) (b)

Figure 5.19: (a) Measured and simulated RR deviation as a function of the FB delay. (b) Measured and simulated TPN PSD at 1 MHz as a function of FB delay. The letters A and B denote the separate simulation results for the delay range around 100 ps and 150 ps respectively.

Having explained the origin of this prominent delay offset now the results in Fig. 5.19b can be compared and discussed. For both delay ranges the shape of the TPN PSD reduction can be well reproduced including the magnitude, the width, the slopes of the minimum and the existence of local TPN PSD maxima located outside of each minimum. However, the magnitude of these simulated local maxima significantly differ from the magnitude of the measured maxima. To clarify this difference the TPN PSDs in experiment and simulation at delays corresponding to each of these local maxima are shown in Fig. 5.20a and

Fig. 5.20b. In Fig. 5.20a for an experimental delay of 78 ps a noise resonance around 1 MHz can be observed and for an experimental delay of 115 ps the shoulder-shaped TPN PSD up to a frequency of 1 MHz is a sign of increase of the RR line-width. This resonance and the increased RR line-width are not observed in the simulations for a delay detuning of −18 ps and +14 ps, respectively and their origin is unknown. Nevertheless, the general increase of TPN PSD up to 3 MHz can be qualitatively reproduced in simulations and also the existence of noise peaks at multiples of 9 MHz is implicated for both delays. In Fig. 5.20b for an experimental delay of 135 ps and 167 ps the increase of TPN PSD up to 3 MHz can be qualitatively reproduced by the simulations for a delay detuning of −18 ps and +14 ps, respectively. In addition, a higher TPN PSD at smaller delays can be observed in experiment and simulation as compared to higher delays. Altogether it is evident that detuned FB can induce a significant TJ increase. This increased TJ noise may stimulate any system resonances which could be represented by the peak at 1 MHz in Fig. 5.20a. However, such parasitics are not part of the simulations.

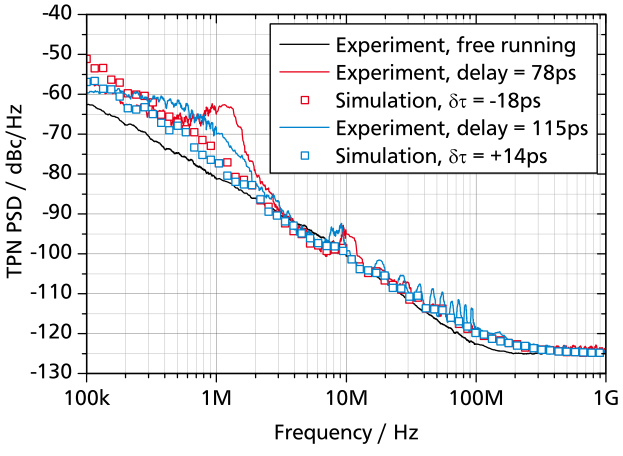

(a)

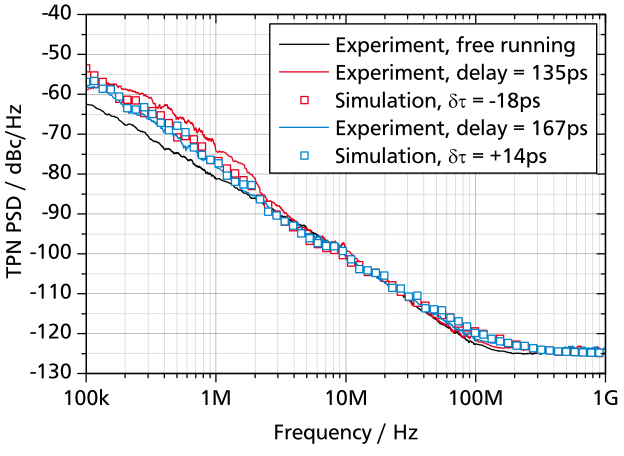

(b)

Figure 5.20: Measured and simulated TPN PSD corresponding to the highest TPN PSD for an experimental FB delay of (a) 78.3 ps and 115.0 ps and (b) 135.0 ps and 166.6 ps. Hereby, $\delta\tau$ denotes the corresponding delay detuning values in simulations.

Having verified the good accordance of simulation and experiment for detuned FB delays, now the impact of FB ratio and pulse width on RR and and TPN PSD is studied in simulations covering the main resonance at an experimental delay of 94 ps. The latter investigation is hardly possible in experiment because although the pulse-width increases almost linearly from sub 2 ps to 12 ps by increasing the gain current also the TPN PSD changes and additional instabilities occur therefore preventing an isolated investigation. In particular, the dominant source of TJ changes with increasing gain current as demonstrated in sub-section 5.4.1. In such a way also the influence of FB ratio on both parameters has to be studied in simulations to allow for a direct comparison. Fig. 5.21a and Fig. 5.21c show the simulated RR and TPN PSD at 1 MHz as a function of FB delay detuning for various pulse widths $\Delta\tau_1$ and Fig. 5.21b and Fig. 5.21d show the simulated RR and TPN PSD at 1 MHz as a function of FB delay detuning for various TIS γ. Hereby the term *delay detuning* is chosen because it highlights that a delay of zero in simulations corresponds to the ideal integer matching of RR and FB frequency. As mentioned in sub-section 5.3 pulse-width corresponds to the FWHM of the weighting function $W(\Delta T)$. If not stated otherwise, the parameters are $\Delta\tau_1 = 4$ ps, $\gamma_1 = 5 \cdot 10^{-2}$, $\Delta\tau_2 = 10$ ps, $\gamma_2 = 7 \cdot 10^{-3}$ and the weighting interaction function asymmetry corresponds to 12 %. The ratio of γ_1 and γ_2 is always kept constant at a a value of 7.1.

In Fig. 5.21a the simulated RR is shown as a function of delay detuning for various pulse-widths. Depending on the sign of the delay the RR can be decreased or increased. For a pulse-width of 2 ps the RR exhibits a sinusoidal trend as also reported in simulation results obtained by a full-featured model of a MLL subject to AO FB in [169, Fig. 11, right] thus showing the validity of the modeling approach presented here. The ratio of maximum and minimum RR deviation amounts to a value of 2 for a pulse-with of 2 ps. This asymmetry of RR detuning decreases gradually down to a ratio of 1.13 for a pulse-width of 16 ps. By increasing the pulse-width the sinusoidal shape gradually changes to an N-shape and also the locking range increases from ≈45 ps to ≈82 ps while keeping the FB strength constant. The shown N-shape or equivalently a limited-locking range was not observed experimentally in literature so far. Hereby, it is noted that a pulse-width of 16 ps amounts to only 8 % of the PRP of 198 ps and allows for a much larger locking range of 41 % of the PRP. The width of the outer regions showing the loss of the locking amounts to a constant value of ≈10 ps. All RR deviation trends align to a common RR line. This line represents the ideal locking condition given by Eq. (5.15)[6].

$$\Delta\nu_0 = \nu_0 \left[(1 - \delta\tau \cdot \nu_{\mathrm{ext}})^{-1} - 1 \right] \tag{5.15}$$

Hereby $\Delta\nu_0$ denotes the deviation from the free-running RR, ν_0 the RR, $\delta\tau$ the delay detuning and ν_{ext} the FB frequency.

In Fig. 5.21b the RR as a function of delay detuning is shown for various TIS which corresponds to a FB strength in experiment. The pulse-width amounts to 4 ps. Increasing the TIS keeps the sinusoidal shape while increasing the locking range. However, the increase of TIS does not have a comparable large impact on the locking range and RR deviation as the increase of the pulse-width shown in Fig. 5.21a.

In Fig. 5.21c the TPN PSD at 1 MHz as a function of delay detuning is shown for various pulse-widths. In general, for a pulse-width of 2 ps and 4 ps the TPN PSD yields the already reported behavior including the minimum which has an offset of ≈-2.5 ps with respect to the integer matching condition as well as the increase of TPN PSD at the locking borders. This offset is constant for all shown pulse-widths. The increase of the TPN PSD at the locking borders is maximal at a pulse width of 4 ps and decreases for further increasing pulse-width. As already evident from Fig. 5.21a the locking range increases with increasing pulse-width. Most interestingly, a saturation of the highest TPN PSD reduction can be observed with increasing pulse-width. The reduction increases from a pulse-width of 2 ps to 8 ps and reaches its highest value at a pulse width of 16 ps.

In Fig. 5.21d the TPN PSD at 1 MHz as a function of delay detuning is shown for various TIS and a pulse-width of 4 ps. As already evident from Fig. 5.21b the locking range increases with increasing TIS.

---

[6] This equation can be comprehensively derived by distributing a given delay detuning among all pulses of a FB loop and calculating the new RR.

Again, the highest TPN PSD reduction is observed at an offset of ≈-2.5 ps. An increase of the TPN PSD at the locking borders is always observed for the selected pulse-width of 4 ps. In contrast to Fig. 5.21c a gradual increase of the TPN PSD reduction with increasing TIS can be observed. No saturation of reduction is observable which is in accordance with experimental results shown in Fig. 5.9. In contrast to Fig. 5.21c no minimal TPN PSD plateau is observed.

The simulation results in Fig. 5.21d also qualitatively reproduce the experimental results reported in [56, Fig. 1(a)] for an attenuation of 53 dB down to 32 dB.[7] Simulations reproduce the asymmetric and increased locking range with increased FB strength denoted by regime 5 and 4 in [56]. However, the regimes 3 to 1 in [56] were never observed in experiment or simulation here.

The presented behavior can be explained by means of the developed timing-interaction picture. The timing-interaction weighting function $W(\Delta T)$ (see Fig. 5.17 on page 124) representing the interaction of intra-cavity pulse and returning FB pulse plays an essential role. Hereby the width of $W(\Delta T)$ is closely related to the pulse-width. It is assumed that $W(\Delta T)$ results from an overlap of temporal **intra-cavity gain shape** in vicinity of the intra-cavity pulse and the FB pulse. Only in such a way $W(\Delta T)$ can be asymmetric with respect to time. In contrast, a direct optical pulse-to-pulse interaction is always symmetric. Such an symmetrical interaction is similar to an optical auto-correlation which is always symmetric. Thus, applying AO FB may be regarded as a kind of probing of the of the gain shape by the optical FB pulse.

As already mentioned, the **RR deviation slope** is given by Eq. (5.15) (on page 128) and states, that decreasing the macroscopic FB length results in an increased RR slope and thus potentially an increased maximum RR deviation. However, the locking range cannot be explained by this equation.

To understand the large **FB locking range** as compared to the pulse-width one has to take into account the random walk characteristics of the MLL. The chosen FB frequency of 9.3 MHz together with the RR of 5.06 GHz leads to $N_\mathrm{d} \approx 544$ pulses in the external cavity. Using a TJ_ptp of 154 fs leads to a standard deviation (SD) after one round-trip in the external cavity of $\sigma_\mathrm{ptp}\sqrt{N_\mathrm{d}} = 154\ \mathrm{fs}\sqrt{544} = 3.6\ \mathrm{ps}$ which is, together with the FWHM pulse-width of 4 ps, a proper base for the locking range which can be approximated by the FWHM measure $\sqrt{2(3.6\ \mathrm{ps}\cdot 2.35)^2 + (4\ \mathrm{ps})^2} \approx 12\ \mathrm{ps}$. Now, the FWHM of a Gaussian function amounts to 50 % of the maximal value. Knowing that AO FB is effective for very weak FB ratios which is evident from Fig. 5.11 this FWHM of 12 ps has to be multiplied towards much larger values in order to account for this high FB sensitivity which may lead to a locking range of ≈50 ps shown in Fig. 5.21b. This discussion also explains why the pulse-with has a bigger impact on the locking-range as compared to the FB strength given by the TIS. Nevertheless, the RR deviation is ultimately limited in a real MLL by the flexibility of the group-velocity of the optical pulse in the active medium.

To explain the **decreasing TJ reduction for increasing delay detuning** the shape and width of $W(\Delta T)$ is important. First, let us assume integer matching of internal and external cavity length. The MLL subject to AO FB exhibits a random walk. Therefore the mean timing-deviation of the internal oscillating pulse

---

[7] Although only the *peak* power of the RR is plotted it can be assumed, that the integrated power of RR line is constant thus increasing in peak power if the line-width is reduced which in turn is related to an TJ reduction.

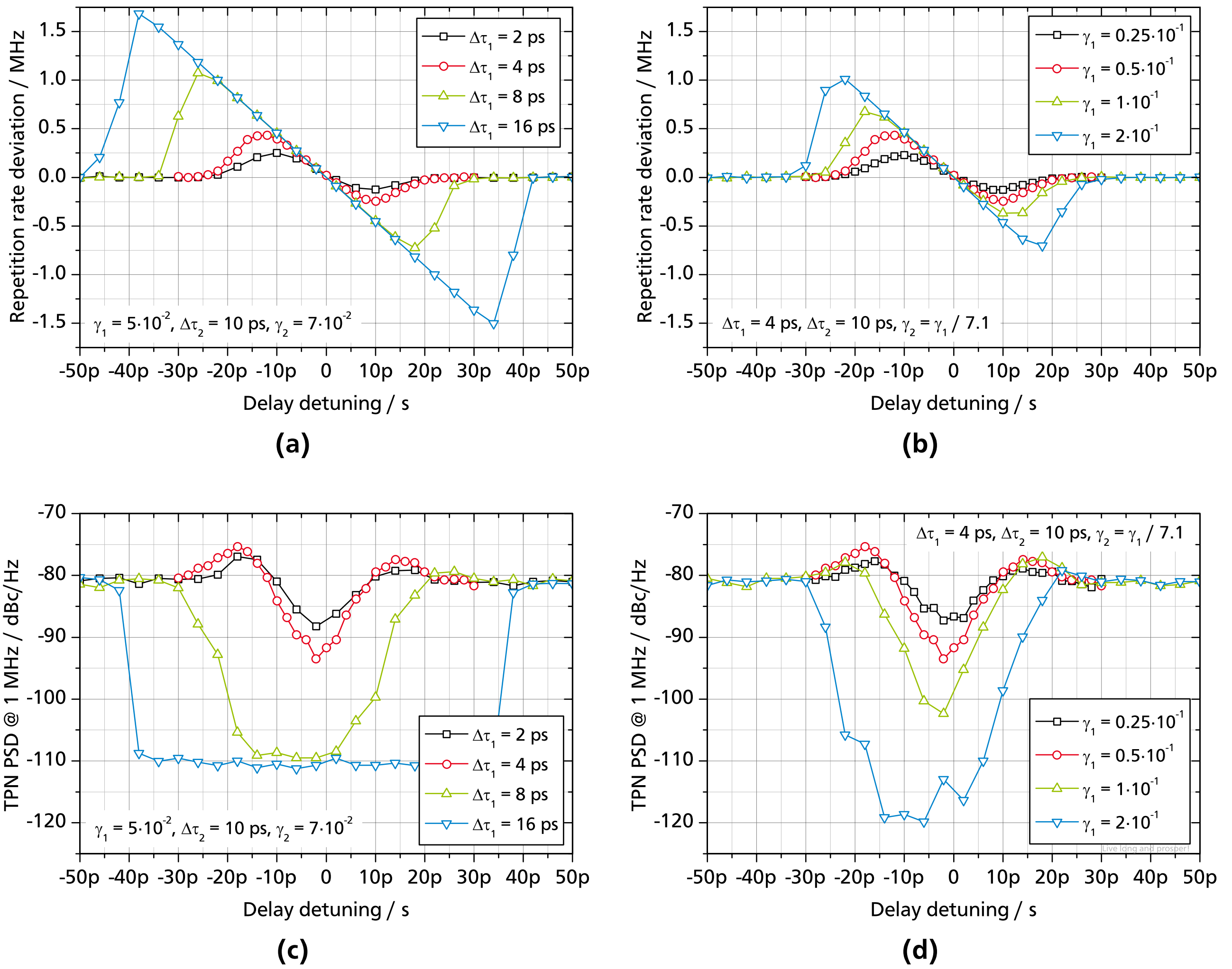

Figure 5.21: Simulated results corresponding to an experimental FB delay of 100 ps. If not stated otherwise, the parameters are $\Delta\tau_1 = 4$ ps, $\gamma_1 = 5 \cdot 10^{-2}$, $\Delta\tau_2 = 10$ ps, $\gamma_2 = 7 \cdot 10^{-3}$ and the weighting interaction function asymmetry corresponds to 12 %. (a) Simulated RR as a function of the FB delay for various pulse-widths $\Delta\tau_1$. (b) Simulated RR as a function of the FB delay for various TIS γ_1. (c) Simulated TPN PSD at 1 MHz as a function of the FB delay for various pulse-widths $\Delta\tau_1$. (d) Simulated TPN PSD at 1 MHz as a function of the FB delay for various TIS γ_1.

and of the returning pulse-train is zero. In such a way the mean temporal overlap of intra-cavity pulse and returning pulse is maximal leading to maximal timing-interaction of both and thus to the strongest TPN PSD reduction. By increasing the FB delay detuning the mean timing deviation of the returning pulse-train deviates from the mean intra-cavity pulse timing systematically. In such a way the mean temporal overlap of intra-cavity pulse and returning pulse represented by $W(\Delta T)$ is reduced leading to a reduced timing-interaction and thus a weaker TPN PSD reduction for non-zero FB delay detuning.

The **asymmetry of the maximum RR deviation** is a consequence of the introduced asymmetry of the pulse-width defined by $W(\Delta T)$ which is shown explicitly in Fig. 5.17 (on page 124). Without this asymmetry the trends of the RR and the TPN PSD would be symmetric as shown in Fig. 5.22. Although an **offset of the zero crossing of RR and the minimum of TPN PSD** is provided by simulations as shown in Fig. 5.22 (on page 131) partially resulting from asymmetry of $W(\Delta T)$ it is unfortunately not enough to reproduce the offset in experiment as shown in Fig. 5.19b (on page 126). This remaining mismatch is attributed to an offset between the temporal gain position and the temporal intra-cavity pulse position which has been discussed on page 126. The chosen asymmetry of 12 % which increases the interaction-strength of the leading edge of the timing-interaction leads to an potential for higher leading-edge detuning which ultimately allows higher positive RR deviations as compared to negative RR deviations. Therefore a study of the RR deviation allows to gain insight into the temporal gain shape in the vicinity of an optical pulse. To be precise $W(\Delta T)$ describes the overlap of the gain shape and the pulse shape. A large positive RR deviation as compared to negative RR deviation may be a sign of a so called leading edge instability (LEI) which originates from a net gain window leading the optical pulse [69, Fig. 5(c)] or [178, Fig. 8(b)]. Whereas a large negative RR deviation as compared to positive RR deviation may result from a so called trailing edge instability [69, Fig. 5(b)] or [178, Fig. 8(a)].

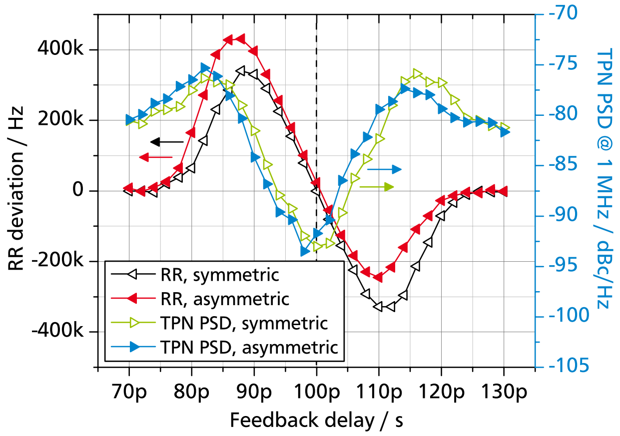

Figure 5.22: Simulated RR and TPN PSD for a symmetric and asymmetric timing-interaction function $W(\Delta T)$. The displayed case corresponds to the experimental results shown in Fig. 5.15a.

The **saturation of the TPN PSD reduction for increasing pulse-width** originates from a reduced mean TIS for short pulse widths with respect to the standard deviation (SD) of the random walk of the pulses in the FB cavity mentioned above. If the SD of the external cavity amounting to $\sigma_{\mathrm{ptp}}\sqrt{N_{\mathrm{d}}} = 154\ \mathrm{fs}\sqrt{544} =$ 3.6 ps is similar or larger than the pulse-width the intra-cavity pulse and FB pulse do not always overlap inside the cavity statistically resulting in a reduced equivalent FB strength. If the pulse-width is much larger than the SD which is the case for a pulse width of 8 ps the SD cannot statistically detune the intra-cavity pulse and the FB pulse. In such a way the full TIS is accessible which is represented by the plateau in Fig. 5.21c. Extrapolating this knowledge towards varying macroscopic FB lengths should result in a decreased locking range for increased FB length because the SD scales with the square-root of the FB length.

Regarding the reason for the **increased TPN PSD at the borders of the locking range** only guesses can be made. For the highest delay detuning within the locking range the mean temporal overlap of intra-cavity pulse and returning pulse is only located on the opposite wings of both pulses. In such a way the timing interaction occurs only for a single case of the negative delay detuning: If the intra-cavity pulse has a negative timing deviation and the FB pulse has a positive timing-interaction the resulting pulse will still have an increased negative timing deviation due to the adjusted negative delay. This breaking of statistical symmetry results in increased noise. This is supported by the mismatch of the locking range defined by the RR detuning and the TPN PSD reduction. The locking range defined by the TPN PSD reduction is much smaller than the locking range defined by the change of the RR. This means, that the statistical effect responsible for TPN PSD reduction requires a significant overlap of intra-cavity pulse-width and the pulse-width of the FB pulse broadened by the SD of the random walk. In contrast, a RR tuning can be achieved with a partial overlap only.

The expected **increase of TPN PSD reduction with increasing FB strength** shown in Fig. 5.21d opens the question if a TIS higher than 1 would have an beneficial effect. Despite the experimental difficulty due to the requirement of an optical amplifier a coherence collapse may occur at high FB strengths. According to the assumption based on Eq. (5.5) (on page 100) a TIS of 1 should have highest TJ reduction at first glance and due to the stochastic independence and identical SD of the random sequences $\Gamma_1(N)$ and $\Gamma_2(N)$ a TIS of 0.5 should naively correspond to an inverse TIS of 2. However, the MLL is described as a dynamical system by a discretized differential equation (Eq. (5.9) on page 101) therefore $\Gamma_i(N)$ cannot be assumed as being stochastically independent. In fact, simulations with a TIS higher than 1 yield further improved TPN PSD reduction at frequencies below the frequency of the fist resonance peak and the line-width of the resonance peaks decreases with increasing FB strength.

In summary the influence of detuned FB with respect to integer matching of the FB frequency and RR has shown a manifold of interesting effects. The presented simple model can reproduce all the trends of the TPN PSD and the RR and in particular the two locking ranges defined by RR and TPN PSD reduction. Hereby, the importance of the pulse-width for the width of the locking ranges is identified. The results obtained by this simple model qualitatively correspond to the results obtained by a full-featured model presented in [169] for short delays. Most importantly, due to the simplicity of the model and the developed timing-interaction picture a comprehensive explanation of the observed features can be given here. Using this knowledge, such delay-detuning AO FB experiments allow to reveal the internal dynamics of a MLL by a careful interpretation of the results.

5.4.6 Optical pulse train injection

To further emphasize the time-domain based picture of TJ, in the following the AO FB or in other words optical self-injection scheme is extended towards an external OPTI by means of a master and a slave MLL. Such an injection approach was qualitatively investigated in [195] and was applied in [196] to reduce the optical pulse-width. Here, a hybridly MLL is used as the master MLL, to force the RR of the master MLL onto the RR of the slave MLL and to be able to clearly see a potential TPN PSD reduction due to the completely different characteristics of the TPN PSD of master and slave MLL. Biasing conditions of the master MLL are adjusted to allow for a spectral overlap with the slave MLL to ensure the possibility of direct optical interaction. The master MLL is operated at a temperature of 14.6 °C, a reverse bias voltage of −4.4 V, a gain current of 84.5 mA and a modulation power of +16 dBm. The TJ_{ptp} of the free running master MLL amounts to 46 fs corresponding to an RR line-width of 1.7 kHz. In Fig. 5.23 the measured and corresponding calculated TPN PSD of the slave MLL in OPTI configuration are shown for different injection ratios κ and corresponding TIS γ, respectively. Injection ratio is defined as the ratio of master MLL input power to slave MLL output power. In the experiment, at a low injection ratio of $1.5 \cdot 10^{-3}$ a broad band reduction of TPN PSD in the low frequency region is observed with a reduction of 5 dB up to a frequency of 1 MHz. At an increased injection ratio of $3.0 \cdot 10^{-3}$ the TPN PSD reduction is significantly higher with a reduction in the range of 20 dB up to a frequency of around 200 kHz and at higher frequencies with a reduction in the range of 5 dB. Finally at an injection ratio above $3.0 \cdot 10^{-3}$ the TPN PSD of the slave MLL completely matches the TPN PSD of the master MLL thus successfully demonstrates optical time-domain locking of the timing jitter. In addition, OPTI represents an experimentally convenient way to optically transfer and distribute the TJ characteristics from one MLL with low TJ to multiple slave MLLs.

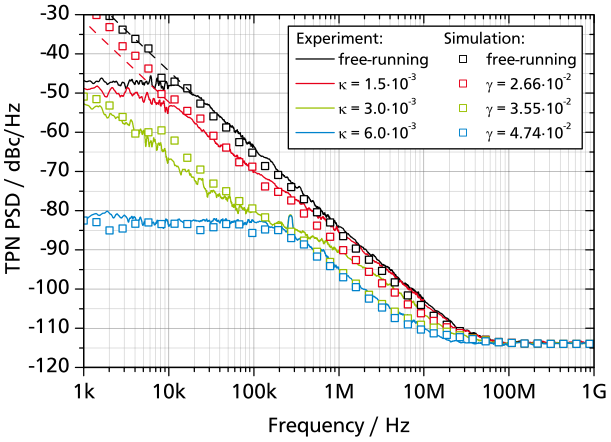

Figure 5.23: Measured and corresponding calculated TPN PSDs of the slave MLL in OPTI configuration for different injection ratios and corresponding TIS, respectively. The TPN PSD for the free-running MLL is given as a reference. Dashed lines indicate extrapolation of experimental TPN PSDs.

In the simulations the master TPN PSD is characterized by a $\mathrm{TJ}_{\mathrm{ptp}}$ of 46 fs and a γ of $3 \cdot 10^{-4}$ for HML operation. The timing interaction width $\Delta\tau$ is kept at 4 ps. The parameter TIS was varied to obtain best possible matching of TPN PSD in simulation and experiment. In general the accordance of experimental and simulated TPN PSD is good and the TJ locking effect can be well reproduced. However, clear differences are evident for a injection ratio κ of $3 \cdot 10^{-3}$ in the frequency range above 300 kHz which may originate from the different performance of the two MLL. First the master and slave MLL have a different spectral width of 0.5 nm and 3.4 nm respectively and second the pulse width of the master MLL could not be estimated due to non-sufficient P_{opt} for nonlinear auto-correlation. Nevertheless simulations reproduce the discontinuous transition from TPN PSD reduction to complete TJ locking above a TIS of $3.55 \cdot 10^{-2}$ thus extending the validity of the timing-interaction approach. In addition, in simulations it is evident, that at TIS values slightly below $3.55 \cdot 10^{-2}$ the occurrence of locking was achieved not for all simulation runs thus indicating the stochastic nature of the locking itself. At this TIS value locking can occur in the middle of the simulation run only or even be lost which is reflected in the simulation result as a superposition of locked and unlocked TPN PSD.

To substantiate the correspondence of the all-optical AO FB and OPTI Fig. 5.24 shows the interaction strength γ as a function of the corresponding FB ratio or input ratio of the AO FB or OPTI configuration, respectively. Both optical configurations yield an almost identical dependency of TIS on input ratio thus validating the proposed TJ interaction also in the OPTI case. In particular, the presented model does not incorporate any coherence effects or optical-mode locking effects and solely relies on the continuous timing-interaction. Sub-harmonic OPTI was also reported in literature [197]. Hereby, it is assumed, that such sub-harmonic injection simply corresponds to fundamental OPTI with reduced injection strength or reduced TIS in simulation.

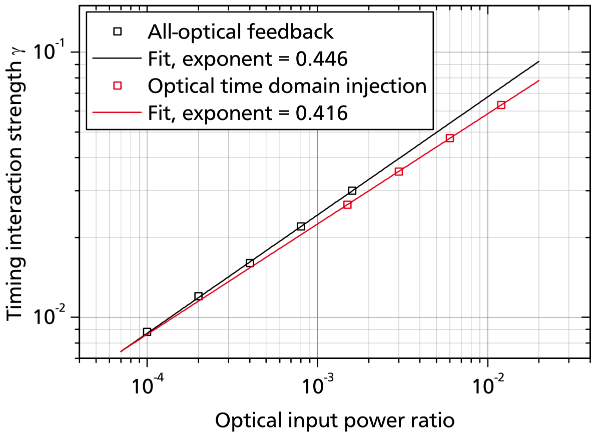

Figure 5.24: TIS as a function of the corresponding FB ratio or input ratio of the AO FB or OPTI configuration, respectively yielding almost identical dependence.

5.4.7 Time domain picture

The TPN PSD can be obtained conveniently in experiment and contains much information about the characteristics of the TJ. The direct time-domain representation of the TJ experimentally investigated in [198] allows for a complementary insight into the different presented mechanisms as well as a clarification of the different quantities used for the description of the TJ. However, experimental access to such a time-domain measurement is complicated. But due to the correspondence of the results from simulation and experiment the time domain data obtained by the developed simulations can be used for these investigations.

A calculated time-domain representation of the absolute timing *deviation* of the MLL with respect to an ideal oscillator is shown in Fig. 5.25 for a single simulation run. Averaging is not applied in order to not eliminate important features. There, the absolute timing deviation of a pulse is shown as a function of the pulse number for the free running MLL with a $\mathrm{TJ}_{\mathrm{ptp}}$ of 152 fs, for the AO FB configuration with a FB ratio of $3 \cdot 10^{-2}$ ($\gamma = 3.0 \cdot 10^{-2}$), for the OE FB configuration with P_{mod} of +31.2 dBm ($\gamma = 1.10 \cdot 10^{-3}$) and HML with an P_{mod} of +31.2 dBm ($\gamma = 1.10 \cdot 10^{-3}$). It can be seen that for the free-running MLL the timing deviation performs a random walk which may lead to an unlimited accumulation of timing deviation for unlimited time-scales. This is a direct consequence of the accumulation of Gaussian distributed pulse-to-pulse timing deviations driven by direct emission of spontaneous emission onto the optical pulse per round-trip. In the AO FB configuration the walk is significantly reduced on this selected time-scale and in addition a particular periodicity is evident with a period of $n_d = 538$ pulses. This periodicity directly corresponds to the resonance peaks shown in the TPN PSD in Fig. 5.9 and represents a recurring noise-pattern which is partially preserved and even enhanced by the external delay. This external delay therefore represents an effective timing noise memory of the system. Hints of this periodicity can also be observed in the OE FB case. The occurrence of the noise resonance peaks is directly related to the statistical mechanism of TJ reduction. If such noise resonance peaks are not observed in experiment for an AO FB configuration which exhibits reduction of the TPN PSD then a completely different mechanism is responsible for TPN PSD reduction. Relatively strong AO FB for example can change the steady state condition of the MLL thus resulting in different behavior and parameters.

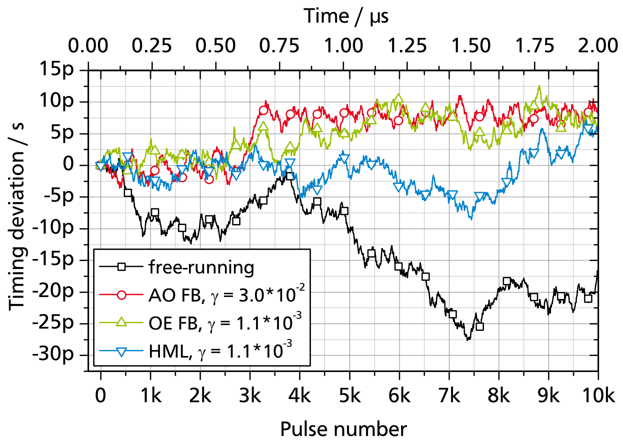

Figure 5.25: Calculated timing deviation T of a pulse as a function of the pulse number n for the free running MLL, the AO FB configuration, OE FB configuration and HML.

For the HML operation the timing deviation is also reduced and tends to be located around a value of 0 ps. Calculating the mean of the timing difference of consecutive pulses yields the expected $\mathrm{TJ}_{\mathrm{ptp}}$ for the passively MLL with a value of around 152 fs. But also for all the other presented schemes the $\mathrm{TJ}_{\mathrm{ptp}}$ amounts to a value around 152 fs. This is clear because from the presented model the noise source ($\mathrm{TJ}_{\mathrm{ptp}}$), namely the spontaneous emission, is hardly influenced by the TIS which for example for the HML operation is three orders of magnitude smaller ($\gamma = 1.10 \cdot 10^{-3}$) than the noise source (σ_{ptp}) itself. As a consequence of the unchanged noise source the TPN PSD is unchanged with respect to the free-running case at very high frequencies above 1 MHz which is most clearly seen for HML in Fig. 5.5 (on page 107). Even for AO FB the TPN PSD is not reduced at very high frequencies above 10 MHz as seen in Fig. 5.9 (on page 111). To conclude, the $\mathrm{TJ}_{\mathrm{ptp}}$ represents solely the unchanged noise-source-strength of the MLL and the TPN PSD represents in addition the important statistical and spectral distribution of TJ. It should be noted that significant TPN PSD reduction and the occurrence of TPN PSD resonances can only be achieved for ratios of FB length to MLL cavity length higher than $1 \cdot 10^2$ due to the required long timing memory of the delay line. Therefore too small ratios used in literature to study FB effects will not reveal statistical timing interaction effects. However, short external cavity FB may change the steady state condition of the MLL thus potentially change the TJ characteristics.

For a random walk process it is known that the dependence of the root mean square (RMS) or SD $\sigma_{RMS}(n)$ of the timing deviation on pulse number n follows a square-root law with $\sigma_{RMS}(n) = \beta\sqrt{n}$ with β describing the standard deviation of the timing deviation per pulse. In Fig. 5.26 $\sigma_{RMS}(n)$ obtained from 100 simulation runs is visualized for the free running MLL, for the AO FB configuration, for the OE FB configuration and for HML. For the free running MLL the law is fulfilled yielding a β of 144 fs close to the expected value of 152 fs which corresponds to $\mathrm{TJ_{ptp}}$. For the AO FB and OE FB configuration the standard deviation σ also follows the square-root law therefore both FB schemes still represent a random walk. However, hereby a reduced β of 37 fs and 102 fs is obtained for the AO FB and OE FB configuration, respectively which correspond well to the values of 36 fs and 94 fs obtained by applying equation (5.3) (on page 98), which is only valid for free running MLL and the RR line-width while excluding the resonance peaks. Thus for both FB schemes β or the RR line-width reflect a measure of the low-frequency fluctuations or the long term drift $\mathrm{TJ_{lt}}$ but disregard the high-frequency timing noise contributions [5]. The validity of this long-term measure was recently verified in [58]. Finally, the HML operation exhibits a bounded timing deviation or a time-independent RMS of around 5 ps as expected thus not representing a random walk process.

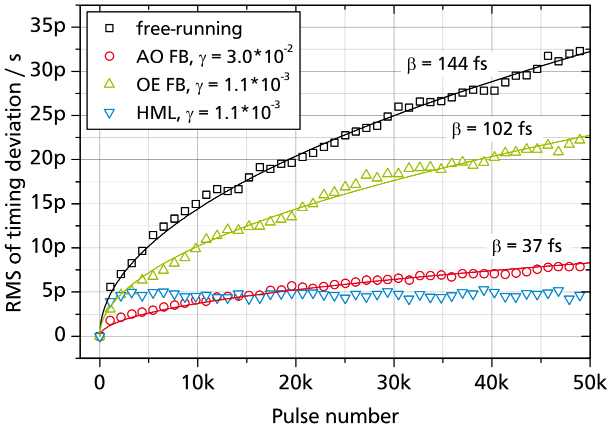

Figure 5.26: Standard deviation σ_{RMS} of the pulse timing deviation as a function of the pulse number n for the free running MLL, the OE FB configuration, AO FB configuration and HML. β describes the mean long term drift obtained from a fit represented by the solid lines.

At this point a deeper discussion of the quantification of TJ in the case of AO FB is reasonable. As shown above, the long-term TJ β which can be obtained from the RR line-width describes the TJ on long time scales. This is represented by the TPN PSD reduction at frequencies well below the noise resonance peaks. The question arises if a TJ reduction is also given for the whole frequency range. To allow a quantification the $\mathrm{TJ}_{\mathrm{int}}^{(f_1,f_2)}$ can be used by integrating the TPN PSD over the maximum frequency range. Fig. 5.27a shows the calculated TPN PSD for a free-running MLL and the AO FB configuration for operating conditions as in Fig. 5.18a in sub-section 5.4.5. In addition the $\mathrm{TJ}_{\mathrm{int}}^{(f_1,f_2)}$ is also plotted as a function of the upper integration frequency f_2 and a lower integration frequency f_1 of 100 kHz. For both displayed cases it is evident that the dominant part of $\mathrm{TJ}_{\mathrm{int}}^{(f_1,f_2)}$ originates from low frequencies and that a saturating behavior of $\mathrm{TJ}_{\mathrm{int}}^{(f_1,f_2)}$ occurs with increasing frequency. The $\mathrm{TJ_{ptp}}$ for the free-running MLL and the AO FB configuration saturates at a value of 12.6 ps and 4.1 ps, respectively. This shows, that AO FB is able to reduce the total TJ by domination of the low-frequency part of the TPN PSD. This saturating behavior for the free-running MLL results from an integration of the f^{-2} slope by Eq. (5.1) leading to a saturating function. The same trend also applies for the AO FB configuration even with the existence of the noise resonance peaks. Another question deals with the high frequency part of the TPN PSD namely if the noise resonance peaks increase the total $\mathrm{TJ}_{\mathrm{ptp}}$ for the high frequency part. Hereby a lower integration frequency of 4.25 MHz is chosen as it represents the half of the frequency of the noise resonance peak. Fig. 5.27b shows the calculated TPN PSD and the $\mathrm{TJ}_{\mathrm{int}}^{(f_1,f_2)}$ for both cases. It can be observed, that the saturation behavior still occurs. The $\mathrm{TJ}_{\mathrm{ptp}}$ for the free-running MLL and the AO FB configuration saturates at a value of 1.96 ps and 1.78 ps, respectively. This slight reduction of TJ in the high frequency part can be expected. But in the worst case only a redistribution of TJ with respect to the free-running case takes place. Summing up, AO FB not only reduces the low frequency part of TJ represented by $\mathrm{TJ}_{\mathrm{lt}}$, β or the RR line width but also reduces the the total TJ represented by $\mathrm{TJ}_{\mathrm{int}}^{(f_1,f_2)}$. The high frequency part of TJ is almost unchanged.

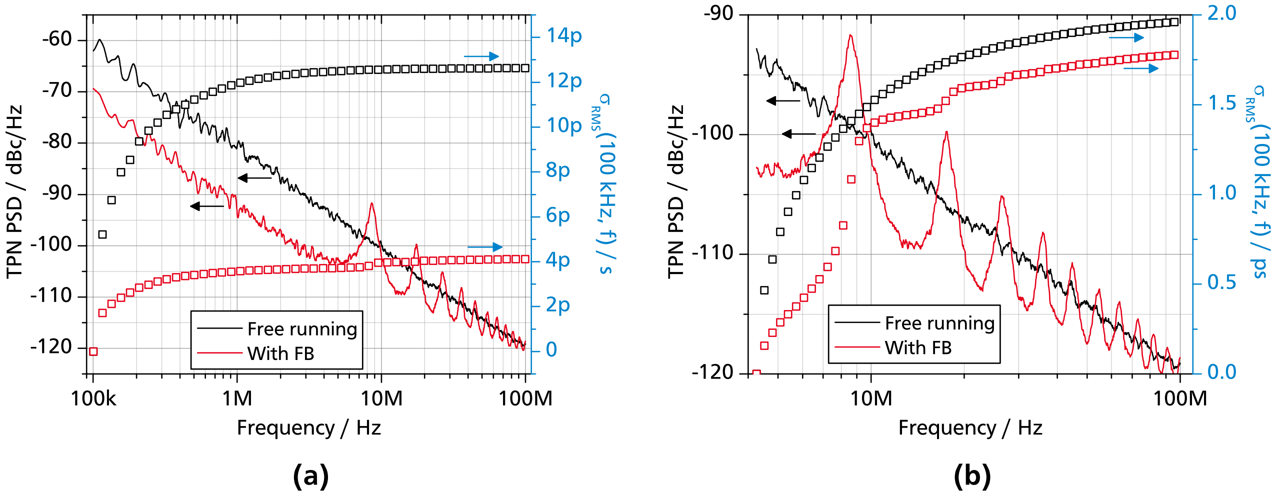

Figure 5.27: Simulated TPN PSD for a free running MLL and a AO FB configuration as well as the corresponding $\mathrm{TJ}_{\mathrm{int}}^{(f_1,f_2)}$ as a function of the upper integration frequency f_2 (a) for a displayed frequency range of 100 kHz to 100 MHz and (b) a displayed frequency range of 4.25 MHz (corresponding to half of the frequency of the noise resonance peaks) to 100 MHz. The lower integration frequency f_1 of $\mathrm{TJ}_{\mathrm{ptp}}$ corresponds to 100 kHz and 4.25 MHz for plot (a) and (b), respectively.

As the calculated $\mathrm{TJ}_{\mathrm{ptp}}$ from Fig. 5.25, representing the timing noise source strength, is found to be unchanged in all investigated configurations a different strategy has to be pursued to target this timing noise source directly to further reduce the TJ. In [70] it was found, that in a passively MLL a net gain window [59] may exist outside the optical pulse position, either preceding or succeeding the main optical pulse. This net gain window amplifies spontaneous emission thus leading to significantly increased noise. In [48] it was suggested that by means of an AO FB configuration the non-coherent noise preceding the optical pulse can be compensated by a sufficiently strong coherent FB pulse realized by detuning the external FB cavity to a slightly higher frequency. It was also found that such a fractional external to internal cavity ratio reduces amplitude noise [170]. A reduction of the noise source strength, therefore a lower $\mathrm{TJ}_{\mathrm{ptp}}$, would be clearly identifiable by a reduced high frequency TPN PSD, which is *not* observed in the here presented AO FB experimental results. In addition in the OPTI configuration which has shown

TPN PSD reduction the required detuning is in principle not possible because the slave MLL pulse-train is locked to the timing-phase and RR of the master MLL pulse-train. Therefore, it can be concluded that this mechanism of noise source strength reduction can be excluded for the investigated MLL and the chosen biasing conditions.

5.4.8 Dual all-optical feedback

The presented explanation and simple model can also be easily extended towards different schemes for example a dual AO FB configuration which is demonstrated in [55] similar to an opto-electrical approach in [50]. A schematic of the experimental setup is shown in Fig. 5.28. There, two different optical delays, which amount to a round-trip frequency of 3.2 MHz and 9.6 MHz, are reinjected at the back facet of the MLL. The free-running MLL exhibits a RR of 19.7 GHz, a TJ_{ptp} of 56 fs and a FB pulse width of 2.1 ps. P_{opt} is 1.26 mW, pulse energy is 64 fJ and FB power is 5 μW (without coupling losses) resulting in a total FB ratio of $4 \cdot 10^{-3}$ corresponding to a γ of $4.5 \cdot 10^{-2}$ obtained by equation (5.12) (on page 113) whereby an identical coupling efficiency as compared to the here presented measurements has been assumed. For dual AO FB a TIS of $4.05 \cdot 10^{-2}$ and a TIS of $0.45 \cdot 10^{-2}$ are assumed for the long and short FB cavity, respectively. In our simulations a timing interaction width of 2.1 ps corresponding to the FB pulse width was used. Hereby, the experimental TPN PSD reduction [55, Fig. 2 (b)] can be reproduced using the given parameters and the calibration given by equation (5.12) for the single and dual AO FB configuration despite the significantly higher resonance peaks in simulation shown in Fig. 5.29a. However, the characteristic resonance peak suppression pattern in the dual AO FB configuration is evident in simulations showing the actual benefit of dual AO FB as compared to single AO FB. Based on the model, this reduction of noise resonances of the dual AO FB configuration is attributed to a mean destructive statistical averaging of the timing deviations of the returning timing noise stemming from the two different FB delay lengths. In addition, it is found in simulations that longer FB delays provide a higher TPN PSD reduction or a narrower RR line-width which is shown in sub-section 5.4.4 and is also found experimentally in [55, Fig. 4 (a)].

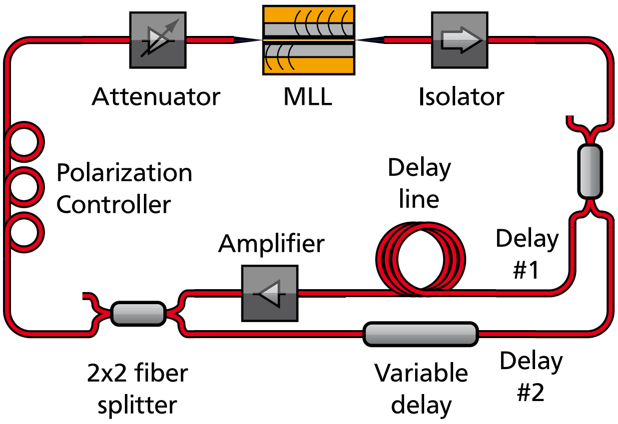

Figure 5.28: Reproduced schematic of experimental setup depicting the dual AO FB configuration which was experimentally investigated in [55]

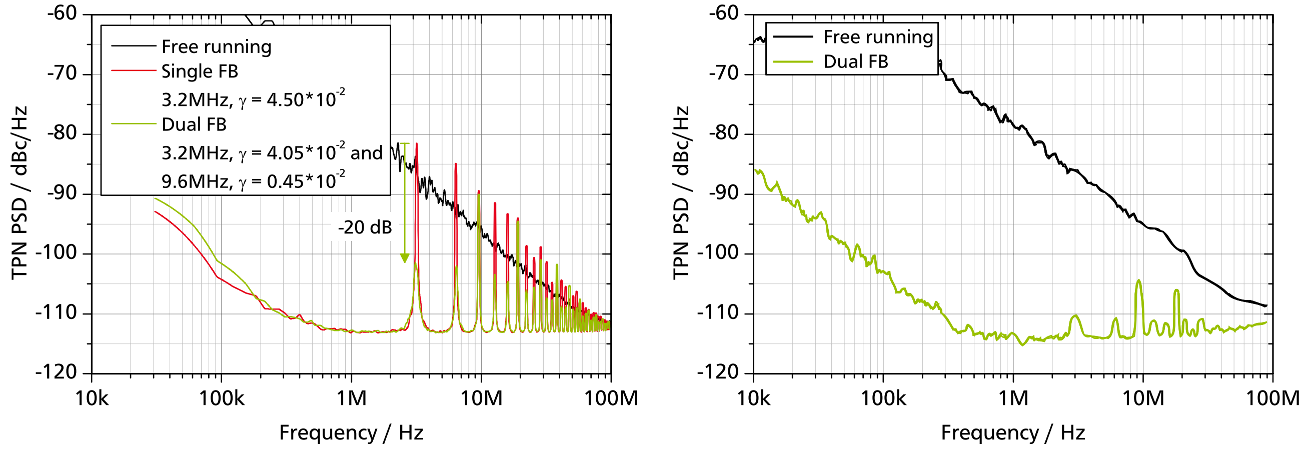

(a)

(b)

Figure 5.29: (a) Calculated TPN PSD of a passively MLL subject to single and dual AO FB. (b) Experimentally obtained TPN PSD of a passively MLL subject to dual AO FB taken from [55]. The free-running TPN PSD is given as a reference.

Bringing sub-section 5.4.5 (on page 118) into mind and in particular the results shown in Fig. 5.15a depicting the TJ reduction and the RR as a function of FB delay detuning a fundamental limitation of any multi-cavity AO FB approach is indicated. As already mentioned a small delay offset between the case of highest TJ reduction and RR zero crossing exists. In experiments it was observed that for other MLLs this offset can be much higher resulting in a complete delay mismatch between both conditions as could be also the case in [167]. Now, according to Eq. (5.15) (on page 128) the RR slope and thus the RR at a fixed delay detuning approximately doubles by halving the FB length. In such a way adjusting the ideal delay for TJ reduction for two different FB lengths separately would result in two different RR changes due to the mentioned offset. Because the MLL can only operate at one RR it is expected that such an case would either result in a locking to one of the FB cavities neglecting the effect of the other FB cavity or would even prevent stable operation.

5.4.9 Timing jitter induced amplitude jitter

As pointed out in sub-section 5.3 the sequence of timing deviations can be applied to an equidistant pulse train from which the PS can be calculated which is also obtained in experiment by means of an ESA. This option allows to demonstrate the impact of TJ on the AJ in case of a coupling of timing deviations to amplitude deviations of the optical pulses which can be observed in the PS. In [106, Fig. 4] the impact of a correlation of TJ and AJ on the PS of a MLL, whereby an asymmetry of the RR line with respect to the frequency could be observed was analytically demonstrated. To model this coupling the most simple relation was chosen here namely a linear relation between intensity and timing-deviation as shown in Eq. (5.16).

$$A(n) = \left(1 + X\frac{T(n) - T(n-1)}{\Delta\tau}\right)A_0 \tag{5.16}$$

Hereby, $A(n)$ denotes the pulse peak intensity of pulse n, A_0 the undisturbed pulse peak intensity, $T(n)$ the timing deviation, $\Delta\tau$ the pulse width and X the dimensionless coupling strength between the dimensionless timing difference $(T(n)-T(n-1))/\Delta\tau$ and the relative pulse peak intensity. It is already evident that the noise characteristics of the amplitude $A(n)$ are white because they depend on the difference of the timing difference between subsequent pulses $T(n)-T(n-1)$ which itself exhibits white noise characteristics according to Eq. (5.7) (on page 101).

In experiments the asymmetry of the RR line can be observed. Fig. 5.30a and Fig. 5.30b show exemplary measured and corresponding simulated PS of a tapered MLL (do 2584 s2b b3) for an absorber voltage of −4.0 V and a gain current of 991 mA and 1472 mA, respectively. In the low-current case (Fig. 5.30a) the left side of the RR signal exhibits a higher magnitude than the right side of the RR signal. In the high-current case (Fig. 5.30b) the left side of the RR signal exhibits a much lower magnitude than the right side of the RR signal and exhibits a dip at a frequency offset of −18 MHz. Thus, comparing both cases the asymmetry has an opposite direction and a different magnitude. For the simulations at the two gain currents the required parameters obtained or derived from *measurements* are the pulse-widths of 1.2 ps and 3.1 ps, the pulse-peak powers of 5.8 W and 5.5 W, the RRs of 10.042 GHz and 10.031 GHz and the TJ_{ptp} of 240 fs and 130 fs, respectively. The AJ is observable up to a frequency of approximately 0.7 GHz. Thus, the AJ is accordingly bandwidth limited by using a Gaussian shaped low-pass filter *after* simulations[8] Furthermore, no independent additional amplitude noise is considered thus the amplitude noise results only from the coupled timing noise. In simulations, the coupling strength X is found to be +1 and −17 for Fig. 5.30a and Fig. 5.30b, respectively (labeled by *TJ and AJ*). These two coupling strength values demonstrate the opposite direction of asymmetry of the PS of both cases as well as their different magnitude. For a better visual comparison and for later discussion also the simulated PS solely considering the TJ or the AJ exclusively are given for both currents (labeled by *TJ only* or *AJ only*, respectively). Although a good quantitative agreement is not evident a good qualitative correspondence is obtained. For the lower current case the decrease of the PS above the RR is indicated which is evident by comparison with the simulated RR solely considering the TJ. However, no increase of the experimental PS for the left side is observed. For the higher current case the qualitative correspondence is much better. The general shape, the prominent dip at an offset of −18 MHz and the higher power for the left and right side of the PS as compared to the simulated TJ only case can be reproduced by simulations. Without this unidirectional coupling of TJ to AJ, the total PS would be just a sum (in linear space) of the plot *TJ only* and *TJ only*. Therefore it can be deduced that TJ induced AJ occurs in experiment for the shown gain currents.

Having found the matching of experimental and simulated PS, now the *variation* of the pulse peak peak power can be investigated in simulation. Calculating the standard deviation (SD) or the root mean square deviation (RMSD) of the pulse peak power from one simulation run ($6.4 \cdot 10^4$ pulses at a RR of 10 GHz yields a bandwidth from 156 kHz to 5 GHz) yields a value of 0.20 W (3.4 % of 5.8 W) and 2.0 W (33 % of 5.5 W) for the low current and the high current case, respectively. Thus, the two cases clearly indicate stability and instability with respect to AJ and demonstrate the impact on the PS.

---

[8] Implementation of a low-pass filter for the TJ induced AJ *during* simulation would require an independent differential equation for the AJ and was therefore omitted.

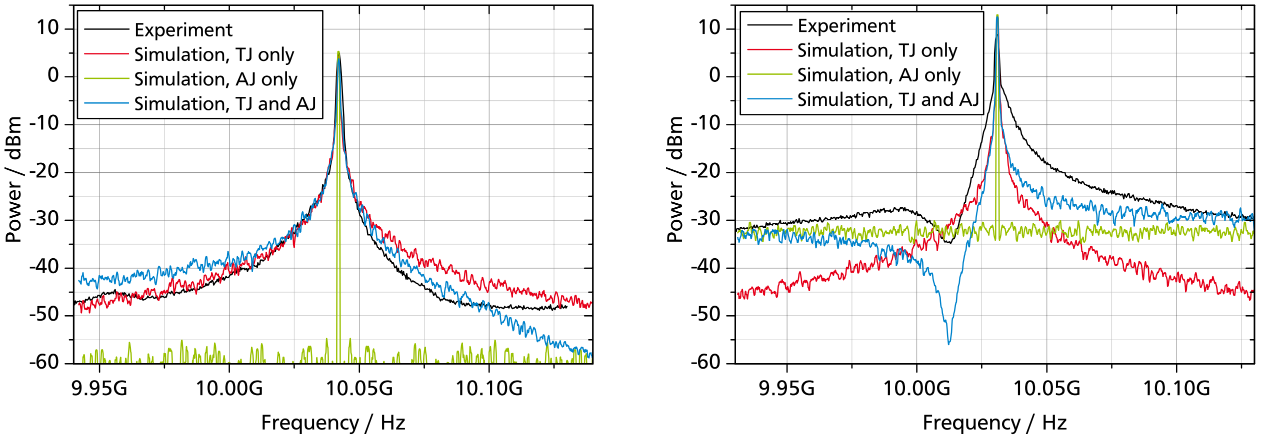

(a) **(b)**

Figure 5.30: Measured and simulated PS of a tapered MLL (do 2584 s2b b3) for an absorber voltage of −4.0 V and a gain current of (a) 991 mA and (b) 1472 mA. The label *TJ only* indicates that only TJ is modeled and the label *TJ and AJ* indicates that TJ and TJ induced AJ is modeled.

With respect to the TPN PSD estimation method by von der Linde [99] is is evident, that this method cannot be used for the right side-band in Fig. 5.30a and for the left side-band in Fig. 5.30b because the total noise is below the TJ or below TJ and AJ, respectively. However, the other side-band can be used, but the first and second harmonic have to be evaluated using the steps given in [100] to separate the TJ from AJ. In fact, using the first and second harmonic PS from simulations to calculate the PS of the TJ and AJ yields the same results as in both figures for the valid side-band. Evaluating the wrong side, yields a too small TJ and not separating the components for the correct side-band leads to an overestimated TJ.

Having found and identified this coupling of TJ to AJ now a physical origin needs to be deduced. An explanation can be derived from [69]. There, strong pulse peak power fluctuations were observed in simulations [69, Fig. 7(a)] which are also reflected in the spectrum[9]. There, no asymmetry could be observed potentially due to the too high frequency span. Theses instabilities were attributed to the so called trailing edge instability (TEI) and LEI basically being a net-gain region located outside the steady state optical pulse. For low currents and high currents TEI and LEI may occur, respectively. They provide a potential explanation for the coupling. In the case of a TEI and if the ASE shifts an optical pulse *backwards* in time (positive timing difference) it experiences increased gain. This positive timing difference together with the increased gain leads to a positive amplitude difference thus being positively correlated resulting a positive coupling $X = +1$ leading to the PS in Fig. 5.30a. In the case of a LEI and if the ASE shifts an optical pulse *forwards* in time (negative timing difference) it experiences increased gain. This negative timing difference together with the increased gain leads to an positive amplitude difference thus being negatively correlated resulting a negative coupling $X = -17$ leading to the PS in Fig. 5.30b. This highlights the importance of the effect of the TEI and LEI on the PS. An unidirectional coupling of TJ to AJ can be well identified in terms of sign and magnitude by means of the PS.

---

[9] There, the spectrum and not the PS is shown.

5.5 Summary and conclusion

In conclusion systematic and consecutive experimental and theoretical investigations of timing jitter (TJ) and TJ control of a passively mode locking (ML) semiconductor laser (SCL) were performed and comprehensively discussed covering a free-running mode-locked laser (MLL), a hybridly MLL, a MLL subject to opto-electrical feedback (OE FB), a MLL subject to all-optical feedback (AO FB) and a MLL subject to optical pulse train injection (OPTI) by means of a master MLL. Hereby, a comprehensive description of TJ and TJ control was proposed based on a direct timing-interaction on intra-cavity pulse and the external signal. With this simple assumption a model was developed which could reproduced all experimental results with good accordance thus validating the proposed description. Based on the performed experiments, the developed model and the accordance of results between experiments and simulations all observed features and peculiarities could be explained comprehensively. The developed description further allows to study various other schemes of TJ control from literature and investigate their dependencies.

Initially, the source of TJ was found to be the dispersion mediated center frequency fluctuation for low gain currents, the so called *Gordon-Haus Jitter*, and the direct projection of amplified spontaneous emission (ASE) on the optical pulse timing for higher gain currents.

To explain the origin of TJ reduction for all the investigated schemes a mechanism or description was proposed which only regards the timing of the optical pulses and keeps the other MLL parameters unchanged. Initially the free-running pulse timing represents a random walk (RW) process. In the most important case of AO FB a direct interaction of the timing between intra cavity pulse and returning feedback (FB) pulse is assumed leading to an averaged timing of both pulses. Hereby, a significant FB length of ≈500 pulses results in a low correlation or reduced memory of the timing noise of the intra cavity pulse with respect to the FB pulse as given by Eq. (2.18) in sub-section 2.4.2. In fact, numerically calculating the auto-correlation of the timing deviation for the AO FB configuration shown in Fig. 5.25 yields also a linear decrease with increasing delay while exhibiting local maxima located at multiples of the external FB period. This reduced correlation together with the statistical averaging of the timing of both pulses is expected to be the origin of the reduced TJ in the case of AO FB.

Based on this idea a model was developed which depends on a few MLL parameters which only regards the TJ and keeps the other parameters of the MLL or its state unchanged. Mathematically it describes the timing-deviation of the intra-cavity pulse by means of a discretized delay differential equation with noise terms. The model is found to be comprehensively valid for all the investigated schemes and can reproduce the experimentally obtained results of TJ with good accordance and in particular the timing phase noise power spectral densities (TPN PSDs) and the repetition rate (RR) as function of FB strength, macroscopic FB length and microscopic delay detuning of the FB in the sub-pulse repetition period (PRP) range. Hereby, the important role of the pulse-width or to be more precise the width and shape of the gain in the vicinity of the intra-cavity pulse (denoted with $W(\Delta T)$) on the behavior of the MLL subject to AO FB was highlighted.

The realized description and the model is applicable to the different investigated external TJ control configurations which exhibit peculiar TPN PSD characteristics. To summarize, Fig. 5.31 shows an overview of the calculated TPN PSD for the investigated configurations. The hybrid mode-locking (HML) configuration (Fig. 5.31 (a)) shows the highly efficient limitation of TPN PSD in the low frequency regime. The OE FB (Fig. 5.31 (b)) and the AO FB configuration (Fig. 5.31 (c)) reduces the TPN PSD in the low frequency regime or equivalently the RR line-width. The observed TPN PSD resonances originate from the timing-noise memory of the FB delay. In particular it was found, that TPN PSD reduction by FB is an all-statistical effect keeping the timing-noise source strength, namely the spontaneous emission noise, unaltered. The timing-interaction is supported by changing this AO FB, which may also be referred to as optical self-injection, to external optical injection by means of a master MLL. An discontinuous TPN PSD locking was observed ((Fig. 5.31 (d)). Extending the simulations to a dual AO FB scheme [55] a reproduction of the TPN PSD reduction and the supermode-noise suppression characteristics was achieved thus showing the universal potential of the presented explanation and model for semiconductor MLL.

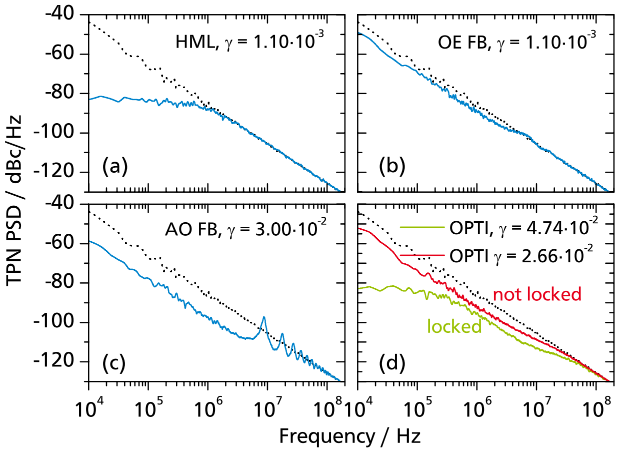

Figure 5.31: Calculated TPN PSD for (a) HML, (b) OE FB configuration, (c) AO FB configuration and (d) OPTI configuration. The dashed line represents the TPN PSD of the free running laser.

Some important highlights of the findings of this part of this works are given in the following:

- The correspondence of OE FB and AO FB in terms of TJ reduction is demonstrated as evident from comparison of Fig. 5.7 and Fig. 5.9, respectively and in particular by the fact, that the TJ dynamics of both schemes can be described by the same discretized differential equation (Eq. (5.9)). This underlying common mechanism of TJ reduction thus cannot be of solely optical origin because in the OE FB case the modulation is only electrical and its bandwidth contains solely the RR. Thus, both schemes base on the the same mechanism which is the reason for TJ reduction.

- This mechanism of TJ reduction for the most important case of AO FB is identified and is found to be attributed to a statistical timing-interaction of intra-cavity pulse and FB pulse together with a reduced correlation of the noise between intra-cavity pulse and FB pulse as indicated by Eq. (5.5).

- The AO FB was found to be efficient in terms of TJ reduction for two different noise sources: The dispersion mediated fluctuations of the optical center frequency and the direct projection of ASE on TJ.

- The AO FB reduces the TJ on long time scales and keeps the TJ almost unchanged on short time-scales represented by the high frequency part of the TPN PSD. The pulse-to-pulse timing jitter (TJ_{ptp}) representing the internal noise source strength is almost not altered by all the investigated schemes including the AO FB configuration.

- The simplicity of the developed model is beneficial in terms of initial understanding as compared to models describing all features of a MLL. In particular most models reported in literature cannot access the long delay which is required to be capable to observe the statistical mechanism of TJ reduction. The model could be extended by inclusion of simulation of amplitude noise motivated by results shown in sub-section 5.4.9.

- The simulation results well reproduced the experimental results for different MLLs exhibiting different waveguide lengths, waveguide geometries, macroscopic FB lengths and operating conditions.

- The shape of the optical pulse and the gain in the vicinity of the intra-cavity pulse has a strong influence on the behavior of the MLL subject to AO FB in terms of TJ reduction and RR change. Thus, such AO FB experiments can be used to indirectly probe the pulse shape and the gain shape of a MLL.

- Due to the general description and its validity it is expected that the results found for mode-locked quantum-dot (QD) lasers are valid for all types of SCLs and potentially even for mode-locked solid-state lasers (SSLs).

- The proposed mechanism is always accompanied by noise-resonance peaks in the TPN PSD which are higher in magnitude than the free-running TPN PSD. Any deviation from this behavior observed in experiment and simulation is an indication for an additional and different effect influencing the TJ.

- The occurrence of asymmetric RR signals in the power spectrum (PS) in experiments is found to be attributed to a coupling of TJ to amplitude jitter (AJ) by means of trailing edge instabilities (TEIs) or leading edge instabilities (LEIs).

- Finally, any fundamental deviation of simulation results from observed experimental results allows to exclude the proposed mechanism for such an observed case which would thus represent a gain of information by elimination of one hypothesis.

6 Summary

> Do I really look like a guy with a plan?
>
> The Joker, Character from The Dark Knight
> (Cinema movie)

The timing stability or timing jitter (TJ) is an important property of an optical pulse train generated by a mode-locked laser (MLL) for any kind of time critical applications and results from various intrinsic sources. To reduce the TJ of MLL a variety of possibilities exists. Hereby, all-optical feedback (AO FB) plays an important role. The effects of long-delay AO FB on TJ were investigated in literature in experiment and in numerical simulations for various types of active gain media of semiconductor laser (SCL). However, a qualitative and quantitative explanation of the origin of this TJ reduction was not provided so far.

In this work a systematic investigation of various selected feedback schemes has been performed allowing to identify and quantify the mechanism of the beneficial effect of these schemes and in particular of the AO FB on TJ. This gain of knowledge is achieved by a combination of specifically selected experiments together with the development of a corresponding simple comprehensive model and corresponding simulations.

The mechanism of TJ reduction is identified for the most important case of AO FB and is found to be attributed to a two-fold effect. First a timing-interaction of intra-cavity pulse and weak feedback (FB) pulse occurs leading to an averaged timing of both pulses. Here, this interaction is intentionally implemented in contrast to sophisticated models which automatically provide such interaction. For this timing-interaction, coherence of both pulses is not necessary. Second, this averaged timing represents a statistical effect exploiting the reduced timing correlation of both pulses due to the long delay. Both, the timing interaction and reduced correlation of timing noise result in a reduced overall TJ. The simplicity of the developed model is beneficial in terms of initial understanding in comparison to models describing all features of a MLL. In particular most models reported in literature cannot access the long delay which is required to be able to observe this statistical mechanism of TJ reduction.

Besides the mentioned timing stability also the amplitude stability is essential for most applications. Indeed, passive mode locking (ML) is not an automatically stable process but requires a delicate balance of a variety of parameters. Undesired amplitude instabilities often manifest in Q-switching (QS) or Q-switched mode-locking (QS ML) and are still a concern for a variety of types of MLL and are investigated in experiment and theory throughout literature. If stability is not achieved by design subsequent external, active and complex measures of stabilization have to be taken.

In this work a simple and passive opto-electrical control-loop is presented, investigated and explained which is able to suppress or eliminate amplitude instabilities for passively mode-locked SCL. This opto-electrical approach consists of a high-pass filter grounding the absorber section therefore representing a differential photo-current detector and control element. The observed suppression is attributed to the reduction of dynamic accumulation of photo generated carriers and thus effectively damps low-frequency fluctuations. Hereby, the absorber section is exploited both as a photo-diode and a control element of the MLL by grounding the undesired absorber AC photo-current. This circuit may also be understood as a differential passive control loop suppressing changes of the photo-current thus preventing strong oscillations.

Having developed an understanding of the TJ and of the possibilities of TJ reduction and having developed an efficient but simple way to eliminate or reduce amplitude instabilities of MLL the increased potential of novel tapered quantum-dot (QD) based MLLs and semiconductor optical amplifiers (SOAs) can be accessed in terms of pulse-width and peak power. Based on this work one important target of recent QD based pulse emitters can be pursued by accessing applications that are currently covered by solid-state laser (SSL) by generation of ultra-short high peak power pulses. One such application range is bio-medical nonlinear microscopy where cheap, compact and robust pulse sources are beneficial for widespread use of such techniques. Hereby, QD based MLL offer the ideal wavelength range allowing for deep penetration depths.

In this work, the generation of ultra-short pulses by novel gain-guided tapered MLL is investigated with an emphasis on stability, pulse-width and peak power. These gain-guided structures offer the benefit of a simplified fabrication process. Furthermore, amplification performance of novel gain-guided tapered SOAs is investigated. The obtained results demonstrate generation and amplification of ultra-short pulses towards peak-power values which offer immediate application potential.

Besides all the systematic investigations, the development of comprehensive beneficial knowledge in the area of TJ, the realization of a directly applicable and simple but effective stabilization method for mode-locked SCL and a demonstration of excellent performance of novel tapered QD based MLL and SOAs even further investigations are suggested relying on the performed work.

Passive semiconductor saturable absorber mirrors (SESAMs) are commonly used for ML of SSL. The presented passive electrical approach may be applied to active electrically controllable SESAMs to investigate potential stabilization properties of these systems.

The simple model could be extended by inclusion of simulation of amplitude noise to gain further insights in the interplay of amplitude and timing instabilities.

From an understanding point of view it would be highly interesting to investigate how AO FB affects TJ in various ML regimes. This is motivated by the demonstrated results showing the potential to experimentally unveil internal pulse dynamics by detuned AO FB.

Exhibiting a wide variety of interesting dynamics on different time-scales, QD based MLLs and SOAs offer the possibility to investigate as well as to control the amplitude and timing dynamics of the generated ultra-short optical pulse train leading to a deeper insight of the underlying mechanisms and to provide improvements in stability.

Bibliography

[1] T. Udem, R. Holzwarth and T. W. Hänsch. "Optical frequency metrology." Nature, vol. 416(6877), pp. 233–237, 2002. DOI: 10.1038/416233a.

[2] T. Ditmire, J. Zweiback, V. P. Yanovsky, T. E. Cowan, G. Hays and K. B. Wharton. "Nuclear fusion from explosions of femtosecond laser-heated deuterium clusters." Nature, vol. 398(6727), pp. 489–492, 1999. DOI: 10.1038/19037.

[3] W. Denk, J. Strickler and W. Webb. "Two-photon laser scanning fluorescence microscopy." Science, vol. 248(4951), pp. 73–76, 1990. DOI: 10.1126/science.2321027.

[4] K. Kuetemeyer, G. Kensah, M. Heidrich, H. Meyer, U. Martin, I. Gruh and A. Heisterkamp. "Two-photon induced collagen cross-linking in bioartificial cardiac tissue." Optics Express, vol. 19(17), p. 15996, 2011. DOI: 10.1364/oe.19.015996.

[5] A. H. Zewail. "Femtochemistry. Past, present, and future." Pure Appl. Chem., vol. 72(12), pp. 2219–2231, 2000. DOI: 10.1351/pac200072122219.

[6] W. Sibbett, A. A. Lagatsky and C. T. A. Brown. "The development and application of femtosecond laser systems." Opt. Express, vol. 20, p. 6989, 2012. DOI: 10.1364/OE.20.006989.

[7] M. Attygalle, A. Nirmalathas and H. Liu. "All-optical coding of mode-locked semiconductor laser pulse trains for high bit rate optical communications." Optics Communications, vol. 217(1-6), pp. 161–167, 2003. DOI: 10.1016/s0030-4018(02)02301-5.

[8] J. Valdmanis and G. Mourou. "Subpicosecond electrooptic sampling: Principles and applications." IEEE J. Quantum Electron., vol. 22(1), pp. 69–78, 1986. DOI: 10.1109/jqe.1986.1072867.

[9] A. Stolow, A. E. Bragg and D. M. Neumark. "Femtosecond Time-Resolved Photoelectron Spectroscopy." Chemical Reviews, vol. 104(4), pp. 1719–1758, 2004. DOI: 10.1021/cr020683w.

[10] J. Eckstein, A. Ferguson and T. Hänsch. "High-Resolution Two-Photon Spectroscopy with Picosecond Light Pulses." Phys. Rev. Lett., vol. 40(13), pp. 847–850, 1978. DOI: 10.1103/physrevlett.40.847.

[11] D. Elson, J. Requejo-Isidro, I. Munro, F. Reavell, J. Siegel, K. Suhling, P. Tadrous, R. Benninger, P. Lanigan, J. McGinty and et al. "Time-domain fluorescence lifetime imaging applied to biological tissue." Photochem. Photobiol. Sci., vol. 3(8), p. 795, 2004. DOI: 10.1039/b316456j.

[12] A. Vogel, J. Noack, G. Hüttman and G. Paltauf. "Mechanisms of femtosecond laser nanosurgery of cells and tissues." Applied Physics B, vol. 81(8), pp. 1015–1047, 2005. DOI: 10.1007/s00340-005-2036-6.

[13] J. Mandon, G. Guelachvili and N. Picque. "Fourier transform spectroscopy with a laser frequency comb." Nature Photon, vol. 3(2), pp. 99–102, 2009. DOI: 10.1038/nphoton.2008.293.

[14] A. Khilo, S. J. Spector, M. E. Grein, A. H. Nejadmalayeri, C. W. Holzwarth, M. Y. Sander, M. S. Dahlem, M. Y. Peng, M. W. Geis, N. A. DiLello and et al. "Photonic ADC: overcoming the bottleneck of electronic jitter." Optics Express, vol. 20(4), p. 4454, 2012. DOI: 10.1364/oe.20.004454.

[15] U. Keller. "Recent developments in compact ultrafast lasers." Nature, vol. 424(6950), pp. 831–838, 2003. DOI: 10.1038/nature01938.

[16] C. T. A. Brown, M. A. Cataluna, A. A. Lagatsky, E. U. Rafailov, M. B. Agate, C. G. Leburn and W. Sibbett. "Compact laser-diode-based femtosecond sources." New J. Phys., vol. 6, p. 175, 2004. DOI: 10.1088/1367-2630/6/1/175.

[17] E. Innerhofer, T. Südmeyer, F. Brunner, R. Höring, A. Aschwanden, R. Paschotta, C. Hönninger, M. Kumkar and U. Keller. "60-W average power in 810-fs pulses from a thin-disk Yb:YAG laser." Opt. Lett., vol. 28(5), p. 367, 2003. DOI: 10.1364/ol.28.000367.

[18] H. Kim, P. Qin, Y. Song, H. Yang, J. Shin, C. Kim, K. Jung, C. Wang and J. Kim. "Sub-20-Attosecond Timing Jitter Mode-Locked Fiber Lasers." IEEE J. Sel. Top. Quantum Electron., vol. 20(5), pp. 1–8, 2014. DOI: 10.1109/JSTQE.2014.2298454.

[19] P. Vasil'ev. Ultrafast Diode Lasers, Fundamentals and Applications. Artech House Inc, 1995. ISBN 978-0890067369.

[20] W. E. Lamb. "Theory of an Optical Maser." Phys. Rev., vol. 134, pp. 1429–1450, 1964. DOI: 10.1103/PhysRev.134.A1429.

[21] K. Kim, S. Lee and P. J. Delfyett. "1.4kW high peak power generation from an all semiconductor mode-locked master oscillator power amplifier system based on eXtreme Chirped Pulse Amplification(X-CPA)." Opt. Express, vol. 13(12), p. 4600, 2005. DOI: 10.1364/OPEX.13.004600.

[22] D. Bimberg, N. Kirstaedter, N. Ledentsov, Z. Alferov, P. Kop'ev and V. Ustinov. "InGaAs-GaAs quantum-dot lasers." IEEE J. Sel. Top. Quantum Electron., vol. 3(2), pp. 196–205, 1997. DOI: 10.1109/2944.605656.

[23] M. J. R. Heck, E. a. J. M. Bente, B. Smalbrugge, Y.-S. Oei, M. K. Smit, S. Anantathanasarn and R. Nötzel. "Observation of Q-switching and mode-locking in two-section InAs/InP (100) quantum dot lasers around 1.55 μm." Opt. Express, vol. 15(25), p. 16292, 2007. DOI: 10.1364/OE.15.016292.

[24] S. K. Ray, K. M. Groom, H. Y. Liu, M. Hopkinson and R. a. Hogg. "Broad-Band Superluminescent Light Emitting Diodes Incorporating Quantum Dots in Compositionally Modulated Quantum Wells." Japanese Journal of Applied Physics, vol. 45(No. 4A), pp. 2542–2545, 2006. DOI: 10.1143/JJAP.45.2542.

[25] C. Xu and F. W. Wise. "Recent advances in fibre lasers for nonlinear microscopy." Nature Photon, vol. 7(11), pp. 875–882, 2013. DOI: 10.1038/nphoton.2013.284.

[26] R. Hall, G. Fenner, J. Kingsley, T. Soltys and R. Carlson. "Coherent Light Emission From GaAs Junctions." Phys. Rev. Lett., vol. 9(9), pp. 366–368, 1962. DOI: 10.1103/physrevlett.9.366.

[27] H. Kroemer. "A proposed class of hetero-junction injection lasers." Proc. IEEE, vol. 51(12), pp. 1782–1783, 1963. DOI: 10.1109/proc.1963.2706.

[28] I. Hayashi. "Junction Lasers Which Operate Continuously At Room Temperature." Appl. Phys. Lett., vol. 17(3), p. 109, 1970. DOI: 10.1063/1.1653326.

[29] R. D. Dupuis, P. D. Dapkus, N. Holonyak, Jr., E. A. Rezek and R. Chin. "Room-temperature laser operation of quantum-well Ga/1-x/AlxAs-GaAs laser diodes grown by metalorganic chemical vapor deposition." Appl. Phys. Lett., vol. 32, pp. 295–297, 1978. DOI: 10.1063/1.90026.

[30] Y. Arakawa and H. Sakaki. "Multidimensional quantum well laser and temperature dependence of its threshold current." Appl. Phys. Lett., vol. 40, pp. 939–941, 1982. DOI: 10.1063/1.92959.

[31] X. Huang, A. Stintz, H. Li, L. F. Lester, J. Cheng and K. J. Malloy. "Passive mode-locking in 1.3 μm two-section InAs quantum dot lasers." Appl. Phys. Lett., vol. 78, 2825, 2001. DOI: 10.1063/1.1371244.

[32] A. R. Kovsh, N. N. Ledentsov, S. S. Mikhrin, A. E. Zhukov, D. A. Livshits, N. A. Maleev, M. V. Maximov, V. M. Ustinov, A. E. Gubenko, I. M. Gadjiev, E. L. Portnoi, J. S. Wang, J. Y. Chi, D. N. Ouyang, D. Bimberg and J. A. Lott. "Long-wavelength (1.3-1.5 micron) quantum dot lasers based on GaAs." In M. Osinski, H. Amano and F. Henneberger, editors, "Physics and Simulation of Optoelectronic Devices XII," vol. 5349 of Society of Photo-Optical Instrumentation Engineers (SPIE) Conference Series, pp. 31–45. 2004. DOI: 10.1117/12.531245.

[33] A. Kovsh, I. Krestnikov, D. Livshits, S. Mikhrin, J. Weimert and A. Zhukov. "Quantum dot laser with 75 nm broad spectrum of emission." Opt. Lett., vol. 32(7), p. 793, 2007. DOI: 10.1364/OL.32.000793.

[34] H. A. Haus. "Parameter ranges for CW passive mode locking." IEEE J. Quantum Electron., vol. 12, pp. 169–176, 1976. DOI: 10.1109/JQE.1976.1069112.

[35] A. J. DeMaria, D. A. Stetser and H. Heynau. "Self Mode-Locking of Lasers with Saturable Absorbers." Appl. Phys. Lett., vol. 8, pp. 174–176, 1966. DOI: 10.1063/1.1754541.

[36] A. G. Vladimirov, U. Bandelow, G. Fiol, D. Arsenijević, M. Kleinert, D. Bimberg, A. Pimenov and D. Rachinskii. "Dynamical regimes in a monolithic passively mode-locked quantum dot laser." J. Opt. Soc. Am. B, vol. 27(10), p. 2102, 2010. DOI: 10.1364/JOSAB.27.002102.

[37] E. a. Viktorov, P. Mandel, M. Kuntz, G. Fiol, D. Bimberg, a. G. Vladimirov and M. Wolfrum. "Stability of the mode-locked regime in quantum dot lasers." Appl. Phys. Lett., vol. 91(23), p. 231116, 2007. DOI: 10.1063/1.2822808.

[38] T. R. Schibli, U. Morgner and F. X. Kärtner. "Control of Q-switched mode locking by active feedback." Opt. Lett., vol. 26(3), p. 148, 2001. DOI: 10.1364/OL.26.000148.

[39] P. Campagnola. "High-Resolution Nonlinear Optical Imaging of Live Cells by Second Harmonic Generation." Biophys. J., vol. 77, pp. 3341–3349, 1999. DOI: 10.1016/S0006-3495(99)77165-1.

[40] F. Helmchen and W. Denk. "Deep tissue two-photon microscopy." Nat. Methods, vol. 2(12), pp. 932–940, 2005. DOI: 10.1038/nmeth818.

[41] M. Ruiz, N. Michel, M. Calligaro, Y. Robert, M. Krakowski, D. I. Nikitichev, M. A. Cataluna, D. Livshits and E. U. Rafailov. "New tapered quantum-dot mode-locked laser diode with high peak power, low divergence and good beam quality." In "22nd IEEE International Semiconductor Laser Conference," pp. 170–171. IEEE, 2010. ISBN 978-1-4244-5683-3. DOI: 10.1109/ISLC.2010.5642658.

[42] F. Quinlan, S. Ozharar, S. Gee and P. J. Delfyett. "Harmonically mode-locked semiconductor-based lasers as high repetition rate ultralow noise pulse train and optical frequency comb sources." J. Opt. A: Pure Appl. Opt., vol. 11(10), p. 103001, 2009. DOI: 10.1088/1464-4258/11/10/103001.

[43] P. J. Delfyett, D. H. Hartman and S. Z. Ahmad. "Optical clock distribution using a mode-locked semiconductor laser diode system." J. Lightwave Technol., vol. 9, p. 1646, 1991. DOI: 10.1109/50.108709.

[44] R. Paschotta. "Noise of mode-locked lasers (Part II): Timing jitter and other fluctuations." Appl. Phys. B, vol. 79(2), pp. 163–173, 2004. DOI: 10.1007/s00340-004-1548-9.

[45] L. Drzewietzki, S. Breuer and W. Elsäßer. "Timing jitter reduction of passively mode-locked semiconductor lasers by self- and external-injection: Numerical description and experiments." Opt. Express, vol. 21(13), p. 16142, 2013. DOI: 10.1364/OE.21.016142.

[46] G. R. Huggett. "Mode-Locking of CW Lasers by Regenerative RF Feedback." Appl. Phys. Lett., vol. 13, pp. 186–187, 1968. DOI: 10.1063/1.1652563.

[47] R. Nietzke, J. Sacher, W. Elsäßer and E. Göbel. “Mode locking of a semiconductor laser by self-synchronising optoelectronic feedback of the longitudinal mode beats.” Electron. Lett, vol. 26(14), p. 1016, 1990. DOI: 10.1049/el:19900658.

[48] P. Beaud, J. Bi, W. Hodel and H. Weber. “Experimental observation of the self-stabilization of a synchronously pumped dye laser.” Opt. Commun., vol. 80(1), pp. 31–36, 1990. DOI: 10.1016/0030-4018(90)90501-J.

[49] H. Kawaguchi and A. K. Sarwar. “Coherent photon seeding of actively mode locked laser diodes.” Appl. Phys. Lett., vol. 62(18), p. 2164, 1993. DOI: 10.1063/1.109456.

[50] X. S. Yao, L. Davis and L. Maleki. “Coupled Optoelectronic Oscillators for Generating Both RF Signal and Optical Pulses.” J. Lightwave Technol., vol. 18, p. 73, 2000. DOI: 10.1109/50.818909.

[51] L. A. Jiang, K. S. Abedin, M. E. Grein and E. P. Ippen. “Timing jitter reduction in modelocked semiconductor lasers with photon seeding.” Appl. Phys. Lett., vol. 80(10), p. 1707, 2002. DOI: 10.1063/1.1459112.

[52] K. Merghem, R. Rosales, S. Azouigui, A. Akrout, A. Martinez, F. Lelarge, G.-H. Duan, G. Aubin and A. Ramdane. “Low noise performance of passively mode locked quantum-dash-based lasers under external optical feedback.” Appl. Phys. Lett., vol. 95(13), p. 131111, 2009. DOI: 10.1063/1.3238324.

[53] S. Breuer, W. Elsäßer, J. G. McInerney, K. Yvind, J. Pozo, E. A. J. M. Bente, M. Yousefi, A. Villafranca, N. Vogiatzis and J. Rorison. “Investigations of Repetition Rate Stability of a Mode-Locked Quantum Dot Semiconductor Laser in an Auxiliary Optical Fiber Cavity.” IEEE J. Quantum Electron., vol. 46(2), pp. 150–157, 2010. DOI: 10.1109/JQE.2009.2033255.

[54] C.-Y. Lin, F. Grillot, Y. Li, R. Raghunathan and L. F. Lester. “Microwave characterization and stabilization of timing jitter in a quantum-dot passively mode-locked laser via external optical feedback.” IEEE J. Sel. Top. Quantum Electron., vol. 17(5), pp. 1311–1317, 2011. DOI: 10.1109/JSTQE.2011.2118745.

[55] M. Haji, L. Hou, A. E. Kelly, J. Akbar, J. H. Marsh, J. M. Arnold and C. N. Ironside. “High frequency optoelectronic oscillators based on the optical feedback of semiconductor mode-locked laser diodes.” Opt. Express, vol. 20(3), p. 3268, 2012. DOI: 10.1364/OE.20.003268.

[56] D. Arsenijević, M. Kleinert and D. Bimberg. “Phase noise and jitter reduction by optical feedback on passively mode-locked quantum-dot lasers.” Appl. Phys. Lett., vol. 103(23), 231101, 2013. DOI: 10.1063/1.4837716.

[57] C. Simos, H. Simos, C. Mesaritakis, A. Kapsalis and D. Syvridis. “Pulse and noise properties of a two section passively mode-locked quantum dot laser under long delay feedback.” Opt. Commun., vol. 313, pp. 248–255, 2014. DOI: 10.1016/j.optcom.2013.10.034.

[58] C. Otto, L. C. Jaurigue, E. Scholl and K. Ludge. “Optimization of Timing Jitter Reduction by Optical Feedback for a Passively Mode-Locked Laser.” IEEE Photonics J., vol. 6(5), pp. 1–14, 2014. DOI: 10.1109/jphot.2014.2352934.

[59] H. A. Haus. “Mode-locking of lasers.” IEEE J. Sel. Top. Quantum Electron., vol. 6(6), pp. 1173–1185, 2000. DOI: 10.1109/2944.902165.

[60] W. Yang, N. J. Sauer, P. G. Bernasconi and L. Zhang. “Self-mode-locked single-section Fabry-Perot semiconductor lasers at 1.56 μm.” Appl. Opt., vol. 46(1), p. 113, 2007. DOI: 10.1364/AO.46.000113.

[61] R. Rosales, S. G. Murdoch, R. Watts, K. Merghem, A. Martinez, F. Lelarge, A. Accard, L. P. Barry and A. Ramdane. “High performance mode locking characteristics of single section quantum dash lasers.” Opt. Express, vol. 20(8), p. 8649, 2012. DOI: 10.1364/OE.20.008649.

[62] E. Rafailov, S. White, A. Lagatsky, A. Miller, W. Sibbett, D. Livshits, A. Zhukov and V. Ustinov. “Fast Quantum-Dot Saturable Absorber for Passive Mode-Locking of Solid-State Lasers.” IEEE Photonics Technol. Lett., vol. 16(11), pp. 2439–2441, 2004. DOI: 10.1109/LPT.2004.835648.

[63] T. Xu and I. Montrosset. “Quantum Dot Passively Mode-Locked Lasers: Relation Between Intracavity Pulse Evolution and Mode Locking Performances.” IEEE J. Quantum Electron., vol. 49(1), pp. 65–71, 2013. DOI: 10.1109/JQE.2012.2229967.

[64] H. Yang, H. Kim, J. Shin, C. Kim, S. Y. Choi, G.-H. Kim, F. Rotermund and J. Kim. “Gigahertz repetition rate, sub-femtosecond timing jitter optical pulse train directly generated from a mode-locked Yb:KYW laser.” Opt. Lett., vol. 39(1), p. 56, 2014. DOI: 10.1364/OL.39.000056.

[65] E. Rafailov. The Physics and Engineering of Compact Quantum Dot-based Lasers for Biophotonics. Wiley-VCH, 2014.

[66] D. J. Derickson, R. J. Helkey, A. Mar, J. R. Karin, J. G. Wasserbauer and J. E. Bowers. “Short pulse generation using multisegment mode-locked semiconductor lasers.” IEEE J. Quantum Electron., vol. 28, pp. 2186–2202, 1992. DOI: 10.1109/3.159527.

[67] M. Rossetti, P. Bardella and I. Montrosset. “Time-Domain Travelling-Wave Model for Quantum Dot Passively Mode-Locked Lasers.” IEEE J. Quantum Electron., vol. 47(2), pp. 139–150, 2011. DOI: 2055550.

[68] M. Radziunas, A. G. Vladimirov, E. a. Viktorov, G. Fiol, H. Schmeckebier and D. Bimberg. “Strong pulse asymmetry in quantum-dot mode-locked semiconductor lasers.” Appl. Phys. Lett., vol. 98(3), p. 031104, 2011. DOI: 10.1063/1.3544579.

[69] M. Rossetti, P. Bardella and I. Montrosset. “Modeling passive mode-locking in quantum dot lasers: A comparison between a finite-difference traveling-wave model and a delayed differential equation approach.” IEEE J. Quantum Electron., vol. 47, pp. 569–576, 2011. DOI: 10.1109/JQE.2010.2104135.

[70] M. Rossetti, T. Xu, P. Bardella and I. Montrosset. “Impact of gain saturation on passive mode locking regimes in quantum dot lasers with straight and tapered waveguides.” IEEE J. Quantum Electron., vol. 47(11), pp. 1404–1413, 2011. DOI: 10.1109/JQE.2011.2167131.

[71] M. Rossetti, T. Xu, P. Bardella and I. Montrosset. “Modelling of passive mode-locking in InAs quantum-dot lasers with tapered gain section.” Phys. Status Solidi C, vol. 9, pp. 286–289, 2012. DOI: 10.1002/pssc.201100243.

[72] C. Hönninger, R. Paschotta, F. Morier-Genoud, M. Moser and U. Keller. “Q-switching stability limits of continuous-wave passive mode locking.” J. Opt. Soc. Am. B, vol. 16(1), p. 46, 1999. DOI: 10.1364/JOSAB.16.000046.

[73] M. Flynn, L. O’Faolain and T. Krauss. “An experimental and numerical study of Q-switched mode-locking in monolithic semiconductor diode lasers.” IEEE J. Quantum Electron., vol. 40(8), pp. 1008–1013, 2004. DOI: 10.1109/JQE.2004.831623.

[74] D. I. Nikitichev, Y. Ding, M. A. Cataluna, E. U. Rafailov, L. Drzewietzki, S. Breuer, W. Elsäßer, M. Rossetti, P. Bardella, T. Xu, I. Montrosset, I. Krestnikov, D. Livshits, M. Ruiz, M. Tran, Y. Robert and M. Krakowski. “High peak power and sub-picosecond Fourier-limited pulse generation from passively mode-locked monolithic two-section gain-guided tapered InGaAs quantum-dot lasers.” Laser Phys., vol. 22, pp. 715–724, 2012. DOI: 10.1134/S1054660X12040147.

[75] H. A. Haus. “Theory of mode locking with a fast saturable absorber.” J. Appl. Phys., vol. 46, pp. 3049–3058, 1975. DOI: 10.1063/1.321997.

[76] M. Thompson, A. Rae, R. Penty and I. White. “InGaAs Quantum-Dot Mode-Locked Laser Diodes.” IEEE J. Sel. Top. Quantum Electron., vol. 15(3), pp. 661–672, 2009. DOI: 10.1109/JSTQE.2008.2012265.

[77] K. Komori, S. Arai and Y. Suematsu. “Noise in semiconductor laser amplifiers with quantum box structure.” IEEE Photon. Technol. Lett., vol. 3(1), pp. 39–41, 1991. DOI: 10.1109/68.68041.

[78] D. B. Malins, A. Gomez-Iglesias, S. J. White, W. Sibbett, A. Miller and E. U. Rafailov. “Ultrafast electroabsorption dynamics in an InAs quantum dot saturable absorber at 1.3 μm.” Appl. Phys. Lett., vol. 89(17), p. 171111, 2006. DOI: 10.1063/1.2369818.

[79] P. Borri, S. Schneider, W. Langbein and D. Bimberg. “Ultrafast carrier dynamics in InGaAs quantum dot materials and devices.” J. Opt. A: Pure Appl. Opt., vol. 8, p. 33, 2006. DOI: 10.1088/1464-4258/8/4/S03.

[80] D. Kobat, M. E. Durst, N. Nishimura, A. W. Wong, C. B. Schaffer and C. Xu. “Deep tissue multiphoton microscopy using longer wavelength excitation.” Opt. Express, vol. 17(16), p. 13354, 2009. DOI: 10.1364/OE.17.013354.

[81] M. Henini and M. Bugajski. “Advances in self-assembled semiconductor quantum dot lasers.” Microelectron. J., vol. 36(11), pp. 950–956, 2005. DOI: 10.1016/j.mejo.2005.04.017.

[82] L. W. Shi, Y. H. Chen, B. Xu, Z. C. Wang, Y. H. Jiao and Z. G. Wang. “Status and trends of short pulse generation using mode-locked lasers based on advanced quantum-dot active media.” J. Phys. D: Appl. Phys., vol. 40(18), pp. R307–R318, 2007. DOI: 10.1088/0022-3727/40/18/R01.

[83] E. U. Rafailov, M. A. Cataluna and W. Sibbett. “Mode-locked quantum-dot lasers.” Nat. Photonics, vol. 1(7), pp. 395–401, 2007. DOI: 10.1038/nphoton.2007.120.

[84] M. Cataluna, Y. Ding, D. I. Nikitichev, K. A. Fedorova and E. U. Rafailov. “High-Power Versatile Picosecond Pulse Generation from Mode-Locked Quantum-Dot Laser Diodes.” IEEE J. Sel. Top. Quantum Electron., vol. 17(5), pp. 1302–1310, 2011. DOI: 10.1109/JSTQE.2011.2141119.

[85] M. G. Thompson, R. V. Penty and I. H. White. “Regimes of mode-locking in tapered quantum dot laser diodes.” In “Proc. IEEE 21st Int. Semiconductor Laser Conf. ISLC 2008,” pp. 27–28. 2008.

[86] E. U. Rafailov, M. a. Cataluna, W. Sibbett, N. D. Il’inskaya, Y. M. Zadiranov, a. E. Zhukov, V. M. Ustinov, D. a. Livshits, a. R. Kovsh and N. N. Ledentsov. “High-power picosecond and femtosecond pulse generation from a two-section mode-locked quantum-dot laser.” Appl. Phys. Lett., vol. 87(8), p. 081107, 2005. DOI: 10.1063/1.2032608.

[87] K. Sala, G. Kenney-Wallace and G. Hall. “CW autocorrelation measurements of picosecond laser pulses.” IEEE J. Quantum Electron., vol. 16, pp. 990–996, 1980. DOI: 10.1109/JQE.1980.1070606.

[88] H. P. Weber and H. G. Danielmeyer. “Multimode Effects in Intensity Correlation Measurements.” Phys. Rev. A, vol. 2, pp. 2074–2079, 1970. DOI: 10.1103/PhysRevA.2.2074.

[89] J.-C. M. Diels, J. J. Fontaine, I. C. McMichael and F. Simoni. “Control and measurement of ultrashort pulse shapes (in amplitude and phase) with femtosecond accuracy.” Appl. Opt., vol. 24(9), p. 1270, 1985. DOI: 10.1364/AO.24.001270.

[90] Y. Takagi, T. Kobayashi, K. Yoshihara and S. Imamura. “Multiple- and single-shot autocorrelator based on two-photon conductivity in semiconductors.” Optics Letters, vol. 17(9), p. 658, 1992. DOI: 10.1364/ol.17.000658.

[91] M. Blazek and W. Elsäßer. “Coherent and thermal light: Tunable hybrid states with second-order coherence without first-order coherence.” Phys. Rev. A, vol. 84(6), 063840, 2011.

DOI: 10.1103/PhysRevA.84.063840.

[92] L. Jiang, S. Wong, M. Grein, E. Ippen and H. Haus. "Measuring timing jitter with optical cross correlations." IEEE J. Quantum Electron., vol. 38(8), pp. 1047–1052, 2002. DOI: 10.1109/JQE.2002.800993.

[93] M. Radziunas, A. G. Vladimirov, E. A. Viktorov, G. Fiol, H. Schmeckebier and D. Bimberg. "Pulse broadening in quantum-dot mode-locked semiconductor lasers: Simulation, analysis, and experiments." IEEE J. Quantum Electron., vol. 47(7), pp. 935–943, 2011. DOI: 10.1109/JQE.2011.2142294.

[94] R. Paschotta. "Sech^2-shaped Pulses." `http://www.rp-photonics.com/sech2_shaped_pulses.html`, 2014. Accessed: 2014.11.21.

[95] H. Yokoyama, H. Guo, T. Yoda, K. Takashima, K. ichi Sato, H. Taniguchi and H. Ito. "Two-photon bioimaging with picosecond optical pulses from a semiconductor laser." Opt. Express, vol. 14(8), pp. 3467–3471, 2006. DOI: 10.1364/OE.14.003467.

[96] S. Hartmann, A. Molitor, M. Blazek and W. Elsäßer. "Tailored first- and second-order coherence properties of quantum dot superluminescent diodes via optical feedback." Opt. Lett., vol. 38, p. 1334, 2013. DOI: 10.1364/OL.38.001334.

[97] T. Habruseva, S. O'Donoghue, N. Rebrova, F. Kéfélian, S. P. Hegarty and G. Huyet. "Optical linewidth of a passively mode-locked semiconductor laser." Opt. Lett., vol. 34(21), p. 3307, 2009. DOI: 10.1364/OL.34.003307.

[98] F. Kefelian, S. O'Donoghue, M. T. Todaro, J. G. McInerney and G. Huyet. "RF linewidth in monolithic passively mode-locked semiconductor laser." IEEE Photonics Technol. Lett., vol. 20(16), pp. 1405–1407, 2008. DOI: 10.1109/LPT.2008.926834.

[99] D. von der Linde. "Characterization of the noise in continuously operating mode-locked lasers." Appl. Phys. B, vol. 39(4), pp. 201–217, 1986. DOI: 10.1007/BF00697487.

[100] A. Rahwanto, Y. Matsuo, N. Nishizawa, T. Goto, M. Mori and K. Yamane. "Timing Jitter in Amplitude Modulated Harmonically Mode-Locked Er-Doped Fiber Ring Lasers." Opt. Rev., vol. 6(4), pp. 355–358, 1999. DOI: 10.1007/s10043-999-0355-2.

[101] F. Quinlan, T. M. Fortier, H. Jiang, A. Hati, C. Nelson, Y. Fu, J. C. Campbell and S. A. Diddams. "Exploiting shot noise correlations in the photodetection of ultrashort optical pulse trains." Nat. Photonics, vol. 33, pp. 1749–4893, 2013. DOI: 10.1038/nphoton.2013.33.

[102] J. Kim, J. Chen, J. Cox and F. X. Kärtner. "Attosecond-resolution timing jitter characterization of free-running mode-locked lasers." Opt. Lett., vol. 32, p. 3519, 2007. DOI: 10.1364/OL.32.003519.

[103] F. Rana, H. L. T. Lee, R. J. Ram, M. E. Grein, L. A. Jiang, E. P. Ippen and H. A. Haus. "Characterization of the noise and correlations in harmonically mode-locked lasers." J. Opt. Soc. Am. B, vol. 19, pp. 2609–2621, 2002. DOI: 10.1364/JOSAB.19.002609.

[104] L. Cutler and C. Searle. "Some aspects of the theory and measurement of frequency fluctuations in frequency standards." Proc. IEEE, vol. 54(2), pp. 136–154, 1966. DOI: 10.1109/PROC.1966.4627.

[105] D. Eliyahu, R. A. Salvatore and A. Yariv. "Effect of noise on the power spectrum of passively mode-locked lasers." J. Opt. Soc. Am. B, vol. 14(1), p. 167, 1997. DOI: 10.1364/JOSAB.14.000167.

[106] H. Haus and A. Mecozzi. "Noise of mode-locked lasers." IEEE J. Quantum Electron., vol. 29(3), pp. 983–996, 1993. DOI: 10.1109/3.206583.

[107] C. Gardiner. Handbook of Stochastic Methods: for Physics, Chemistry and the Natural Sciences (Springer Series in Synergetics). Springer, 2004. ISBN 3540208828.

[108] D. Elliott, R. Roy and S. Smith. “Extracavity laser band-shape and bandwidth modification.” Phys. Rev. A, vol. 26(1), pp. 12–18, 1982. DOI: 10.1103/physreva.26.12.

[109] R. Paschotta. “Timing jitter and phase noise of mode-locked fiber lasers.” Opt. Express, vol. 18, pp. 5041–+, 2010. DOI: 10.1364/OE.18.005041.

[110] L. Jiang, M. Grein, H. Haus and E. Ippen. “Noise of mode-locked semiconductor lasers.” IEEE J. Sel. Top. Quantum Electron., vol. 7(2), pp. 159–167, 2001. DOI: 10.1109/2944.954125.

[111] Y. Ding, M. A. Cataluna, D. Nikitichev, I. Krestnikov, D. Livshits and E. Rafailov. “Broad Repetition-Rate Tunable Quantum-Dot External-Cavity Passively Mode-Locked Laser with Extremely Narrow Radio Frequency Linewidth.” Appl. Phys. Express, vol. 4(6), p. 062703, 2011. DOI: 10.1143/APEX.4.062703.

[112] N. Joly and S. Bielawski. “Suppression of Q-switch instabilities by feedback control in passively mode-locked lasers.” Opt. Lett., vol. 26, pp. 692–694, 2001. DOI: 10.1364/OL.26.000692.

[113] L. Drzewietzki, G. A. P. Thè, M. Gioannini, S. Breuer, I. Montrosset, W. Elsäßer, M. Hopkinson and M. Krakowski. “Theoretical and experimental investigations of the temperature dependent continuous wave lasing characteristics and the switch-on dynamics of an InAs/InGaAs quantum-dot semiconductor laser.” Opt. Commun., vol. 283(24), pp. 5092–5098, 2010. DOI: 10.1016/j.optcom.2010.07.013.

[114] B. Hüttl, R. Kaiser, C. Kindel, S. Fidorra, W. Rehbein, H. Stolpe, G. Sahin, U. Bandelow, M. Radziunas, A. Vladimirov and H. Heidrich. “Experimental investigations on the suppression of Q switching in monolithic 40 GHz mode-locked semiconductor lasers.” Appl. Phys. Lett., vol. 88(22), p. 221104, 2006. DOI: 10.1063/1.2208277.

[115] E. A. Avrutin and E. L. Portnoi. “Suppression of Q-switching instabilities in broadened-waveguide monolithic mode-locked laser diodes.” Opt. Quantum Electron., vol. 40(9), pp. 655–664, 2008. DOI: 10.1007/s11082-008-9253-2.

[116] R. Grange, M. Haiml, R. Paschotta, G. J. Spühler, L. Krainer, M. Golling, O. Ostinelli and U. Keller. “New regime of inverse saturable absorption for self-stabilizing passively mode-locked lasers.” Appl. Phys. B, vol. 80, pp. 151–158, 2005. DOI: 10.1007/s00340-004-1622-3.

[117] T. Schibli, E. Thoen, F. Kartner and E. Ippen. “Suppression of Q-switched mode Locking and break-up into multiple pulses by inverse saturable absorption.” Appl. Phys. B, vol. 70(S), pp. S41–S49, 2000. DOI: 10.1007/s003400000331.

[118] G. J. Valentine, E. A. Bente, D. Burns and A. I. Ferguson. “Active stabilization of quasi-CW passively mode-locked Nd:based lasers using closed-loop feedback.” In G. Huber, I. A. Scherbakov and V. Y. Panchenko, editors, “International Conference on Lasers, Applications, and Technologies 2002: Advanced Lasers and Systems,” vol. 5137 of Society of Photo-Optical Instrumentation Engineers (SPIE) Conference Series, pp. 88–99. 2003. DOI: 10.1117/12.517923.

[119] F. J. Grawert, Ö, F. . Ilday, D. F. Kielpinski, J. T. Gopinath, G. S. Petrich, L. A. Kolodziejski, E. P. Ippen and F. X. Kärtner. “Automatic feedback control of an Er-doped fiber laser with an intracavity loss modulator.” Opt. Lett., vol. 30, pp. 1066–1068, 2005. DOI: 10.1364/OL.30.001066.

[120] G. Giuliani, M. Norgia, S. Donati and T. Bosch. “Laser diode self-mixing technique for sensing applications.” J. Opt. A: Pure Appl. Opt., vol. 4(6), pp. S283–S294, 2002. DOI: 10.1088/1464-4258/4/6/371.

[121] D. J. Derickson, R. J. Helkey, A. Mar, J. R. Karin, J. E. Bowers and R. L. Thornton. "Suppression of multiple pulse formation in external-cavity mode-locked semiconductor lasers using intrawaveguide saturable absorbers." IEEE Photonics Technol. Lett., vol. 4, pp. 333–335, 1992. DOI: 10.1109/68.127204.

[122] F. Kefelian, S. O'Donoghue, M. T. Todaro, J. McInerney and G. Huyet. "Experimental investigation of different regimes of mode-locking in a high repetition rate passively mode-locked semiconductor quantum-dot laser." Opt. Express, vol. 17(8), p. 6258, 2009. DOI: 10.1364/OE.17.006258.

[123] C.-Y. Lin, Y.-C. Xin, J. H. Kim, C. G. Christodoulou and L. F. Lester. "Compact Optical Generation of Microwave Signals Using a Monolithic Quantum Dot Passively Mode-Locked Laser." IEEE Photonics J., vol. 1(4), pp. 236–244, 2009. DOI: 2035523.

[124] D. A. B. Miller, D. S. Chemla, T. C. Damen, A. C. Gossard, W. Wiegmann, T. H. Wood and C. A. Burrus. "Novel hybrid optically bistable switch: The quantum well self-electro-optic effect device." Appl. Phys. Lett., vol. 45(1), pp. 13–15, 1984. DOI: 10.1063/1.94985.

[125] S. Breuer, W. Elsäßer and M. Hopkinson. "State-switched modelocking of two-segment quantum dot laser via self-electro-optical quantum dot absorber." Electron. Lett, vol. 46(2), p. 161, 2010. DOI: 10.1049/el.2010.3360.

[126] S. Breuer, M. Rossetti, L. Drzewietzki, I. Montrosset, M. Krakowski, M. Hopkinson and W. Elsäßer. "Dual-State Absorber-Photocurrent Characteristics and Bistability of Two-Section Quantum-Dot Lasers." IEEE J. Sel. Top. Quantum Electron., vol. 19(5), pp. 1901609–1901609, 2013. DOI: 10.1109/JSTQE.2013.2255264.

[127] F. Grawert and F. Kartner. "Analysis and suppression of Q-switching instabilities in mode-locked lasers-a control systems approach." IEEE J. Quantum Electron., vol. 41(12), pp. 1518–1527, 2005. DOI: 10.1109/JQE.2005.858795.

[128] L. Drzewietzki, S. Breuer, W. Elsäßer, M. Krakowski and I. Krestnikov. "Investigation of passive electric and optical-feedback stabilization of a passively mode-locked tapered two-section quantum-dot laser." In "Conference on Lasers and Electro-Optics Europe (CLEO)," 2011. DOI: 10.1109/CLEOE.2011.5942612.

[129] C. Mesaritakis, C. Simos, H. Simos, A. Kapsalis, I. Krestnikov and D. Syvridis. "External optical feedback-induced wavelength selection and Q-switching elimination in an InAs/InGaAs passively mode-locked quantum dot laser." J. Opt. Soc. Am. B, vol. 29, p. 1071, 2012. DOI: 10.1364/JOSAB.29.001071.

[130] S. A. Zolotovskaya, M. Butkus, R. Häring, A. Able, W. Kaenders, I. L. Krestnikov, D. A. Livshits and E. U. Rafailov. "p-i-n junction quantum dot saturable absorber mirror: electrical control of ultrafast dynamics." Opt. Express, vol. 20(8), p. 9038, 2012. DOI: 10.1364/oe.20.009038.

[131] D. M. Shcherbakova and V. V. Verkhusha. "Near-infrared fluorescent proteins for multicolor in vivo imaging." Nat. Methods, vol. 10(8), pp. 751–754, 2013. DOI: 10.1038/nmeth.2521.

[132] D. Kobat, N. G. Horton and C. Xu. "In vivo two-photon microscopy to 1.6-mm depth in mouse cortex." J. Biomed. Opt., vol. 16(10), p. 106014, 2011. DOI: 10.1117/1.3646209.

[133] C.-K. Sun, I.-H. Chen, S.-W. Chu, B.-L. Lin and P.-C. Cheng. "Wavelength dependent damage in biological multi-photon microscopy: Ti:sapphire vs. Cr:forsterite lasers." The 14th Annual Meeting of the IEEE Lasers and Electro-Optics Society, 2001. LEOS 2001., vol. 1, pp. 393 – 394, 2001. DOI: 10.1109/leos.2001.969342.

[134] Y. Ding, R. Aviles-Espinosa, M. A. Cataluna, D. Nikitichev, M. Ruiz, M. Tran, Y. Robert, A. Kapsalis, H. Simos, C. Mesaritakis, T. Xu, P. Bardella, M. Rossetti, I. Krestnikov, D. Livshits, I. Montrosset, D. Syvridis,

M. Krakowski, P. Loza-Alvarez and E. Rafailov. “High peak-power picosecond pulse generation at 1.26um using a quantum-dot-based external-cavity mode-locked laser and tapered optical amplifier.” Opt. Express, vol. 20(13), pp. 14308–14320, 2012. DOI: 10.1364/OE.20.014308.

[135] C. Mesaritakis, C. Simos, H. Simos, A. Kapsalis, E. Roditi, I. Krestnikov and D. Syvridis. “Effect of the number of quantum dot layers and dual state emission on the performance of InAs/InGaAs passively mode-locked lasers.” Appl. Phys. Lett., vol. 101(25), 251115, 2012. DOI: 10.1063/1.4772592.

[136] A. Mar, R. Helkey, W. X. Zou, D. B. Young and J. E. Bowers. “High-power mode-locked semiconductor lasers using flared waveguides.” Appl. Phys. Lett., vol. 66, pp. 3558–3560, 1995. DOI: 10.1063/1.113786.

[137] D. I. Nikitichev, Y. Ding, M. Ruiz, M. Calligaro, N. Michel, M. Krakowski, I. Krestnikov, D. Livshits, M. A. Cataluna and E. U. Rafailov. “High-power passively mode-locked tapered InAs/GaAs quantum-dot lasers.” Appl. Phys. B, vol. 103, pp. 609–613, 2011. DOI: 10.1007/s00340-010-4290-5.

[138] J. J. Plant, J. T. Gopinath, B. Chann, D. J. Ripin, R. K. Huang and P. W. Juodawlkis. “250 mW, 1.5um monolithic passively mode-locked slab-coupled optical waveguide laser.” Opt. Lett., vol. 31(2), p. 223, 2006. DOI: 10.1364/ol.31.000223.

[139] T. Oki, R. Koda, S. Kono, T. Miyajima, H. Watanabe, M. Kuramoto, M. Ikeda and H. Yokoyama. “Direct generation of 20 W peak power picosecond optical pulses from an external-cavity mode-locked GaInN laser diode incorporating a flared waveguide.” Appl. Phys. Lett., vol. 99(11), 111105, 2011. DOI: 10.1063/1.3640499.

[140] T. Xu, P. Bardella, M. Rossetti and I. Montrosset. “Beam propagation method simulation and analysis of quantum dot flared semiconductor optical amplifiers in continuous wave high-saturation regime.” IET Optoelectron, vol. 6(2), pp. 110 –116, 2012. DOI: 10.1049/iet-opt.2011.0056.

[141] M. Rossetti. “Report.” private communication with M. Rossetti, Politecnico di Torino, Department of Electronics and Telecommunications, Semiconductor Integrated Optoelectronics and Photonics Group, 2012.

[142] M. Thompson, A. Rae, R. Penty, I. White, A. Kovsh, S. Mikhrin, D. Livshits and I. Krestnikov. “Absorber length optimisation for sub-picosecond pulse generation and ultra-low jitter performance in passively mode-locked 1.3 μm quantum-dot laser diodes.” In “2006 Optical Fiber Communication Conference and the National Fiber Optic Engineers Conference,” 2006. ISBN 1-55752-803-9. DOI: 10.1109/OFC.2006.215717.

[143] A. R. Rae, M. G. Thompson, A. R. Kovsh, R. V. Penty and I. H. White. “InGaAs-GaAs Quantum-Dot Mode-Locked Laser Diodes: Optimization of the Laser Geometry for Subpicosecond Pulse Generation.” IEEE Photonics Technol. Lett., vol. 21, pp. 307–309, 2009. DOI: 10.1109/LPT.2008.2010778.

[144] H. Simos, M. Rossetti, C. Simos, C. Mesaritakis, T. Xu, P. Bardella, I. Montrosset and D. Syvridis. “Numerical Analysis of Passively Mode-Locked Quantum-Dot Lasers With Absorber Section at the Low-Reflectivity Output Facet.” IEEE J. Quantum Electron., vol. 49(1), pp. 3–10, 2013. DOI: 10.1109/JQE.2012.2222352.

[145] Y. C. Xin, Y. Li, V. Kovanis, a. L. Gray, L. Zhang and L. F. Lester. “Reconfigurable quantum dot monolithic multisection passive mode-locked lasers.” Opt. Express, vol. 15(12), p. 7623, 2007. DOI: 10.1364/OE.15.007623.

[146] T. Schlauch, M. Li, M. Hofmann, A. Klehr, G. Erbert and G. Tränkle. “High peak power femtosecond pulses from modelocked semiconductor laser in external cavity.” Electron. Lett, vol. 44(11), p. 678, 2008. DOI: 10.1049/el:20080953.

[147] A. Mar, R. Helkey, J. Bowers, D. Mehuys and D. Welch. “Mode-locked operation of a master oscillator power amplifier.” IEEE Photonics Technol. Lett., vol. 6(9), pp. 1067–1069, 1994. DOI: 10.1109/68.324670.

[148] R. Koda, T. Oki, T. Miyajima, H. Watanabe, M. Kuramoto, M. Ikeda and H. Yokoyama. “100 W peak-power 1 GHz repetition picoseconds optical pulse generation using blue-violet GaInN diode laser mode-locked oscillator and optical amplifier.” Appl. Phys. Lett., vol. 97(2), p. 021101, 2010. DOI: 10.1063/1.3462942.

[149] L. Drzewietzki, S. Breuer, M. Rossetti, T. Xu, P. Bardella, H. Simos, C. Mesaritakis, M. Ruiz, I. Krestnikov, D. Livshits, M. Krakowski, D. Syvridis, I. Montrosset, E. Rafailov and W. Elsäßer. “Picosecond pulse generation with 34W peak power using a monolithic quantum-dot tapered mode-locked laser and tapered optical amplifier.” In “Conference on Lasers and Electro-Optics Europe (CLEO),” pp. 1–1. 2013. DOI: 10.1109/CLEOE-IQEC.2013.6800704.

[150] R. P. Ratowsky, S. Dijaili, J. Walker, F. Patterson, J. Kallman and R. Deri. “Calculation of farfield distortion for a tilted-facet SOA.” In “Integrated Photonics Research,” vol. 6 of OSA Technical Digest Series, p. PDP5. Optical Society of America, 1996. ISBN 1-55752-439-4. DOI: 10.1364/IPR.1996.PDP5. Postdeadline Paper.

[151] K. Petermann. “Some relations for the far-field distribution of semiconductor lasers with gain-guiding.” Opt. Quantum Electron., vol. 13(4), pp. 323–333, 1981. DOI: 10.1007/BF00619797.

[152] G. P. Agrawal and N. A. Olsson. “Self-phase modulation and spectral broadening of optical pulses in semiconductor laser amplifiers.” IEEE J. Quantum Electron., vol. 25, pp. 2297–2306, 1989. DOI: 10.1109/3.42059.

[153] C. Weber, L. Drzewietzki, I. Montrosset, D. Syvridis, M. Krakowski, I. Krestnikov, D. Livshits, E. U. Rafailov, W. Elsäßer and S. Breuer. “Experimental investigations on the generation and amplification of high power short pulses by a quantum dot laser and amplifier.” In “International Conference on Transparent Optical Networks,” IEEE, 2014. ISBN http://id.crossref.org/isbn/978-1-4799-5601-2. DOI: 10.1109/icton.2014.6876659.

[154] E. Avrutin, J. Marsh and E. Portnoi. “Monolithic and multi-GigaHertz mode-locked semiconductor lasers: Constructions, experiments, models and applications.” IEE Proc.: Optoelectron., vol. 147(4), p. 251, 2000. DOI: 10.1049/ip-opt:20000282.

[155] K. A. Williams, M. G. Thompson and I. H. White. “Long-wavelength monolithic mode-locked diode lasers.” New J. Phys., vol. 6, pp. 179–179, 2004. DOI: 10.1088/1367-2630/6/1/179.

[156] B. Mathason and P. Delfyett. “Pulsed injection locking dynamics of passively mode-locked external-cavity semiconductor laser systems for all-optical clock recovery.” J. Lightwave Technol., vol. 18(8), pp. 1111–1120, 2000. DOI: 10.1109/50.857757.

[157] Y. Song, C. Kim, K. Jung, H. Kim and J. Kim. “Timing jitter optimization of mode-locked Yb-fiber lasers toward the attosecond regime.” Opt. Express, vol. 19(15), p. 14518, 2011. DOI: 10.1364/OE.19.014518.

[158] A. Nejadmalayeri, M. Grein, S. J. Spector, A. Khilo, M. Y. Peng, M. Sander, J. Wang, A. J. Benedick, C. M. Sorace, M. W. Geis, M. M. Willis, D. M. Lennon, J. U. Yoon, T. M. Lyszczarz, E. Ippen and F. Kartner. “Attosecond photonics for optical communications.” In “Optical Fiber Communication Conference,” p. OM2C.1. Optical Society of America, 2012. DOI: 10.1364/OFC.2012.OM2C.1.

[159] R. Paschotta. “Noise of mode-locked lasers (Part I): Numerical model.” Appl. Phys. B, vol. 79(2), pp. 153–162, 2004. DOI: 10.1007/s00340-004-1547-x.

[160] M. J. Heck, E. J. Salumbides, A. Renault, E. A. Bente, Y.-S. Oei, M. K. Smit, R. van Veldhoven, R. Nötzel, K. S. Eikema and W. Ubachs. “Analysis of hybrid mode-locking of two-section quantum dot lasers operating at 1.5 μm.” Opt. Express, vol. 17(20), p. 18063, 2009. DOI: 10.1364/OE.17.018063.

[161] G. Fiol, D. Arsenijevic, D. Bimberg, A. G. Vladimirov, M. Wolfrum, E. A. Viktorov and P. Mandel. “Hybrid mode-locking in a 40 GHz monolithic quantum dot laser.” Appl. Phys. Lett., vol. 96(1), p. 011104, 2010.

DOI: 10.1063/1.3279136.

[162] G. Carpintero, M. Thompson, R. Penty and I. White. "Low noise performance of passively mode-locked 10 GHz quantum-dot laser diode." IEEE Photonics Technol. Lett., vol. 21(6), pp. 389–391, 2009. DOI: 10.1109/LPT.2008.2011918.

[163] R. J. Helkey, D. J. Derickson, A. Mar, J. G. Wasserbauer, J. E. Bowers and R. L. Thornton. "Repetition frequency stabilisation of passively mode-locked semiconductor lasers." Electron. Lett, vol. 28(20), pp. 1920–1922, 1992. DOI: 10.1049/el:19921229.

[164] M. Nakazawa, E. Yoshida and K. Tamura. "Ideal phase-locked-loop (PLL) operation of a 10 GHz erbium-doped fibre laser using regenerative modelocking as an optical voltage controlled oscillator." Electron. Lett, vol. 33(15), pp. 1318–1320, 1997. DOI: 10.1049/el:19970902.

[165] L. Drzewietzki, S. Breuer and W. Elsäßer. "Timing phase noise reduction of modelocked quantum-dot lasers by time-delayed optoelectronic feedback." Electron. Lett, vol. 49(8), pp. 557–559, 2013. DOI: 10.1049/el.2013.0763.

[166] F. van Dijk, A. Enard, X. Buet, F. Lelarge and G.-H. Duan. "Phase Noise Reduction of a Quantum Dash Mode-Locked Laser in a Millimeter-Wave Coupled Opto-Electronic Oscillator." J. Lightwave Technol., vol. 26, pp. 2789–2794, 2008. DOI: 10.1109/JLT.2008.927608.

[167] G. Fiol, M. Kleinert, D. Arsenijevic and D. Bimberg. "1.3 um range 40 GHz quantum-dot mode-locked laser under external continuous wave light injection or optical feedback." Semicond. Sci. Technol., vol. 26(1), p. 014006, 2011. DOI: 10.1088/0268-1242/26/1/014006.

[168] O. Solgaard and K. Lau. "Optical feedback stabilization of the intensity oscillations in ultrahigh-frequency passively modelocked monolithic quantum-well lasers." IEEE Photonics Technol. Lett., vol. 5(11), pp. 1264–1267, 1993. DOI: 10.1109/68.250039.

[169] C. Otto, K. Lüdge, A. G. Vladimirov, M. Wolfrum and E. Schöll. "Delay-induced dynamics and jitter reduction of passively mode-locked semiconductor lasers subject to optical feedback." New J. Phys., vol. 14(11), p. 113033, 2012. DOI: 10.1088/1367-2630/14/11/113033.

[170] E. A. Avrutin and B. M. Russell. "Dynamics and spectra of monolithic mode-locked laser diodes under external optical feedback." IEEE J. Quantum Electron., vol. 45(11), pp. 1456–1464, 2009. DOI: 10.1109/JQE.2009.2028242.

[171] E. Sooudi, C. de Dios, J. G. McInerney, H. Huyet, L. Lelarge, K. Merghem, R. Rosales, A. Martinez, A. Ramdane and S. P. Hegarty. "A Novel Scheme for Two-Level Stabilization of Semiconductor Mode-Locked Lasers Using Simultaneous Optical Injection and Optical Feedback." IEEE J. Sel. Top. Quantum Electron., vol. 19(4), pp. 1101208–1101208, 2013. DOI: 10.1109/JSTQE.2013.2249045.

[172] D. Arsenijevic, M. Kleinert and D. Bimberg. "Breakthroughs in Photonics 2013: Passive Mode-Locking of Quantum-Dot Lasers." IEEE Photonics J., vol. 6(2), pp. 1–6, 2014. DOI: 10.1109/jphot.2014.2308195.

[173] A. Vladimirov and D. Turaev. "Model for passive mode locking in semiconductor lasers." Phys. Rev. A, vol. 72(3), p. 033808, 2005. DOI: 10.1103/PhysRevA.72.033808.

[174] Y. Takushima, H. Sotobayashi, M. E. Grein, E. P. Ippen and H. A. Haus. "Linewidth of mode combs of passively and actively mode-locked semiconductor laser diodes." In A. K. Dutta, A. A. S. Awwal, N. K. Dutta and Y. Ohishi, editors, "Active and Passive Optical Components for WDM Communications IV," Proc. SPIE 5595, pp. 213–227. 2004. DOI: 10.1117/12.580046.

[175] J. A. Cox, A. H. Nejadmalayeri, J. Kim and F. X. Kärtner. "Complete characterization of quantum-limited timing jitter in passively mode-locked fiber lasers." Opt. Lett., vol. 35(20), p. 3522, 2010. DOI: 10.1364/OL.35.003522.

[176] A. Demir. "Computing Timing Jitter From Phase Noise Spectra for Oscillators and Phase-Locked Loops With White and 1/f Noise." IEEE Trans. Circuits Syst. Regul. Pap., vol. 53(9), pp. 1869–1884, 2006. DOI: 10.1109/TCSI.2006.881184.

[177] J. Mulet and J. Mork. "Analysis of timing jitter in external-cavity mode-locked semiconductor lasers." IEEE J. Quantum Electron., vol. 42(3), pp. 249–256, 2006. DOI: 10.1109/JQE.2006.869808.

[178] H. Simos, C. Simos, C. Mesaritakis and D. Syvridis. "Two-section quantum-dot mode-locked lasers under optical feedback: Pulse broadening and harmonic operation." IEEE J. Quantum Electron., vol. 48, pp. 872–877, 2012. DOI: 10.1109/JQE.2012.2193387.

[179] X. S. Yao and L. Maleki. "Optoelectronic microwave oscillator." J. Opt. Soc. Am. B, vol. 13, pp. 1725–1735, 1996. DOI: 10.1364/JOSAB.13.001725.

[180] W. Lee and P. Delfyett. "Dual-mode injection locking of two independent modelocked semiconductor lasers." Electron. Lett, vol. 40(19), p. 1182, 2004. DOI: 10.1049/el:20045959.

[181] F. R. Ahmad and F. Rana. "Fundamental and subharmonic hybrid mode-locking of a high-power (220 mW) monolithic semiconductor laser." IEEE Photonics Technol. Lett., vol. 20(15), pp. 1308–1310, 2008. DOI: 10.1109/LPT.2008.926911.

[182] M.-H. Mao, T.-Y. Wu, D.-C. Wu, F.-Y. Chang and H.-H. Lin. "Relaxation oscillations and damping factors of 1.3 μm In(Ga)As/GaAs quantum-dot lasers." Opt. Quantum Electron., vol. 36(10), pp. 927–933, 2004. DOI: 10.1007/s11082-004-2742-z.

[183] T. Habruseva, S. O'Donoghue, N. Rebrova, D. A. Reid, L. P. Barry, D. Rachinskii, G. Huyet and S. P. Hegarty. "Quantum-dot mode-locked lasers with dual-mode optical injection." IEEE Photonics Technol. Lett., vol. 22(6), pp. 359–361, 2010. DOI: 10.1109/LPT.2009.2039347.

[184] H. Kurita, T. Shimizu and H. Yokoyama. "Experimental investigations of harmonic synchronization conditions and mechanisms of mode-locked laser diodes induced by optical-pulse injection." IEEE J. Sel. Top. Quantum Electron., vol. 2(3), pp. 508–513, 1996. DOI: 10.1109/2944.571751.

[185] N. Yu, E. Salik and L. Maleki. "Ultralow-noise mode-locked laser with coupled optoelectronic oscillator configuration." Opt. Lett., vol. 30, pp. 1231–1233, 2005. DOI: 10.1364/OL.30.001231.

[186] F. Grillot, C.-Y. Lin, N. A. Naderi, M. Pochet and L. F. Lester. "Optical feedback instabilities in a monolithic InAs/GaAs quantum dot passively mode-locked laser." Appl. Phys. Lett., vol. 94(15), p. 153503, 2009. DOI: 10.1063/1.3114409.

[187] C. M. DePriest, T. Yilmaz, P. J. Delfyett, Jr., S. Etemad, A. Braun and J. Abeles. "Ultralow noise and supermode suppression in an actively mode-locked external-cavity semiconductor diode ring laser." Opt. Lett., vol. 27, pp. 719–721, 2002. DOI: 10.1364/OL.27.000719.

[188] S. Gee, F. Quinlan, S. Ozharar and P. Delfyett. "Simultaneous optical comb frequency stabilization and super-mode noise suppression of harmonically mode-locked semiconductor ring laser using an intracavity etalon." IEEE Photonics Technol. Lett., vol. 17(1), pp. 199–201, 2005. DOI: 10.1109/LPT.2004.838920.

[189] G. T. Harvey and L. F. Mollenauer. "Harmonically mode-locked fiber ring laser with an internal Fabry-Perot stabilizer for soliton transmission." Opt. Lett., vol. 18(2), p. 107, 1993. DOI: 10.1364/OL.18.000107.

[190] M. Margalit, M. Orenstein and H. Haus. “Noise in pulsed injection locking of a passively modelocked laser.” IEEE J. Quantum Electron., vol. 32(5), pp. 796–801, 1996. DOI: 10.1109/3.493003.

[191] F. Kefelian, S. O’Donoghue, M. T. Todaro, J. McInerney and G. Huyet. “High Repetition Rate Monolithic Passively Mode-Locked Semiconductor Quantum-Dot Laser: Investigation of the Locking Regimes and the RF Linewidth.” In “2007 Conference on Lasers and Electro-Optics (CLEO),” pp. 1–2. Institute of Electrical and Electronics Engineers, 2007. DOI: 10.1109/CLEO.2007.4453127.

[192] B. Leonhäuser-Rein, L. Drzewietzki, F. Schad and W. Elsäßer. “Investigations of mode beat frequencies of external cavity semiconductor lasers.” Appl. Phys. B, vol. 113, pp. 215–220, 2013. DOI: 10.1007/s00340-013-5459-5.

[193] C.-Y. Lin, F. Grillot, N. a. Naderi, Y. Li and L. F. Lester. “Rf Linewidth Reduction in a Quantum Dot Passively Mode-Locked Laser Subject To External Optical Feedback.” Appl. Phys. Lett., vol. 96(5), p. 051118, 2010. DOI: 10.1063/1.3299714.

[194] D. Baums, W. Elsaesser and E. O. Goebel. “Farey tree and devil’s staircase of a modulated external-cavity semiconductor laser.” Phys. Rev. Lett., vol. 63, pp. 155–158, 1989. DOI: 10.1103/PhysRevLett.63.155.

[195] T. Habruseva, G. Huyet and S. Hegarty. “Dynamics of quantum-dot mode-locked lasers with optical injection.” IEEE J. Sel. Top. Quantum Electron., vol. 17(5), pp. 1272–1279, 2011. DOI: 10.1109/JSTQE.2011.2123875.

[196] J. Kim, A. Ardey and P. J. Delfyett. “Coherent spectral bandwidth combining by optical pulse injection locking in quantum dot modelocked semiconductor diode lasers.” Electron. Lett, vol. 48(12), pp. 720–721, 2012. DOI: 10.1049/el.2012.1280.

[197] S. Arahira and Y. Ogawa. “Synchronous mode-locking in passively mode-locked semiconductor laser diodes using optical short pulses repeated at subharmonics of the cavity round-trip frequency.” IEEE Photonics Technol. Lett., vol. 8(2), pp. 191–193, 1996. DOI: 10.1109/68.484237.

[198] H. Tsuchida. “Time-domain measurement of pulse-timing fluctuations in a mode-locked laser diode.” IEEE Photonics Technol. Lett., vol. 14(4), pp. 513–515, 2002. DOI: 10.1109/68.992595.

Publication list: Peer reviewed journals

[1] S. Rauch, L. Drzewietzki, A. Klehr, J. Sacher, W. Elsäßer and S. Breuer. "Experimental Study of the Timing Jitter of a Passively Mode-Locked External-Cavity Semiconductor Laser Subject to Repetition Rate Transitions and Optical Feedback." IEEE J. Quantum Electron., vol. 51(4), p. 1300107, 2015. DOI: 10.1109/jqe.2015.2402431.

[2] C. Weber, L. Drzewietzki, M. Rossetti, T. Xu, P. Bardella, H. Simos, C. Mesaritakis, M. Ruiz, I. Krestnikov, D. Livshits, M. Krakowski, D. Syvridis, I. Montrosset, E. U. Rafailov, W. Elsäßer and S. Breuer. "Picosecond pulse amplification up to a peak power of 42W by a quantum-dot tapered optical amplifier and a mode-locked laser emitting at 1.26um." Opt. Lett., vol. 40(3), pp. 395, 2015. DOI: 10.1364/OL.40.000395.

[3] M. Gioannini, M. Dommermuth, L. Drzewietzki, I. Krestnikov, D. Livshits, M. Krakowski and S. Breuer. "Two-state semiconductor laser self-mixing velocimetry exploiting coupled quantum-dot emission-states: Experiment, simulation and theory." Opt. Express, vol. 22(19), pp. 23402, 2014. DOI: 10.1364/OE.22.023402.

[4] S. Breuer, M. Rossetti, L. Drzewietzki, I. Montrosset, M. Krakowski, M. Hopkinson and W. Elsäßer. "Dual-State Absorber-Photocurrent Characteristics and Bistability of Two-Section Quantum-Dot Lasers." IEEE J. Sel. Top. Quantum Electron., vol. 19(5), pp. 1901609, 2013. DOI: 10.1109/JSTQE.2013.2255264.

[5] L. Drzewietzki, S. Breuer and W. Elsäßer. "Timing jitter reduction of passively mode-locked semiconductor lasers by self- and external-injection: Numerical description and experiments." Opt. Express, vol. 21(13), p. 16142, 2013. DOI: 10.1364/OE.21.016142.

[6] L. Drzewietzki, S. Breuer and W. Elsäßer. "Timing phase noise reduction of modelocked quantum-dot lasers by time-delayed optoelectronic feedback." Electron. Lett, vol. 49(8), pp. 557, 2013. DOI: 10.1049/el.2013.0763.

[7] C. Juretzka, S. Breuer, L. Drzewietzki, F. Schad, M. Carras and W. Elsäßer. "9.5 dB relative intensity noise reduction in quantum cascade laser by detuned loading." Electron. Lett, vol. 49, pp. 1548, 2013. DOI: 10.1049/el.2013.2366.

[8] B. Leonhäuser-Rein, L. Drzewietzki, F. Schad and W. Elsäßer. "Investigations of mode beat frequencies of external cavity semiconductor lasers." Appl. Phys. B, vol. 113, pp. 215, 2013. DOI: 10.1007/s00340-013-5459-5.

[9] D. I. Nikitichev, Y. Ding, M. A. Cataluna, E. U. Rafailov, L. Drzewietzki, S. Breuer, W. Elsäßer, M. Rossetti, P. Bardella, T. Xu, I. Montrosset, I. Krestnikov, D. Livshits, M. Ruiz, M. Tran, Y. Robert and M. Krakowski. "High peak power and sub-picosecond Fourier-limited pulse generation from passively mode-locked monolithic two-section gain-guided tapered InGaAs quantum-dot lasers." Laser Phys., vol. 22, pp. 715, 2012. DOI: 10.1134/S1054660X12040147.

[10] S. Breuer, M. Rossetti, L. Drzewietzki, P. Bardella, I. Montrosset and W. Elsäßer. "Joint Experimental and Theoretical Investigations of Two-State Mode Locking in a Strongly Chirped Reverse-Biased Monolithic Quantum Dot Laser." IEEE J. Quantum Electron., vol. 47(10), pp. 1320, 2011. DOI: 10.1109/JQE.2011.2165834.

[11] L. Drzewietzki, S. Breuer and Elsäßer. "Suppression of Q-switching instabilities of passively mode-locked semiconductor lasers by a passive electrical circuit." Electron. Lett, vol. 47(17), pp. 988, 2011. DOI: 10.1049/el.2011.1802.

[12] S. Breuer, M. Rossetti, W. Elsäßer, L. Drzewietzki, P. Bardella, I. Montrosset, M. Krakowski and M. Hopkinson. "Reverse-emission-state-transition mode locking of a two-section InAs/InGaAs quantum dot laser." Appl. Phys. Lett., vol. 97(7), p. 071118, 2010. DOI: 10.1063/1.3480405.

[13] L. Drzewietzki, G. A. P. Thè, M. Gioannini, S. Breuer, I. Montrosset, W. Elsäß er, M. Hopkinson and M. Krakowski. "Theoretical and experimental investigations of the temperature dependent continuous wave lasing characteristics and the switch-on dynamics of an InAs/InGaAs quantum-dot semiconductor laser." Opt. Commun., vol. 283(24), pp. 5092, 2010. DOI: 10.1016/j.optcom.2010.07.013.

[14] P. Dziendziel, L. Drzewietzki, J.-P. Boucher, A. Trivedi, S. Hardt, W. Elsäßer and S. Breuer. "Two-dimensional vectorial velocity profile of secondary flow in a microchannel measured by low-coherence interferometry." Submitted to Opt. Letters.

Publication list: Conference contributions

[1] O. Nikiforov, L. Jaurigue, L. Drzewietzki, K. Lüdge and S. Breuer. “Repetition rate deviations and timing jitter of passively mode-locked lasers subject to optical feedback from two external optical cavities.” In “Conference on Lasers and Electro-Optics Europe (CLEO),” p. CB9.5. 2015.

[2] R. Pawlus, M. Gioannini, L. Drzewietzki, W. Elsäßer and S. Breuer. “Amplitude stability of a two-state quantum dot laser.” In “Conference on Lasers and Electro-Optics Europe (CLEO),” p. CB9.4. 2015.

[3] S. Rauch, L. Drzewietzki, A. Klehr, J. Sacher, W. Elsäßer and S. Breuer. “Timing Jitter Reduction of a Passively Mode-Locked External-Cavity Semiconductor Laser Via Repetition Rate Transitions and Optical Feedback.” In “Conference on Lasers and Electro-Optics (CLEO),” p. JTh2A.12. 2015. DOI: 10.1364/CLEO_AT.2015.JTh2A.12.

[4] S. Rauch, L. Drzewietzki, A. Klehr, J. Sacher, W. Elsäßer and S. Breuer. “Timing jitter reduction of a two-section external-cavity semiconductor laser by harmonic mode-locking and optical feedback.” In “Conference on Lasers and Electro-Optics Europe (CLEO),” p. CB8.4. 2015.

[5] C. Weber, L. Drzewietzki and S. Breuer. “Increased nonlinear-imaging signal-intensity by amplitude-modulated mode-locking.” In “Conference on Lasers and Electro-Optics Europe (CLEO),” p. CB.P.20. 2015.

[6] S. Breuer, M. Rossetti, L. Drzewietzki, I. Montrosset, M. Krakowski, M. Hopkinson and W. Elsäßer. “Investigations on photocurrent bi-stability of a two-color mode-locked quantum dot laser.” In “16th International Conference on Transparent Optical Networks (ICTON),” pp. 1–4. 2014. DOI: 10.1109/icton.2014.6876378.

[7] M. Gioannini, M. Dommermuth, L. Drzewietzki and S. Breuer. “Dual-state quantum dot laser self-interferometric sensing.” In “24th International Semiconductor Laser Conference (ISLC),” pp. 94–95. 2014. DOI: 10.1109/ISLC.2014.180.

[8] M. Gioannini, M. Dommermuth, L. Drzewietzki and S. Breuer. “Quantum dot laser two-state self-mixing velocimetry: Simulation and experiment.” In “Conference on Lasers and Electro-Optics (CLEO),” p. SF2G.2. 2014. DOI: 10.1364/CLEO_SI.2014.SF2G.2.

[9] X. Porte, M. C. Soriano, I. Fischer, S. Breuer, L. Drzewietzki and W. Elsäßer. “Scaling Properties of the Dynamics of Semiconductor Lasers in External Cavities.” In “24th International Semiconductor Laser Conference (ISLC),” pp. 135–136. 2014. DOI: 10.1109/ISLC.2014.200.

[10] C. Weber, L. Drzewietzki, I. Montrosset, D. Syvridis, M. Krakowski, I. Krestnikov, D. Livshits, E. U. Rafailov, W. Elsäßer and S. Breuer. “Experimental investigations on the generation and amplification of high power short pulses by a quantum dot laser and amplifier.” In “International Conference on Transparent Optical Networks,” pp. 1–3. 2014. DOI: 10.1109/icton.2014.6876659.

[11] L. Drzewietzki, S. Breuer and W. Elsäßer. “Self-stabilization of mode-locked quantum-dot lasers by time-delayed opto-electronic feedback.” In “Conference on Lasers and Electro-Optics (CLEO),” p. CTh4G.4. 2013. DOI: 10.1364/CLEO_SI.2013.CTh4G.4.

[12] L. Drzewietzki, S. Breuer, M. Rossetti, T. Xu, P. Bardella, H. Simos, C. Mesaritakis, M. Ruiz, I. Krestnikov, D. Livshits, M. Krakowski, D. Syvridis, I. Montrosset, E. Rafailov and W. Elsäßer. “Picosecond pulse generation with 34W peak power using a monolithic quantum-dot tapered mode-locked laser and

tapered optical amplifier.” In “Conference on Lasers and Electro-Optics Europe (CLEO),” p. CB4.2. 2013. DOI: 10.1109/CLEOE-IQEC.2013.6800704.

[13] S. Breuer, M. Rossetti, L. Drzewietzki, I. Montrosset, M. Hopkinson and W. Elsäßer. “Intra-cavity absorber photocurrent characteristics of a quantum dot laser emitting on two emission-states: experiment and simulation.” In “Proceedings of SPIE,” vol. 8432, pp. 84320H–84320H–8. 2012. DOI: 10.1117/12.927081.

[14] S. Breuer, L. Drzewietzki and W. Elsäßer. “Extended ground-state and excited-state carrier dynamics control in a mode-locked two-section quantum dot laser: Joining absorber reverse-bias and resistor self-electro-optic effect (SEED) emission-state regimes.” In “Conference on Lasers and Electro-Optics Europe (CLEO),” p. CB3.2. 2011. DOI: 10.1109/CLEOE.2011.5942558.

[15] S. Breuer, M. Rossetti, L. Drzewietzki, P. Bardella, I. Montrosset, M. Hopkinson and W. Elsäßer. “Extended ground-state and excited-state emission-state control in a mode-locked two-section quantum dot laser.” In “International Conference on Transparent Optical Networks,” pp. 1–4. 2011. DOI: 10.1109/ICTON.2011.5970825.

[16] L. Drzewietzki, S. Breuer, W. Elsäßer, M. Krakowski and I. Krestnikov. “Investigation of passive electric and optical-feedback stabilization of a passively mode-locked tapered two-section quantum-dot laser.” In “Conference on Lasers and Electro-Optics Europe (CLEO),” p. CB.P.3. 2011. DOI: 10.1109/CLEOE.2011.5942612.

[17] L. Drzewietzki, M. Ruiz, S. Breuer, M. Tran, Y. Robert, M. Rossetti, T. Xu, P. Bardella, W. Elsäßer, M. Krakowski, I. Montrosset and I. Krestnikov. “Passively mode-locked monolithic two-section gain-guided tapered quantum-dot lasers: I. Ultrashort and stable pulse generation.” In “Conference on Lasers and Electro-Optics Europe (CLEO),” p. CB3.3. 2011. DOI: 10.1109/CLEOE.2011.5942559.

[18] M. Gioannini, M. Rossetti, I. Montrosset, L. Drzewietzki, G. Grozman, W. Elsäßer and I. Krestnikov. “Modeling of InAsGaAs QD-SOAs for amplification of ultra-short high power pulses.” In “International Conference on Numerical Simulation of Optoelectronic Devices (NUSOD),” pp. 171–172. 2011. DOI: 10.1109/NUSOD.2011.6041200.

[19] S. Breuer, M. Rossetti, W. Elsäßer, L. Drzewietzki, P. Bardella, I. Montrosset and M. Hopkinson. “Reverse ground-state excited-state emission transition dynamics in two-section quantum dot semiconductor lasers: Simultaneous two-state mode-locking and state-switching via a resistor Self-Electro-optic Effect Device (SEED).” In “IEEE International Semiconductor Laser Conference (ISLC),” pp. 65–66. 2010. DOI: 10.1109/ISLC.2010.5642749.

[20] S. Breuer, M. Rossetti, W. Elsäßer, L. Drzewietzki, P. Bardella, I. Montrosset, M. Krakowski and M. Hopkinson. “Reverse ground-state excited-state transition dynamics in two-section quantum dot semiconductor lasers: mode-locking and state-switching.” In “Proceedings of SPIE,” vol. 7720, pp. 772011–772011–10. 2010. DOI: 10.1117/12.854418.

[21] S. Breuer, M. Rossetti, W. Elsäßer, L. Drzewietzki, P. Bardella, I. Montrosset, M. Krakowski and M. Hopkinson. “Two-state passive mode-locking of quantum dot semiconductor lasers: Classical state scenario and novel reverse state dynamics.” In “International Conference on Transparent Optical Networks,” pp. 1–4. 2010. DOI: 10.1109/ICTON.2010.5549102.

[22] L. Drzewietzki, G. The, S. Breuer, M. Gioannini, W. Elsäßer, I. Montrosset, M. Hopkinson and M. Krakowski. “Joint theoretical and experimental investigations of the CW lasing and turn-on dynamics of a quantum-dot semiconductor laser.” In “Conference on Lasers and Electro-Optics Europe (CLEO),” p. CB3.2. 2009. DOI: 10.1109/CLEOE-EQEC.2009.5194650.

Deutsche Zusammenfassung

Die zeitliche Stabilität eines optischen Pulszugs, welcher von einem modengekoppelten Laser erzeugt wird, ist für alle zeitkritischen Anwendungen wichtig. Ein Maß für die zeitliche Instabilität ist die Periodenschwankung. Diese Periodenschwankung hat ihre Ursache primär in der Spontanemission. Um diese Periodenschwankungen zu verringern existiert eine Vielzahl an Stabilisierungsmöglichkeiten. Hierbei spielt die optische Rückkopplung eine wichtige und verbreitete Rolle. Der Einfluss der optischen Rückkopplung auf die Periodenschwankung wurde in der Litaratur experimentell und in numerischen Simulationen untersucht. Eine qualitative als auch quantitative Erklärung der Verringerung der Periodenschwankungen konnte bisher allerdings nicht gefunden werden.

In dieser Arbeit wird eine systematische Untersuchung verschiedener ausgewählter Rückkopplungskonfigurationen und insbesondere der optische Rückkopplung durchgeführt, welche es letztendlich erlaubt, den Mechanismus zu identifizieren und zu quantifizieren, welcher für die Verringerung der Periodenschwankungen verantwortlich ist. Der dabei erhaltene Zugewinn an Wissen wird durch eine Kombination aus speziell ausgewählten Experimenten und durch die Entwicklung eines entsprechenden einfachen und intuitiven Modells und den damit erhaltenen Simulationsergebnissen erreicht.

Dieser Reduktionsmechanismus der Periodenschwankungen wird unter anderem für den wichtigsten Fall der optischen Rückkopplung identifiziert und es kann herausgefunden werden, dass dieser auf zwei Effekten basiert. Einerseits findet eine Wechselwirkung zwischen der zeitlichen Phase des optischen Pulses im Resonator und des rückgekoppelten Pulses statt, welche zu einer gemittelten zeitlichen Phase des resultierenden Gesamtpulses führt. Im Modell wird nur diese eine Wechselwirkung bewusst implementiert. Solch eine Wechselwirkung ist bei hoch entwickelten Modellen automatisch und intrinsisch gegeben. Kohärenz ist für solch eine Wechselwirkung nicht notwendig. Die gemittelte zeitliche Phase des resultierenden Gesamtpulses repräsentiert einen statistischen Effekt welcher sich aus der reduzierten statistischen Korrelation der zeitlichen Phase zwischen beiden Pulsen ergibt, welche ihre Ursache in der langen Verzögerungsdauer der optischen Rückkopplung hat. Diese reduzierte Korrelation resultiert zusammen mit der wechelwirkung der zeitlichen Phase in reduzierten Periodenschwankungen. Die Einfachheit des entwickelten Modells erleichtert im Gegensatz zu hoch entwickelten und damit komplexen Modellen den Erkenntnisgewinn. Insbesondere ermöglichen die meisten Modelle aufgrund der erforderlichen langen Rechenzeiten nicht den Zugang zu der langen Verzögerungsdauer welche erforderlich ist, um den statistischen Effekt des Mechanismus der Periodenschwankungsreduktion zu beobachten.

Neben dieser zeitlichen Stabilität des optischen Pulszugs spielt die Stabilität der Amplitude des Pulszugs eine essentielle Rolle für viele Anwendungen. In der Tat ist die passive Modenkopplung kein automatisch stabiler Prozess, sondern erfordert ein delikates Gleichgewicht einer Vielzahl an Parametern. Solche ungewünschten Amplitudeninstabilitäten äußern sich oft im Güteschalten oder in der gütegeschalteten Modenkopplung und stellen immer noch ein unerwünschtes Phänomen für eine Vielzahl an Lasertypen dar und sind immer noch Gegenstand experimenteller und theoretischer Untersuchungen. Wenn die Amplitudenstabilität eines Lasers nicht durch korrekte Projektierung erreicht werden kann müssen nachträgliche, externe, aktive und aufwändige Maßnahmen durchgeführt werden.

In dieser Arbeit wird eine einfache und passive optoelektrische Schleife präsentiert, untersucht und erklärt, welche in der Lage ist, Amplitudeninstabilitäten passiv modengekoppelter Halbleiterlaser zu reduzieren. Dieser optoelektrischer Ansatz besteht aus einem Hochpassfilter welcher die Aborbersektion des Halbleiterlasers erdet und damit wie ein differentieller Photostromempfänger und Regler wirkt. Die beobachtete Reduktion der Amplitudeninstabilitäten resultiert aus der Reduktion der dynamischen Ansammlung der photoerzeugten Ladungsträger und dämpft damit Niederfrequenzfluktuationen. Hierbei wird die Absorbersektion gleichzeitig als Photodiode und Kontrollelement genutzt indem der ungewünschte photogenerierte Wechselstrom am Absorber geerdet wird. Diese Schaltung kann als differentielle, passive Kontrollschleife angesehen werden, die die Änderungen des Photostroms verringert und damit starke Oszillationen der Ausgangsleistung unterdrückt.

Nach der Entwicklung eines Verständnisses der Periodenschwankungen und der Untersuchung der Möglichkeiten der Reduktion dieser Periodenschwankungen als auch durch die Demonstration einer einfachen experimentellen Möglichkeit der Reduktion von Amplitudeninstabilitäten von passiv modengekoppelten Halbleiterlasern kann das erweiterte Potential in Bezug auf die Erzeugung von ultrakurzen Pulsen mit hoher Leistung durch neuartige trapezförmige quantenpunktbasierte modengekoppelte Halbleiterlaser als auch durch neuartige trapezförmige quantenpunktbasierte optischen Verstärker ausgenutzt werden. Das Ziel ist es, Anwendungen erreichen zu können, die im Moment von Festkörperlasern bedient werden. Ein solcher Anwendungsbereich ist die biomedizinische nichtlineare Mikroskopie wobei günstige, kompakte und robuste Pulsquellen für eine weite Verbreitung vorteilhaft wären. Hierbei bieten quantenpunktbasierte Quellen die ideale Wellenlänge um hohe optische Eindringtiefen zu erreichen.

In dieser Arbeit wird die Erzeugung ultrakurzer Pulse durch neuartige gewinngeführte trapezförmige modengekoppelte Halbleiterlaser mit einem Schwerpunkt auf zeitliche Stabilität, Amplitudenstabilität, optische Pulslänge und Pulsspitzenleistung untersucht. Diese gewinngeführten Strukturen bieten den Vorteil einer vereinfachten Herstellung. Weiterhin wird die Verstärkungsfähigkeit neuartiger gewinngeführter trapezförmiger quantenpunktbasierter optischer Verstärker untersucht. Die erzielten Ergebnisse demonstrieren Erzeugung und Verstärkung ultrakurzer Pulse mit Pulsspitzenleistungen die unmittelbares Anwendungspotential bieten.

Neben all diesen systematischen Untersuchungen, der Entwicklung einer verständlichem, nützlichen und simplen aber trotzdem effektiven Stabilisierungsmethode für Amplitudenfluktuationen und der Demonstration der exzellenten Leistungsfähigkeit der neuartigen trapezförmigen quantenpunktbasierten modengekoppelten Laser und optischen Verstärker ergeben sich weitere interessante Untersuchungen für die Zukunft.

Halbleiterbasierte sättigbare Absorberspiegel werden weitläufig genutzt um Modenkopplung von Festkörperlasern zu ermöglichen. Der hier vorgestellte passive elektrische Stabilisierungsansatz könnte für elektrisch kontrollierbare halbleiterbasierte sättigbare Absorberspiegel angewendet werden, um die Stabilisierungseigenschaften dieser Lasersysteme zu untersuchen.

Das entwickelte einfache Modell für die Periodenschwankungen könnte durch Hinzufügen der Simulation von Amplitudeninstabilitäten erweitert werden, um weitere Erkenntnisse der Wechselwirkung von Amplitudeninstabilität und Periodenschwankungen zu untersuchen.

Von der Blickrichtung des Verständnisses aus wäre es spannend zu untersuchen wie sich die optische Rückkopplung auf die Periodenschwankungen in verschiedenen Betriebszuständen des modengekoppelten Lasers auswirkt. Das wird motiviert durch die hier gewonnenen Ergebnisse, die zeigen, wie durch verstimmte optische Rückkopplung die Pulsdynamik untersucht werden kann.

Dadurch, dass quantenpunktbasierte modengekopplete Halbleiterlaser und Verstärker eine reichhaltige Dynamik auf unterschiedlichen Zeitskalen aufweisen, bieten sie die Möglichkeit, diese zu untersuchen als auch die auftretende Amplituden- und Zeitdynamik des erzeugten optischen Pulszugs zu kontrollieren, was einerseits einen tieferen Einblick in die zugrundeliegenden Mechnismen als auch andereseits die Verbesserung der Stabilität des Pulszugs ermöglicht.

Lebenslauf

Persönliche Daten

Name	Lukas Drzewietzki
Geburtsort	Nikolai, Polen

Chronologie

seit 05.2008	Wissenschaftlicher Mitarbeiter und Doktorand, Arbeitsgruppe Halbleiteroptik, Institut für angewandte Physik, Technische Universität Darmstadt
02.2008	Physikdiplom, Technische Universität Darmstadt
10.2001 - 02.2008	Physikstudium, Technische Universität Darmstadt
09.1991 - 06.2000	Abitur, Immanuel Kant Schule, Rüsselsheim